Theoretische Physik

Thin-Film Modelling of Complex Fluids and Bacterial Colonies

Inaugural-Dissertation
zur Erlangung des Doktorgrades
der Naturwissenschaften im Fachbereich Physik
der Mathematisch-Naturwissenschaftlichen Fakultät
der Westfälischen Wilhelms-Universität Münster

angefertigt im Rahmen eines Cotutelle-Verfahrens
zwischen der Westfälischen Wilhelms-Universität Münster
und der Communauté Université Grenoble Alpes

vorgelegt von
Sarah Christine Trinschek
aus Hamm

2018

Communauté UNIVERSITÉ Grenoble Alpes

WWU MÜNSTER

THÈSE

Pour obtenir le grade de

DOCTEUR DE LA

COMMUNAUTÉ UNIVERSITÉ GRENOBLE ALPES

préparée dans le cadre d'une cotutelle entre la *Communauté Université Grenoble Alpes* et le *Westfälische Wilhelms-Universität Münster*

Spécialité : **Physique de matière condensée et du rayonnement**

Arrêté ministériel : le 6 janvier 2005 – 25 mai 2016

Présentée par

Sarah Christine Trinschek

Thèse dirigée par **Uwe Thiele** et **Chaouqi Misbah**
et codirigée par **Karin John**

préparée au sein du **Laboratoire Interdisciplinaire de Physique**
et de **l'Institut für Theoretische Physik**

dans **l'École Doctorale de Physique**

Modélisation de films minces de fluides complexes et de colonies bactériennes

Thèse soutenue publiquement le 28 mars 2019 devant le jury composé de:

Monsieur Uwe Thiele
Professeur, Westfälische Wilhelms-Universität Münster, Rapporteur

Monsieur Mathis Plapp
Directeur de Recherche, CNRS, École Polytechnique Palaiseau, Rapporteur

Monsieur Jan Vermant
Professeur, ETH Zürich, Rapporteur

Monsieur Lionel Bureau
Chargé de Recherche, CNRS, Laboratoire Interdisciplinaire de Physique, Membre

Madame Cornelia Denz
Professeur, Westfälische Wilhelms-Universität Münster, Présidente du jury

Abstract

Bacteria colonise interfaces by the formation of dense aggregates. In this thesis, we develop and analyse simple models to clarify the role of passive physico-chemical forces and processes - such as osmosis, surface tension effects and wettability - in the spreading of bacterial colonies at solid-air interfaces. In particular, we focus on two spreading mechanisms: The osmotically driven spreading and the promotion of spreading by the presence of bio-surfactants. The models are based on a hydrodynamic description for thin films of liquid mixtures and suspensions that is supplemented by bioactive processes. They explicitly include surface tension effects and wettability.

The first part of the thesis focuses on the osmotic spreading mechanism of bacterial colonies that relies on the generation of osmotic pressure gradients. The bacteria secrete a polymeric matrix which acts as an osmolyte and triggers the influx of nutrient-rich water from the moist substrate into the colony. The analysis of the model shows that in accordance with the experimental observation, the colony first swells and subsequently expands laterally with a nearly constant contact angle at the advancing contact line. In addition, we find that wettability crucially affects the spreading dynamics and determines whether the colony is able to expand laterally over a substrate or not. At low wettability, the expansion is arrested, albeit the colony is biologically active. However, a small reduction of the surface tension and the resulting improvement of the wettability suffices to induce continuous spreading. This can, e.g., result from the production of bio-surfactants, i.e. surface-active molecules, by the bacteria. This is a widespread strategy that allows bacterial colonies to efficiently expand over substrates. In addition to improving the wettability, gradients in the surface concentration of surfactant at the edges of the colony result in Marangoni fluxes that drive cooperative spreading.

In the second part, we lay the groundwork for the incorporation of a non-uniform surfactant concentration into the model by studying passive liquid films covered by insoluble surfactant. We first consider static drops and establish the link between the mesoscopic and macroscopic descriptions of the system by energetic considerations. The requirement of consistency of the two approaches relates the solid-gas interfacial tension in the macroscopic description to the mesoscopic wetting energy. We find that in the presence of surfactants, the structural form of Young's law remains unchanged. However, the surfactant concentrations and the resulting interfacial tensions adapt self-consistently.

In the third part, we develop and study a model for the surfactant-driven spreading of bacterial colonies. The model includes the production of bio-surfactants and accounts for Marangoni fluxes arising due to a non-uniform surfactant concentration. We show that the interplay between wettability and Marangoni fluxes strongly affects the expansion behaviour and morphology of bacterial colonies. The presence of bio-surfactants can enable a bacterial colony to expand laterally under conditions which are otherwise unfavourable. In addition, it may cause an instability of the circular shape of bacterial colonies. We find that variations in the wettability and surfactant production are sufficient to reproduce four different types of colony growth, namely, arrested and continuous spreading of circular colonies, slightly modulated front lines and the formation of pronounced fingers.

In the final part, we take a first step towards the incorporation of active collective bacterial motion in the employed thin-film framework and present a phenomenologically derived model for active polar films. The approach couples a thin-film equation for the film height

to the dynamics of a polarisation field connected to self-propulsion and active stresses. It can describe resting and moving drops of active liquids.

Kurzzusammenfassung

Bakterien können Grenzflächen besiedeln, indem sie dichte Kolonien ausbilden. In dieser Arbeit werden einfache Modelle entwickelt und untersucht, die den Einfluss passiver physikochemischer Kräfte und Prozesse – wie Osmose, Oberflächenspannungseffekte und Benetzbarkeit – auf die Ausbreitung bakterieller Kolonien beleuchten. Der Fokus liegt dabei insbesondere auf zwei Ausbreitungsmechanismen: dem osmotisch getriebenen Spreiten und dem Spreiten angetrieben durch oberflächenaktive Moleküle, sogenannte *Bio-Surfactants*. Diese Mechanismen werden von Bakterienkolonien an Grenzflächen zwischen feuchten Substraten und Atmosphäre ausgenutzt. Die in dieser Arbeit entwickelten Modelle basieren auf einer hydrodynamischen Beschreibung dünner, aus Mischungen und Suspensionen bestehender Flüssigkeitsfilme, die um bioaktive Terme erweitert wird. Sie berücksichtigen daher explizit Oberflächenspannungseffekte und Benetzbarkeit.

Der erste Teil der Arbeit widmet sich dem osmotisch getriebenen Spreiten von Bakterienkolonien, das auf der Erzeugung von osmotischen Druckgradienten beruht. Die Bakterien produzieren extrazelluläre polymere Substanzen, die als Osmolyte wirken und einen Fluss von nährstoffreicher Flüssigkeit aus dem feuchten Substrat in die Kolonie hervorrufen. Die Analyse der entwickelten Modelle zeigt in Übereinstimmung mit experimentellen Befunden, dass die Kolonie zunächst vorrangig vertikal anschwillt und sich anschließend mit einem annähernd konstanten Kontaktwinkel lateral über das Substrat ausbreitet. Es zeigt sich, dass Benetzbarkeit die Spreitdynamik von Biofilmen drastisch beeinflusst und entscheidend dafür ist, ob sich die Kolonie auf dem Substrat ausbreiten kann oder nicht. Bei schlechter Benetzbarkeit wird die laterale Expansion der Kolonie unterdrückt, obwohl die Bakterien biologisch aktiv sind und Wachstumsprozesse stattfinden. Eine leichte Verringerung der Oberflächenspannung und die damit verbundene Verbesserung der Benetzbarkeit kann jedoch ausreichen, um ein laterales Spreiten der Kolonie zu ermöglichen. Dies kann beispielsweise durch Bio-Surfactants geschehen, welche die Eigenschaften der Oberfläche modifizieren. Im Allgemeinen ist die Produktion von Bio-Surfactants eine weitverbreitete Strategie, die Bakterienkolonien eine effektive Ausbreitung ermöglicht. Zusätzlich zur Verbesserung der Benetzbarkeit können Gradienten in der Surfactant-Konzentration am Rand der Kolonie Marangoni-Flüsse hervorrufen, die das Spreiten unterstützen.

Im zweiten Teil der Arbeit werden passive, von unlöslichem Surfactant bedeckte Tropfen untersucht, um die Basis für die Berücksichtigung inhomogener Surfactant-Konzentrationen in der Modellierung zu schaffen. Zunächst werden statische passive Tropfen betrachtet und die in dieser Arbeit verwendete mesoskopische Beschreibungsebene des Systems wird mit einer makroskopischen Beschreibung verknüpft. Aus der Tatsache, dass beide Bilder zu konsistenten Resultaten führen müssen, können Beziehungen zwischen den jeweiligen Größen der beiden Beschreibungsebenen abgeleitet werden. Im Speziellen wird gezeigt, dass die Eigenschaften der mesoskopischen Benetzungsenergie mit der makroskopischen Oberflächenspannung der Grenzfläche zwischen Substrat und Atmosphäre verknüpft sind. Aus energetischen Überlegungen zu statischen Tropfen kann abgeleitet werden, dass die Struktur des Youngschen Gesetzes im Vergleich zum Surfactant-freien Fall unverändert bleibt. Die Surfactant-Konzentrationen auf dem Tropfen sowie auf der umliegenden Absorptionsschicht passen sich jedoch selbstkonsistent mit den daraus resultierenden Grenzflächenspannungen an.

Im nächsten Schritt wird ein Modell für das Surfactant-getriebene Spreiten bakterieller

Kolonien entwickelt und analysiert. Dieses berücksichtigt die Produktion von Bio-Surfactants durch die Bakterien und die aus einer nicht-homogenen Surfactant-Verteilung resultierenden Marangoni-Flüsse. Es zeigt sich, dass das Zusammenspiel zwischen Benetzbarkeit und Marangoni-Flüssen die Ausbreitungsdynamik und Morphologie bakterieller Kolonien stark beeinflusst. Die Produktion von Bio-Surfactants kann die laterale Expansion unter für die Bakterien ansonsten ungünstigen Bedingungen ermöglichen. Zusätzlich bewirkt sie eine Instabilität der kreisrunden Form der Kolonie. Die Analyse des Modells zeigt, dass Variationen von Benetzbarkeit und Surfactant-Produktion ausreichen, um vier verschiedene Arten von Wachstum zu reproduzieren: Kolonien, deren laterales Spreiten verhindert wird, spreitende Kolonien mit kreisrunder oder leicht modulierter Form sowie die Ausbildung ausgeprägter Finger im Höhenprofil.

Im letzten Teil der Arbeit wird ein phenomenologisches Modell für aktive polare Flüssigkeiten hergeleitet, das einen ersten Schritt hin zur Einbeziehung der aktiven kollektiven Bewegung der Bakterien in die entwickelte Dünnfilm-Beschreibung der Kolonien darstellt. Das Modell verknüpft die Dynamik der freien Grenzfläche mit der eines Polarisationsfeldes, das den Eigenantrieb der Bakterien und aktive Spannungen beschreibt. In einer ersten Analyse des Modells werden ruhende und bewegte aktive Flüssigkeitstropfen untersucht.

Résumé

Les bactéries se répandent aux interfaces en formant des colonies, qui peuvent être considérées comme des suspensions denses actives. L'objet de cette thèse est le développement et l'analyse de modèles simples pour élucider le rôle des phénomènes physico-chimiques et passifs - tels que l'osmose, la tension de surface et le mouillage - dans l'expansion des colonies bactériennes aux interfaces solide/air. En particulier, nous nous sommes penchés sur deux mécanismes qui ont été bien étudiés sur le plan expérimental : le gonflement osmotique et les écoulements de Marangoni. Les modèles proposés dans cette thèse sont basés sur une description hydrodynamique des couches minces de suspensions liquides, qui incluent explicitement les effets de tension de surface et de mouillage. Ce cadre de phénomènes purement passifs est complété par des processus bioactifs.

La première partie de la thèse porte sur le mécanisme d'expansion osmotique des biofilms. Dans ce mécanisme, la bactérie sécrète une matrice polymérique qui agit comme un osmolyte et entraîne un afflux d'eau, riche en nutriments, du substrat humide vers le biofilm. L'analyse du modèle montre que, conformément à l'observation expérimentale, la colonie gonfle d'abord et se dilate ensuite latéralement avec un angle de contact d'avancement presque constant. De plus, nous avons constaté que la mouillabilité du substrat est une des déterminantes principales de la vitesse d'expansion du biofilm. En-dessous d'une mouillabilité critique l'expansion s'interrompt, bien que la colonie soit biologiquement active. Cependant, une légère réduction de la tension de surface et une amélioration de la mouillabilité qui en résulte suffisent à induire un étalement continu. Or, il a été démontré expérimentalement que les bactéries peuvent activement contrôler la tension de surface par la production de *bio-surfactants*, c'est-à-dire de molécules tensioactives. Il s'agit d'une stratégie répandue qui permet aux colonies bactériennes de s'étendre efficacement sur les substrats. En plus d'améliorer la mouillabilité, les gradients dans la concentration surfacique de molécules tensioactives aux bords de la colonie peuvent entraîner des écoulements de Marangoni qui favorisent l'expansion coopérative.

Dans la deuxième partie, nous nous sommes intéressés à l'effet de molécules tensioactives sur l'état d'équilibre d'une goutte de liquide simple sur une surface solide. Cette étude nous a aidé à établir, via des considérations énergétiques, le lien entre les descriptions mésoscopique et macroscopique pour des gouttes recouvertes de molécules tensioactives. L'exigence de cohérence des deux approches relie la tension interfaciale solide-gaz dans la description macroscopique à l'énergie de mouillage mésoscopique. Nous avons constaté qu'en présence d'agents tensioactifs, la forme structurelle de la loi d'Young reste valable. Cependant, les concentrations en agents tensioactifs et les tensions interfaciales qui en résultent s'adaptent d'une manière cohérente.

Dans la troisième partie, nous avons développé et étudié un modèle pour l'expansion de colonies bactériennes aidée par des molécules biologiques tensioactives auto-produites. Le modèle inclut la production de ces *bio-surfactants* et tient compte des flux de Marangoni résultant d'une concentration non uniforme de molécules tensioactives. Nous avons montré que l'interaction entre la mouillabilité et les flux de Marangoni affecte fortement le comportement d'expansion et la morphologie des colonies bactériennes. La présence de *bio-surfactants* permet à une colonie bactérienne de s'étaler latéralement dans des conditions qui, sinon, seraient défavorables. De plus, elle peut provoquer une instabilité de la forme axi-symétrique des colonies bactériennes. Malgré étant très simple, notre modèle

nous a permis de reproduire quatre modes de développement différentes, qui ont été observés expérimentalement, à savoir l'étalement arrêté et continu des colonies circulaires, l'étalement des colonies avec des bords légèrement modulées et la formation de doigts prononcés.

Dans la dernière partie, nous avons fait un premier pas vers l'incorporation de la motilité actif des bactéries dans notre modèle. La motilité rajout un nouveau élément au modèle: une direction de polarisation relié à la propulsion. Nous présentons donc un modèle phénoménologique pour un film mince active. L'approche associe une équation pour l'évolution de une surface libre à la dynamique d'un champ de polarisation. Avec ce modèle préliminaire nous avons pu décrire des gouttes de liquides actifs au repos et en mouvement en fonction de l'état de polarisation.

Contents

Contents

1. Introduction

1.1. Surface Tension Effects and Wetting

Phenomena based on surface tension effects and wetting are observed in our day-to-day life: Beads of droplets grace spider webs catching the morning dew, bubbles are created in soap water and 'tears of wine' form at glasses filled with an alcoholic beverage. Liquids represent a state of condensed matter in which the molecules experience mutual attraction. At a liquid-air interface, the cohesive attraction between liquid molecules is larger than their adhesive attraction to the molecules in the air. The balance of adhesion and cohesion results in an effective energy of the liquid-gas interface, also called *interface* or *surface tension*. This interface energy is, e.g., responsible for the spherical shape of small (free) liquid droplets that minimises their surface area [dGBWQ04]. In the presence of other forces, e.g. gravity, deviations from the spherical shape occur.

When a drop of liquid is deposited on a solid substrate, the situation becomes more complicated and different *wetting* scenarios may occur. Whether the droplet wets the substrate or not, is determined by a force balance at the three-phase contact line between the liquid, the solid substrate and the surrounding gaseous phase [dGBWQ04]. One speaks of complete wetting if the droplet spreads until a macroscopic uniform liquid layer covers the whole solid substrate as, e.g., water on clean glass. If the substrate is less wettable as, e.g., in the case of water on plastic, the liquid forms a drop with a finite *contact angle* θ_{eq} as depicted in Fig. 1.1. For contact angles $0° < \theta_{eq} < 180°$, this behaviour is classified as partial wetting. The contact angle can be determined from the famous Young's law [You05] that relates the macroscopic angle and the interfacial tensions of the three involved interfaces. The extreme case of a contact angle that approaches $180°$ is called non-wetting.

When the interfacial tension is not constant along the surface of the film or droplet (which may, e.g., be caused by a non-uniform temperature) additional longitudinal forces at the interface render the situation more complicated. These so-called *Marangoni stresses* - named after the Italian physicist Carlo Marangoni - cause hydrodynamic fluxes that drive the liquid from regions of lower surface tension to regions of higher surface tension [dGBWQ04].

complete wetting   partial wetting   non-wetting
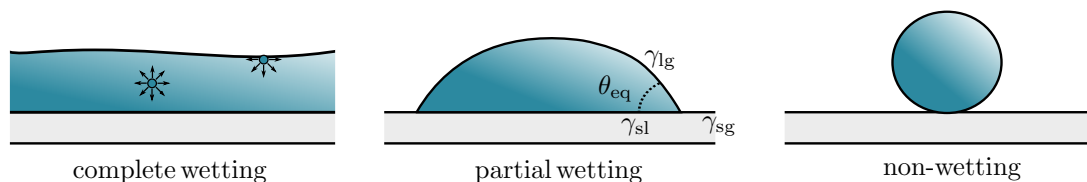
Figure 1.1.: Sketch of three possible wetting scenarios. The contact angle increases from complete wetting ($\theta_{eq} = 0°$) over partial wetting to non-wetting ($\theta_{eq} = 180°$). At liquid–air interfaces, surface tension results from the greater attraction of liquid molecules to each other than to the molecules in the air as sketched in the left picture. The macroscopic contact angle θ_{eq} can be determined from the interfacial tensions γ_{sl}, γ_{sg} and γ_{lg} of the three involved interface, namely the solid-liquid, the solid-gas and the liquid-gas interface, respectively.

Marangoni stresses can also be caused by the presence of so-called *surfactants*. These amphiphilic molecules consist of a hydrophilic head and a hydrophobic tail and adsorb to interfaces, thereby lowering their surface tension. They may act as detergents, wetting agents, emulsifiers, foaming agents or dispersants [RK12]. A non-uniform concentration of surfactants at an interface gives rise to surface tension gradients and Marangoni flows. In situations in which such surface forces dominate over bulk forces, surface tension and wetting become important effects. Two of the most famous examples observed in nature are shown in Fig. 1.2 (a) and (b). For leaves of the lotus plant, dirt particles are picked up by water droplets rolling down their superhydrophobic surface that results from its micro- and nanoscopic architecture [KBB08]. Another example are water striders - small insects that are adapted for life on the surface of stagnant water. They use surface tension to their advantage so they can "walk on water" [HCB03]. The physics of wetting can, however, also serve to understand the dynamics of processes occurring in active living systems on a smaller length scale. In the context of cancer aggregates spreading on a solid surface, the collective cell migration can be modelled as the spreading of viscoelastic droplets [DGN+11]. Recently, it has been shown that also in the embryogenesis of the zebrafish, collective cell migration follows the laws of wetting [WTY+18]. In this system, epiboly starts with a cluster of cells at one pole of the spherical egg yolk as shown in Fig. 1.2 (c). These cells are actively spreading in a continuous movement toward the other pole of the yolk until they fully cover it [KBK+95, MGB+17]. By determining the contact angle between the cells and the yolk and assuming that an interfacial force balance holds during the quasi-static spreading process, one can draw conclusions about the biological processes that change the interfacial tensions.

Another example of a biological system for which surface tension and wettability can play an important role are bacterial colonies. In this thesis, we develop and analyse simple mathematical models to clarify the influence of these passive physical forces on the spreading dynamics of living bacterial colonies.
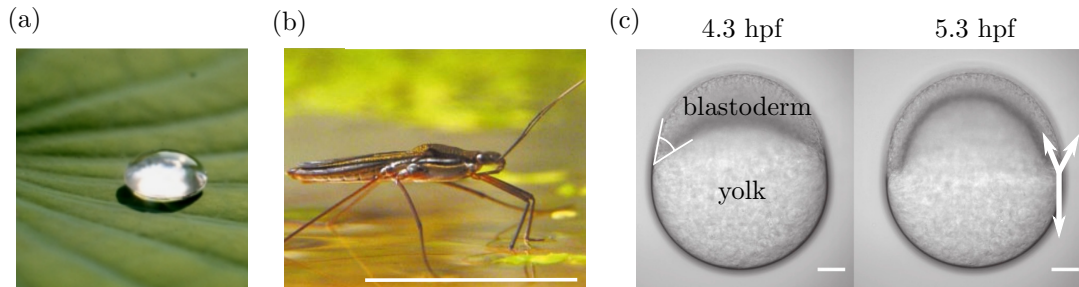
Figure 1.2.: Examples of natural phenomena connected to surface tension and wettability. (a) The micro- and nanoscopic architecture of its surface render the leaves of the lotus plant superhydrophobic, resulting in self-cleaning properties. Reprinted with permission from [EDKNB11] © Beilstein-Institut (2011). (b) Water striders use surface tension to their advantage to "walk on water" (scale bar: 1cm). Reprinted with permission from [HCB03] © Springer Nature (2004). (c) In the embryogenesis of the zebrafish, collective cell migration follows the laws of wetting. Driven by a modification of the interfacial tensions over time, the initial cluster of cells located at one pole of the yolk actively spreads in a continuous movement towards the other pole until the yolk is fully covered (scale bar: 100μm). Adapted with permission from [WTY+18] © Biophysical Society (2017).

1.2. Bacterial Colonies as Complex Fluids

Bacteria are able to colonise interfaces by the formation of dense aggregates. After the attachment of individual bacteria to the interface, they proliferate and a colony starts to form. The resulting multi-cellular lifestyle has advantages over individual bacteria as it offers protection against unfavourable environmental conditions. Additionally, growth and survival can be optimised by having different specialised cell types performing several different functions. Bacterial colonies develop at various kinds of interfaces and are often found on solid substrates submerged in a fluid. Here, we focus on colonies growing on moist solid substrates in contact with a gas phase. When nutrients become scarce, very motile colonies can rapidly reach novel nutrient sources by expanding along the interface. In many cases, the active motion of individual bacteria is important for the expansion of the colony. Bacteria can move across surfaces by employing various types of motility, including swimming, twitching or gliding [Kea10]. In general, the active self-propulsion of bacteria can give rise to interesting effects such as bacterial turbulence [WDH+12], large-scale vortex structures [WWD+13] or dynamical clustering and phase separation [ZBFS10]. In rapidly expanding *swarming* colonies, bacteria move collectively by rotating flagella and form groups of parallely oriented elongated cells called rafts [Kea10]. Swarming bacteria form various types of macroscopic colony patterns as shown in Fig. 1.3. A famous example is the characteristic bull's eye formed by *P. mirabilis* that results from cyclic waves of motility followed by a period of swarming cessation. Other possible patterns include featureless swarms, the formation of dendrites or spiraling vortices as for example observed in *P. vortex* bacteria [Kea10].

(a)   (b)   (c)   (d)   (e)
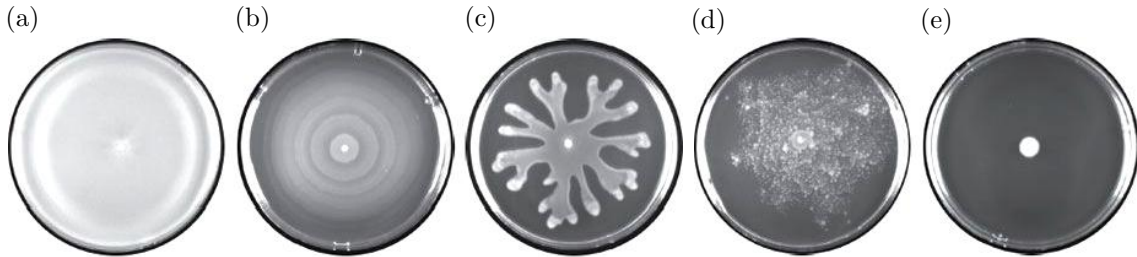
Figure 1.3.: Macroscopic colony patterns formed by different bacterial strains. (a) Featureless mat formed by *Bacillus subtilis*. (b) Bull's eye patterns formed by *Proteus mirabilis*. (c) Dentrites formed by *Pseudomonas aeruginosa*. (d) Vortex structure formed by *Paenibacillus vortex*. (e) A non-swarming mutant of *Bacillus subtilis*. Reprinted with permission from [Kea10] ©︎ Springer Nature (2010).

Another strategy of bacteria to deal with nutrient limitation is the formation of *biofilms*, relatively sessile communities that only expand slowly over the substrate.[1] In this colony type, the bacteria are embedded in a self-produced extracellular matrix that consists of polysaccharides, bio-surfactants, peptides and proteins. Figure 1.4 (a) shows high resolution images of biofilms. For the wild type, the bacterial cells are surrounded by the extracellular matrix that is absent in a mutant strain deficient in matrix production. The matrix protects the bacteria and determines the mechanical properties of the biofilm, which govern its morphogenesis and allow it to resist mechanical stresses [FW10]. Although the

---

[1]Note that the usage of the terms 'biofilms' and 'swarming colonies' is not entirely uniform in the literature. Here, we use 'bacterial colonies' as a generic term (that includes all expansion modes) and 'biofilm' when explicitly referring to slowly expanding colonies that produce an extracellular polymeric matrix.

morphologies of biofilms vary wildly, the ability to form highly structured colonies is correlated with the production of the extracellular matrix by the bacteria [BVFK05]. Figure 1.4 (b) shows a *Bacillus subtilis* biofilm grown on an agar substrate. In the middle of the mature colony, a complex wrinkled morphology occurs that is thought to facilitate the transport of liquid through the colony [AKR⁺12, WZDV⁺13].

The decision, whether a bacterial colony expands rapidly as a swarming colony or forms a slowly spreading biofilm is determined by cell density and environmental conditions such as the nature and rigidity of the underlying substrate and the availability of nutrients. For many bacterial strains, the two modes are oppositely regulated [VBD⁺08] and coupled to quorum sensing – a process that allows for a basic communication between cells by the production of signalling molecules [DVM04]. The thickness of bacterial colonies ranges from ten to a thousand times that of a single bacterium. Typically, the horizontal extension is much larger (see Fig. 1.4 (c)).

(a) (b) (c)

wild type   matrix-deficient
                mutant
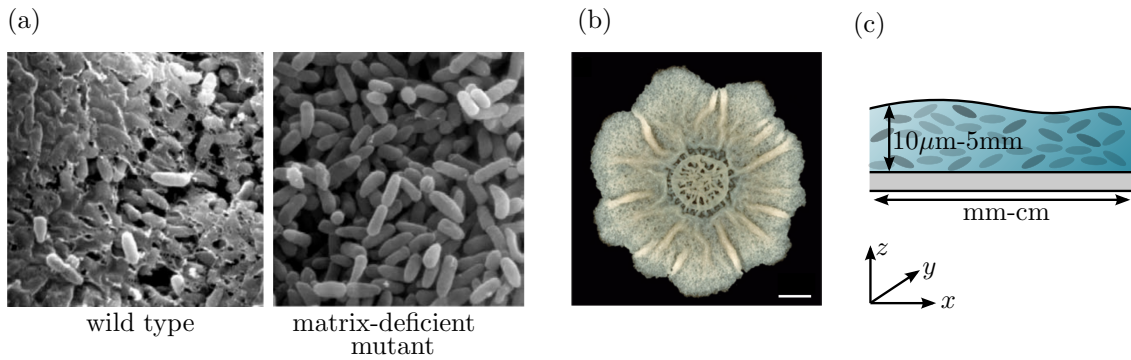
Figure 1.4.: (a) Biofilms formed by wild-type *Pseudomonas aeruginosa* (left) and a matrix-deficient mutant (right) visualised by scanning electron microscopy. Reprinted with permission from [BVFK05] © Elsevier (2005). (b) Top-down view of a *Bacillus subtilis* biofilm grown on agar for 7 days (scale bar: 2mm). Reprinted with permission from [VCB⁺13] © Springer Nature (2013). (c) The thickness of bacterial colonies that ranges from ten to a thousand times that of a single bacterium is typically much smaller than the horizontal extension of the colony.

From the viewpoint of soft matter physics, bacterial colonies can be seen as *complex fluids* consisting of self-propelled colloidal particles (describing the bacteria) embedded in a polymer gel or fluid. This interpretation facilitates the understanding of some of their properties and observed dynamical effects [WAS⁺11]: One example is the control of the structure and mechanical properties of the colony. In general, the equilibrium water content of polymer gels is determined by their composition. As bacteria can tune the polymer or surfactant concentration of the self-produced polymeric matrix in response to environmental conditions, they can in this manner regulate the water concentration in the colony which governs its mechanical properties. When modulating the material properties locally, e.g., in response to spatial heterogeneities in the concentration of nutrients, oxygen or intercellular signalling molecules, spreading forces can be generated [WAS⁺11]. Indeed, the spreading of the colony is in many cases not driven by the active motion of individual bacteria but rather by growth processes and passive flows that result from the physico-chemical properties of the bacterial film and the substrate [SSDC02, YTST17].

One well-studied example is the *osmotic spreading of biofilms* growing on moist substrates. In general, osmosis is the transport of solvent across an interface that can not be passed by the solute. In bacterial colonies, the osmotic spreading mechanism relies on the gen-

eration of osmotic pressure gradients between the colony and the underlying substrate [TJT16, TJLT17]. The extracellular matrix secreted by the bacteria acts as an osmolyte and triggers the influx of nutrient-rich water from the moist agar substrate. This leads to a subsequent swelling and spreading of the colony [SAW$^+$12, YTST17, TJT16, DTH14, YNS$^+$17]. *Bacillus subtilis* colonies that employ the osmotic spreading mechanism first swell (mainly) vertically. Subsequently, they expand laterally over the substrate with a nearly constant contact angle [SAW$^+$12]. Experiments show that in some situations, surface forces determine whether a biofilm is able to expand over a substrate or not [TJLT17]. At low wettability, arrested spreading can be observed, i.e. the lateral expansion of the biofilm is restricted, albeit the colony is biologically active. However, a small reduction in surface tension suffices to induce continuous spreading [TJLT17].

For many bacterial strains, the chemical signalling molecules involved in the quorum sensing mechanism have been found to play a double role. Besides allowing for a cell-cell communication, they act as bio-surfactants at physiologically relevant concentrations [RR01, RDBNO10]. The surface-active nature of these molecules [DRH$^+$06] can be employed by the bacteria to modify the surface tension of the colony and generate fluid flows [DDFMV15]. Bio-surfactants promote the spreading of bacterial colonies in two ways: Measurements of surface tension and contact angle indicate that they improve the wettability [KHC$^+$15, LMB$^+$06]. In addition, gradients in surfactant concentration at the edges of the colony give rise to outward-pointing Marangoni flows which further drive the expansion [DDFMV15]. For *Bacillus subtilis* and *Pseudomonas aeruginosa* colonies, it was shown by genetic and physico-chemical experiments [KSF03, CSO05, ARK$^+$09, FPB$^+$12, YTST17] that the surface tension gradient induced by the respective bio-surfactants *surfactin* and *rhamnolipids* is important for the spreading of the colony [TJT18]. In the surfactant-assisted spreading of liquid drops, Marangoni flows are known to cause a front instability that gives rise to fingering [MC09, ML81, TWS89]. Therefore – besides enhancing the spreading speed – Marangoni flows may also be the cause for the striking dendritic or finger-like patterns of bacterial colonies observed in experiments [TJT18]. Genetic experiments [FPB$^+$12] show that surfactant-producing *Pseudomonas aeruginosa* wild-type colonies spread outwards and form pronounced fingers. A mutant strain deficient in surfactant production is arrested in a small circular shape and cannot expand.

In natural and industrial processes, almost every moist surface with some nutrients is prone to the formation of bacterial colonies. On the one hand, they can be beneficial and are for example employed in waste-water treatment [RM12]. On the other hand, they are responsible for various problems such as medical implant infections, tooth-decay or fouling during industrial processes [Don02]. The widespread occurrence of bacterial colonies led to the development of a variety of theoretical models in the past decades (for reviews see for example [PVL03, WZ10, HL14]) designed to understand the physico-chemical and biological principles of their formation and spreading at different types of interfaces. They are based on a broad spectrum of modelling approaches depending on the specific problem to be solved. The approaches include reaction-diffusion models [KMM$^+$97, GKCBJ98, MSM00], stochastic models based on diffusion-limited aggregation [MF90, BJST$^+$94], discrete dynamical models which implement biological rules in a cellular automaton [WC97, PVLH$^+$98, Her01], individual-based biofilm models [KPWvL01, PKvL04], hybrid discrete-continuum models [DFFGI96, PVLH00], full continuum descriptions [KD02, AK07] and phase-field models [ZCW08b, ZCW08a].

The evolution of bacterial colonies on flat solid substrates in contact with a bulk liquid, i.e., at solid-*liquid* interfaces, has been an active field of research. Typically, models consider the following processes [TJT16]: cell division and cell death, cell attachment to and
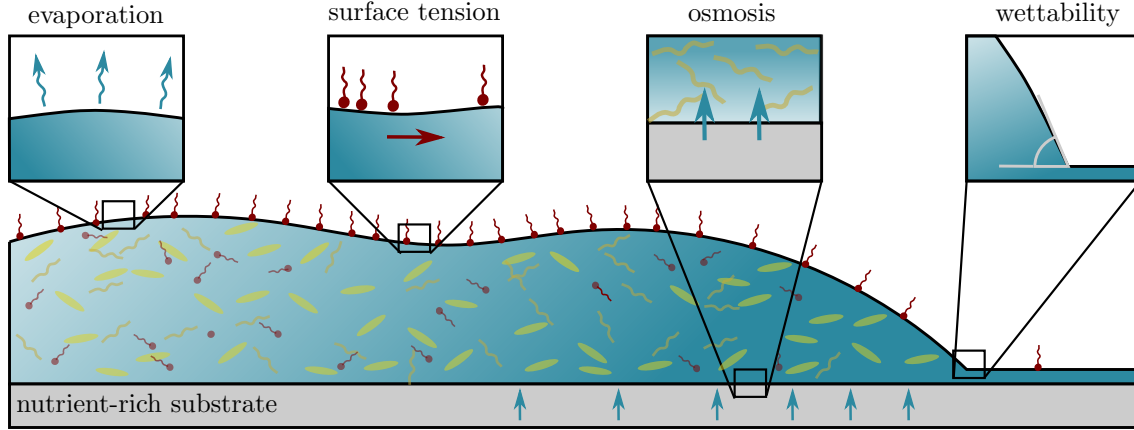
Figure 1.5.: Physical effects that determine the spreading of bacterial colonies at solid-air interfaces. The water content of the colony is regulated by evaporation on the one hand and osmotic influx of fluid from the moist substrate on the other hand. The contact angle of the colony edge is determined by the wettability and thus related to the tensions of the involved interfaces. Gradients in surface tension can for example be induced by a non-uniform distribution of surfactant molecules. They lead to Marangoni flows that can promote colony expansion. In this thesis, these effects are studied within a thin-film approach. The colony is treated as a complex fluid composed of water (blue), biomass consisting of bacteria and polymeric matrix (yellow) and surfactant molecules (red).

detachment from the surface, matrix production as well as nutrient and oxygen uptake by the cell. Relevant questions which have been addressed are, e.g., the effect of nutrient concentration [WC97, Her01], cell transport mechanisms [PVLH⁺98, EPVL01], cell-to-cell signalling [WK12], biofilm matrix properties [CK04, ZCW08a, ZCW08b], or the presence of multiple bacterial species [WG86, PKvL04, AK07] on the evolution of the colony.

The spreading of bacterial colonies at solid-*gas* interfaces involves the motion of the three-phase contact line between the viscous colony, the gas phase and the solid substrate. In the contact line region, wetting phenomena are likely to play a major role. This thesis presents an approach that specifically aims at investigating the role of surface forces, i.e. surface tension and wettability, on the spreading of bacterial colonies. The colony is treated as a thin film of complex fluid composed of water, bacteria, nutrients and other molecules which are secreted by the bacteria (for example extracellular polymeric substances and surfactants). The use of a wetting energy avoids ad hoc assumptions regarding a contact line law, a typical problem of macroscopic descriptions of the dynamics of bacterial colonies [TJLT17]. Other thin-film models that neglect the influence of wettability have been applied to study osmotically driven colony spreading [SAW⁺12], the early stage dynamics of biofilms and quorum sensing [WK12], the effect of surfactant production on the spreading of a bacterial colony up a non-nutritive wall [ARK⁺09] and surfactant-driven spreading in one dimension [FPB⁺12]. In such thin-film models, the biomass is only transported by passive mechanisms – as opposed to active transport via bacterial motility.

In this thesis, we supplement a hydrodynamic description of a thin film of a biologically passive liquid suspension [Thi11, TTL13, XTQ15] by bioactive processes. Thereby, we neglect many aspects of the complexity of bacterial colonies (e.g. the nutrient and oxygen dynamics), but obtain an approach that allows us to study how colony expansion results from the interplay between passive surface forces, osmotic fluxes between agar and biofilm and active growth processes. Figure 1.5 illustrates and summarises the physical effects

that are in the focus of the analysis. In particular, the developed thin-film models are employed to gain a better understanding of the osmotic and surfactant-driven spreading of bacterial colonies. These mechanisms are examples of modes of colony expansion that are driven by passive physical processes rather than by the active motion of bacteria. Central questions that we address are: How does wettability influence the spreading dynamics? Can bacterial colonies always expand over substrates? Where is the osmotic influx into the colony localised? How does the expansion velocity depend on the physical parameters? What is the influence of surfactant produced by the bacteria on the colony shape? Can it indeed be responsible for the dendritic fingers observed in experiments?

1.3. Outline

The structure of this thesis is as follows. In Chapter 2, the basics of wetting and the properties of droplets on a horizontal homogeneous substrate are briefly reviewed. Special emphasis is given to the comparison of a macroscopic description of droplets and the mesoscopic approach that we apply. Next, a dynamical model for thin films of simple liquids is introduced by deriving the thin-film equation from the governing equations of hydrodynamics. This equation will serve as a basis for the models developed in the remainder of the thesis for more complex systems.

In Chapter 3, we turn our attention to the first biological application and develop a thin-film model for the osmotic spreading of biofilms focussing on the influence of wetting phenomena near the contact line. In the first part of its analysis, we study the transition from the initial swelling of biofilms to the subsequent horizontal spreading. In addition, the influence of the physical parameters on the spreading speed is discussed. A central question is whether the colony always spreads or if its expansion can be prevented by unfavourable wetting conditions.

As discussed above, the production of bio-surfactants is of key importance for spreading in many bacterial strains. The groundwork for the incorporation of inhomogeneous surfactant concentrations in our model is laid in Chapter 4. To that end, we first focus on the passive case and derive a mesoscopic model that consistently describes static droplets covered by surfactants. After discussing the equilibrium solutions, a dynamical thin-film model is introduced and employed to illustrate some dynamical effects connected to the presence of surfactants, namely the enhanced spreading rate of surfactant-covered droplets and the transversal instability of their contact line. We are then well-equipped to develop a model for the surfactant-driven spreading of bacterial colonies in Chapter 5. Here, we focus on the influence of the interplay of wetting and the Marangoni effect on the morphology of the evolving bacterial colonies. Recent experiments have suggested that bacterial surfactant-production may be responsible for the formation of fingers in bacterial colonies [FPB+12]. This hypothesis is tested by the analysis of our model.

In Chapter 6, we make a first step towards the incorporation of active bacterial motion into our approach and propose a model that couples equations for the film height and a polarisation field that is connected to self-propulsion of bacteria and resulting active stresses. Finally, the thesis is concluded in Chapter 7 with a summary and outlook.

The results presented in this thesis have in part been published in [TJT16], [TJLT17], [TJT18], [TSTJ18] and [TSTJ19] as detailed in the list of publications.

2. Thin Films and Droplets of Simple Liquids

Wetting phenomena are ubiquitous in nature and also of key importance in many technological applications, such as ink-jet printing, coating or water-resistant fabrics. In the following chapter, we briefly review the basic physics of wetting, beginning with the properties of static droplets. Many interesting phenomena connected to the physics of wetting, such as spreading or dewetting of liquid films are, however, dynamical effects. Therefore, we deal with the modelling of the dynamics of thin liquid films in the second part of this chapter and review the derivation of the thin-film equation from the hydrodynamic description of liquid films. This equation – which describes the dynamics of thin films of a simple liquid – will serve as a basis for the models developed in the remainder of the thesis for more complex systems such as, e.g., films of mixtures, films covered by surfactants or bacterial colonies.

2.1. Equilibrium Droplets

When a drop of liquid is deposited on a solid substrate, different wetting scenarios are possible. In the following, we focus on partially wetting liquids that form a drop with a finite contact angle at the three-phase contact line between substrate, liquid and gas phase. First, we analyse the equilibrium states for stationary droplets sitting on a substrate from energetic considerations in a macroscopic picture on a scale above that of long-range intermolecular forces. In this framework, the contact angle is determined solely by a balance of the interfacial tensions of the interfaces that meet at the contact line. In a next step, we perform the same analysis in a mesoscopic picture which directly takes interactions between liquid, substrate and the surrounding gas phase into account by introducing a *wetting energy*. A comparison between the macroscopic and the mesoscopic description reveals the connection between the respective quantities of the two pictures, namely the interfacial tensions and the wetting energy. Note that the calculations presented in this section have in part been published[1] in

[TSTJ18]   U. Thiele, J. Snoeijer, S. Trinschek, K. John *Equilibrium contact angle and adsorption layer properties with surfactants* Langmuir 34, 7210–7221 (2017).

2.1.1. Equilibrium Droplets in the Macroscopic Picture

In this section, we briefly review how the contact angle which a droplet in equilibrium forms with an underlying solid can be calculated from a corresponding macroscopic free energy. We follow a well-known approach, which can, e.g., also be found in [dGBWQ04] and which represents a very useful formalism that we later apply to more complex situations.
We consider a liquid drop of extension $2R$ on a one-dimensional[2] dry solid substrate as

---

[1]Sec. 2.1.1 and 2.1.3 follow [TSTJ18] and contain figures and text adapted from Thiele, Snoeijer, Trinschek, John (2018), Langmuir 34 (24), pp. 7210–7221 © American Chemical Society (2018).

[2]Throughout this thesis, we work either in a two-dimensional or one-dimensional configuration corresponding to two-dimensional or one-dimensional substrates. For simplicity, we always call the (half) extension of droplets "radius".

2. Thin Films and Droplets of Simple Liquids

sketched in Fig. 2.1 (a). The shape of the drop is characterised by the height profile $h(x)$. The free energy densities of the liquid-gas, solid-liquid and solid-gas interfaces correspond to the respective interfacial tensions and are denoted by γ, γ_{sl} and γ_{sg}. Using the reflection symmetry, the (half) free energy of the drop is given by

$$\mathcal{F}_{\mathrm{macro}} = \int_0^R \mathrm{d}x \, [\gamma \xi + \gamma_{\mathrm{sl}} - ph] + \int_R^\infty \mathrm{d}x \, \gamma_{\mathrm{sg}} + \lambda_h h(R) \tag{2.1}$$

where the metric factor

$$\xi = \sqrt{1 + (\partial_x h)^2} \tag{2.2}$$

describes the curved liquid-gas interface and ∂_x denotes the derivative with respect to x. The finite liquid volume $V = \int dxh$ is controlled via the Lagrange multiplier p.

We independently vary the profile $h(x)$ and the position of the contact line R which are coupled via the boundary condition $h(R) = 0$, as imposed through the Lagrange multiplier λ_h. For equilibrium droplets, these variations of the free energy functional vanish. This can be used to characterise their profile. Varying $h(x)$ implies

$$\delta \mathcal{F}_{\mathrm{macro}} = \int_0^R \mathrm{d}x \, \left[\gamma \frac{\partial_x h}{\xi} \delta(\partial_x h(x)) - p\delta h(x) \right] + \lambda_h \delta h(R) \tag{2.3}$$

$$= \left[\gamma \frac{\partial_x h}{\xi} + \lambda_h \right] \delta h(R) - \gamma \frac{\partial_x h}{\xi} \delta h(0) - \int_0^R \mathrm{d}x \, \delta h(x) \left[\gamma \frac{\partial_{xx} h}{\xi^3} + p \right] \tag{2.4}$$

where we used integration by parts. For equilibrium droplets, the variation vanishes in the droplet and at the boundaries, which gives

$$\lambda_h = -\gamma \frac{\partial_x h}{\xi}, \quad \text{for} \quad x = R, \tag{2.5}$$

$$p = -\gamma\kappa, \quad \text{for} \quad x \in [0, R], \tag{2.6}$$

where we introduced the curvature

$$\kappa = \frac{\partial_{xx} h}{\xi^3} \,. \tag{2.7}$$

In the centre of the drop at $x = 0$, symmetry implies $\partial_x h = 0$. Evaluating the variation of the radius R gives

$$\delta \mathcal{F}_{\mathrm{macro}} = \left[\gamma \xi|_{x=R} + \gamma_{\mathrm{sl}} - \gamma_{\mathrm{sg}} - ph(R) + \lambda_h(\partial_x h) \right] \delta R \,. \tag{2.8}$$

Together with the constraint $h(R) = 0$, λ_h given by Eq. (2.5) and the relation

$$\cos\theta_{\mathrm{eq}} = \frac{1}{\sqrt{1 + \tan^2\theta_{\mathrm{eq}}}} = \frac{1}{\sqrt{1 + (\partial_x h(R))^2}} = \frac{1}{\xi}|_{x=R} \,, \tag{2.9}$$

requiring the variation of the free energy functional to vanish in equilibrium results in the well-known Young law [You05]

$$\gamma \cos\theta_{\mathrm{eq}} = \gamma_{\mathrm{sg}} - \gamma_{\mathrm{sl}} \tag{2.10}$$

that relates the equilibrium contact angle to the interfacial tensions. By introducing the *spreading coefficient*

$$S = \gamma_{\mathrm{sg}} - \gamma_{\mathrm{sl}} - \gamma \,, \tag{2.11}$$

we find the Young-Dupré law [DD69]

$$\gamma \cos\theta_{\mathrm{eq}} = \gamma + S \,, \tag{2.12}$$

(a) macroscopic picture   (b) mesoscopic picture
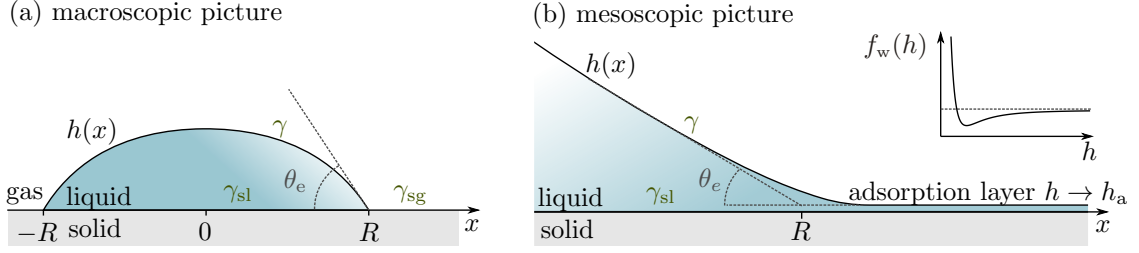
Figure 2.1.: Liquid drop on a solid substrate. (a) In the macroscopic description, the equilibrium contact angle θ_{eq} is determined by the interfacial tensions γ, γ_{sg} and γ_{sl}, which characterize the liquid-gas, solid-gas and solid-liquid interface, respectively. (b) In the mesoscopic description, the wetting energy $f_{\text{w}}(h)$ accounts for intermolecular forces between solid and liquid. The substrate is covered by an equilibrium adsorption layer of height h_{a} which corresponds to the minimum of the wetting energy $f_{\text{w}}(h)$. (cf. [TSTJ18])

which has only physical solutions for θ_{eq} if $S < 0$. This relation is discussed in more detail in, e.g., [Sha93] and [BWDMQDG91] for different wetting scenarios. We see that the spreading coefficient is a useful parameter to gauge wetting. When $S < 0$, partial wetting occurs and the droplet has a finite contact angle. This is, e.g., the case if the liquid-gas interfacial tension γ is large as it then exceeds the difference $\gamma_{\text{sg}} - \gamma_{\text{sl}}$ between the other interfacial tensions. Otherwise, for $S > 0$, no equilibrium contact angle exists and the liquid wets the surface completely.[1]

2.1.2. Interactions between Film and Substrate

If the liquid layer is very thin, the macroscopic approach is no longer sufficient to describe the situation because intermolecular interactions between the solid and the liquid lead to deviations from the above described behaviour. We now investigate the situation on a smaller *mesoscopic* scale where a continuum picture is still applicable, but where the molecular interactions between liquid and the solid substrate become relevant. They can be introduced using an effective *interface-* or *wetting potential* $f_{\text{w}}(h)$ which depends on the thickness of the liquid layer. The corresponding pressure contribution

$$\Pi(h) = -\partial_h f_{\text{w}}(h) \tag{2.13}$$

arising due to the molecular interactions is called *disjoining pressure* or *Derjaguin pressure* – named after Derjaguin who first studied this additional pressure contribution for thin films [Der87]. The form of the wetting potential can be derived from microscopic considerations, asymptotically or numerically [Die88, Sch90, TMTT13, HTA17]. Typically, for partially wetting liquids, the interaction combines long range stabilising van der Waals forces [Isr85] with short range destabilising polar interactions. Consequently, $f_{\text{w}}(h)$ has a minimum at some film height $h = h_{\text{a}}$ corresponding to the height of an equilibrium adsorption layer (in hydrodynamics often referred to as "precursor film") and approaches zero as $h \to \infty$ as depicted in Fig. 2.1 (b). A common choice [Thi07, BEI$^+$09] for the functional form of the wetting energy – which is also used in this thesis unless stated otherwise – is

$$f_{\text{w}}(h) = A \left(-\frac{1}{2h^2} + \frac{h_{\text{a}}^3}{5h^5} \right), \tag{2.14}$$

where A denotes the Hamaker constant [Isr85]. The incorporation of such a disjoining pressure results in a model in which the solid substrate is always at least covered by a

thin adsorption layer $h = h_{\mathrm{a}}$. We discuss the consequences of this approach for a partially wetting equilibrium droplet in the following section.

2.1.3. Equilibrium Droplets in the Mesoscopic Picture

In the mesoscopic description of a partially wetting scenario, we take the wetting energy $f_{\mathrm{w}}(h)$ introduced in the previous section into account and consider a droplet that sits on a thin adsorption layer. In analogy with the variational approach applied in the macroscopic case in Sec. 2.1.1, we start from a free energy functional that is now given by

$$\mathcal{F}_{\mathrm{meso}} = \int_0^\infty \mathrm{d}x \, [\gamma \xi + \gamma_{\mathrm{sl}} + f_{\mathrm{w}}(h) - ph] \,, \tag{2.15}$$

considering the half energy of a reflection symmetric droplet. In the mesoscopic picture, there is no direct influence of the solid-gas interfacial tension, because the substrate is always at least covered by the adsorption layer. The two integrals appearing in the macroscopic description for the droplet and the dry substrate are replaced by one integral over the whole domain that now contains the wetting energy $f_{\mathrm{w}}(h)$. The Lagrange multiplier p again ensures the conservation of volume within the drop.
Varying the free energy functional $\mathcal{F}_{\mathrm{meso}}$ with respect to the profile $h(x)$ gives

$$\delta \mathcal{F}_{\mathrm{meso}} = \int_0^\infty \mathrm{d}x \, \delta h(x) \, [-\gamma \kappa + \partial_h f_{\mathrm{w}} - p] \tag{2.16}$$

where we used $[\gamma \frac{\partial_x h}{\xi} \delta h(x)]_0^\infty = 0$. For droplets in equilibrium, this variation vanishes and the free surface profile can be derived from the Euler-Lagrange equation

$$0 = -\gamma \kappa + \partial_h f_{\mathrm{w}} - p \,. \tag{2.17}$$

Multiplying by $\partial_x h$ and integrating with respect to x gives the *first integral*[3]

$$\begin{aligned} E &= -\gamma \int \frac{\partial_x h}{\xi^3} (\partial_{xx} h) \, \mathrm{d}x + f_{\mathrm{w}}(h) - ph + \gamma_{\mathrm{sl}} \\ &= \frac{\gamma}{\xi} + f_{\mathrm{w}}(h) - ph + \gamma_{\mathrm{sl}} \,, \end{aligned} \tag{2.18}$$

where E has a constant value across the considered domain and can be interpreted as an energy density or as the horizontal force acting on a cross-section of the film.
To determine the shape of equilibrium droplets in the mesoscopic picture, we now consider the wedge geometry in Fig. 2.1 (b). To determine the thickness h_{a} of the coexisting adsorption layer on the right and the angle θ_{eq} formed by the wedge on the left, we first analyse the wedge region far away from the adsorption layer[4]. There, the curvature κ vanishes and the influence of wettability is negligible, i.e., the film height is sufficiently large that $f, \partial_h f_{\mathrm{w}} \to 0$ and $hp \to 0$. In the wedge region, Eqs. (2.17) and (2.18) give

$$p = 0 \tag{2.19}$$

$$E = \frac{\gamma}{\xi_{\mathrm{w}}} + \gamma_{\mathrm{sl}} = \gamma \cos \theta_{\mathrm{eq}} + \gamma_{\mathrm{sl}} \,. \tag{2.20}$$

---

[3]Note that if the integrand of (2.15) is seen as Lagrangian L, the generalised coordinate and corresponding momentum are $q = h$ and $p = \partial L / \partial(\partial_x h) = \gamma(\partial_x h)/\xi$, respectively. Then the first integral E which is independent of x corresponds to the negative of the Hamiltonian $H = p\partial_x q - L$.

[4]Note that the wedge region with $\partial_x h \approx$ const is distinct from the region of the macroscopic droplet governed by the Laplace law $p = -\gamma \kappa$ as discussed more extensively in [Sha93].

Second, we consider the flat adsorption layer of height h_a far away from the wedge. There, Eqs. (2.17) and (2.18) result in

$$p = \partial_h f|_{h_\mathrm{a}} \tag{2.21}$$

$$E = \gamma + f_\mathrm{w}(h_\mathrm{a}) - h_\mathrm{a}p + \gamma_\mathrm{sl}. \tag{2.22}$$

For equilibrium states, the pressure p and the first integral E are constant across the system. Therefore, the adsorption layer height h_a and the contact angle θ_eq can be determined from a comparison of Eqs. (2.19)-(2.20) with Eqs. (2.21)-(2.22) as

$$\partial_h f|_{h_\mathrm{a}} = 0 \quad \text{and} \tag{2.23}$$

$$\gamma \cos \theta_\mathrm{eq} = \gamma + f_\mathrm{w}(h_\mathrm{a}) \tag{2.24}$$

respectively. For small contact angles $\theta_\mathrm{eq} \ll 1$, Eq. (2.24) simplifies to

$$\theta_\mathrm{eq} = \sqrt{-\frac{2 f_\mathrm{w}(h_\mathrm{a})}{\gamma}} \,. \tag{2.25}$$

We see that in the mesoscopic description, the contact angle is determined by the liquid-gas surface tension γ and the wetting energy $f_\mathrm{w}(h)$ instead of by all three interfacial tensions in the macroscopic description. The value of the wetting energy at the adsorption layer height thus contains the information on the relative strengths of the remaining two interfacial tensions γ_sg and γ_sl. Comparing Eq. (2.24) with the macroscopic Young law (2.10) in Sec. 2.1.1 results in the expected relation

$$f_\mathrm{w}(h_\mathrm{a}) = \gamma_\mathrm{sg} - \gamma_\mathrm{sl} - \gamma = S \tag{2.26}$$

as condition for the consistency of mesoscopic and macroscopic description. It also ensures that the mesoscopic energy density (2.15) approaches γ_sg in the adsorption layer at $p = 0$ which should be the case as the solid substrate with adsorption layer in the mesoscopic picture in Sec. 2.1.3 corresponds to the solid-gas interface in the macroscopic picture in Sec. 2.1.1 .[1]

2.2. Dynamical Equations

Up to now, we were dealing with equilibrium droplets. However, many interesting phenomena connected to wetting, such as the spreading of droplets, dewetting or film rupture are dynamical effects. In this section, we discuss the mathematical modelling of thin films of simple liquids, which allows us to study wetting hydrodynamics. We present the standard derivation of the so-called *thin-film equation* [ODB97, Thi07], in Sec. 2.2.1 - 2.2.3 following [Wil16]. First, the general description of a liquid film on a substrate in terms of the Navier-Stokes equation is briefly reviewed. Then, we derive a simplification of the full hydrodynamic description which exploits a disparity of length scales in *thin* liquid films.

2.2.1. Hydrodynamic Description of Liquid Films

For an incompressible, non-volatile liquid with a constant density ρ, the continuity equation is given by

$$\nabla^{(3)} \cdot \mathbf{u}^{(3)} = 0 \tag{2.27}$$

where $\mathbf{u}^{(3)} = (u_x, u_y, u_z)^T$ is the three-dimensional velocity field and $\nabla^{(3)} = (\partial_x, \partial_y, \partial_z)^T$ the three-dimensional nabla operator. Note that all three-dimensional vectors are indicated by a superscript $^{(3)}$. Later, in the derivation of the thin-film equation, quantities

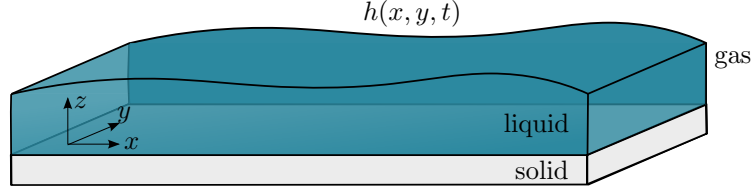## 2. Thin Films and Droplets of Simple Liquids

Figure 2.2.: Sketch of a thin liquid film with height profile $h(x, y, t)$ on a solid substrate surrounded by a gaseous phase.

without superscript indicate two-dimensional vectors.

Without external body forces, the transport of momentum in such a liquid is described by the Navier-Stokes equations

$$\rho \left(\partial_t \mathbf{u}^{(3)} + \mathbf{u}^{(3)} \cdot \nabla^{(3)} \mathbf{u}^{(3)} \right) = -\nabla^{(3)} p + \eta \Delta^{(3)} \mathbf{u}^{(3)} \,. \tag{2.28}$$

Here, p denotes the pressure field, η the kinematic viscosity and $\Delta^{(3)}$ the Laplace operator. The right-hand side of the Navier-Stokes can also be written as the divergence of the Cauchy stress tensor that is composed of the hydrostatic pressure and stresses related to gradients in the velocity [Thi07]

$$\underline{\tau} = -p \mathbf{1}^{(3)} + \eta \left(\nabla^{(3)} \mathbf{u}^{(3)} + (\nabla^{(3)} \mathbf{u}^{(3)})^T \right) \,. \tag{2.29}$$

In the following, we consider free-surface liquid films of height $h(x, y, t)$ on a solid substrate as depicted in Fig. 2.2. In this case, the transport equations (2.27) and (2.28) need to be accompanied by suitable boundary conditions at the (smooth) solid-liquid interface and the (free) liquid-gas interface. At the solid substrate ($z = 0$), we assume no-slip and no-penetration boundary conditions for the velocity, which postulate

$$\mathbf{u}^{(3)}|_{z=0} = 0 \,. \tag{2.30}$$

At the free surface ($z = h(x, y)$), the kinematic condition

$$u_z|_{z=h} = \partial_t h + \mathbf{u}|_{z=h} \cdot \nabla h \tag{2.31}$$

ensures that no flux through the interface is present and that the dynamics of the height profile $h(x, y, t)$ is solely governed by the flux of mass resulting from the two-dimensional flow field $\mathbf{u}|_{z=h}$ at the free surface [Thi07].

The description of wetting hydrodynamics which includes spreading of droplets or dewetting requires a model to resolve the so-called moving-contact line problem. If the no-slip boundary condition is used at the solid-liquid interface and the substrate in front of the droplet is truly "dry", then the viscous dissipation diverges at the contact line and it can not move [dG85]. The problem can be resolved by different approaches. One possibility is to release the no-slip boundary condition and allow for a finite slip velocity of the liquid at the solid substrate [ODB97]. A drawback of this approach is that it introduces an additional length scale in the model but the equation still lacks a boundary condition for the contact angle [SA13]. Another possibility to allow for moving contact lines that we pursue here is to use a model which incorporates a wetting potential (as introduced in Sec. 2.1.2) that has a minimum for a certain (small) film thickness h_a. The disjoining pressure $\Pi(h)$ enters either as an additional body force in the Navier-Stokes equations or in the force equilibrium at the free surface (as done here in the following). Then – assuming that enough liquid is present in the system – the entire solid substrate is always at least covered with a liquid layer of thickness h_a. This method leads to both, a selection of the

contact angle and to a regularisation of the viscous stress.

The force-equilibrium at the free interface can be formulated using the stress tensor $\underline{\tau}$ defined in Eq. (2.29). One finds

$$(\underline{\tau} - \underline{\tau}_{\text{air}}) \cdot \mathbf{n}^{(3)} = \kappa\gamma\mathbf{n}^{(3)} + \Pi(h)\mathbf{n}^{(3)} \tag{2.32}$$

where γ is the surface tension, $\mathbf{n}^{(3)}$ is the normal vector to the liquid-gas interface, κ is the sum of the two principal curvatures of the interface and $\Pi(h)$ is the disjoining pressure introduced in Sec. 2.1.2. We assume here that the ambient gas does not transmit any force and thus $\underline{\tau}_{\text{air}} = 0$. The term proportional to $\kappa\gamma$ represents the Laplace pressure which gives a large contribution for highly curved films, e.g., bubbles. Note that variations in the surface tension caused, e.g., by Marangoni effects would result in an additional term tangential to the interface. This contribution is neglected in the following as we are here concerned with the basic principles of the derivation of the thin-film equation which is best illustrated for a simple example. We will re-introduce and discuss the effect of spatial variations in surface tension in chapter 4.

2.2.2. Thin-Film Approximation

In the case of *thin* incompressible liquid films, the Navier Stokes equations (2.28) can be simplified to an evolution equation for the height profile which is of a reduced mathematical complexity but preserves many important physical features of the original free boundary problem [ODB97, Thi07]. The so-called *thin-film* or *lubrication* approximation exploits the disparity of the typical vertical and the lateral length scales in thin films. In an alternative formulation, this corresponds to the fact that the height profile of the film exhibits only small gradients in the direction parallel to the substrate. Following this definition of a *thin* film, the approximation does not depend on the absolute dimensions of the film, but finds applications ranging from tear films in the eye [SR85] to lava flows [BC00].

We begin the derivation of the thin-film equation by reformulating the continuity condition (2.27) as

$$\partial_z u_z = -\nabla \cdot \mathbf{u} \tag{2.33}$$

with $\mathbf{u} = (u_x, u_y)$. Integrating in the z-direction and using the no-penetration boundary condition (2.30) yields

$$u_z|_{z=h} = -\int_0^h \nabla \cdot \mathbf{u}\, dz\,. \tag{2.34}$$

This can be used to substitute the vertical component of the velocity $u_z|_{z=h}$ in the evolution equation for the height profile (2.31). By applying the Leibniz integral rule, we find

$$\partial_t h = -\int_0^h \nabla \cdot \mathbf{u}\, dz - \mathbf{u}|_{z=h} \cdot \nabla h = -\nabla \cdot \int_0^h \mathbf{u}\, dz = -\nabla \cdot (h\bar{\mathbf{u}})\,, \tag{2.35}$$

which connects the evolution of the height profile $h(x, y)$ and the mean velocity

$$\bar{\mathbf{u}} = \frac{1}{h}\int_0^h \mathbf{u}\, dz\,. \tag{2.36}$$

In the next step, we derive an expression for this mean velocity for thin films which exhibit a disparity of length scales from the momentum equation (2.28). To this end, we introduce scalings [ODB97] for the length and time scales and the pressure p

$$z = h_0\tilde{z} \qquad\qquad x, y = \frac{h_0}{\epsilon}\tilde{x}, \frac{h_0}{\epsilon}\tilde{y} \qquad\qquad t = t_0\tilde{t} = \frac{h_0}{\epsilon u_0}\tilde{t}$$

$$\mathbf{u} = u_0\tilde{\mathbf{u}} \qquad\qquad u_z = \epsilon u_0\tilde{u}_z \qquad\qquad p = \frac{\eta u_0}{\epsilon h_0}\tilde{p} \tag{2.37}$$

where the small parameter $\epsilon \ll 1$ reflects the ratio of the vertical and the horizontal length scales and the tildes denote dimensionless quantities. The respective derivatives consequently rescale as

$$\partial_z = \frac{1}{h_0}\partial_{\tilde{z}} \qquad \partial_{x,y} = \frac{\epsilon}{h_0}\partial_{\tilde{x},\tilde{y}} \qquad \partial_t = \frac{\epsilon u_0}{h_0}\partial_{\tilde{t}}. \tag{2.38}$$

In this scaling, the momentum equations (2.28) read

$$\epsilon\left(\partial_{\tilde{t}}\tilde{\mathbf{u}} + (\tilde{\mathbf{u}}\cdot\tilde{\nabla} + \tilde{u}_{\tilde{z}}\partial_{\tilde{z}})\tilde{\mathbf{u}}\right) = \frac{1}{\mathrm{Re}}(-\tilde{\nabla}\tilde{p} + (\epsilon^2\tilde{\Delta} + \partial_{\tilde{z}}^2)\tilde{\mathbf{u}}) \tag{2.39}$$

$$\epsilon^2\left(\partial_{\tilde{t}}\tilde{u}_{\tilde{z}} + (\tilde{\mathbf{u}}\cdot\tilde{\nabla} + \tilde{u}_{\tilde{z}}\partial_{\tilde{z}})\tilde{u}_{\tilde{z}}\right) = \frac{1}{\mathrm{Re}}(-\frac{1}{\epsilon}\partial_{\tilde{z}}\tilde{p} + \epsilon(\epsilon^2\tilde{\Delta} + \partial_{\tilde{z}}^2)\tilde{u}_{\tilde{z}}) \tag{2.40}$$

where we introduced the Reynolds number

$$\mathrm{Re} = \frac{u_0 h_0 \rho}{\eta} \tag{2.41}$$

that is determined by the ratio of inertial to viscous forces. In lowest order of ϵ, the equations are given by

$$\tilde{\nabla}\tilde{p} = \partial_{\tilde{z}}^2\tilde{\mathbf{u}} \tag{2.42}$$

$$\partial_{\tilde{z}}\tilde{p} = 0 \tag{2.43}$$

and the pressure $\tilde{p}$ does thus not depend on the $\tilde{z}$ position. These equations need to be accompanied by appropriate boundary conditions: At the solid substrate, the no-slip boundary condition (2.30) yields

$$\tilde{\mathbf{u}}|_{\tilde{z}=0} = 0. \tag{2.44}$$

At the liquid-air interface, the force balance (2.32) is projected onto the normal and tangential vectors of the surface and expanded in the thin-film scaling. The derivation of the final expressions is straight-forward, but rather lengthy. Therefore, we refer to the literature [ODB97, Thi07] for the detailed calculation and only give the result

$$\partial_{\tilde{z}}\tilde{\mathbf{u}}|_{\tilde{z}=\tilde{h}} = 0 \tag{2.45}$$

$$\tilde{p}|_{\tilde{z}=\tilde{h}} = -\frac{1}{\mathrm{Ca}}\tilde{\Delta}\tilde{h} - \tilde{\Pi}(\tilde{h}) \tag{2.46}$$

where we introduced the capillary number

$$\mathrm{Ca} = \frac{u_0 \eta}{\gamma \epsilon^3} \tag{2.47}$$

that represents the ratio of the viscous forces to the surface tension γ. Note that in order to keep the physically essential surface tension effects at leading order and thus in the equations, the capillary number adsorbs a factor ϵ^{-3} in contrast to its classical definition. The momentum equations (2.42) in lowest order can now be solved for the velocity $\tilde{\mathbf{u}}$. Integrating once with respect to $\tilde{z}$ and determining the integration constant $\mathbf{c}_1$ from the boundary condition (2.45) gives

$$\partial_{\tilde{z}}\tilde{\mathbf{u}} = \tilde{z}\tilde{\nabla}\tilde{p} + \mathbf{c}_1 = \tilde{z}\tilde{\nabla}\tilde{p} - \tilde{h}(\tilde{\nabla}\tilde{p})|_{\tilde{z}=\tilde{h}}. \tag{2.48}$$

A second integration yields

$$\tilde{\mathbf{u}} = \frac{1}{2}\tilde{z}^2\tilde{\nabla}\tilde{p} - \tilde{z}\tilde{h}(\tilde{\nabla}\tilde{p})|_{\tilde{z}=\tilde{h}} + \mathbf{c}_2 = \frac{1}{2}\tilde{z}^2\tilde{\nabla}\tilde{p} - \tilde{z}\tilde{h}(\tilde{\nabla}\tilde{p})|_{\tilde{z}=\tilde{h}} \tag{2.49}$$

where the integration constant $\mathbf{c}_2$ is zero because of the no-slip boundary condition (2.44) at the solid substrate. In a last step, we can now evaluate the mean velocity, which is needed to express the evolution of the height profile $h(x, y, t)$ with Eq. (2.35). After applying the force balance boundary condition (2.46), we find

$$\tilde{\mathbf{u}} = \frac{1}{\tilde{h}} \int_0^{\tilde{h}} \frac{1}{2} \tilde{z}^2 \tilde{\nabla} \tilde{p} - \tilde{z} \tilde{h} (\tilde{\nabla} \tilde{p})|_{\tilde{z}=\tilde{h}} \mathrm{d}\tilde{z} = -\frac{\tilde{h}^2}{3} (\tilde{\nabla} \tilde{p})|_{\tilde{z}=\tilde{h}} = \frac{\tilde{h}^2}{3} \tilde{\nabla} \left[\frac{1}{\mathrm{Ca}} \tilde{\Delta} \tilde{h} + \tilde{\Pi}(\tilde{h}) \right] . \quad (2.50)$$

Inserting this expression for the mean velocity in the rescaled Eq. (2.35) gives the thin-film equation

$$\partial_{\tilde{t}} \tilde{h} = -\tilde{\nabla} \cdot \left[\frac{\tilde{h}^3}{3} \tilde{\nabla} \left(\frac{1}{\mathrm{Ca}} \tilde{\Delta} \tilde{h} + \tilde{\Pi}(\tilde{h}) \right) \right] . \quad (2.51)$$

In the dimensional form, it reads

$$\partial_t h = -\nabla \cdot \left[\frac{h^3}{3\eta} \nabla \left(\gamma \Delta h + \Pi(h) \right) \right] . \quad (2.52)$$

When using the thin-film equation in dimensional from, care should be taken that in the process of its derivation, we assumed a separation of the horizontal and vertical length scales. In the next section, we give an alternative formulation of the thin-film equation which facilitates the generalisation of the mathematical model to more complex situations.

2.2.3. Gradient Dynamics Formulation of the Thin-Film Equation

The structure of the thin-film equation (2.52) allows one to write the equation in a form similar to the well-known Cahn-Hilliard equation [Cah65, Mit93] as

$$\partial_t h = -\nabla \cdot \mathbf{j} = \nabla \cdot \left[Q(h) \nabla \frac{\delta \mathcal{F}}{\delta h} \right] , \quad (2.53)$$

i.e., the dynamics of the field h is governed by a continuity equation with a flux $\mathbf{j}$ [Thi10, TAP16, WTG$^+$15]. This flux itself is the product of a mobility $Q(h)$ and the gradient of the functional derivative of a free energy functional $\mathcal{F}[h]$ with respect to the variable h, which is denoted as $\frac{\delta \mathcal{F}}{\delta h}$. For the thin-film equation, we find by comparison with Eq. (2.52) that the mobility is given by $Q(h) = \frac{h^3}{3\eta}$ and an appropriate free energy functional is

$$\mathcal{F} = \int_\Omega \left[\gamma \xi + f_\mathrm{w}(h) + \gamma_\mathrm{sl} \right] \mathrm{d}\mathbf{x} \quad (2.54)$$

on a two-dimensional domain Ω. It corresponds to the free energy functional introduced in Eq. (2.15) for the mesoscopic description of stationary droplets sitting on a solid substrate. Note that here, volume conservation is ensured via the structure of Eq. (2.53) and the free energy functional does in consequence not contain a Lagrange multiplier for volume conservation. The metric factor

$$\xi = \sqrt{1 + (\partial_x h)^2} \quad (2.55)$$

again describes the curved interface $h(x, y)$. In the limit of small interface slopes, it can be approximated by

$$\xi \approx 1 + \tfrac{1}{2} |\nabla h|^2 . \quad (2.56)$$

The interfacial tension between solid substrate and liquid film is denoted by γ_sl and assumed to be constant.

Formulation (2.53) of the thin-film equation is also called *gradient dynamics* formulation, because the temporal evolution of the height profile h follows gradients of the free energy functional $\mathcal{F}[h]$ in function space [TAP16]. An important property of such a dynamics is that the free energy monotonically decreases with time. Stationary profiles correspond to minima of the free energy functional characterised by $\frac{\delta \mathcal{F}}{\delta h} = p$, in accordance with the analysis of stationary droplets performed in Sec. 2.1.3.

The thin-film equation given in (2.52) describes a simple liquid and includes only surface tension and disjoining pressure as physical effects. If one wants to account for more complex situations in which, e.g., gravitation or gradients in surface tension induced by a temperature gradient should be considered, one could introduce the corresponding terms in the Navier-Stokes equation and redo the derivation presented in Sec. 2.2.2. However, this procedure is quite error-prone and the formulation as a gradient dynamics allows for a much simpler way to incorporate additional effects by simply adding the corresponding energetic contributions to the free energy functional [Wil16]. Furthermore, the approach can be extended to more complex systems which consist of more than one independent field. For instance, thin films of solutions or suspensions are described by a height field $h(x, y, t)$ *and* the concentration of the solute [TTL13, XTQ15]. Another example are films covered by an insoluble surfactant, where also the surfactant concentration contributes to the free energy of the system [TAP12, TAP16]. In the two cases, the respective spatially varying solvent or surfactant concentrations evolve dynamically. To account for such situations, the gradient dynamics formulation can be extended towards multiple coupled fields $\boldsymbol{\psi} = (\psi_1, \psi_2, ... \psi_n)^T$ as e.g. discussed in [WTG$^+$15] and [TAP16]. Note that the fields ψ_i have to be independent variables such that a variation of one field should not influence the other. This is for instance important for the description of mixtures, where film height and concentration of solvent do *not* represent independent variables. In the general framework, the resulting n equations read

$$\partial_t \boldsymbol{\psi} = \nabla \cdot \left[\mathbf{Q}(\boldsymbol{\psi}) \nabla \frac{\partial \mathcal{F}}{\partial \boldsymbol{\psi}} \right] \tag{2.57}$$

where $\boldsymbol{\psi}$ and the variation of the free energy functional with respect to the order parameter fields

$$\frac{\partial \mathcal{F}}{\partial \boldsymbol{\psi}} = \left(\frac{\partial \mathcal{F}}{\partial \psi_1}, \frac{\partial \mathcal{F}}{\partial \psi_2}, ..., \frac{\partial \mathcal{F}}{\partial \psi_n} \right)^T \tag{2.58}$$

are n-dimensional vectors while the nabla operator ∇ and the dot product are performed in the two-dimensional coordinate space [WTG$^+$15]. The mobility is generalised to an $n \times n$ dimensional mobility matrix $\mathbf{Q}(\boldsymbol{\psi})$ which fulfils the following two criteria: To be in agreement with the Onsager reciprocity relations [Ons31], the mobility matrix has to be symmetric. Second, a positive definite mobility matrix ensures that the free energy of the system decreases over time and $\mathcal{F}[h]$ represents a Lyapunov functional [WTG$^+$15] since

$$
\begin{aligned}
\frac{\mathrm{d}}{\mathrm{d}t} \mathcal{F}(\boldsymbol{\psi}) &= \int_\Omega \frac{\partial \mathcal{F}}{\partial \boldsymbol{\psi}} \partial_t \boldsymbol{\psi} \, \mathrm{d}\mathbf{x} \\
&= \int_\Omega \frac{\partial \mathcal{F}}{\partial \boldsymbol{\psi}} \nabla \cdot \left[\mathbf{Q} \nabla \frac{\partial \mathcal{F}}{\partial \boldsymbol{\psi}} \right] \mathrm{d}\mathbf{x} \\
&= - \int_\Omega (\nabla \frac{\partial \mathcal{F}}{\partial \boldsymbol{\psi}}) \cdot \mathbf{Q} (\nabla \frac{\partial \mathcal{F}}{\partial \boldsymbol{\psi}}) \mathrm{d}\mathbf{x} \leq 0 \, .
\end{aligned}
\tag{2.59}
$$

When extending the gradient dynamics description towards more complex situations, the additional energetic effects connected to the different fields ψ_i can be added to the free energy functional. The mobility matrix, however, depends on the particular set of boundary

conditions at the substrate and the free interface of the film [WTG$^+$15]. The exact form of the entries of the mobility matrix, which often consist of polynomials of the order parameter fields [TAP16], has to be determined once for each set of boundary conditions from a thin-film approximation of the corresponding dynamical equations [Wil16] as discussed in Sec. 2.2.2 for films of simple liquid. In this thesis, we apply the gradient dynamics formulation of the thin-film equation to suspensions and to films of simple liquids which are covered by an insoluble surfactant. The resulting model equations are discussed in sections 3.2.1 and 4.3, respectively.

Furthermore, thin-film equations can be used as a basis for developing models for complex biological fluids. They provide a useful tool to study, e.g., the influence of surface tension effects or wettability in such systems. One field of application are bacterial colonies that can – in a simplified view – be interpreted as complex suspensions of liquid and biomass [WAS$^+$11]. In this approach, bioactive processes such as the proliferation of biomass or the production of surfactant by the bacteria need to be accounted for by additional terms that supplement the thin-film description. In the following chapter, we derive a model for osmotically driven biofilm spreading.

3. Osmotic Biofilm Spreading

One strategy of biofilms to achieve colony expansion on moist substrates in contact with a gas phase is osmotically driven spreading. In the following section, we first briefly introduce this spreading mechanism and discuss experimental observations. The focus of the chapter lies on the development and analysis of a mathematical model. It is build on a thin-film model for passive suspensions and allows for a systematic study of the interplay of passive physical forces such as wettability, surface tension and osmosis on the one hand and biological growth processes on the other hand.

Note that the results presented in this chapter have in part been published[1] in

[TJT16]   Sarah Trinschek, Karin John and Uwe Thiele. *From a thin-film model for passive suspensions towards the description of osmotic biofilm spreading* AIMS Materials Science, 3, 1138-1159 (2016)

[TJLT17]   Sarah Trinschek, Karin John, Sigolène Lecuyer and Uwe Thiele. *Continuous versus arrested spreading of biofilms at solid-gas interfaces: The role of surface forces.* Physical Review Letters, 119.7, 078003 (2017).

3.1. Mechanism and Experimental Findings

In the osmotic spreading mechanism, the expansion of a bacterial colony over a substrate is not driven by the active motility of individual bacteria, but by the physico-chemical properties of the biofilm and the interfaces. The mechanism relies on the generation of osmotic pressure gradients caused by the consumption of water and nutrient by the bacteria and the production of further biomass. The resulting osmotic imbalance between biofilm and moist agar substrate – caused for example by the exopolysaccharide component of the polymeric matrix acting as an osmolyte – results in a physical swelling and spreading of the biofilm and an increased nutrient uptake through an influx of nutrient-rich water from the agar [TJLT17].

Figure 3.1 shows experimental data from a study of the osmotic spreading of *B. subtilis* biofilms performed by Seminara et al. [SAW+12] demonstrating that colony expansion depends on the production of osmolytes. The top view of biofilms on agar plates at different points in time (a) shows that the wild-type strain (WT) spreads over the substrate with a speed of roughly 0.2mm/h. The expansion of a mutant strain lacking flagella (hag) is only slightly reduced as compared to the wild type. This excludes the active motion of individual bacteria as the driving of the spreading. In contrast, the expansion of a mutant strain (Δeps) deficient in the production of the exopolysaccharide component of the polymeric matrix is dramatically slower. Figure 3.1 (b) shows the evolution of shapes of the evolving biofilms over time. The wild-type colony first swells (mainly) vertically with increasing steepness of the colony height. Subsequently, it expands laterally over the

---

[1]Chapter 3 is based on [TJT16] and [TJLT17] and contains figures and text adapted from Trinschek et al. AIMS Materials Science, 3, 1138-1159 (2016) © AIMS Press (2016) particularly in Sec. 3.2.1 (p.28 l.4-14) and Sec. 3.2.2 (p.26 l.18 - p.29 l.14) and from Trinschek et al. Physical Review Letters 119.7 078003 (2017) © American Physical Society (2017) particularly in Sec. 3.1 (p.23 l.1-30), Sec. 3.2.2 (p.27 l.23 - p.28 l.17 and p.31 l.18-p.32 l.12) and Sec. 3.5.

substrate with a nearly constant contact angle. The mutant strain deficient in matrix production cannot undergo this transition from vertical swelling to horizontal spreading and its spreading is arrested.
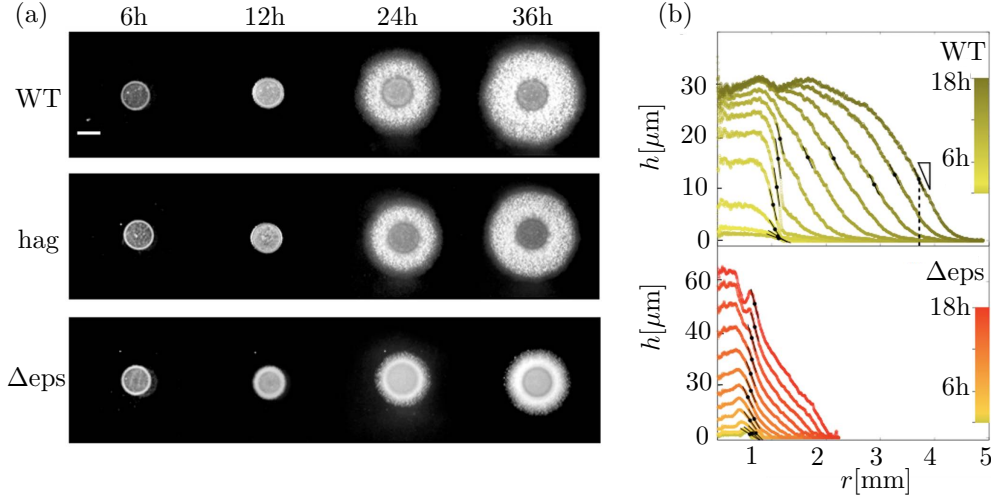
Figure 3.1.: The expansion of *B. subtilis* biofilms depends on the production of extracellular matrix. (a) Top view of colonies on agar planes at different points in time for the wild-type strain 3610 (WT), a strain lacking flagella (hag) and a strain deficient in matrix production (Δeps). The scale bar is 1mm. (b) The biofilm shapes at intervals of 1.5h for the wild-type (WT) and eps mutant strain Δeps obtained by averaging of the transmitted light intensity show a transition from swelling to spreading. Figures adapted from [SAW+12] with permission © National Academy of Sciences (2004).

Further experimental insight into the osmotic spreading of *B. subtilis* comes from experiments showing that nutrient depletion within a colony growing on a nutrient-rich agar substrate triggers an increase in matrix production. The resulting subsequent colony spreading provides the bacteria with fresh nutrients [ZSS+14]. Experimental tracking of the distribution of the main phenotypes in bacterial colonies also suggests that the matrix-producing cells play a crucial role in the spreading of the front [TJT16]. For *B. subtilis* biofilms, fluorescence imaging techniques have been employed to show that they are predominantly located in the outer rim of the biofilm [WKW+16]. Recently, it has been reported that bacterial cells at the edge the expanding colony switch off matrix production and transition to sporulation after a set time delay of approximately 100min. The process is driven by a pair of gene expression waves and the expression patterns localise to propagating fronts [SVK+18].

The osmotic spreading mechanism is not only used by *B. subtilis*, but also exploited by many other organisms, such as *S. meliloti* colonies, [DTH14], *E. coli* bacterial swarms [PWH+14, YTST17], *S. Aureus* colonies [LKLY16] and *V. cholerae* biofilms [YNS+17]. Probing the osmolarity with osmolarity sensitive fluorescent liposomes [PWH+14] shows that in *E. coli* swarms, the osmolarity rises abruptly near the leading edge of the swarm and then drops to a level close to that of the bare agar substrate $\approx 100\mu$m behind. Water is drawn into the swarm in a narrow region from the colony edge and then pushed back into the agar at a smaller rate. For *V. cholerae* biofilms, the growth of the wild-type (matrix-producing) strain depends on the agar concentration which determines the osmotic pressure in the agar, whereas the growth of a mutant strain deficient in matrix production does not [YNS+17].[2]

---

[2]In principle, this observation can also be induced by a modified stiffness of the agar substrate but the

The spreading of biofilms at solid-gas interfaces involves the motion of a three-phase contact line between the viscous biofilm, the agar and the gas phase, so that wetting phenomena are likely to play a role. Indeed, surface tension and wettability strongly affect the spreading dynamics, which can be demonstrated by performing spreading experiments using a *B. subtilis* wild-type strain (WT) and a mutant strain deficient in the production of surfactin – a natural bio-surfactant produced by wild-type *B. subtilis*. Typically, the production of *surfactin* is induced at high cell density by cell-to-cell communication (quorum sensing) [OSDMM14, vGVK15]. Here, we exploit the fact that *surfactin* alters the surface tension of the biofilm-gas interface. In the presence of *surfactin*, the contact angle of the colony is lower which corresponds to an increased wettability. In an experiment performed by Sigolène Lecuyer as published in [TJLT17], agar plates with appropriate nutrient medium are inoculated with a small droplet of cell suspension. The subsequent growth and spreading of the biofilm are monitored for three days. The colonies of the wild-type and the mutant strain deficient in *surfactin* production are shown in Figs. 3.2 (a) and (d), respectively, on the first day and after three days of incubation. The wild type (a) expands and forms circular biofilms with a diameter of about 2 cm after three days. For the mutant strain in (d), the surface tension is not lowered by the presence of surfactants and the contact angle is high. As the mutant strain can not profit from an improved wettability, the colony is not able to spread. The external addition of *surfactin* shortly after agar inoculation has no effect on the spreading of the wild-type strain (b). Howexer, it restores a wild-type morphology in the *surfactin*-deficient strain (e). Interestingly, the wild-type phenotype can also be recovered by adding the non-physiological surfactants *Tween 20* (c)-(f) or *Span80* (not shown), which points at a physical role of *surfactin* in the spreading mechanism [TJLT17].[1]
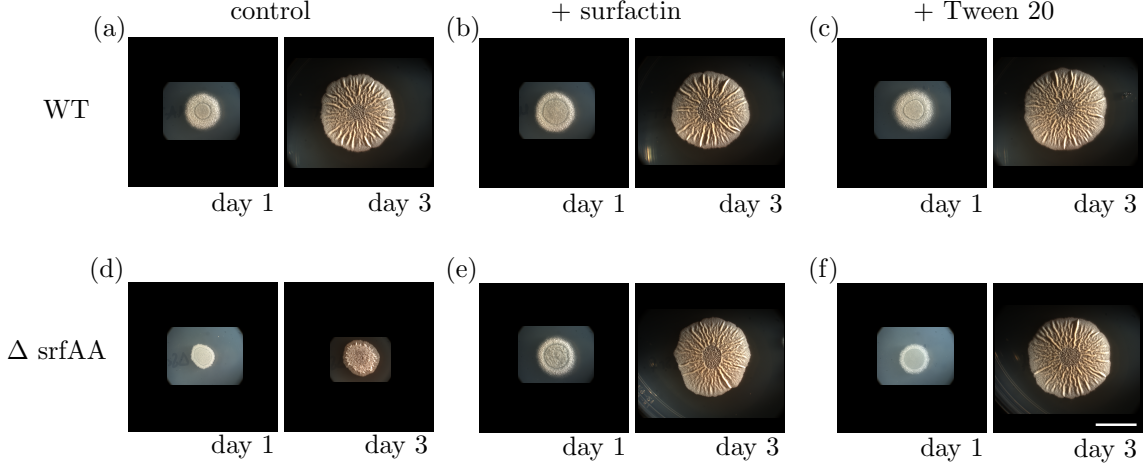
Figure 3.2.: Experimental observation of the influence of wettability (mediated by the presence of surfactants altering the surface tension) on the osmotic spreading of biofilms [TJLT17]. (a) The *B. subtilis* wild type NCIB 3610 spreads laterally with a velocity of 0.2 mm/h over the agar substrate. (d) A mutant strain deficient in surfactin production (ΔsrfAA) can not expand over the substrate. The external addition of the surfactants (e) surfactin or (f) Tween 20 enables the spreading of the mutant strain but does not affect the wild type (b), (c). Scale bar: 1cm (cf. [TJLT17])

Also in other experimental studies, the spreading of *B. subtilis* biofilms or the swarming of *B. subtilis* colonies were shown to require or to be facilitated by the production of

---

effect was excluded by growing the biofilm on a semi-permeable membrane on top of the agar.

surfactin [GSC+12, KHC+15, LMB+06, JOHS05, KSF03]. The bio-surfactant promotes the spreading of the colony by decreasing the surface tension of the water in the colony and acting as a wetting agent. Goniometry measurements allow for the observation of a 'halo' around surfactant-producing bacterial colonies which is characterised by a higher wettability [LMB+06]. In *P. aeruginosa* colonies, *rhamnolipids* act as wetting agents [TRLD07, CSO05]. In *S. marcescens* colonies, this role is taken by *serrawettin* [MN96a, MN96b].

3.2. Mathematical Modelling

As discussed in the previous section, the influence of physical effects – such as osmotic swelling and surface forces – on the spreading of bacterial colonies at solid-liquid interfaces is a field of intense experimental research. In general, the literature concerning the mathematical models for bacterial colony growth is very rich and the models are diverse in the used modelling approaches and the considered processes (see, e.g., [WZ10, KD10, HL14, PVL03] for reviews). However, the aspect of physical surface forces has up to now found only little attention.

In this section, we introduce a thin-film model for osmotically spreading biofilms which explicitly includes surface tension effects and wettability. Similar thin-film models which neglect the influence of wettability have been employed to study early stage colony growth and quorum sensing [WK12, WKK+01], the effect of surfactant production on the spreading of a bacterial colony up a non-nutritive wall [ARK+09] and osmotically driven biofilm spreading [SAW+12]. Here, we supplement a consistent hydrodynamic description of a thin film of a biologically passive liquid suspension by biomass growth processes and also account for osmotic influx and evaporation of the solvent. The structure of the model automatically guarantees a thermodynamically consistent description of the passive (i.e., non-biological) limiting case even for more complex interactions between the components. Basing the description on a model for passive mixtures also has the advantage that the dynamics of the contact line between the biofilm, the substrate and the gas phase is naturally encoded in the evolution equations. Therefore – and in contrast to other modelling approaches employed in the literature – no additional assumptions on the relation between forces and the contact line velocity have to be made [TJT16] .

3.2.1. Thin-Film Equation for (Passive) Mixtures and Suspensions

In this section, we present a model for the description of thin layers of passive mixtures and suspensions which was introduced in [Thi11, TTL13, XTQ15] and will serve as a basis for the modelling of osmotically spreading biofilms. The model is presented in a gradient dynamics formulation and represents one possible extension of the thin-film equation for simple liquids towards more complicated systems as discussed in Sec. 2.2.3.

Free Energy Functional for Mixtures and Suspensions

We consider a thin film of a binary suspension or solution of height $h(\mathbf{x}, t)$ on a flat solid substrate as shown in Fig. 3.3 where the local, z-averaged concentration of the solute is denoted by $\phi(\mathbf{x}, t)$. The behaviour of the passive suspension is determined by a free energy functional. An appropriate choice for this functional is

$$\mathcal{F}_{\mathrm{mix}}[h, \phi] = \int \left[f_{\mathrm{w}}(h, \phi) + h f_{\mathrm{m}}(\phi) + \tfrac{\gamma}{2}(\nabla h)^2 \right] \mathrm{d}\mathbf{x}, \tag{3.1}$$
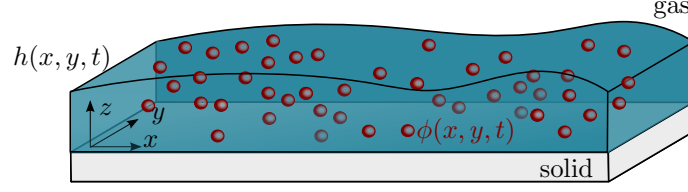
Figure 3.3.: Sketch of a thin film of a binary mixture of height $h(\mathbf{x}, t)$ on a flat solid substrate surrounded by a gaseous phase. The z-averaged local concentration of solute is denoted by $\phi(\mathbf{x}, t)$.

where γ is again the surface tension and $\nabla = (\partial_x, \partial_y)^T$ is the planar gradient operator. In addition to the surface term and the wetting energy $f_{\mathrm{w}}(h, \phi)$ (see Sec. 2.1.2) which already occur in the description of simple liquids, the free energy now also contains a mixing energy $f_{\mathrm{m}}(h, \phi)$.

In general, the contributions to the free energy functional in Eq. (3.1) underlying the passive part of the dynamics can be chosen to include complex solvent-solute interactions and composition-dependent wetting properties [TTL13, XTQ15]. Our modelling of osmotic biofilm spreading focusses on the interplay between bio-active processes and passive forces. Therefore, we restrict ourselves to relatively simple choices [TJT16]: The wetting energy

$$f_{\mathrm{w}}(h) = A \left(-\frac{1}{2h^2} + \frac{h_{\mathrm{a}}^3}{5h^5} \right) \tag{3.2}$$

which has already been introduced in Eq. (2.14) depends only on the overall film height h and describes a biofilm that partially wets the substrate. As discussed in Sec. 2.1.2, h_{a} denotes the height of a thin wetting layer and

$$A = \tfrac{10}{3} h_{\mathrm{a}}^2 (\gamma - \gamma_{\mathrm{sg}} + \gamma_{\mathrm{sl}}) \tag{3.3}$$

is the Hamaker constant, here expressed through the interface energies. The film bulk contribution

$$f_{\mathrm{m}}(\phi) = \frac{k_{\mathrm{B}}T}{a^3} [\phi \ln(\phi) + (1 - \phi) \ln(1 - \phi)] \tag{3.4}$$

represents the entropic free energy of mixing of solute and solvent where $k_{\mathrm{B}}T$ denotes the thermal energy. We assume for simplicity that biomass and solvent are represented by the same microscopic length a [TJLT17].[1]

Gradient Dynamics Formulation

To derive evolution equations, one has to notice that the fields h and ϕ can not be varied independently, i.e. the concentration ϕ changes if h is varied at fixed local solute amount. One choice for conserved parameter fields suitable for a gradient dynamics formulation as introduced in Sec. 2.2.3 is given by h and the effective layer thickness of solute $\psi = h\phi$. After transforming the free energy functional to these fields via

$$F_{\mathrm{mix}}[h, \psi] = \mathcal{F}_{\mathrm{mix}}[h, \phi(h, \psi)], \tag{3.5}$$

one can write the evolution equations

$$\partial_t h = \nabla \cdot \left[Q_{hh} \nabla \frac{\delta F_{\mathrm{mix}}}{\delta h} + Q_{h\psi} \nabla \frac{\delta F_{\mathrm{mix}}}{\delta \psi} \right] \tag{3.6}$$

$$\partial_t \psi = \nabla \cdot \left[Q_{\psi h} \nabla \frac{\delta F_{\mathrm{mix}}}{\delta h} + Q_{\psi\psi} \nabla \frac{\delta F_{\mathrm{mix}}}{\delta \psi} \right] \tag{3.7}$$

for the film height and the effective layer thickness of the solute where the symmetric and positive definite mobility matrix $\mathbf{Q}$ is defined as

$$\mathbf{Q}(h, \psi) = \begin{pmatrix} Q_{hh} & Q_{h\psi} \\ Q_{\psi h} & Q_{\psi\psi} \end{pmatrix} = \frac{1}{3\eta} \begin{pmatrix} h^3 & h^2\psi \\ h^2\psi & h\psi^2 \end{pmatrix} + \begin{pmatrix} 0 & 0 \\ 0 & D\psi \end{pmatrix}. \tag{3.8}$$

It contains contributions from convective and diffusive transport and can be determined from a long-wave approximation of the full hydrodynamic model as discussed in [TTL13, Thi11, XTQ15, TAP12, WTG+15, NT10]. The biomass diffusivity is $D = \frac{a^2}{6\pi\eta}$, consistent with the diffusion constant $D_{\text{diff}} = D\frac{k_{\text{B}}T}{a^3} = \frac{k_{\text{B}}T}{6\pi a\eta}$. The mobility depends on the viscosity of the solution $\eta(\phi) = \eta_0\hat{\eta}(\phi)$, which is written in terms of a reference viscosity η_0 (corresponding to the viscosity of the solvent), the viscosity of the solute η_b and a dimensionless scaling function $\hat{\eta}(\phi)$ that captures the composition dependence of the viscosity. Here, we use the linear ansatz

$$\hat{\eta}(\phi) = (1 - \phi) + \frac{\eta_b}{\eta_0}\phi \tag{3.9}$$

for the viscosity of the colony [TJT16].[1]

Hydrodynamic Formulation

The evolution equations (3.6)-(3.7) can also be written in the usual hydrodynamic form expressed in film height and solute concentration as

$$\partial_t h = -\nabla \cdot \mathbf{j}_{\text{conv}} \tag{3.10}$$

$$\partial_t(h\phi) = -\nabla \cdot (\phi\mathbf{j}_{\text{conv}} + \mathbf{j}_{\text{diff}}). \tag{3.11}$$

The passive convective flux $\mathbf{j}_{\text{conv}}$ and the diffusive flux $\mathbf{j}_{\text{diff}}$ can be derived from (3.6)-(3.7) by rewriting the variations of the free energy $F_{\text{mix}}[h, \psi]$ with respect to h and ψ as variations of the energy functional $\mathcal{F}_{\text{mix}}[h, \phi]$ with respect to h and ϕ using the relations

$$\frac{\delta F_{\text{mix}}[h, \psi]}{\delta h} = \frac{\delta \mathcal{F}_{\text{mix}}[h, \phi]}{\delta h} - \frac{\phi}{h}\frac{\delta \mathcal{F}_{\text{mix}}[h, \phi]}{\delta \phi} \tag{3.12}$$

$$\frac{\delta F_{\text{mix}}[h, \psi]}{\delta \psi} = \frac{1}{h}\frac{\delta \mathcal{F}_{\text{mix}}[h, \phi]}{\delta \phi} \tag{3.13}$$

and expressing the mobility matrix $\mathbf{Q}$ as a function of h and ϕ. For the energy functional given in Eq. (3.1) and under the assumption of a composition-independent wetting energy $f_{\text{w}}(h)$, one obtains (for details see [XTQ15])

$$\mathbf{j}_{\text{conv}} = -\frac{h^3}{3\eta}\nabla(\partial_h f_{\text{w}} - \gamma\Delta h) \tag{3.14}$$

$$\mathbf{j}_{\text{diff}} = -D_{\text{diff}}h\phi\nabla(\partial_\phi f_{\text{m}}). \tag{3.15}$$

From the height evolution equation (3.10), which exactly corresponds to the thin-film equation (2.52), one can directly see that the inclusion of a mixing energy does not give rise to an additional bulk flow. Therefore, the height profile of a drop of suspension evolves identical to a simple liquid.

Spreading of Droplets of Mixtures Towards an Equilibrium Shape

Before incorporating bioactive terms into the model, it is instructive to briefly study the spreading of a simple droplet as a reference for comparison to more complex situations. To that end, we perform a finite element time simulation as outlined in the appendix
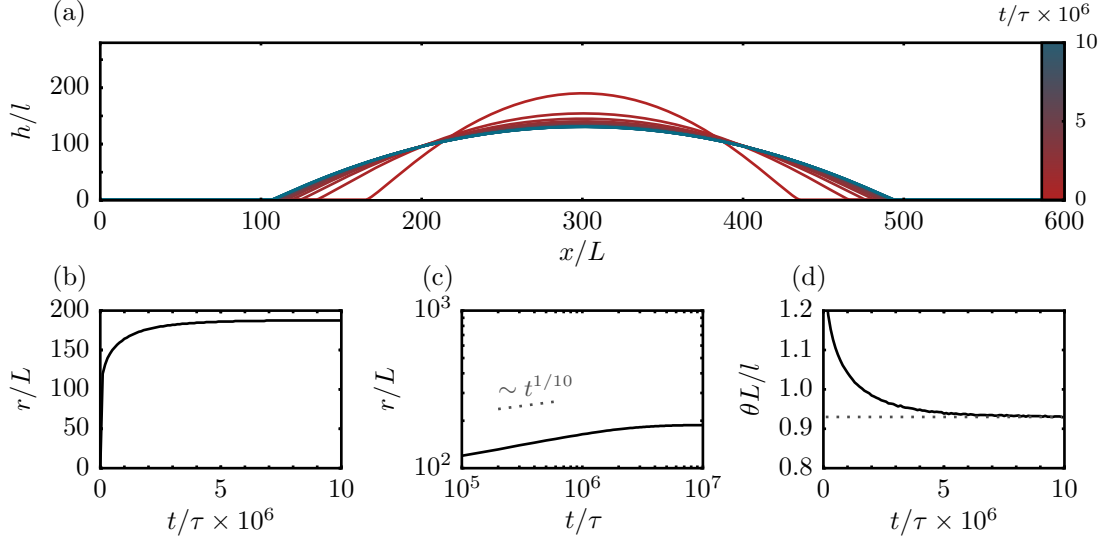
Figure 3.4.: Spreading of a passive droplet towards its equilibrium profile. (a) Height profiles taken at equidistant points in time. (b)-(c) Time evolution of the droplet radius defined by the inflection points of the height profile in normal and logarithmic scaling. (d) Contact angle determined from the curvature in the centre of the drop (solid line) and analytical equilibrium value (dotted line). The domain of length $L_x = 600$ is discretised on $N_x = 1024$ grid points. The wettability parameter (see Sec. 3.2.2) is $W_m = 3$.

Sec. A.1.1 for the above described model (3.1)-(3.9). The simulation is initiated by a height profile with a steep contact angle and the subsequent spreading of the droplet is monitored. Figure 3.4 (a) shows height profiles at equidistant points in time during the evolution of a passive droplet towards its equilibrium shape.[3] At the beginning, the radius of the droplet (b,c) rapidly increases with a time evolution $r \sim t^{1/10}$. This is known as Tanner's law [Tan79] and corresponds well to experiments on the viscous spreading of small droplets as, e.g., performed in [CS86, CW89]. The contact angle (d) is determined from the curvature of the height profile in the centre of the drop under the assumption of a parabolic profile and decreases accordingly over time. At later times, the droplet reaches the equilibrium profile discussed in Sec. 2.1.3 with a contact angle determined by Eq. (2.25) (dotted grey line).

3.2.2. Bioactive Additions

In the previous section, we have presented a model for films of passive mixtures. Now we supplement this model by bioactive processes such as proliferation and death of bacteria and the production of the polymeric matrix and also account for osmotic influx and evaporation of the solvent. The biofilm of height $h(\mathbf{x}, t)$ is modelled as a mixture of solvent (nutrient-rich water) and of biomass (bacteria and the extracellular polymeric matrix) with the height-averaged biomass concentration $\phi(\mathbf{x}, t)$ as shown schematically in Fig. 3.5 [TJLT17].

---

[3]For better comparability with later simulations, the figure is already presented in the scaling which will be introduced in Sec. 3.2.2 .

3. Osmotic Biofilm Spreading
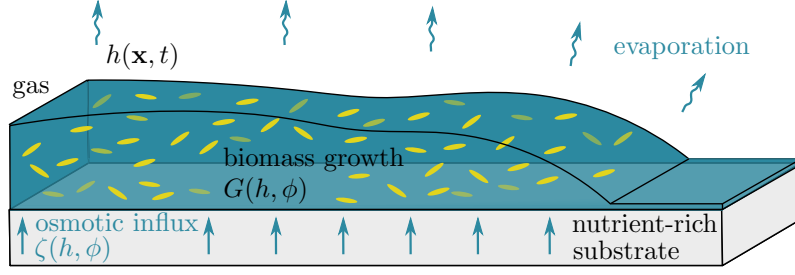
Figure 3.5.: Sketch of the osmotically driven spreading of biofilms. The bacteria in the colony consume water and nutrients to produce biomass via bacterial proliferation and matrix secretion which is described by the growth term $G(h, \phi)$. This results in osmotic pressure gradients which cause the influx of nutrient-rich water $\zeta(h, \phi)$ from the moist agar substrate into the biofilm. (cf. [TJLT17])

Incorporation of Growth Processes and Osmotic Influx

The osmotic spreading mechanism is driven by the generation of an osmotic pressure imbalance between the biofilm and the underlying agar substrate due to the production of biomass. We assume that the agar constitutes a large reservoir of nutrient rich water at a constant osmotic pressure Π_{agar}, corresponding to an equilibrium water concentration $(1 - \phi_{eq})$ in a flat biofilm. As the bacteria in the biofilm consume water and new biomass is produced, the water concentration is modified from this equilibrium value. Since the biomass cannot diffuse into the agar, the biomass growth creates an osmotic imbalance between the biofilm and the agar [TJLT17]. The osmotic pressure in the biofilm, defined as the negative of the variation of the free energy (3.1) with respect to the height h at a fixed number of osmotically active particles $h\phi$ [Doi13], is given by

$$\Pi_s = -\frac{\delta F_{\text{mix}}[h, \psi]}{\delta h} = -\frac{\delta \mathcal{F}_{\text{mix}}[h, \phi]}{\delta h} + \frac{\phi}{h}\frac{\delta \mathcal{F}_{\text{mix}}[h, \phi]}{\delta \phi} = -\partial_h f_{\text{w}} - f_{\text{m}} + \phi \partial_\phi f_{\text{m}} + \gamma \Delta h \,. \quad (3.16)$$

Note that for a flat film without wettability influences, this expression reduces to $\Pi_s = -\frac{k_B T}{a^3} \ln(1 - \phi)$ which in the dilute case of small biomass concentration $\phi \ll 1$ yields the classical linear result $\Pi_s \approx \frac{k_B T}{a^3}\phi$ [Isr85]. However, the general form (3.16) is valid for any concentration and mixing energy.

The resulting osmotic flux of water from the agar substrate into the biofilm

$$\zeta(h, \phi) = Q_{\text{osm}}\left(\Pi_s - \Pi_{\text{agar}}\right) \quad (3.17)$$

depends linearly on the osmotic pressure difference with Q_{osm} being a positive mobility constant.[4] Recall that in the employed long-wave approximation, concentration variations along the z-axis are not captured as such variations in concentrations are assumed to equilibrate fast as compared to horizontal variations. Furthermore, the osmotic fluxes between the substrate and the biofilm on the one hand and evaporation/condensation processes between the gas phase and the biofilm on the other hand are not separated but both contained in Eq. (3.17) [TJT16].

For the biomass growth, we assume that the cells proliferate and secrete the polymeric matrix while consuming the nutrient-rich water. Lumping cell growth and matrix production together into one growth rate constant g, these processes result in a gain term for the biomass concentration ϕ in the form of a bimolecular reaction

$$\partial_t \phi \propto g\phi(1 - \phi) \,. \quad (3.18)$$

---

[4]Note that the osmotic pressure corresponds to a negative mechanical pressure which causes the sign of Eq. (3.17).

The growth rate g may further depend, e.g., on the nutrient concentration in the agar substrate and on the bacterial strain. Translating this growth into an evolution for the effective height of biomass yields

$$\partial_t(h\phi) \propto gh\phi(1-\phi)\,. \tag{3.19}$$

The growth of bacteria in a biofilm is not unlimited because processes such as nutrient and oxygen depletion prevent further growth when the biofilm reaches a critical thickness [ZSS$^+$14]. These limiting processes prescribe a maximal height $h^\star$ that is related to the thickness for which nutrient diffusion and consumption of nutrients by the bacteria throughout the vertical profile of the film equilibrate [WK12]. As it is beyond the scope of this work to model oxygen and nutrient concentration directly, we introduce a limiting amount of biomass that can maximally be sustained by the substrate and which depends, e.g., on the nutrient concentration of the agar [TJT16]. This can be achieved by multiplying the growth term with the factor $(1 - \frac{h\phi}{\phi_{\mathrm{eq}}h^\star})$. It then corresponds to the well-known logistic growth law [Mur02]. In addition, we account for the fact that at least one bacterial cell is needed for cell division (and thus proliferation of biomass does not take place in the wetting layer) by introducing a growth threshold at a small value $\phi_{\mathrm{eq}}h_{\mathrm{u}}$ and a stable fixed point at $\phi_{\mathrm{eq}}h_{\mathrm{a}}$. The growth term is then given by

$$G(h,\phi) = gh\phi(1-\phi)\left(1 - \tfrac{h\phi}{\phi_{\mathrm{eq}}h^\star}\right)f_{\mathrm{mod}}(h,\phi)\,. \tag{3.20}$$

The explicit form of $f_{\mathrm{mod}}(h,\phi)$ – which models the local modifications of the growth law for very small amounts of biomass – is chosen as

$$f_{\mathrm{mod}}(h,\phi) = \left(1 - \frac{\phi_{\mathrm{eq}}h_{\mathrm{u}}}{\phi h}\right)\left(1 - \exp\left(\frac{\phi_{\mathrm{eq}}h_{\mathrm{a}} - \phi h}{h_{\mathrm{a}}}\right)\right) \tag{3.21}$$

but other choices for $f_{\mathrm{mod}}(h,\phi)$ with the same fixed point structure do not change the results qualitatively [TJLT17].

In summary, we employ a growth term that accounts for the fact that the biomass production ceases if the biofilm becomes too thick and that a small threshold value of biomass needs to be overcome to initiate growth. The production term $G(h,\phi_{\mathrm{eq}})$ is shown in Fig. 3.6 assuming a fixed biomass concentration ϕ_{eq} which corresponds to the case of an osmotic influx which is very fast as compared to the biomass growth, as we will discuss below.

To obtain the model for the osmotic spreading of biofilms, biomass growth and osmotic influx are now incorporated into the passive model (3.1)-(3.15) as two non-conserved terms which results in the evolution equations [TJT16]

$$\partial_t h = -\nabla \cdot \mathbf{j}_{\mathrm{conv}} + \zeta(h,\phi) \tag{3.22}$$

$$\partial_t(h\phi) = -\nabla \cdot (\phi\mathbf{j}_{\mathrm{conv}} + \mathbf{j}_{\mathrm{diff}}) + G(h,\phi)\,. \tag{3.23}$$

for the colony height h and the effective layer thicknesses of biomass $h\phi$.[1]

Derivation of a Reduced Model in the Limit of a Fast Osmotic Influx

Before we introduce a scaling for the model, we consider a limiting case in which the complexity of the model can be considerably reduced. Following the discussion and the parameters given in Refs. [YTST17] and [DTH14], the influx of water into the colony ζ can be estimated by Darcy's Law which describes the flow of a liquid per area through a porous medium (in the units of $\frac{\mathrm{m}}{\mathrm{s}}$) as

$$|\zeta| = Q_{\mathrm{osm}}\Delta P \approx \frac{\chi RT}{\eta_f L}\Delta n \tag{3.24}$$

3. Osmotic Biofilm Spreading
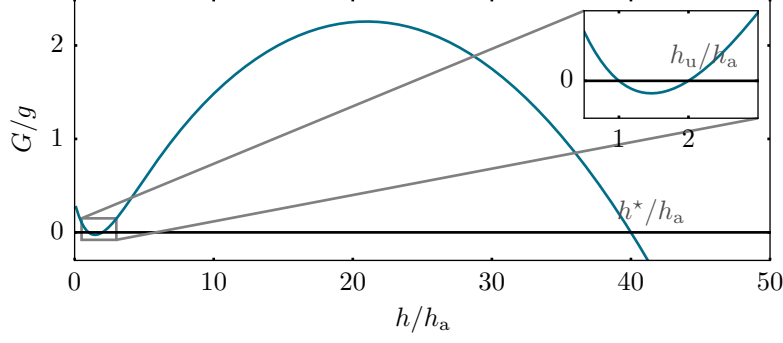
Figure 3.6.: The bioactivity $G(h, \phi)$ has the form of a modified logistic term and leads to growth if the amount of biomass is smaller then a limiting amount $h^\star$. Here, $G(h, \phi_{\mathrm{eq}})/g$ is shown for the quasi-steady state of the osmotic influx for $\phi_{\mathrm{eq}} = 0.5$, $h_{\mathrm{u}} = 2\, h_{\mathrm{a}}$, and $h^\star = 40\, h_{\mathrm{a}}$. The inset zooms into the region of small film height and shows the fixed point structure resulting from $f_{\mathrm{mod}}(h, \phi)$. (cf. [TJT16])

where χ is the intrinsic permeability of the medium, ΔP is the difference in the pressure, η_f is the fluid viscosity and L is the length over which the total pressure drop is taking place. Neglecting gravity, the pressure difference ΔP can be approximated by the difference in osmotic pressure $RT\Delta n$, with R and T denoting the gas constant and temperature, respectively, and Δn denoting the difference in osmolarity between the agar and the colony. Assuming a permeability $\chi \approx 3000\,\mathrm{nm}^2$ [DTH14], the viscosity of water $\eta_f = 10^{-3}\,\mathrm{Pa\,s}$, a crude estimate of the interface width of $L = 0.1...1000\,\mu\mathrm{m}$ and an agar concentration of $0.5\,\%$ with a molecular weight of $10^5\,\mathrm{g/mol}$ results in an osmotic influx ζ ranging from $1\,\mathrm{mm/h}$ to $3\,\mathrm{mm/s}$.

In comparison, a typical bacterial growth rate constant is $g \approx 1\frac{1}{\mathrm{h}}$ and the typical height of a swarming bacterial colony is $h = 20\,\mu\mathrm{m}$ [FPB+12]. Therefore, the ratio between growth (gh) and osmotic water influx ζ is $\frac{\zeta}{gh} \approx 4\times10^3 \ldots 4\times10^7$ and it is thus plausible to assume a quasi instantaneous osmotic equilibrium between the agar and the colony.

If the influx of water is fast as compared to biomass growth but not as fast as the hydrodynamic fluxes, large biofilm droplets are always in 'osmotic equilibrium' $\Pi_{\mathrm{s}} = \Pi_{\mathrm{agar}}$ with the substrate on the time scale of the biomass growth [TJLT17]. In this case, the biomass concentration is given by

$$\phi = \phi_{\mathrm{eq}}\,. \tag{3.25}$$

The osmotic influx instantaneously compensates the modification in the osmotic pressure induced by the biomass growth, i.e. it replaces the nutrient-rich water consumed during the production of biomass and causes an additional influx to reach the osmotic equilibrium for the new (higher) amount of biomass in the film. It can thus be written as

$$\zeta(h, \phi_{\mathrm{eq}}) = \frac{1}{\phi_{\mathrm{eq}}} G(h, \phi_{\mathrm{eq}})\,. \tag{3.26}$$

In this case, one can reduce the model (3.22)-(3.23) to an effective description of the biofilm height

$$\partial_t h = \nabla \cdot \left[\frac{h^3}{3\eta} \nabla(\partial_h f_{\mathrm{w}} - \Delta h)\right] + \frac{1}{\phi_{\mathrm{eq}}} G(h, \phi_{\mathrm{eq}}) \tag{3.27}$$

with a constant viscosity $\eta = \eta_0[(1 - \phi_{\mathrm{eq}}) + \phi_{\mathrm{eq}}\frac{\eta_b}{\eta_0}]$ [TJLT17].

Dimensionless Form of the Equations

To facilitate the analysis, a dimensionless form of the model for osmotically spreading biofilms can be obtained by introducing the scaling

$$t = \tau \tilde{t} \qquad (x,y) = L(\tilde{x}, \tilde{y}) \qquad h = l\tilde{h} \qquad f_{w,m} = \kappa \tilde{f}_{w,m} \tag{3.28}$$

with $l \ll L$ for time, the horizontal and vertical coordinates and energy. Dimensionless quantities are indicated by tildes. Inserting the scaling

$$\tau = \frac{L^2 \eta_0}{\kappa l} \qquad \kappa = \frac{kT}{a^3} l \qquad l = h_a \qquad L = \sqrt{\frac{\gamma}{\kappa}} l \,, \tag{3.29}$$

into the evolution equation results in the dimensionless growth rate $\tilde{g} = g\tau$, the osmotic mobility $\tilde{Q}_{osm} = Q_{osm} \tau \kappa / l^2$, the dimensionless diffusivity $\tilde{D} = \frac{\delta^2}{6\pi\tilde{\eta}}$ with $\delta = \frac{a}{h_a}$ and the wettability parameter

$$W_m = \frac{A}{\kappa l^2} = \frac{A}{k_B T} \frac{a^3}{l^3} \tag{3.30}$$

that measures the relative strength of the wetting energy as compared to the entropic free energy of mixing. From Eq. (2.25), it can be shown that the parameter W_m is connected to the (passive) equilibrium contact angles via $\tan^2(\theta_{eq}) = \frac{3}{5} W_m$. Therefore, larger values of W_m result in larger equilibrium contact angles and describe a less wettable substrate. The model in the dimensionless form can be found in the Appendix A.2.1.

Experimental Calibration

A biofilm is a complex system which can only be expected to be described qualitatively, not quantitatively by a simple model. However, the parameters and scales of the model are in the following exemplarily estimated by a calibration with experiments. Comparing with the typical biofilm height of $\sim 400 \, \mu$m measured in [VALK08, ZSS$^+$14, WKW$^+$16] and using the viscosity and surface tension of water, as well as the typical solvent/biomass length summarised in Table 3.1 results in

$$l = h_a \approx 3 \, \mu\text{m} \qquad L \approx 85 \, \mu\text{m} \qquad \tau \approx 0.02 \, \text{s} \qquad \kappa \approx 9.6 \, 10^{-5} \text{J/m}^2 \tag{3.31}$$

for the length, time and energy scales.

surface tension	$\gamma \approx 70$mN/m
height of the wetting layer	$h_a \approx 3\mu$m
viscosity of water	$\eta_0 \approx 10^{-3}$Pas
typical surfactant length scale	$a \approx 50$nm
thermal energy at 25°	$k_B T \approx 4 \cdot 10^{-21}$J

Table 3.1.: Parameters used to determine the time and length scales.

Throughout the analysis, we fix the maximal amount of biomass that can be sustained by the substrate to $\tilde{h}^\star \phi_{eq} = 60$, the equilibrium water concentration to $(1 - \phi_{eq}) = 0.5$, the ratio $\delta = 1$, the adsorption layer height to $\tilde{h}_a = 1$, the growth threshold to $\tilde{h}_u = 2$ and the ratio of the viscosities of biomass and liquid to $\eta_b/\eta_0 = 10000$ [WAS$^+$11]. The biofilm spreading behaviour is studied depending on the growth rate $\tilde{g}$, the wettability parameter W_m and the osmotic mobility $\tilde{Q}_{osm}$.

With the above scales, a wettability parameter $W_m = 8$ corresponds to an equilibrium contact angle of $5\,°$, comparable to the dynamic contact angle measured in [ZSS$^+$14]. A dimensionless expansion rate of 10^{-5} corresponds to a speed of $0.1 - 0.2 \, \text{mm/h}$.[1]

	dimensionless value	corresponding dim. value	literature value
growth rate	$\tilde{g} = l\tau = 2 \times 10^{-5}$	$g \approx 3.6\frac{1}{\text{h}}$	Doubling time of *B. subtilis* when grown at 35°C in minimal media : 120min [BKW86]
colony height	$\tilde{h} = \frac{h}{l} = 120$	$h \approx 360\mu\text{m}$	colony height of a *B. subtilis* colony: $\approx 400\mu\text{m}$ [ZSS$^+$14, WKW$^+$16]
mobility of the osmotic flux	$\tilde{Q}_{\text{osm}} = Q_{\text{osm}}\tau\kappa/l^2 = 0.01$	$Q_{\text{osm}} \approx 5\times10^{-6}\frac{\text{m}^2\text{s}}{\text{kg}}$	

Table 3.2.: Estimation of some parameters in the model for the scaling given in (3.31) and comparison to values found in the literature.

3.3. Continuously Spreading Biofilms

In this section, we employ the developed biofilm model (3.22)-(3.23) to explore the influence of wettability and surface tension on the osmotic spreading of biofilms. The model also allows us to study the interplay between these passive forces and bioactive growth and production processes. We find that the model reproduces the non-equilibrium transition between continuously spreading biofilms and arrested spreading observed in experiments (see Sec. 3.1). On the one hand, at relatively high wettability, the biofilm initially rapidly swells vertically and horizontally until a stationary film height is reached before expanding continuously over the substrate. On the other hand, at lower wettability, the spreading of the biofilm is arrested.

In the first part of this section, we focus on continuously spreading biofilms and discuss the transition from swelling to spreading as well as the front solutions which evolve at large times. Next, we explore conditions for which biofilm spreading is arrested and construct a phase diagram.

3.3.1. Transition from Swelling to Spreading

First, we focus on situations with relatively high wettability and perform numerical time simulations employing a finite element scheme as described in the appendix A.1.1. The biofilm is studied for a one-dimensional geometry (corresponding biofilm ridges instead of circular colonies) with no-flux boundary conditions. The simulations are initiated with a small droplet of biofilm at equilibrium water concentration. In the early stages of growth, the droplet undergoes a transition from initial rapid swelling to subsequent horizontal spreading. Fig. 3.7 (a) shows height profiles for a growing biofilm at equidistant points in time. Initially, the droplet rapidly grows vertically and horizontally. When the biofilm height approaches the limiting value $\tilde{h}^\star$, the vertical growth slows down and only horizontal spreading prevails and provides the film with fresh nutrients and water at the edges. At this stage, the biofilm only spreads horizontally with a constant speed and shape of the biofilm edge [TJT16]. Note that the front profiles in the dimensional scaling are much more shallow than in the dimensionless representation shown in the Fig. 3.7.

The transition between vertical and horizontal swelling can by studied more quantitatively by analysing the time evolution of the drop radius, the maximal film height and the contact angle which are shown in Figures 3.7 (b), (c) and (d) respectively. We define the drop size of the biofilm $r(t)$ as the position of the inflection points of the height profile $h(\mathbf{x}, t)$ at the edge of the droplet. In the very beginning of the colony growth, up to
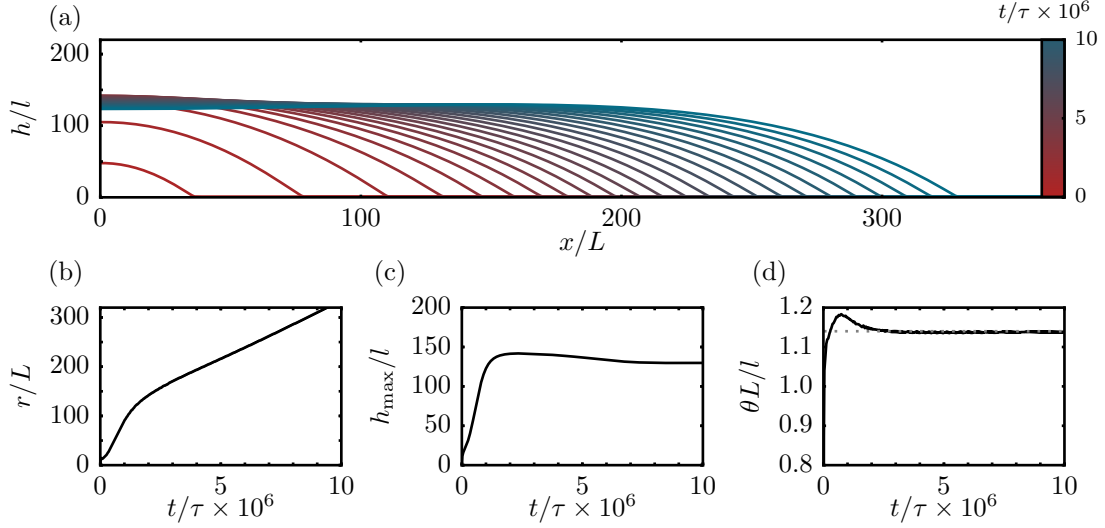
Figure 3.7.: Continuously spreading biofilm for $W_{\mathrm{m}} = 8$. (a) Height profiles taken at equidistant points in time. (b) Time evolution of the biofilm extension r/L measured at the inflection point of the height profile. (c) Maximal biofilm height h_{max}/l (d) Contact angle determined from the slope of h at the inflection point. The dotted grey line corresponds to the passive equilibium contact angle θ_{eq}. The remaining parameters are $\tilde{g} = 2 \times 10^{-5}$ and $\tilde{Q}_{\mathrm{osm}} = 0.01$.

$t \approx 0.5 \times 10^6 \tau$, the radius only increases slowly. In this phase, vertical growth is more dominant than horizontal spreading and the contact angle of the droplet increases. After this initial phase, the radius and the colony height increase rapidly until the height reaches a maximum. Then, the height decreases slightly to approach the plateau value $\tilde{h}^\star$ at time $t \approx 5 \times 10^6 \tau$. Beyond this time the biofilm is expanding by a growth front that advances horizontally with a constant velocity and a constant front profile, i.e., the dynamic contact angle is also constant [TJT16]. The plateau value for the contact angle corresponds to a value that is slightly larger than the passive equilibrium contact angle $\tan^2(\theta_{\mathrm{eq}}) = \frac{3}{5} W_{\mathrm{m}}$ (i.e., $\theta_{\mathrm{eq}} \approx 1.14$ for $W_{\mathrm{m}} = 8$ in the dimensionless scaling). The above described growth dynamics agrees with the experimental observations [SAW+12, ZSS+14] for *B. subtilis* colonies.

Fig. 3.8 shows snapshots of two exemplary profiles, one in the swelling regime at the beginning of the time evolution (a) and the other one in the spreading regime at a late time when all transients have decayed (b). The distinct features of the two expansion modes become clear by studying the height profile (solid lines, top row) and biomass concentration (colour coding, top row). The direction and strength of the osmotic influx are indicated by the blue arrows underneath the biofilm. The influx and biomass growth profiles are shown in the middle and bottom row, respectively.

In the swelling regime, the biofilm has not yet reached the limiting height and the growth term G is positive throughout the colony. The biomass concentration is overall higher than the equilibrium value, so that water is drawn into the film along its whole profile via the osmotic influx ζ. At late stages, the situation is different: Far from the advancing edges, the biofilm has reached the limiting film height $\tilde{h}^\star$ and the biomass concentration corresponds to the equilibrium value ϕ_{eq}. In the centre of the colony, biomass production and degradation are in dynamic equilibrium as are osmotic influx and evaporation of water, i.e., no net growth or influx takes place ($G = 0$ and $\zeta = 0$). The biofilm height h

(a) Swelling at $t/\tau = 0.5 \times 10^6$ — (b) Spreading at $t/\tau = 10 \times 10^6$
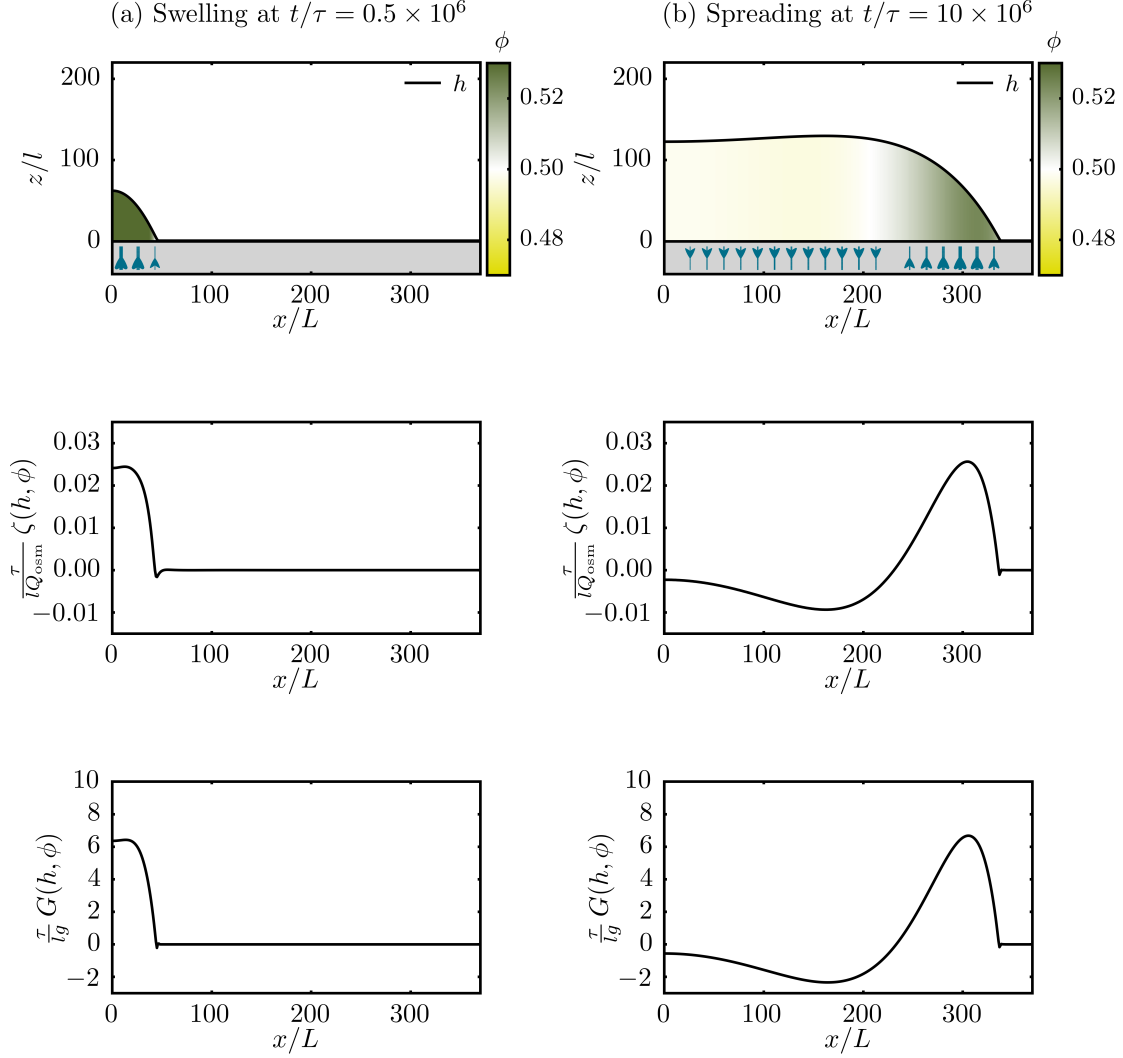
Figure 3.8.: Swelling regime in the beginning of the expansion (a) and spreading fronts which occur for large times (b) in a continuously spreading biofilm for $W_{\mathrm{m}} = 8$. The height profiles are shown in the top row with solid lines. The shading within the film indicates the biomass concentration ϕ. The direction and strength of the effective osmotic flux $\zeta(h, \phi)$ are represented by the direction and thickness of the blue arrows below the biofilm. The middle and bottom figures show the osmotic influx profile and the biomass growth term, respectively. The remaining parameters are $\tilde{g} = 2 \times 10^{-5}$ and $\tilde{Q}_{\mathrm{osm}} = 0.01$.

and the biomass concentration are constant in the central region of the biofilm. Near the edges, the biomass has not yet reached the limiting amount and the production of matrix and new bacterial cells is localised to a propagating front [TJT16]. This is in accordance with observations on the spatial distribution of matrix production in *B. subtilis* biofilms [SVK+18]. The biomass production modifies the water concentration from the equilibrium value $(1 - \phi_{\text{eq}})$ which results in an osmotic influx of water from the agar substrate into the biofilm. We find that the osmotic influx mainly takes place at the edges of the biofilm. Shortly behind the front edge, the influx is slightly negative and water is pushed back into the agar. This influx profile is in qualitative agreement with the experimental observations of the osmolarity and osmotic fluxes in *B. subtilis* colonies [PWH+14].

In the next section, we analyse the regime of continuously spreading fronts which evolve at large times in more detail.[1]

3.3.2. Front Solutions for Continuously Spreading Biofilms

The time simulations presented in the previous section showed that for high wettability, the biofilm advances at large times with constant velocity and shape. This allows for an efficient and more systematic analysis of the system using parameter continuation. This technique, which is outlined in appendix Sec. A.1.2 enables a direct observation of the influence of the model parameters on front profile and velocity. To that end, we interpret the solutions as stationary fronts in a co-moving coordinate frame which moves with the velocity of the expanding colony. We transform the evolution equations (3.22)-(3.23) written in the fields h and $\psi = h\phi$ into the co-moving coordinate system with a constant velocity v via the coordinate transformation $x \to x + vt$. In this co-moving frame, the equations are given by

$$
\begin{aligned}
\partial_t h &= -\nabla \cdot \mathbf{j}_{\text{conv}} + \zeta(h, \psi) + v\partial_x h \\
&= \mathscr{F}_1(\nabla, v)[h, \psi]
\end{aligned}
\tag{3.32}
$$

$$
\begin{aligned}
\partial_t \psi &= -\nabla \cdot (\phi \mathbf{j}_{\text{conv}} + \mathbf{j}_{\text{diff}}) + G(h, \psi) + v\partial_x \psi \\
&= \mathscr{F}_2(\nabla, v)[h, \psi] \,.
\end{aligned}
\tag{3.33}
$$

where we introduced $\mathscr{F}_{1,2}(\nabla, v)$ as a short hand notation for the nonlinear operators defined by the right-hand sides of the evolution equations (3.32)-(3.33). Thus, planar fronts $(h_0(x), \psi_0(x))$ which depend only on one spatial coordinate, x, and move with a stationary profile and velocity v correspond to stationary solutions

$$
\partial_t h_0(x) = \mathscr{F}_1(\nabla, v)[h_0(x), \psi_0(x)] = 0
\tag{3.34}
$$

$$
\partial_t \psi_0(x) = \mathscr{F}_2(\nabla, v)[h_0(x), \psi_0(x)] = 0
\tag{3.35}
$$

in the co-moving frame. The explicit formulation necessary for the analysis with the continuation package *AUTO-07p* is given in the appendix Sec. A.2.2.

The dependence of the front velocity v and the dynamic contact angle θ on various parameters of the model is presented in Fig. 3.9. The first and second row show the influence of (a) biomass production $\tilde{g}$, (b) osmotic mobility $\tilde{Q}_{\text{osm}}$, (c) colony height $\tilde{h}^\star$ and (d) wettability parameter W_{m} on the velocity and the contact angle. The third and fourth row show the profiles of height h and biomass ϕh for two parameter combinations indicated by circles in the velocity and contact angle plots. The system exhibits stable front solutions over a broad parameter range which can be seen as a sign of its robustness. Recall that the model is analysed in the dimensionless long-wave form and $l \ll L$ holds for the dimensional vertical and horizontal length scale. Consequently, the dimensional front profiles
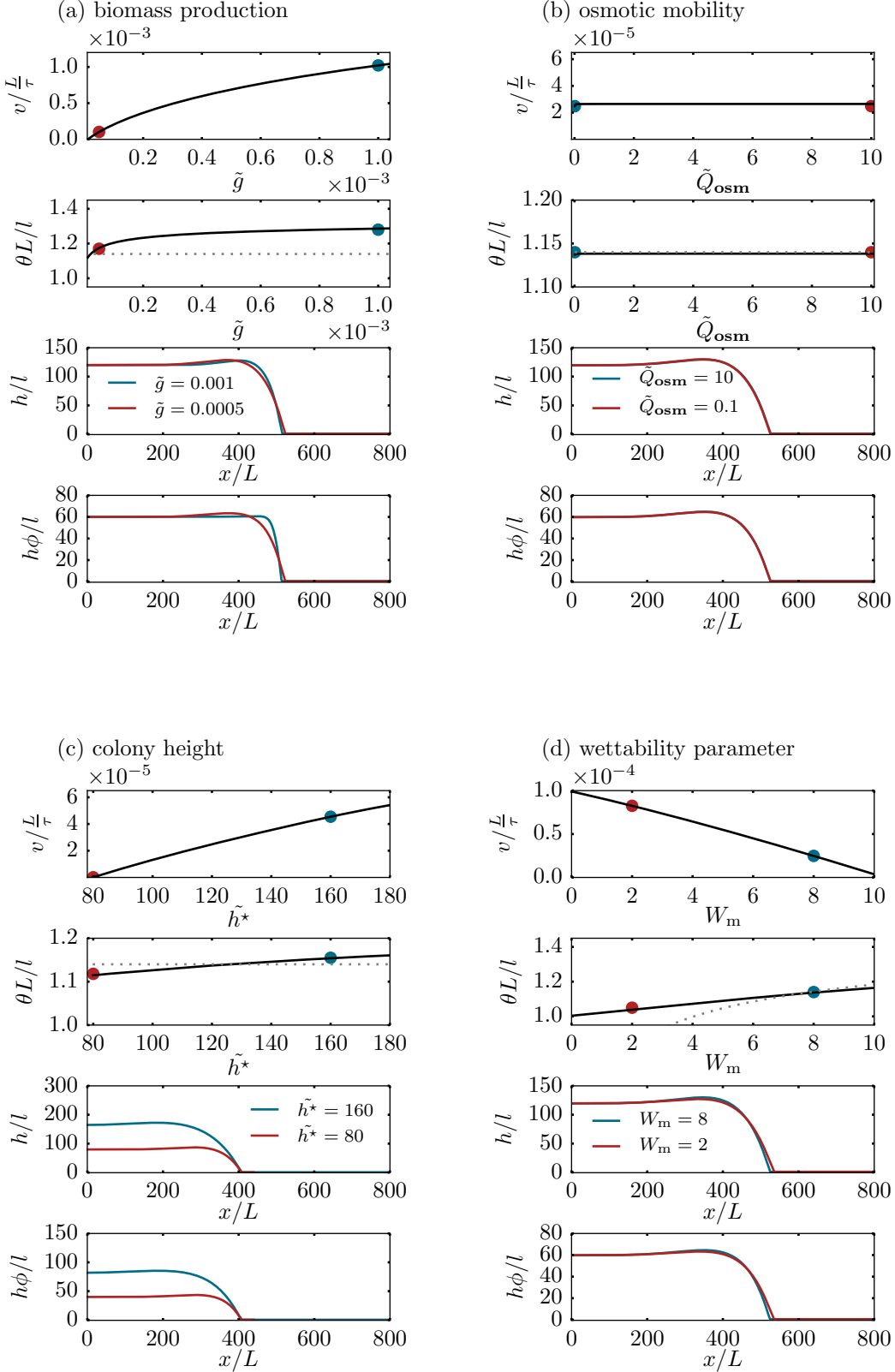
Figure 3.9.: Front velocity (top row) and contact angle (second row) depending on (a) the biomass production $\tilde{g}$, (b) the osmotic mobility $\tilde{Q}_{\mathrm{osm}}$, (c) the limiting colony height $\tilde{h}^{\star}$ and (d) the wettability parameter W_{m}. One parameter is varied in a parameter continuation, respectively, taking a solution for $\tilde{g} = 2 \times 10^{-5}$, $W_{\mathrm{m}} = 8$, $\tilde{Q}_{\mathrm{osm}} = 0.01$ and $\tilde{h}^{\star} = 120$ as a reference. The dotted grey line corresponds to the passive equilibrium contact angle θ_{eq}. The third (fourth) row shows the profiles of height h (biomass ϕh) for two parameter combinations indicated by circles in the respective line colour in the velocity and contact angle plots.

are much more shallow than in the dimensionless representation of the profiles shown in our figures. This also concernes the measured contact angles.

As expected, the front velocity increases with the biomass production rate $\tilde{g}$ (see Fig. 3.9 (a)), as this parameter represents the strength of the non-conserved part of the model causing the osmotic imbalance in the biofilm and triggering the subsequent influx of water. For small bioactivity rates $\tilde{g}$, the front advances very slowly and the contact angle approximately corresponds to the equilibrium contact angle of a droplet of passive mixture (dotted lines) given by Eq. (2.25). For a fast biomass growth, the growth term $G(h, \phi)$ dominates the shape of the biofilm. The front profile becomes steeper when a stronger biomass growth pushes the biofilm front forward [TJT16]. This indicates that the dynamic contact angle increases with the front velocity. This behaviour is also known from the passive advance of fronts or drops, e.g. spreading drops or sliding drops on an incline [BEI$^+$09, TVN$^+$01].

The velocity of the biofilm also increases with increasing biofilm height $\tilde{h}^\star$ (see Fig. 3.9 (c)). In contrast, the osmotic mobility – which reflects the permeability of the interface between moist substrate and biofilm – has only a small influence on the front velocity and front profile (see Fig. 3.9 (b)). This is because the time scale of the osmotic flux is always faster than the hydrodynamic time scale and the time scale of biomass growth in the considered parameter regime, so that the biofilm can always reach osmotic equilibrium relatively fast. Interestingly, also the wettability parameter W_m, which represents the influence of passive wetting forces, strongly influences the spreading velocity (see Fig. 3.9 (d)). The biofilm drastically slows down for a low wettability (large W_m). We focus on this feature in the next section.

3.4. Arrested Spreading of Biofilms

The analysis of the fronts in the model for *continuously* spreading biofilms at large times in the previous section has shown that the wettability can dramatically slow down the lateral expansion. In this section, we analyse the mechanism behind the *arrested* biofilm spreading by studying the time evolution of bacterial colonies in our model at low wettability (large W_m). Then, the evolution of the biofilm dramatically differs from the continuous spreading mode described in the previous section. We first analyse this regime by performing numerical time simulations starting from a small biofilm droplet. Fig. 3.10 shows snapshots of the height profile (a), as well as the time evolution of colony radius (b), height (c) and contact angle (d) for a large value of W_m corresponding to a low wettability. Again, the biofilm initially rapidly swells. The influx and biomass production profile at this stage are shown in Fig. 3.11 and quantitatively resemble those observed previously for continuously spreading biofilms. However, in contrast to the case of higher wettability, the biofilm soon evolves towards a stationary profile of fixed extension and contact angle [TJLT17]. From a snapshot of the solution at a large time shown in Fig. 3.11 (b), it can be clearly seen that the stationary biofilm drops are still bioactive. Biomass is being produced at the biofilm edges where $G > 0$ and is degraded at the centre where $G < 0$ as there, the biomass exceeds the limiting amount $\phi_\mathrm{eq}h^\star$. The influx profile shows that accordingly, water is drawn into the biofilm at the edges where the biomass concentration is high, and pushed back into the substrate in the middle of the colony. The arrested state is possible as hydrodynamic and diffusive fluxes within the biofilm and osmotic fluxes between agar and biofilm rearrange biomass and water such that their profiles are stationary [TJLT17].
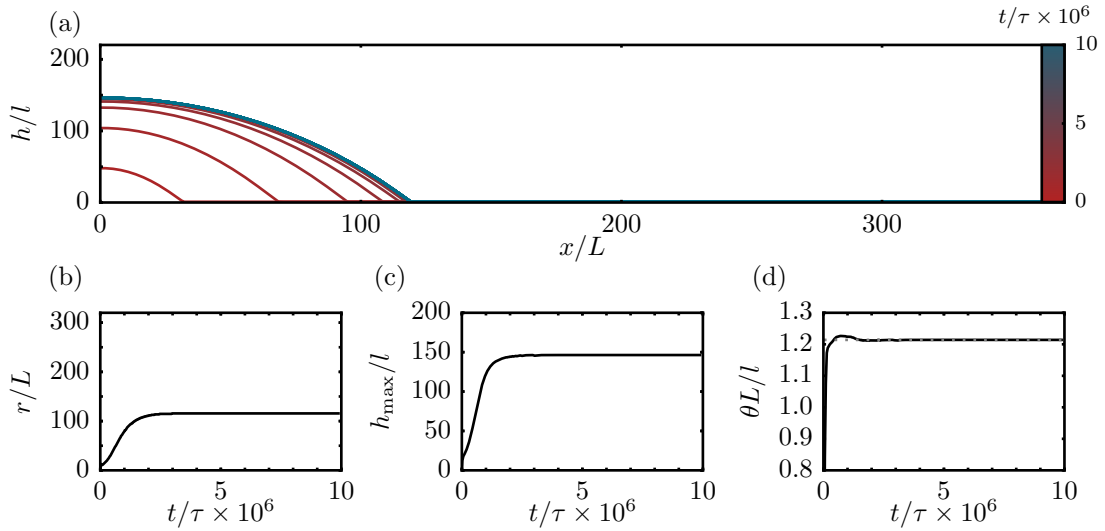
Figure 3.10.: Arrested biofilm spreading for low wettability $W_\mathrm{m} = 12$. (a) Height profiles taken at equidistant points in time. (b) Time evolution of the biofilm extension $r(t)$ defined by the inflection point of the height profile. (c) Maximal biofilm height $h_\mathrm{max}(t)$. (d) Contact angle determined from the slope of h at the inflection point. The remaining parameters are $\tilde{g} = 2 \times 10^{-5}$ and $\tilde{Q}_\mathrm{osm} = 0.01$.
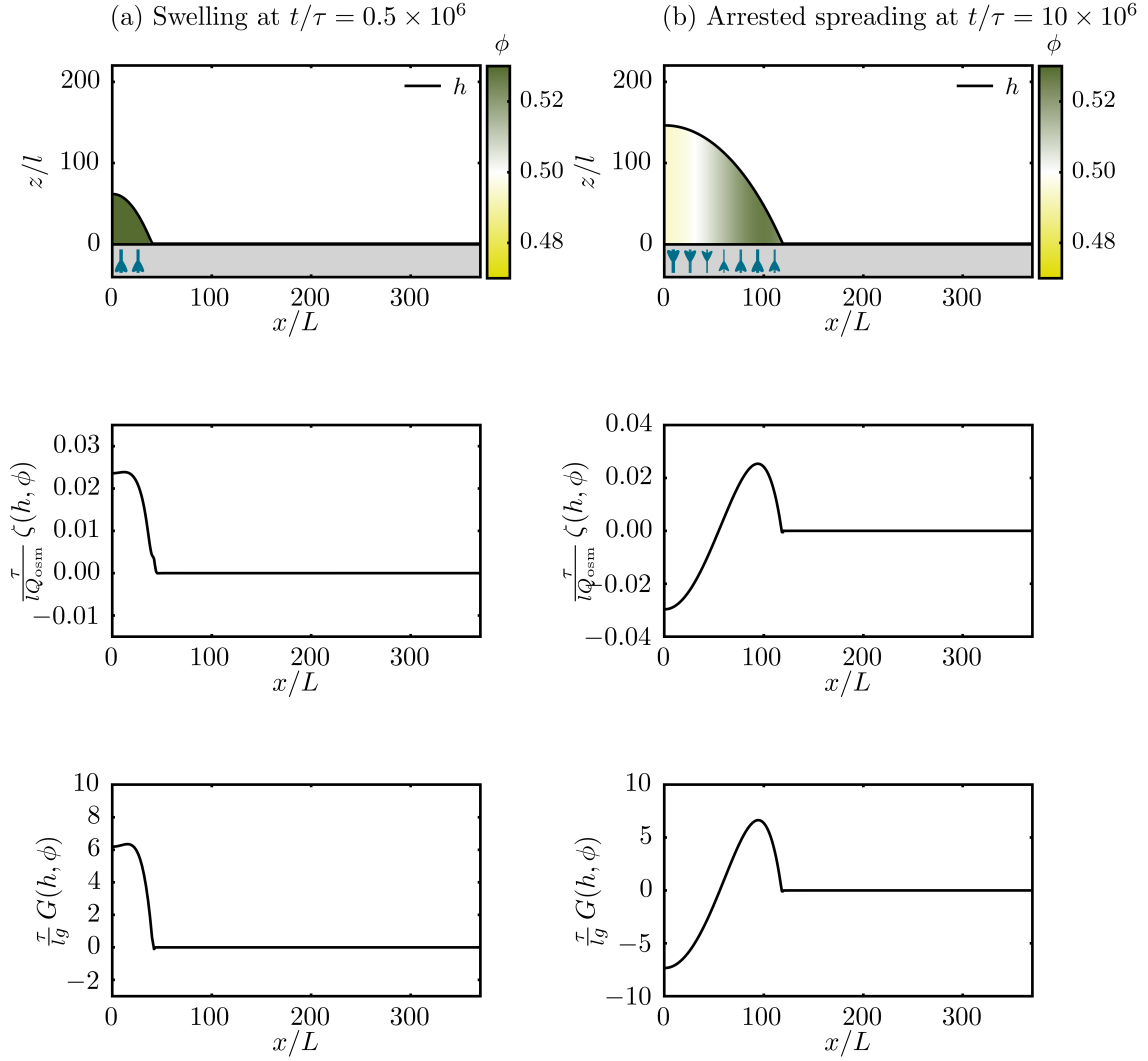
Figure 3.11.: Swelling regime in the beginning of the expansion (a) and stationary profile occurring for large times (b) in a biofilm with arrested spreading for low wettability $W_{\mathrm{m}} = 12$. The height profiles are shown in the top row with solid lines. The shading within the film indicates the biomass concentration ϕ. The direction and strength of the effective osmotic flux $\zeta(h, \phi)$ are represented by the direction and thickness of the blue arrows below the biofilm. The middle figures and the bottom figures show the osmotic influx profile and the biomass growth term, respectively. The remaining parameters are $\tilde{g} = 2 \times 10^{-5}$ and $\tilde{Q}_{\mathrm{osm}} = 0.01$.

3. Osmotic Biofilm Spreading

Bifurcation Analysis

In the previous sections, we have seen that the biofilm model possesses two qualitatively different equilibrium solutions: For high wettability (low W_m), the biofilm expands via a front solution with constant velocity v and profile. At low wettability (large W_m), the biofilm evolves towards a stationary droplet. Before we generate a phase diagram that identifies the regions of the two spreading modes in parameter space and compare it to the experimental observations, we briefly address a more technical issue and perform a bifurcation analysis of the problem. In particular, we analyse how the stationary, arrested biofilm droplet loses its stability, when the wettability is enhanced (lower W_m) or the biomass growth rate $\tilde{g}$ is increased.
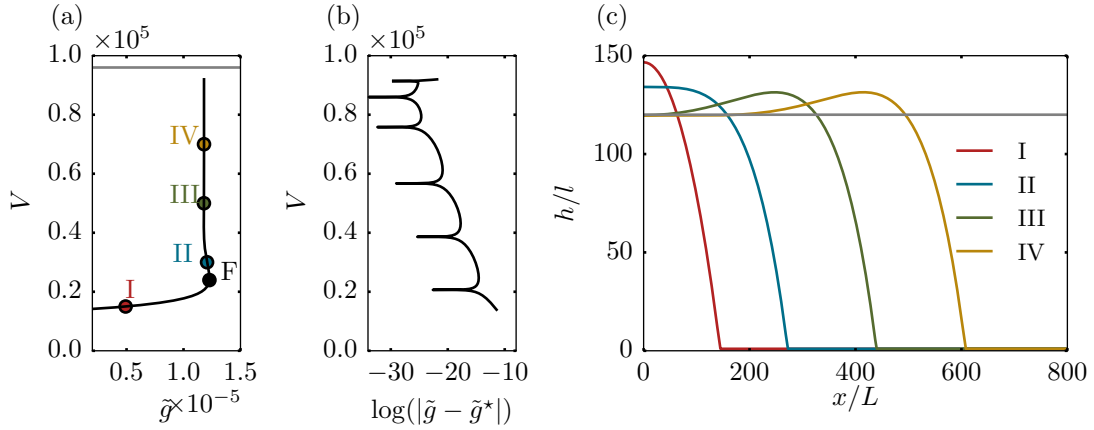
Figure 3.12.: Parameter continuation in the growth rate $\tilde{g}$ at fixed velocity $v = 0$ and varying drop volume $V = \int h \, dx$. (a) The solution branch of arrested biofilm droplets loses its stability in a fold bifurcation (F) at $\tilde{g} \approx 1.227 \times 10^{-5}$. The subsequent snaking is shown in more detail in (b). The height profiles, which correspond to the solutions indicated in (a) are presented in (c) and show a transition from 'droplet-like' to 'front-like' biofilms. The remaining parameters are $\tilde{Q}_{osm} = 0.01$ and $\tilde{h}^\star = 120$.

Figure 3.12 (a) shows the solution branch for a parameter continuation in the growth rate at fixed velocity $v = 0$ and adapting drop volume $V = \int h \, dx$. For low biomass rates $\tilde{g}$, the arrested droplet is a stable solution. The height profile (I) shown in Fig. 3.12 (c) indicates that along this branch, the solution is 'droplet-like' with a maximum at $x = 0$. When the biomass growth $\tilde{g}$ is increased, this solution loses its stability in a fold bifurcation (F) at $\tilde{g} \approx 1.227 \times 10^{-5}$. After this bifurcation, the solutions form a *snaking* branch [BK07] in the bifurcation diagram. Along this branch of alternate stability, the profiles are 'front-like' (see II - IV in 3.12 (c)) and their volume increases, i.e., the front edge is shifted further to the right in the domain. The *snaking* nature of this branch is more visible in Fig. 3.12 (b), where the volume is shown against the difference between the biomass growth $\tilde{g}$ and the value $\tilde{g}^\star \approx 1.1798 \times 10^{-5}$ that the branch converges to. A qualitatively different solution is the flat biofilm of height $h = h^\star$ which is shown in grey in Fig. 3.12 (a) and (c). Presumably due to the Neumann boundary conditions, the snaking branch can, however, not be followed until it reaches this solution branch, i.e., until the front solution fills the whole domain.

The branch of arrested solutions discussed above is connected to the branch of moving front solutions. Starting for example from point IV, one can perform a second parameter continuation in the velocity v at fixed volume and obtain solutions corresponding to the

continuously spreading fronts presented, e.g., in Fig. 3.9 (a). The model is thus multistable in a (small) parameter region, i.e., different solutions coexist.

In the next section, the results obtained from the bifurcation analysis will be employed to generate a morphological phase diagram.

3.5. Phase Diagram

The bifurcation analysis at fixed wettability has shown that a fold bifurcation represents a limiting point for the existence of the arrested biofilm droplets. To obtain their stability region in the $(\tilde{g}, W_{\mathrm{m}})$ parameter space, we now perform various continuation runs for different values of W_{m} similar to the one discussed above in Fig. 3.12 . For each run, the fold point is detected. This information can be used to generate the morphological phase diagram in Fig. 3.13 which summarises the spreading behaviour in dependence of wettability parameter W_{m} and the biomass growth rate $\tilde{g}$.
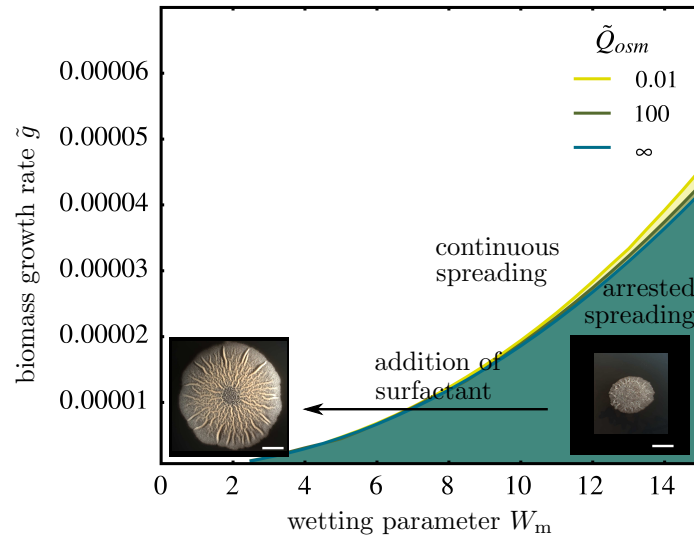
Figure 3.13.: Spreading behaviour of the biofilm in the $(\tilde{g}, W_{\mathrm{m}})$ parameter plane for various values of the osmotic mobility $\tilde{Q}_{\mathrm{osm}}$ as indicated in the legend. In the shaded regions, the spreading of the biofilm is arrested, i.e., the colony reaches a stationary profile. Outside of this region, lateral spreading is not limited. These two regimes correspond, e.g., to arrested biofilms deficient in surfactant production which do not expand laterally but for which continuous spreading can be induced by increasing the wettability (lowering W_{m}) by the external addition of surfactant. Scale bar: 5mm (cf. [TJLT17])

At constant $\tilde{g}$, corresponding, e.g., to a specific bacterial strain, spreading of the biofilm is arrested at low wettability (high value of W_{m}) but the colony spreads continuously if the wettability is enhanced (low value of W_{m}). In the context of the experiments described in Sec. 3.1, an enhanced wettability corresponds to the situation in which a self-produced or artificial homogeneously distributed surfactant lowers the surface tension. The presence of surfactant can thus trigger a transition from a biofilm with arrested spreading to a continuously spreading biofilm [TJLT17] – in agreement with the experimental results in Fig. 3.2 and Ref. [LMB+06]. This transition only slightly depends on the strength of the osmotic mobility $\tilde{Q}_{\mathrm{osm}}$ (see Fig. 3.13) and one may consider the limiting case of

an instantaneous osmotic solvent transfer between agar and biofilm (i.e., $\tilde{Q}_{osm} \gg 1$). In this parameter regime, the model reduces to a one-variable model for the evolution of the biofilm height as discussed in Sec. 3.2.2. The simplified model still reproduces all relevant experimental features. For the limiting case of infinitely fast osmosis, the parameter region of arrested spreading is only slightly smaller than for finite $\tilde{Q}_{osm}$. This indicates that surface and entropic mixing forces rather than time scales of transport and bioactive processes are dominant in the determination of the transition between stationary and laterally expanding biofilms [TJLT17].[1]

4. Thin Liquid Films and Droplets Covered by Insoluble Surfactants

In the previous chapter, we have seen that the presence of bio-surfactants can have a strong influence on the spreading dynamics of bacterial colonies by modifying the wettability. However, the effect of surfactants on the spreading dynamics is not limited to a variation of the equilibrium contact angle: Gradients in surfactant concentration – which we have not accounted for in the previous section – may lead to additional flows. These so-called *Marangoni flows* arise due to gradients in surface tension. In bacterial colonies, bio-surfactants are being produced by the bacteria over time and a dynamical distribution of surfactant molecules with concentration gradients (giving rise to Marangoni flows) is to be expected. To study their effect on the spreading of the colony, it is necessary to introduce a surfactant dynamics into the model. Before we investigate in more detail how surfactants affect the expansion of bacterial colonies, we first study a related but simpler passive system, namely a droplet of simple liquid covered by insoluble surfactants.

After reviewing some experimental findings related to the presence of surfactants, we focus on the influence of surfactants on static partially wetting droplets. To that end, we discuss the macroscopic and mesoscopic equilibrium descriptions for droplets covered by insoluble surfactants and show the conditions for consistency between the two approaches in terms of the contact angle and the distribution of surfactants. In the next part of this section, we introduce a mathematical model that allows for a study of the spreading dynamics by extending the thin-film equation for simple liquids to droplets covered by insoluble surfactant. This model is then employed to briefly illustrate the influence of surfactants on the spreading of droplets. We exemplarily study some dynamical effects – such as the occurrence of a fingering instability and a temporary state of non-coalescence of droplets.

Note that the results presented in this chapter have in part been published[1] in

[TSTJ18]   U. Thiele, J. Snoeijer, S. Trinschek, K. John *Equilibrium contact angle and adsorption layer properties with surfactants* Langmuir 34, 7210–7221 (2017)

[TSTJ19]   U. Thiele, J. Snoeijer, S. Trinschek, K. John *Correction to "Equilibrium contact angle and adsorption layer properties with surfactants"* Langmuir 35, 4788-4789 (2019).

4.1. Experimental Findings

Surfactants are amphiphilic molecules or particles that adsorb at interfaces, thereby decreasing its interfacial tension. The relation between the surfactant concentration and the interfacial tension is described by an equation of state. The chemico-physical properties of surfactants crucially alter the dynamics of thin liquid films with free surfaces. They

---

[1]Sections 4.1 - 4.3 closely follow [TSTJ18] and [TSTJ19]. They contain figures and text adapted from Thiele et al. Langmuir, 2018, 34 (24), pp. 7210–7221 © American Chemical Society (2018) particularly in Sec. 4.1 (p.43 l.32 - p.44 l.19), 4.2 and 4.3 (p.56 l.9-23) and from Thiele et al. Langmuir, 2019, 35 (13), pp. 4788-4789 © American Chemical Society (2019) in Sec. 4.2.3.

may act as detergents, wetting agents, emulsifiers, foaming agents and dispersants [RK12]. This is exploited for many industrial and biomedical applications ranging from dish soap to surfactant replacement therapy for premature infants (see [CM09, MC09] for reviews). The detailed mechanisms of surfactant-driven flows are, however, still an active field of experimental and theoretical research.

For spreading surfactant-laden droplets on solid surfaces, the presence of surfactants causes an enhanced spreading rate and deviations from Tanner's law.[2] This phenomenon can be explained by the interfacial Marangoni stresses that result from gradients in the surface tension. They drive the fluid flow and the convective and diffusive transport of surfactant molecules with and along the interface. In addition to the enhanced spreading rate, the interplay between surfactant dynamics and free surface thin-film flows leads to a variety of other intriguing phenomena. These include super-spreading of aqueous droplets on hydrophobic surfaces [Hil98, RSB+02], surfactant-induced fingering of spreading droplets [ML81, TWS89, THS90, CCB+99, CC99, MC09, MC09] and autophobing of aqueous drops on hydrophilic substrates [ASLM04, CM07, BDS+16]. Besides the creation of Marangoni stresses, several other properties of surfactants, such as bulk solubility, their propensity to form micelles or lamellar structures at high concentrations, the surfactant mobility on the solid substrate and their ability to spread through the three-phase contact region enrich the spectrum of the observed dynamical behaviour [TSTJ18].[1]
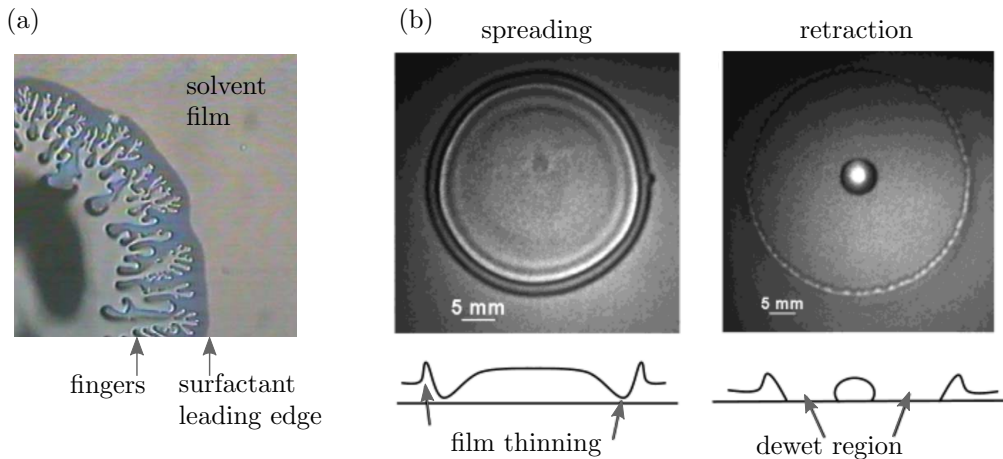
Figure 4.1.: (a) Fingering instability observed at the contact line of a drop of surfactant solution below the critical micelle concentration spreading on a solid substrate prewetted with a 100nm thick layer of solvent. The main drop (lower left corner) spreads and feeds the fingers which thicken and subsequently branch. Reprinted with permission from [HCPC04] © Elsevier (2004). (b) Autophobing process of a drop of aqueous anionic surfactant solution below the critical micelle concentration on a 100μm water film. The drop first spreads and the contact angle decreases. Then, the contact line spontaneously retracts as the surfactant is transferred onto the substrate and renders it less hydrophilic. This leads to dewetting and film rupture. The bottom row shows a schematic view of the height profiles. Reprinted with permission from [ASLM04] © American Chemical Society (2018).

Figure 4.1 (a) shows the surfactant-induced *fingering instability* occurring at the contact line of a drop of surfactant solution spreading on a solid substrate coated by a film of solvent as observed experimentally in [HCPC04]. During the spreading of the surfactant-

---

[2]Recall that Tanner's law states that the spreading rate of a droplet of simple fluid is $r(t) \sim t^{(1/10)}$ (see Sec. 3.2.1).

laden droplet, fingers evolve at the contact line. These are fed by the main drop and grow, thicken and subsequently branch. The leading edge of the surfactant distribution lies ahead of the region of the fingering instability. The spreading dynamics of the drop and the fingers is strongly influenced by the thickness of the prewetting solvent film and the surfactant concentration.

Figure 4.1 (b) illustrates the *autophobing* process of a drop of aqueous anionic surfactant solution on a thin water film as observed in [ASLM04]. Initially, the drop spreads and a thinned region evolves. When surfactant is transferred onto the substrate in this thinned region, it renders it less hydrophilic. The contact line spontaneously retracts, which leads to the development of a dewet region.
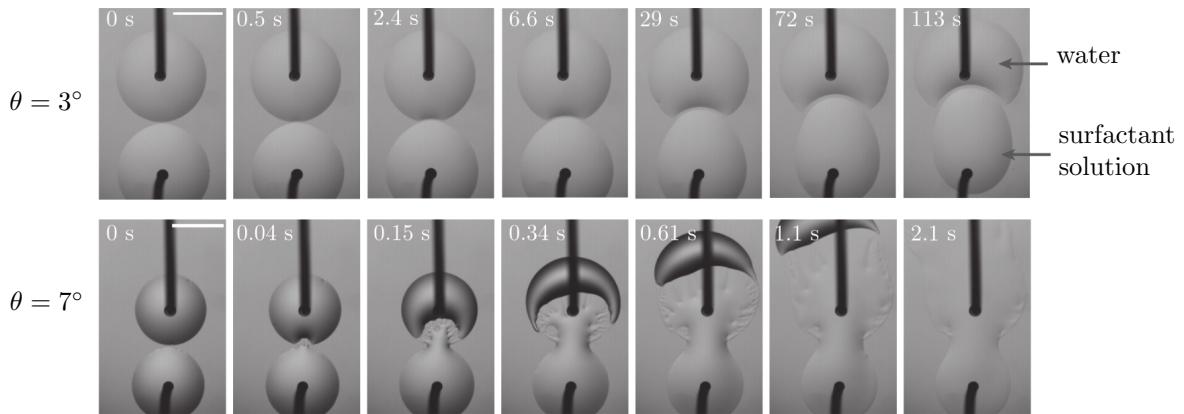
Figure 4.2.: Coalescence behaviour for a pure water drop and a drop containing surfactant [BCKS18]. The lower surface tension drop containing surfactant is attracted towards the other drop, which is itself pushed away. A state of temporary non-coalescence occurs (top row). At higher mean contact angle θ of the two droplets at the time of contact (bottom row), a fingering instability can be observed in the connecting region. The scale bar represents 3 mm. Reprinted with permission from [BCKS18] © American Physical Society (2018).

Another interesting dynamical effect related to the presence of surfactant is the *delayed coalescence* of droplets. When two droplets of the same liquid touch, capillarity usually drives their coalescence. The thin liquid bridge forming between the droplets fills with time and the droplet merge into one. The understanding of droplet interaction and co-alescence is of key importance for many industrial processes such as ink-jet printing and has thus been the subject of intensive research (see, e.g., [ALG+05, RMRS06, HSLES12, LKYY12, EWS13]). Interestingly, the coalescence can be delayed for a substantial period of time, when the droplets have different surface tensions, despite being perfectly miscible [KR12, KR14, KHFR14]. In this situation, a temporary state of non-coalescence arises, in which the droplets move together over the substrate, connected by a thin neck region. The height of this liquid bridge does not increase with time. Instead, the droplet with the lower surface tension "chases" the other droplet over the substrate. This behaviour can not be explained from a perspective of the free energy, which would favour a single droplet. It arises due to a Marangoni flow caused by the surface tension gradient that drains the neck region and competes with the opposed flow due to capillarity [KR12, BCKS18].

This qualitative behaviour can also be observed for aqueous droplets with different con-centrations of surfactant. Figure 4.2 shows the coalescence behaviour of a pure water drop and a drop containing surfactant. The surface tension is lowered in the droplet containing

surfactant. It is attracted towards the drop of pure water and 'chases' it over the substrate in a state of temporary non-coalescence. Experiments [BCKS18] show that the coalescence behaviour is determined by two main parameters: the (mean) contact angle at which the droplets touch and the difference in surface tension. At low contact angles, the non-coalescence behaviour is precursor-mediated (top row). If the contact angle is higher, a fingering instability occurs in the connecting region (bottom row). At even higher contact angles, this instability disappears again and a smooth, stable neck separates the droplet which move over the substrate with a high velocity (not shown) [BCKS18].

The presence of surfactants does, however, not only affect the flow dynamics. Also in the static situation of a surfactant-covered droplet on a substrate at equilibrium, the spatially inhomogeneous distribution of surfactant causes a non-trivial dependence of the contact angle on the surfactant concentration. In the following, we discuss the influence of surfactants on partially wetting droplets in equilibrium.

4.2. Equilibrium Droplets Covered by Insoluble Surfactants

Although many effects connected to the presence of surfactants and the respective induced flows are dynamic out of equilibrium phenomena, the mathematical models that describe such systems have to be consistent with the equilibrium conditions at the meso- and macroscale. Due to their chemico-physical properties, surfactants affect the wettability of droplets on substrates. If one introduces a surfactant-dependent wetting potential $f_{\mathrm{w}}(h, \Gamma)$ in the mesoscopic description, it therefore needs to be discussed how it has to be related to the respective dependencies of the interface energies in the macroscopic description.

For simple fluids, we have investigated the relationship between the description of static equilibrium droplets on the macroscale (on which the situation is determined solely by the interfacial tensions) and on the mesoscale (on which interactions between the liquid and the solid substrate become relevant and are accounted for through the introduction of a wetting potential) in Sec. 2.1. In the following, we establish this mesoscopic-macroscopic link in the presence of surfactants. In general, the surfactant adopts different concentrations on the droplet and on the substrate. Therefore, the problem not only consists in determining the adsorption layer height and the contact angle, but also the respective surfactant concentrations.

The calculations are illustrated by explicitly choosing a functional form for the interface energies, consistent with a linear equation of state for the surfactant. We propose a simple modification of the wetting energy which yields consistency with the Young law in the presence of surfactants.

The considerations presented in the following sections are, e.g., relevant for situations that involve substrates covered by ultra-thin films or bare substrates, where polar and apolar forces between interfaces cannot be neglected and the dynamics is governed by the contact line. One example is the autophobing process during which surfactant is transferred onto the substrate, rendering it less hydrophilic [ASLM04, CM07] and leading to dewetting and film rupture. Another example is the onset of Marangoni flows for surfactant-driven spreading and fingering of droplets, which depends on the ability of the surfactant to diffuse in front of the droplet, thereby establishing a gradient that drives the flow [CCB+99, CC99].[1]

(a) macroscopic picture

(b) mesoscopic picture
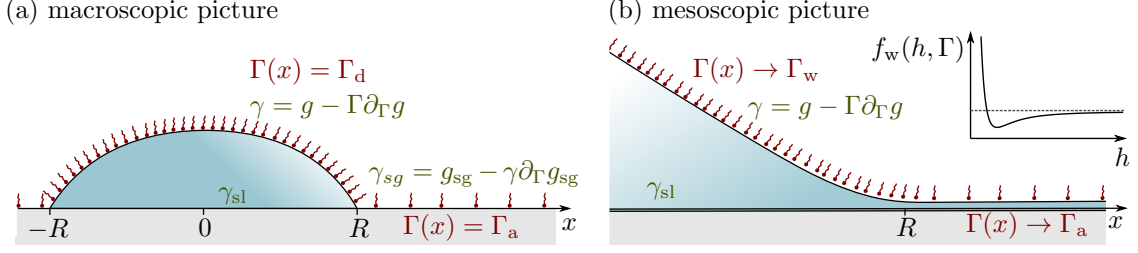
Figure 4.3.: Liquid drop covered by insoluble surfactant on a solid substrate. (a) In the macroscopic description, the shape of the droplet and thus the equilibrium contact angle is determined by the solid-liquid interfacial tension γ_{sl} and the interfacial tensions γ and γ_{sg} of the liquid-gas and the solid-gas interface that depend on the respective surfactant concentrations Γ_{d} and Γ_{a} on the droplet and on the adsorption layer. (b) In the mesoscopic description, the substrate is covered by an adsorption layer. The contact angle is determined by the solid-liquid interfacial tension γ_{sl}, the liquid-gas interfacial tension γ which depends on the surfactant concentration, and the minimum of the wetting energy $f_{\mathrm{w}}(h_{\mathrm{a}}, \Gamma_{\mathrm{a}})$. (cf. [TSTJ18])

4.2.1. Equilibrium Droplets in the Macroscopic Picture

Let us consider a liquid drop covered by insoluble surfactants on a one-dimensional solid substrate as depicted in Fig. 4.3 (a). As for the case of pure liquid in Sec. 2.1.1, we first consider a macroscopic formulation of the problem.

The surfactant molecules exhibit a surface number density Γ (per unit length of the free film surface) on the liquid-gas interface $h(x)$. There may also be surfactant at the solid-gas interface but for simplicity we assume the solid-liquid interface to be free of surfactant. The free energies of the liquid-gas and solid-gas interfaces are characterised by the functions $g(\Gamma)$ and $g_{\mathrm{sg}}(\Gamma)$, respectively. The total amount of surfactant, $N = \int \mathrm{d}s\,\Gamma = \int \mathrm{d}x\xi\Gamma$, is conserved, which is imposed by a Lagrange multiplier λ_Γ that can be interpreted as a chemical potential. The condition $h(R) = 0$ defining the contact line at R and the conservation of the liquid volume $V = \int h\,\mathrm{d}x$ are ensured via further Lagrange multipliers p and λ_h. The free energy functional to be minimised reads

$$\mathcal{F}_{\mathrm{macro}}[h, \Gamma] = \int_0^R \mathrm{d}x\,[\xi g\,(\Gamma) + \gamma_{\mathrm{sl}} - ph] + \int_R^\infty \mathrm{d}x\,g_{\mathrm{sg}}\,(\Gamma)$$
$$- \lambda_\Gamma\left(\int_0^R \mathrm{d}x\,\xi\Gamma + \int_R^\infty \mathrm{d}x\,\Gamma\right) + \lambda_h h(R) \tag{4.1}$$

with ξ again being the metric factor (2.55). Varying the field $\Gamma(x)$ yields

$$\delta F_{\mathrm{macro}} = \int_0^R \mathrm{d}x\,\xi(\partial_\Gamma g - \lambda_\Gamma)\delta\Gamma + \int_R^\infty \mathrm{d}x\,(\partial_\Gamma g_{\mathrm{sg}} - \lambda_\Gamma)\delta\Gamma\,. \tag{4.2}$$

This results in the chemical potentials

$$\lambda_\Gamma = \partial_\Gamma g \text{ for } x \in [0, R]$$
$$\text{and} \quad \lambda_\Gamma = \partial_\Gamma g_{\mathrm{sg}} \text{ for } x \in [R, \infty] \tag{4.3}$$

in the drop region and on the surrounding substrate, respectively. Since λ_Γ is a constant and $\partial_\Gamma g$ is a function of Γ, Eq. (4.3) implies that the surfactant is homogeneously distributed albeit with different concentrations in each region, i.e.,

$$\partial_x\Gamma = 0. \tag{4.4}$$

4. Thin Liquid Films and Droplets Covered by Insoluble Surfactants

We introduce the equilibrium surfactant concentrations $\Gamma(x) = \Gamma_a$ on the substrate and $\Gamma(x) = \Gamma_d$ on the droplet. For the equilibrium distribution of surfactants characterized by a constant chemical potential λ_Γ, Eq. (4.3) implies

$$\partial_\Gamma g|_{\Gamma_d} = \partial_\Gamma g_{sg}|_{\Gamma_a}. \tag{4.5}$$

Varying the field $h(x)$ gives

$$\begin{aligned}
\delta \mathcal{F}_{\text{macro}} &= \int_0^R dx \left[-p - \frac{\partial_{xx} h}{\xi^3} (g - \lambda_\Gamma \Gamma) \right] \delta h(x) \\
&\quad + \left[\left(\frac{\partial_x h}{\xi} (g - \lambda_\Gamma \Gamma) \right) \delta h \right]_0^R + \lambda_h \delta h(R) \\
&= \int_0^R dx \left[-p - \kappa \gamma \right] \delta h(x) + \left[\frac{\partial_x h}{\xi} \gamma + \lambda_h \right] \delta h(R)
\end{aligned} \tag{4.6}$$

where we introduced the surfactant-dependent liquid-gas interfacial tension

$$\gamma = g - \Gamma \partial_\Gamma g \tag{4.7}$$

and used Eq. (4.3). At the centre of the droplet, at $x = 0$, the reflection symmetry enforces $\partial_x h = 0$. The Laplace pressure and λ_h can be obtained from Eq. (4.6) as

$$p = -\gamma \kappa, \quad \text{for} \quad x \in [0, R] \tag{4.8}$$

$$\lambda_h = -\gamma \frac{\partial_x h}{\xi} \quad \text{at} \quad x = R. \tag{4.9}$$

Finally, evaluating the variation of R at the position $x = R$ yields

$$\delta \mathcal{F}_{\text{macro}} = \left[\xi g(\Gamma) + \gamma_{sl} - ph - g_{sg}(\Gamma_a) - \lambda_\Gamma \xi \Gamma_d - \lambda_\Gamma \Gamma_a + \lambda_h \partial_x h(R) \right] \delta R. \tag{4.10}$$

Using the constraint $h(R) = 0$, the relation $1/\xi = \cos\theta_{eq}$ (see Eq. (2.9)), as well as the obtained values for λ_Γ and λ_h results in the boundary condition

$$\begin{aligned}
0 &= \gamma_{sl} - \gamma_{sg}(\Gamma_a) + \gamma(\Gamma_d) \cos\theta_{eq} \\
\text{with} \quad &\gamma(\Gamma_d) = g(\Gamma_d) - \Gamma_d \partial_\Gamma g|_{\Gamma_d}, \\
\text{and} \quad &\gamma_{sg}(\Gamma_a) = g_{sg}(\Gamma_a) - \Gamma_a \partial_\Gamma g_{sg}|_{\Gamma_a}.
\end{aligned} \tag{4.11}$$

We have again found the Young law that relates the equilibrium contact angle to the interfacial tensions. However, the interfacial tensions γ_i are not given by the local free energies g and g_{sg} which would enter at fixed concentration Γ. Instead, they are at conserved total amount of surfactant defined by the local grand potentials $g - \Gamma \partial_\Gamma g$ and $g_{sg} - \Gamma \partial_\Gamma g_{sg}$. Importantly, the values of the interfacial tensions γ and γ_{sg} are not fixed a priori. They have to be determined self-consistently from the equilibration of the surfactant concentrations on the drop and the surrounding substrate. The observed contact angle thus involves a subtle coupling between the distribution of surfactants and the interfacial tensions.[1]

4.2.2. Equilibrium Droplets in the Mesoscopic Picture

In Sec. 2.1.3, we have discussed the mesoscopic description of droplets without surfactant. We now generalise this approach and consider such a description for a droplet covered by insoluble surfactants. Again, we study equilibrium situations involving a contact line as

depicted in Fig. 4.3 (b). We focus on the problem how the dependency of the wetting potential on surfactant concentration in the mesoscopic description has to be related to the respective dependencies of the involved surface energies in the macroscopic description to ensure the consistency of the two approaches.

To begin with, we consider a free energy functional

$$F_{\mathrm{meso}}[h, \Gamma] = \int_0^\infty [\gamma_{\mathrm{sl}} + f_{\mathrm{w}}(h, \Gamma) + g(\Gamma)\xi - ph - \lambda_\Gamma \Gamma \xi]\, dx, \qquad (4.12)$$

where $f_{\mathrm{w}}(h, \Gamma)$ and $g(\Gamma)$ represent the wetting and interface energy, respectively. The solid-liquid interface energy γ_{sl} is treated as constant. The conservation of the amounts of liquid and surfactant are ensured by the Lagrange multipliers p and λ_Γ, respectively. In analogy to Sec. 2.1.3, there is again no direct influence of the solid-liquid interfacial tension γ_{sl}, as in the mesoscopic description, the whole domain is at least covered by an adsorption layer. In consequence, the two integrals for the droplet and substrate regions in the macroscopic free energy (4.1) are replaced by one integral over the whole domain. Varying the mesoscopic free energy functional (4.12) with respect to $h(x)$ and $\Gamma(x)$ gives the Euler-Lagrange equations

$$p = \partial_h f_{\mathrm{w}} - \partial_x [(g - \lambda_\Gamma \Gamma)\tfrac{\partial_x h}{\xi}] \qquad (4.13)$$

$$\text{and} \qquad \lambda_\Gamma = \frac{1}{\xi}\partial_\Gamma f_{\mathrm{w}} + \partial_\Gamma g, \qquad (4.14)$$

respectively. We introduce the generalised positions $q_1 = h$ and $q_2 = \Gamma$ and obtain[3] the *first integral E*

$$E = \gamma_{\mathrm{sl}} + f_{\mathrm{w}} + \frac{g - \Gamma \lambda_\Gamma}{\xi} - h\, p, \qquad (4.15)$$

corresponding to Eq. (2.18) with γ replaced by $g(\Gamma) - \Gamma \lambda_\Gamma$.

In equilibrium, p, λ_Γ and E are constant across the system, which allows us to study the coexistence of states. As in section 2.1.3, we consider the equilibrium between an adsorption layer of thickness h_{a} and a wedge region with constant slope $\tan \theta_{\mathrm{eq}}$ as depicted in Fig. 4.3 (b). The wetting potential $f_{\mathrm{w}}(h, \Gamma)$ now depends on film height *and* surfactant concentration. Therefore, it is not only necessary to determine the coexisting adsorption layer height and wedge slope as in Sec. 2.1.3, but also the coexisting surfactant concentrations Γ_{a} on the adsorption layer and Γ_{w} on the wedge. We assume that the wedge is far away from the adsorption layer ($h \gg h_{\mathrm{a}}$, $f_{\mathrm{w}} \to 0$, $|\partial_x h| \to \tan \theta_{\mathrm{eq}}$, $\Gamma \to \Gamma_{\mathrm{w}}$) and the adsorption layer is far away from the wedge ($h \to h_{\mathrm{a}}$, $\partial_x h \to 0$, $\Gamma \to \Gamma_{\mathrm{a}}$), i.e., both are sufficiently far away from the contact line region. Comparing the expressions for p, λ_Γ and E given by Eqs. (4.13), (4.14) and (4.15) in wedge and adsorption layer (in analogy to the calculation in Sec. 2.1.3), yields

$$0 = \partial_h f_{\mathrm{w}}|_{(h_{\mathrm{a}}, \Gamma_{\mathrm{a}})}, \qquad (4.16)$$

$$\partial_\Gamma g|_{\Gamma_{\mathrm{w}}} = \partial_\Gamma f_{\mathrm{w}}|_{(h_{\mathrm{a}}, \Gamma_{\mathrm{a}})} + \partial_\Gamma g|_{\Gamma_{\mathrm{a}}}, \qquad (4.17)$$

$$\gamma(\Gamma_{\mathrm{w}}) \cos \theta_{\mathrm{eq}} = f_{\mathrm{w}}(h_{\mathrm{a}}, \Gamma_{\mathrm{a}}) - \Gamma_{\mathrm{a}} \partial_\Gamma f_{\mathrm{w}}|_{(h_{\mathrm{a}}, \Gamma_{\mathrm{a}})} + \gamma(\Gamma_{\mathrm{a}}), \qquad (4.18)$$

respectively. To obtain Eq. (4.18), we have already used $\xi_{\mathrm{w}} = 1/\cos \theta_{\mathrm{eq}}$ as well as Eqs. (4.7), (4.16) and (4.17). Equation (4.18) is the generalisation of the mesoscopic Young law

---

[3] Note that if the integrand of (4.12) is seen as Lagrangian L, the corresponding generalised momenta are $p_1 = (g - \lambda_\Gamma \Gamma)(\partial_x h)/\xi$ and $p_2 = 0$, respectively. Then, the first integral E which is independent of x corresponds to the negative of the Hamiltonian $H = p \partial_x q - L$.

in the presence of surfactants. The concentrations are different on the wedge ($\Gamma = \Gamma_\mathrm{w}$) and on the adsorption layer ($\Gamma = \Gamma_\mathrm{a}$) such that the liquid-gas interfacial tensions are also different. Without surfactant we recover Eq. (2.24) as $g(0)$ is γ of Sec. 2.1.3.

The obtained Eqs. (4.16) to (4.18) characterize the states of coexisting wedge and adsorption layer, which are determined by four quantities: the adsorption layer height h_a, the contact angle θ_eq and the surfactant concentrations on wedge and adsorption layer Γ_w and Γ_a, respectively. In practice, one may chose any of these quantities as control parameter and determine the other three quantities from the three relations (4.16)-(4.18). It is convenient to choose Γ_a as control parameter and first use Eq. (4.16) to obtain h_a, then employ Eq. (4.17) to determine Γ_w and, finally, Eq. (4.18) to calculate the equilibrium contact angle θ_eq. To obtain specific results, it is necessary to specify the free energies of the liquid-gas interface $g(\Gamma)$ and the solid-gas interface $g_\mathrm{sg}(\Gamma)$ as well as the wetting energy $f_\mathrm{w}(h, \Gamma)$. In Sec. 4.2.3, we present a simple but illustrative example.[1]

Consistency of Mesoscopic and Macroscopic Approach

The mesoscopic and the macroscopic description of the system need to result in the same equilibrium contact angle of the drop. Comparing the generalized mesoscopic Young law given by Eq. (4.18) with the macroscopic one given by Eq. (4.11) in Sec. 4.2.1 gives the consistency condition

$$f_\mathrm{w}(h_\mathrm{a}, \Gamma_\mathrm{a}) - \Gamma_\mathrm{a} \partial_\Gamma f_\mathrm{w}|_{(h_\mathrm{a}, \Gamma_\mathrm{a})} = \gamma_\mathrm{sg}(\Gamma_\mathrm{a}) - \gamma_\mathrm{sl} - \gamma(\Gamma_\mathrm{a}) = S(\Gamma_\mathrm{a}). \tag{4.19}$$

This corresponds to a generalisation of Eq. (2.26) in the presence of surfactant. It relates the macroscopic equations of state (or interface energies) with the height- and surfactant-dependent wetting energy.

The surfactant concentrations should be identical in the macroscopic and the mesoscopic description. Note that Eq. (4.14) implies that the surfactant concentration Γ_w on the wedge in the mesoscopic description corresponds to the concentration Γ_d on the droplet in the macroscopic description. The consistency of the surfactant concentrations in both pictures results in another condition: The mesoscopic chemical equilibrium in Eq. (4.17), i.e. $\partial_\Gamma g|_{\Gamma_\mathrm{w}} = \partial_\Gamma f_\mathrm{w}|_{(h_\mathrm{a}, \Gamma_\mathrm{a})} + \partial_\Gamma g|_{\Gamma_\mathrm{a}}$, has to coincide with the macroscopic one given by Eq. (4.3), i.e. $\partial_\Gamma g|_{\Gamma_\mathrm{w}} = \partial_\Gamma g_\mathrm{sg}|_{\Gamma_\mathrm{a}}$. The comparison of the two conditions implies

$$\partial_\Gamma g_\mathrm{sg}|_{\Gamma_\mathrm{a}} = \partial_\Gamma f_\mathrm{w}|_{(h_\mathrm{a}, \Gamma_\mathrm{a})} + \partial_\Gamma g|_{\Gamma_\mathrm{a}}. \tag{4.20}$$

Introducing the resulting relation for $\partial_\Gamma f_\mathrm{w}|_{(h_\mathrm{a}, \Gamma_\mathrm{a})}$ into Eq. (4.19) results in the condition

$$f_\mathrm{w}(h_\mathrm{a}, \Gamma_\mathrm{a}) = g_\mathrm{sg}(\Gamma_\mathrm{a}) - \gamma_\mathrm{sl} - g(\Gamma_\mathrm{a}) \tag{4.21}$$

for the consistency of the macroscopic and mesoscopic description.
In the next section we explore the consequences of the consistency conditions for a simple example and derive the form of the surfactant-dependent wettability.[1]

4.2.3. Application for a Simple Energy

Now, we illustrate our considerations for a simple free energy $g(\Gamma)$ describing low surfactant concentrations Γ, before extending the result to arbitrary g. We use a wetting energy that is a product of height- and concentration-dependent factors implying that the presence of surfactant only modifies the contact angle but not the adsorption layer height.[4]

---

[4]Note that the results presented in this section have been revised in response to the constructive remarks of M. Plapp.

Macroscopic Consideration

First, we consider a droplet in the presence of a low concentration of insoluble surfactant on the drop and the surrounding substrate in a macroscopic description. In general, the surfactant will even in the dilute limit affect the liquid-gas and solid-gas interfaces differently. The different intermolecular interactions result in different molecular areas on the two interfaces. Therefore, we introduce different effective molecular length scales a and a_{sg} and consider the purely entropic interfacial free energies[5]

$$g(\Gamma) = \gamma^0 + k_{\mathrm{B}}T\Gamma\left[\ln(\Gamma a^2) - 1\right] \tag{4.22}$$

$$g_{\mathrm{sg}}(\Gamma) = \gamma^0_{\mathrm{sg}} + k_{\mathrm{B}}T\Gamma\left[\ln(\Gamma a^2_{\mathrm{sg}}) - 1\right]. \tag{4.23}$$

This results in the linear equations of state

$$\gamma(\Gamma) = g - \Gamma\partial_\Gamma g = \gamma^0 - k_{\mathrm{B}}T\Gamma \tag{4.24}$$

$$\gamma_{\mathrm{sg}}(\Gamma) = g_{\mathrm{sg}} - \Gamma\partial_\Gamma g_{\mathrm{sg}} = \gamma^0_{\mathrm{sg}} - k_{\mathrm{B}}T\Gamma. \tag{4.25}$$

The macroscopic concentration-dependent interfacial tension $\gamma_{\mathrm{sg}}(\Gamma)$ reflects the fact that at equilibrium, surfactant is found on the drop as well as on the adsorption layer.

Inserting these interface energies into the macroscopic Young law in the presence of surfactants given by Eq. (4.11) results in

$$\cos\theta_{\mathrm{eq}} = \frac{\gamma^0\cos\theta_{\mathrm{eq0}} - k_{\mathrm{B}}T\Gamma_{\mathrm{a}}}{\gamma^0 - k_{\mathrm{B}}T\Gamma_{\mathrm{d}}}, \tag{4.26}$$

where $\theta_{\mathrm{eq0}} = (\gamma^0_{\mathrm{sg}} - \gamma_{\mathrm{sl}})/\gamma^0$ represents the contact angle in the absence of surfactant. The ratio of the surfactant concentrations on the drop and on the surrounding substrate can directly be obtained from Eq. (4.5) as

$$\Gamma_{\mathrm{d}} = \frac{a^2_{\mathrm{sg}}}{a^2}\Gamma_{\mathrm{a}} = \frac{1}{\delta}\Gamma_{\mathrm{a}} \tag{4.27}$$

where $\delta = a^2/a^2_{\mathrm{sg}}$ represents the ratio of the different molecular length scales. Depending on this parameter, adding surfactant to the system has a qualitatively different effect on the contact angle. We discuss a number of limiting cases:

(A) The surfactant concentrations on adsorption layer and drop are identical ($\Gamma_{\mathrm{d}} = \Gamma_{\mathrm{a}} = \Gamma$) if dependencies of the interface energies g and g_{sg} on the surfactant concentration are identical, i.e., $a = a_{\mathrm{sg}}$ and therefore $\delta = a^2/a^2_{\mathrm{sg}} = 1$. The dependence of the equilibrium contact angle θ_{eq} on the surfactant concentration is given by

$$\cos\theta_{\mathrm{eq}} = \frac{\gamma^0\cos\theta_{\mathrm{eq0}} - k_{\mathrm{B}}T\Gamma}{\gamma^0 - k_{\mathrm{B}}T\Gamma}. \tag{4.28}$$

(B) The surfactant prefers to stay on the liquid-gas interface for $a \ll a_{\mathrm{sg}}$ and $\delta = a^2/a^2_{\mathrm{sg}} \ll 1$, which implies $\Gamma_{\mathrm{d}} \gg \Gamma_{\mathrm{a}}$. The equilibrium contact angle takes the form

$$\cos\theta_{\mathrm{eq}} \approx \frac{\gamma^0\cos\theta_{\mathrm{eq0}}}{\gamma^0 - k_{\mathrm{B}}T\Gamma_{\mathrm{d}}}, \tag{4.29}$$

corresponding to the classical surfactant effect in which the equilibrium contact angle decreases with increasing concentration.

---

[5]Note that in this example, Γ describes the surface number density of surfactant per unit area of the free surface.

(C) The surfactant prefers to stay on the solid-gas interface for $a \gg a_{\mathrm{sg}}$ and $\delta = a^2/a_{\mathrm{sg}}^2 \gg 1$, which implies $\Gamma_{\mathrm{d}} \ll \Gamma_{\mathrm{a}}$. The equilibrium contact angle

$$\cos\theta_{\mathrm{eq}} \approx \cos\theta_{\mathrm{eq}0} - \frac{k_{\mathrm{B}}T}{\gamma^0}\Gamma_{\mathrm{a}} \qquad (4.30)$$

increases with increasing surfactant concentration such that this case corresponds to an autophobing effect.

These limiting cases illustrate that the equilibrium contact angle depends subtly on the nature of the free energies in the presence of surfactants. This is further investigated numerically below in Sec. 4.2.3.[1]

Mesoscopic Consideration

Now, we consider a drop in the presence of a low concentration of insoluble surfactant on the liquid-gas interface in a mesoscopic description. We employ the ideal gas local free energy $g(\Gamma)$ as defined in Eq. (4.22) and the liquid-gas interfacial tension $\gamma(\Gamma)$ as defined in (4.24). As the whole domain is at least covered by a thin adsorption layer in the mesoscopic description, the free energy of the solid-liquid interface g_{sg} does not occur. We use the strong assumption that the wetting energy

$$f_{\mathrm{w}}(h,\Gamma) = \chi(\Gamma)\hat{f}_{\mathrm{w}}(h) \qquad (4.31)$$

can be written as the product of height- and concentration-dependent factors $\hat{f}_{\mathrm{w}}(h)$ and $\chi(\Gamma)$ with $\chi(0) = 1$. For this choice, the surfactant-independent adsorption layer height h_{a} is still given by $\partial_h \hat{f}_{\mathrm{w}}|_{h_{\mathrm{a}}} = p$ as in Sec. 2.1.3. We thus investigate the case of a surfactant that changes the contact angle but does not affect the adsorption layer height (in the limit $p \to 0$). Note that, in consequence, the restriction to this ansatz implies that surfactant-induced wetting transitions characterised by a diverging adsorption layer height can not be investigated. We expect the ansatz to break down for $\theta_{\mathrm{eq}} \to 0$.[6]
The equilibrium contact angle θ_{eq} is obtained by inserting the product ansatz (4.31) for the wetting energy $f_{\mathrm{w}}(h,\Gamma)$ into Eq. (4.18). This results in the expression

$$\gamma(\Gamma_{\mathrm{w}})\cos\theta_{\mathrm{eq}} = \gamma(\Gamma_{\mathrm{a}}) + \hat{f}_{\mathrm{w}}(h_{\mathrm{a}})\left[\chi(\Gamma_{\mathrm{a}}) - \Gamma_{\mathrm{a}}\partial_\Gamma\chi|_{\Gamma_{\mathrm{a}}}\right] \qquad (4.32)$$

for the contact angle.[1]

Consistency of Mesoscopic and Macroscopic Approach

The concentration-dependence of $\chi(\Gamma)$ in (4.31) needs to account for the consistency of mesoscopic and macroscopic picture and can thus not be chosen freely. It can be obtained by inserting the product ansatz (4.31) for the wetting energy and the entropic local free energies into the consistency condition (4.21), which yields

$$\chi(\Gamma_{\mathrm{a}}) = 1 - \frac{k_{\mathrm{B}}T}{\hat{f}_{\mathrm{w}}(h_{\mathrm{a}})}\ln(\delta)\Gamma_{\mathrm{a}}\,. \qquad (4.33)$$

This expression has to hold for any surfactant concentration Γ_{a}. Therefore, the surfactant-dependent wetting energy can be written as

$$f_{\mathrm{w}}(h,\Gamma) = \hat{f}_{\mathrm{w}}(h)\left[1 - \frac{k_{\mathrm{B}}T}{\hat{f}_{\mathrm{w}}(h_{\mathrm{a}})}\ln(\delta)\Gamma\right]\,. \qquad (4.34)$$

---

[6]In general, two (independent) critical exponents characterise the change in wetting behaviour close to the wetting transition [BEI+09]: They characterise (i) how θ_{eq} approaches zero and (ii) how the thickness of the adsorption layer diverges. Choosing a product ansatz corresponds to the limiting case of zero critical exponent for the adsorption layer height.

Let us summarise the macroscopic and mesoscopic description of a drop covered by insoluble surfactant: Macroscopically, the situation is characterized by the free energies g, g_{sg} and the interfacial tension γ_{sl}. For a given concentration Γ_{a} or Γ_{d}, the other Γ and the contact angle θ_{eq} can be determined. Mesoscopically, the interfacial free energy g_{sg} is not defined. However, it is via the consistency conditions reflected in the wetting energy $f_{\text{w}}(h, \Gamma)$, that itself is not part of the macroscopic description. In the example treated in this section, g is determined by a, the macroscopic quantity g_{sg} is determined by a_{sg}, and the concentration-dependent mesoscopic wetting energy $f_{\text{w}}(h, \Gamma)$ depends on both, a and a_{sg}.[1]
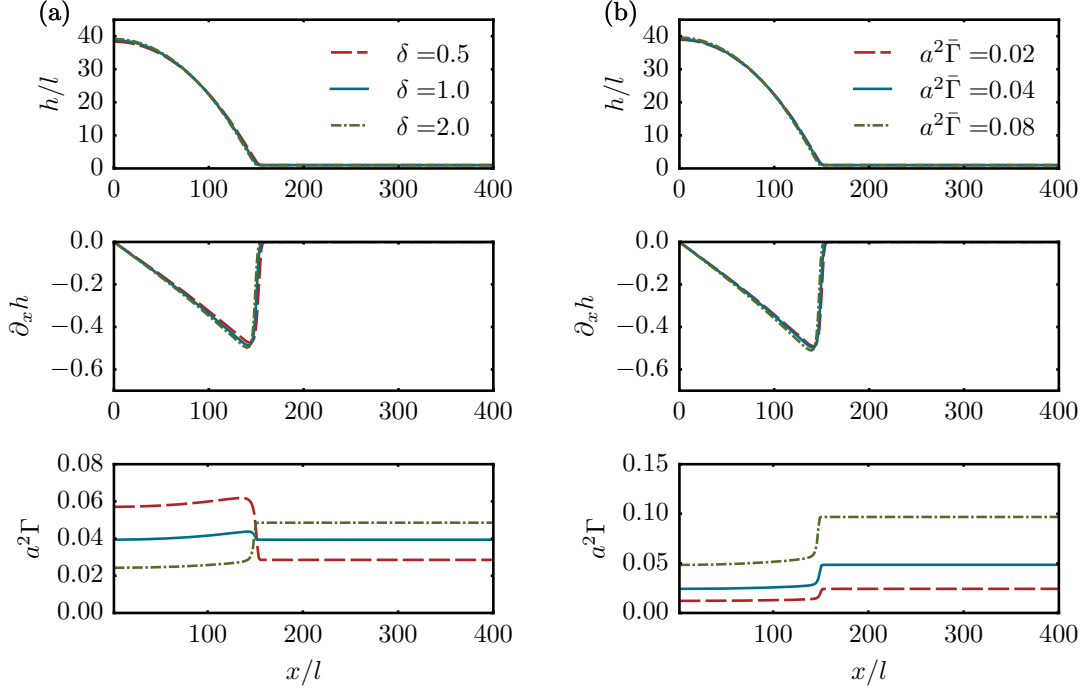
Figure 4.4.: Profiles of film height h (top), its spatial derivative $\partial_x h$ (middle) and surfactant concentration Γ (bottom) determined by parameter continuation of the equations on a finite domain. We study three different ratios $\delta = \frac{a^2}{a_{\text{sg}}^2}$ of the effective molecular length scales of the surfactant at $a^2\bar{\Gamma} = 0.04$ in (a) and three different mean surfactant concentrations $\bar{\Gamma}$ at $\delta = 2$ in (b) while keeping the remaining parameters fixed to $\epsilon_1 = 0.2$ and $\epsilon_2 = 0.4$. Note that the surfactant concentration Γ_{w} occurring in the mesoscopic description on the wedge corresponds to the concentration Γ_{d} occurring in the macroscopic description on the droplet. (cf. [TSTJ19])

Surfactant-Covered Drops on a Finite Domain

To illustrate the equilibrium described by the model, we perform parameter continuation runs [DWC+14] on finite domains employing the software package *AUTO-07p* [DO09] as discussed in the appendix A.1.2 and analyse the film height and surfactant concentration. In the following, we consider the wetting energy

$$f_{\text{w}}(h, \Gamma) = \chi(\Gamma)\hat{f}_{\text{w}}(h) = \chi(\Gamma)A\left(-\frac{1}{2h^2} + \frac{h_{\text{a}}^3}{5h^5}\right), \tag{4.35}$$

4. Thin Liquid Films and Droplets Covered by Insoluble Surfactants

where $\hat{f}_w(h)$ is the wetting energy introduced in Eq. (2.14). Recall that for $A > 0$, it describes a partially wetting fluid, i.e., a droplet of finite contact angle sitting on a stable adsorption layer of height h_a. The model is rescaled for the analysis as outlined in appendix Sec. A.3.1 by introducing the time scale $\tau = \eta l/\gamma^0$, the length scale $l = h_a$, and the rescaled surface concentration $\tilde{\Gamma} = a^2\Gamma$. The solutions are then characterised by three dimensionless parameters

$$\delta = \frac{a^2}{a_{\mathrm{sg}}^2} \qquad \epsilon_1 = \frac{k_B T}{a^2\gamma^0} \qquad \text{and} \qquad \epsilon_2 = -\frac{10\hat{f}_w(h_a)}{3\gamma^0} = \frac{A}{h_a^2\gamma^0} \,. \tag{4.36}$$

These are connected to the ratio of the effective molecular length scales of the surfactant at the liquid-gas and the solid-gas interface, the ratio between the entropic energetic contribution of the surfactant and the interfacial tension without surfactant, and the equilibrium contact angle without surfactant, respectively.

(a)

(b)
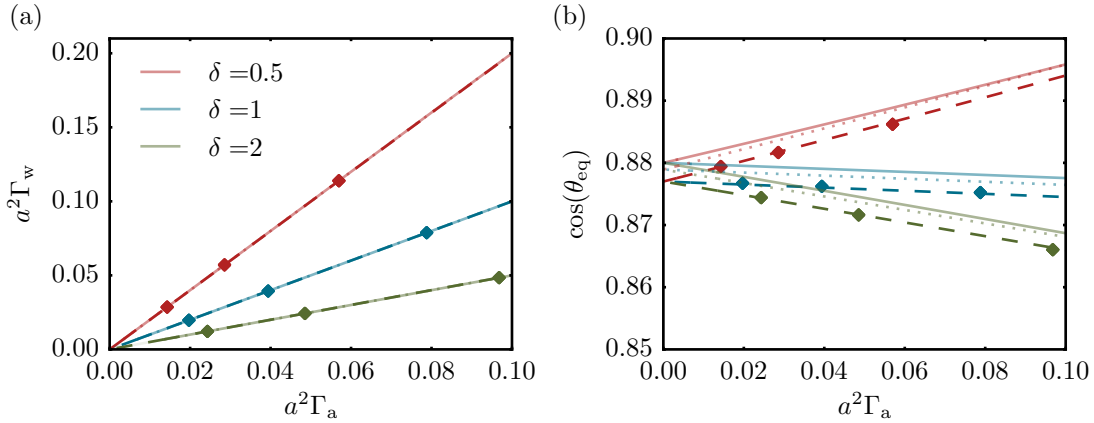
Figure 4.5.: Surfactant concentration on the droplet (left) and equilibrium contact angle (right) depending on the surfactant concentration Γ_a on the adsorption layer. The values obtained by parameter continuation for the domain size $L_x/l = 400$ (dashed lines) and $L_x/l = 6000$ (dotted lines) are compared to the analytically obtained equilibrium conditions (solid lines). The contact angle of the profiles is determined from the curvature of h at the centre of the droplet, assuming a parabolic height profile. The diamonds represent values extracted from time simulations of the evolution equations (4.49)-(4.50) introduced in Sec. 4.3 for a domain size $L_x/l = 400$, however, without using the approximation (4.42) for the curvature. (cf. [TSTJ19])

Figure 4.4 shows the profiles for film height and surfactant concentration obtained by parameter continuation of the equations on a finite domain. We exemplarily study three different ratios δ of the effective molecular length scales of the surfactant while keeping the remaining parameters fixed to $\epsilon_1 = 0.2$ and $\epsilon_2 = 0.4$. The resulting profiles presented in Fig. 4.4 (a) confirm the limiting cases discussed in Sec. 4.2.3. The surfactant concentration is identical on drop and adsorption layer, if the dependencies of the interface energies g and g_{sg} on the surfactant concentration are identical, i.e., $a = a_{\mathrm{sg}}$ and thus $\delta = 1$ (solid blue lines). The contact angle is in this case only slightly modified by the addition of surfactant to the system. The surfactant prefers to stay on the liquid-gas interface for $a < a_{\mathrm{sg}}$ and thus $\delta < 1$ (dashed red lines) and accumulates on the droplet. In this case, the addition of surfactant slightly lowers the contact angle. If the surfactant prefers to stay on the solid-gas interface for $a > a_{\mathrm{sg}}$ and thus $\delta > 1$ (dash-dotted green lines), the surfactant concentration on the drop is smaller than on the adsorption layer and the contact angle of the droplet increases. The influence of the amount of surfactant for fixed

$\delta = 2$ is presented in Fig. 4.4 (b). From the height profiles, it can be seen that the contact angle decreases slightly with increasing surfactant concentration.

For a more thorough analysis of the effect of the amount of surfactant on the equilibrium solution, the surfactant concentrations on the adsorption layer and on the droplet as well as the equilibrium contact angle are extracted from the parameter continuation and compared to the analytical equilibrium conditions obtained by Eqs. (4.26) and (4.27). Figure 4.5 shows the analytically obtained equilibrium values (solid lines) and the values extracted from parameter continuation on a finite domain with $L_x/l = 400$ (dashed lines) for three different values of δ, using the surfactant concentration on the adsorption layer Γ_a as control parameter. The surfactant concentrations measured in the continuation are very close to the analytical prediction as shown in Fig. 4.5 (a). However, there is a small discrepancy for the contact angles presented in 4.5 (b). In order to understand this offset, the domain size in the parameter continuation is increased to $L_x/l = 6000$ with accordingly adjusted liquid volume. Then, the values obtained on the finite domain (dotted lines) match the analytical prediction well. For very large domain and droplet sizes, the analytical predictions for surfactant concentration and contact angle obtained by parameter continuation perfectly match. The observed deviations in 4.5 (b) can thus be explained by the finite size of the simulation domain and droplet.[1]

Generalisation to Arbitrary Interface Energies

In the previous section, we have studied a situation with a low concentration of surfactant resulting in purely entropic surface free energies $g(\Gamma)$ and $g_{sg}(\Gamma)$ and we have established the form of the function $\chi(\Gamma)$ which guarantees the consistency of the macroscopic and mesoscopic approach. However, these considerations can be easily generalised to arbitrary interface energies by writing a free energy on the mesoscale which is consistent with the macroscale. By identifying χ with

$$\chi = \frac{1}{\hat{f}_w(h_a)} \left[g_{sg}(\Gamma) - g(\Gamma) - \gamma_{sl} \right] , \qquad (4.37)$$

the free energy functional in (4.12) can be rewritten as

$$F_{meso}[h, \Gamma] = \int \left\{ \gamma_{sl} + \frac{\hat{f}_w(h)}{\hat{f}_w(h_a)} \left[g_{sg}(\Gamma) - g(\Gamma) \right] + \xi \left[g(\Gamma) - \lambda_\Gamma \Gamma \right] - ph \right\} dx . \qquad (4.38)$$

We can split the integral (4.38) into three contributions stemming from the droplet F_{drop}, the adsorption layer F_a and the contact line region F_{int}, i.e., $F_{meso} = F_{drop} + F_{int} + F_a$. In the droplet away from the contact line, where $\hat{f}_w(h) << \hat{f}_w(h_a)$, the free energy functional reduces to

$$F_{drop} = \int \left\{ \gamma_{sl} + \xi \left[g(\Gamma) - \lambda_\Gamma \Gamma_w \right] - ph \right\} dx . \qquad (4.39)$$

In the adsorption layer, where $\xi = 1$ and $\hat{f}(h) = \hat{f}_a$, Eq. (4.38) simplifies to

$$F_a = \int \left\{ g_{sg} - \lambda_\Gamma \Gamma_a - ph_a \right\} dx . \qquad (4.40)$$

Expressions (4.39) and (4.40) are now identical[7] to the macroscopic description by the free energy functional given by Eq. (4.1) in Sec. 4.2.1. The expression for $\chi(\Gamma)$ given in (4.37) is thus not restricted to simple entropic energies, but instead valid for arbitrary expressions g if the product ansatz for $f_w(h, \Gamma)$ is used.[1]

---

[7]We can drop the constant pressure term ph_a in F_a by assuming that outside the adsorption layer $h \gg h_a$ holds and that the volume constraint on the liquid is determined by the droplet and not the adsorption layer.
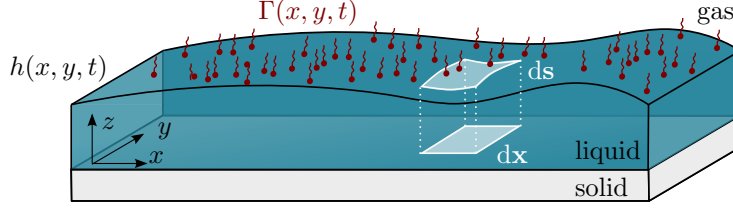
Figure 4.6.: Sketch of a thin liquid film with height profile $h(x, y, t)$ covered by insoluble surfactants of concentration Γ on a solid substrate surrounded by a gaseous phase. The projection of the concentration onto the flat solid substrate is given by $\Gamma_\mathrm{p} = \xi\Gamma$.

4.3. Dynamical Equations

Up to now, we have studied the equilibrium solutions of droplets covered by an insoluble surfactant. However, many interesting phenomena connected to the presence of surfactants like, e.g., the occurrence of a fingering instability in spreading drops, are dynamical effects. Therefore, we now present a mathematical model for the time evolution of such systems. At low surfactant concentrations and in situations where the influence of wettability is negligible, the governing equations for coupled film flow and surfactant dynamics are well established. The dynamics of a surfactant-covered liquid film is typically described by coupling an evolution equation for the surfactant concentration to an evolution equation for the film height (derived from the long-wave approximation of a viscous Stokes flow). Capillarity and Marangoni stresses are usually included via an equation of state for the surfactant. Wettability is in some models incorporated via a disjoining pressure [WCM02, CM07]. However, specific model features (such as nonlinear equations of state) are often included in an ad hoc fashion at the level of the dynamic equations. This approach neglects that the system has to respect symmetries imposed by the laws of thermodynamics, as discussed in [TAP12, TSTJ18]. The recent formulation of the dynamic equations as a gradient dynamics based on an energy functional [TAP12, TAP16] sheds some light on the question, how features like a nonlinear equation of state for the surfactant and a concentration-dependent wettability can be incorporated into a mesoscopic description in a consistent manner.[1]

We consider a thin film of height $h(x, y, t)$ which is covered by an insoluble surfactant of surface number density $\Gamma(x, y, t)$ on a flat solid substrate surrounded by a gaseous phase as depicted in Fig. 4.6. To describe the system in a gradient dynamics formulation [TAP12], it is necessary to formulate the problem in variables that can be varied independently. Therefore, we introduce the projection of the surface number density onto the flat surface of the substrate as

$$\Gamma_\mathrm{p}(x, y, t) = \xi\Gamma(x, y, t) \tag{4.41}$$

by using the relation

$$\mathrm{d}\mathbf{s} = \xi\mathrm{d}\mathbf{x} \quad \text{with } \xi = \sqrt{1 + |\nabla h|^2} \approx 1 + \tfrac{1}{2}|\nabla h|^2 \,. \tag{4.42}$$

Here, $\mathrm{d}\mathbf{s}$ is the surface element of the curved liquid surface and $\mathrm{d}\mathbf{x}$ is the surface element on the euclidean flat plane. The model is based on the free energy functional

$$\mathcal{F}_\mathrm{surf}[h, \Gamma_\mathrm{p}] = \int [f_\mathrm{w}(h, \tfrac{\Gamma_\mathrm{p}}{\xi}) + f_\mathrm{s}(\tfrac{\Gamma_\mathrm{p}}{\xi})\xi + \gamma_\mathrm{sl}] \, \mathrm{d}\mathbf{x} \tag{4.43}$$

as introduced in Eq. (4.12) for the mesoscopic description of films covered by insoluble

surfactants[8]. Recall that it contains the wetting energy f_{w} and the local free energy of the surfactant layer, now called f_{s}. It can be used to write evolution equations for $h(x, y, t)$ and $\Gamma_{\mathrm{p}}(x, y, t)$

$$\partial_t h = \nabla \cdot [Q_{hh} \nabla \frac{\delta \mathcal{F}_{\mathrm{surf}}}{\delta h} + Q_{h\Gamma} \nabla \frac{\delta \mathcal{F}_{\mathrm{surf}}}{\delta \Gamma_{\mathrm{p}}}] \tag{4.44}$$

$$\partial_t \Gamma_{\mathrm{p}} = \nabla \cdot [Q_{\Gamma h} \nabla \frac{\delta \mathcal{F}_{\mathrm{surf}}}{\delta h} + Q_{\Gamma\Gamma} \nabla \frac{\delta \mathcal{F}_{\mathrm{surf}}}{\delta \Gamma_{\mathrm{p}}}] \tag{4.45}$$

with the positive definite mobility matrix [TAP12] [WTG$^+$15]

$$\mathbf{Q} = \begin{pmatrix} Q_{hh} & Q_{\Gamma h} \\ Q_{h\Gamma} & Q_{\Gamma\Gamma} \end{pmatrix} = \begin{pmatrix} \frac{h^3}{3\eta} & \frac{h^2 \Gamma}{2\eta} \\ \frac{h^2 \Gamma}{2\eta} & \frac{h \Gamma^2}{\eta} + D\Gamma \end{pmatrix} . \tag{4.46}$$

Performing the variations of the free energy functional gives

$$\frac{\delta \mathcal{F}_{\mathrm{surf}}}{\delta h} = \partial_h f_{\mathrm{w}} - \nabla \cdot [\frac{1}{\xi}(f_{\mathrm{s}} - \Gamma \partial_\Gamma f_{\mathrm{s}} - \frac{\Gamma}{\xi}\partial_\Gamma f_{\mathrm{w}})\nabla h] \tag{4.47}$$

$$\frac{\delta \mathcal{F}_{\mathrm{surf}}}{\delta \Gamma_{\mathrm{p}}} = \frac{1}{\xi}\partial_\Gamma f_{\mathrm{w}} + \partial_\Gamma f_{\mathrm{s}} . \tag{4.48}$$

Inserting these variations into Eqs. (4.44)-(4.45), we obtain the following equations in the long-wave limit $\xi \approx 1$

$$\partial_t h = \nabla \cdot \left[Q_{hh} \nabla [\partial_h f_{\mathrm{w}} - \nabla \cdot [(f_{\mathrm{s}} - \Gamma \partial_\Gamma f_{\mathrm{s}} - \Gamma \partial_\Gamma f_{\mathrm{w}})\nabla h]] + Q_{h\Gamma} \nabla [\partial_\Gamma f_{\mathrm{w}} + \partial_\Gamma f_{\mathrm{s}}] \right] \tag{4.49}$$

$$\partial_t \Gamma = \nabla \cdot \left[Q_{\Gamma h} \nabla [\partial_h f_{\mathrm{w}} - \nabla \cdot [(f_{\mathrm{s}} - \Gamma \partial_\Gamma f_{\mathrm{s}} - \Gamma \partial_\Gamma f_{\mathrm{w}})\nabla h]] + Q_{\Gamma\Gamma} \nabla [\partial_\Gamma f_{\mathrm{w}} + \partial_\Gamma f_{\mathrm{s}}] \right] . \tag{4.50}$$

The final term of the evolution equation for the film height $h(x, y, t)$ represents the Marangoni flux.

The gradient dynamics description of liquid layers and drops covered by insoluble or soluble surfactants is discussed more generally in [TAP12][9] and [TAP16], respectively. There, various thermodynamically consistent extensions of thin-film hydrodynamics (including, e.g., surfactant-dependent interface energies and wetting potentials that affect not only hydrodynamic flows but also diffusion fluxes) are discussed and contrasted to approaches employed in the literature.[1]

4.4. Spreading of Surfactant-Laden Droplets

In the following section, we briefly discuss some of the properties of spreading droplets covered by insoluble surfactants as they will serve as a basis to understand the influence of bio-surfactants on the expansion of bacterial colonies. To that end, we perform numerical time simulations of the model presented in Sec. 4.3 employing relatively simple choices for the energetic contributions f_{w} and f_{s}.

If the wetting energy $f_{\mathrm{w}}(h)$ does not depend on the surfactant concentration, the evolution equations (4.49)-(4.50) are valid for any measure of the concentration of surfactant molecules at the interface [TAP12]. In the following, we chose Γ to be a (dimensionless) packing fraction.

---

[8]There, additional Lagrange multipliers p and λ_Γ have been used to prescribe a conservation of liquid and surfactant.

[9]Note that there a term was missed and a correction is contained in the appendix of [TAP16].

4. Thin Liquid Films and Droplets Covered by Insoluble Surfactants

For relatively low densities of surfactant, the energetic contribution of a non-interacting surfactant can be written as an entropic term of the form

$$f_{\text{s}}(\Gamma) = \gamma^0 + \frac{kT}{a^2}\Gamma[\log(\Gamma) - 1] \tag{4.51}$$

as already employed in Eq. (4.22) in Sec. 4.2.3. For simplicity, the wetting energy

$$f_{\text{w}}(h) = A(-\frac{1}{2h^2} + \frac{h_{\text{a}}^3}{5h^5}) \tag{4.52}$$

is assumed to depend only on the film height, neglecting the influence of the surfactant on the equilibrium contact angle. This corresponds to the case $\delta = 1$ in Sec. 4.2.3 and the functional form of $f_{\text{w}}(h)$ is identical to Eq. (2.14) introduced for partially wetting simple liquids. For these choices, the evolution equations (4.49)-(4.50) take the classical form

$$\partial_t h = \nabla \cdot \left[\frac{h^3}{3\eta}\nabla[\partial_h f - \nabla \cdot (\omega\nabla h)] + \frac{kT}{a^2}\frac{h^2}{2\eta}\nabla\Gamma \right] \tag{4.53}$$

$$\partial_t \Gamma = \nabla \cdot \left[\frac{h^2\Gamma}{2\eta}\nabla[\partial_h f - \nabla \cdot (\omega\nabla h)] + \frac{kT}{a^2}\frac{h\Gamma}{\eta}\nabla\Gamma + \frac{kT}{a^2}D\nabla\Gamma \right] \tag{4.54}$$

employed in many modelling approaches, if we identify

$$\omega = f_{\text{s}} - \Gamma\partial_\Gamma f_{\text{s}} = \gamma^0 - \frac{kT}{a^2}\Gamma \tag{4.55}$$

with the surface tension. In our model, the value of the surface tension thus decreases linearly with the surfactant concentration and the Marangoni flux is given by

$$\mathbf{j}_{\text{M}} = \frac{kT}{a^2}\frac{h^2}{2\eta}\nabla\Gamma\,, \tag{4.56}$$

corresponding to the classical linear Marangoni effect with a coefficient $\gamma_\Gamma = -kT/a^2$. We follow the approach employed in most hydrodynamical models [MC09] and assume that the change of the surface tension with the surfactant concentration is small as compared to the reference surface tension γ^0. In consequence, only γ^0 is used in the Laplace pressure term, i.e. $\nabla \cdot (\omega\nabla h) \approx \gamma^0\Delta h$.

The model is analysed in a dimensionless form obtained by introducing the scaling

$$t = \tau\tilde{t} \qquad x = L\tilde{x} \qquad y = L\tilde{y} \qquad h = l\tilde{h} \qquad f_{\text{w,s}} = \kappa\tilde{f}_{\text{w,s}} \tag{4.57}$$

where tildes indicate dimensionless quantities. For time, energy and vertical and horizontal lengths, we employ the scales

$$\tau = \frac{L^2\eta}{\kappa l} \qquad \kappa = \frac{kT}{a^2} \qquad l = h_{\text{a}} \qquad L = \sqrt{\frac{\gamma^0}{\kappa}}l\,. \tag{4.58}$$

Note that here we assume Γ to be a dimensionless packing fraction of surfactant molecules at the interface. This scaling results in the dimensionless diffusivity $\tilde{D} = \frac{\eta}{l}D$ and the wettability parameter

$$W_{\text{s}} = \frac{Aa^2}{h_{\text{a}}^2 k_B T}\,, \tag{4.59}$$

that defines the relative strength of wetting as compared to the entropic influence of the surfactant. Similar to the wettability parameter W_m appearing in the thin-film model for mixtures and suspensions introduced in Sec. 3.2.1, it is connected to the equilibrium contact angle θ_{eq} of passive stationary droplets by $\theta_{\text{eq}} \propto \sqrt{W_{\text{s}}}$ so that larger values of W_{s}

result in a less wettable substrate and larger contact angles. The evolution equations in the dimensionless form are given in the appendix A.4.1.

In the following, we employ the model to exemplarily demonstrate, how the presence of surfactant affects the spreading speed of droplets as well as the transversal stability of spreading fronts.

4.4.1. Spreading of a Droplet

Figure 4.7 shows the spreading of a surfactant-laden droplet on a one-dimensional substrate. The time simulation is initiated with a parabolic liquid droplet covered by surfactant with a constant concentration $\Gamma = 0.3$ sitting on an adsorption layer with negligible surfactant concentration. The initial contact angle is larger than the equilibrium value determined by W_s.
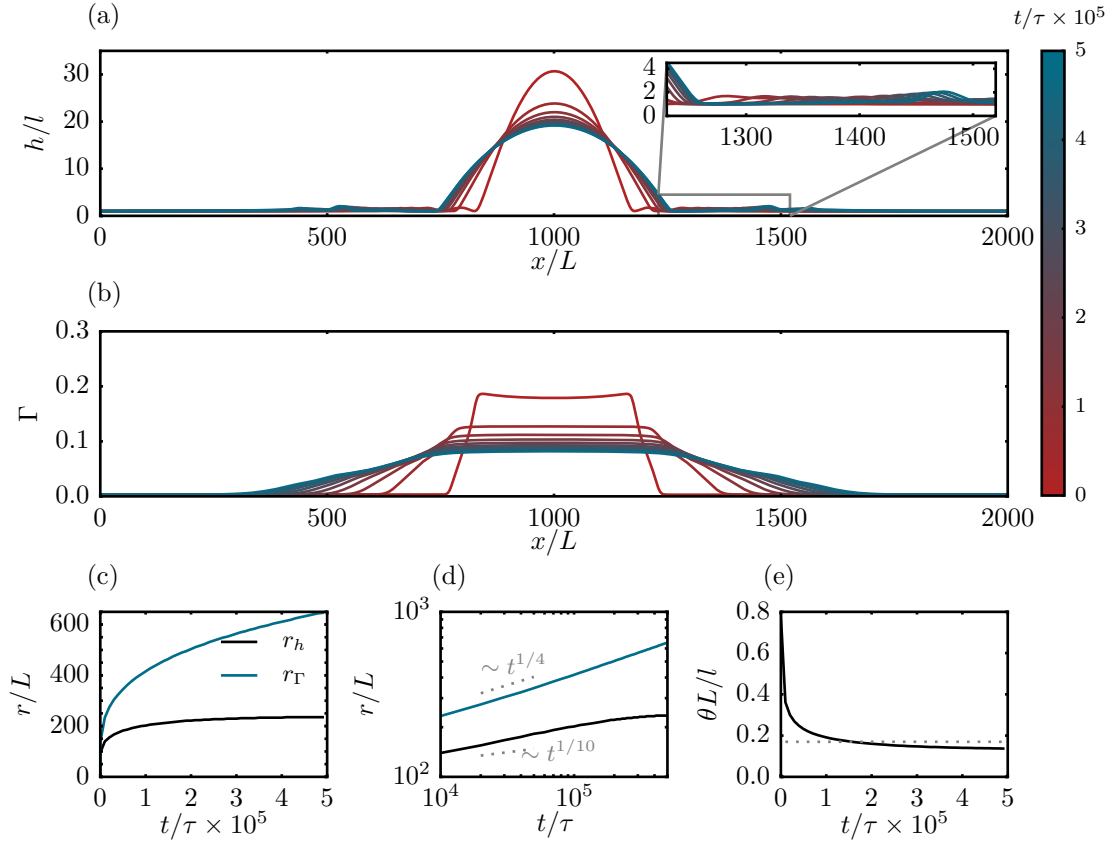
Figure 4.7.: Spreading of a passive droplet with $W_s = 0.05$ covered by insoluble surfactant of initial concentration $\Gamma = 0.3$ and with diffusivity $\tilde{D} = 0.01$. (a) Height profiles and (b) surfactant concentration profiles taken at equidistant points in time. The time evolution of the droplet radius r_h (defined by the inflection point of the height profile) and the surfactant radius r_Γ (determined as the point where $\Gamma = 0.01$) is given in normal (c) and logarithmic scaling (d). The contact angle determined from the curvature in the centre of the drop (solid line) and the analytical equilibrium value (dotted line) are shown in (e). The domain of length $L_x = 2000$ is discretised on $N_x = 1024$ grid points.

The evolving height and surfactant concentration profiles are shown in Fig. 4.7 (a) and (b) at equidistant points in time. During the spreading of the droplet, the surfactant concentration is nearly constant in the droplet but decays linearly at the edges. The time evolution of the extension of the height and surfactant profile and contact angle presented in Fig. 4.7 (c)-(e) shows that the droplet height evolves towards a stationary profile. Interestingly, the spreading towards this shape is faster than for droplets of simple liquid (compare to Fig. 3.4 for the spreading of droplets without surfactant) which can best be seen in the logarithmic plot of the radius (d) which grows slightly faster[10] than $r_h \propto t^{1/10}$, corresponding to a modification of Tanner's law [Tan79]. This is caused by outward-pointing Marangoni fluxes in regions with strong gradients in the surfactant concentration - mostly at the edges of the droplet – which promote its spreading. The edge of the surfactant profile (here determined as the point where $\Gamma = 0.01$) evolves with $r_\Gamma \propto t^{1/4}$ [MC09]. Another interesting feature is the presence of a small "foot" in the height profile at a position that roughly corresponds to the leading edge of the surfactant profile. This has also been discussed in [CM07, CM06, WCM04b] where thin-film models have been employed to study autophobing and fingering phenomena in surfactant-laden droplets. In contrast to these models, we do not observe a "thinning region" between the droplet and the advancing foot, as we employ a wetting potential that favours an adsorption layer of constant height. The contact angle of the spreading droplet approaches a value slightly below the equilibrium value prescribed by Eq. (2.25). This is also a consequence of the outward-pointing Marangoni fluxes. In the long time limit, when the surfactant reaches the boundaries of the simulation domain, the surfactant will be distributed homogeneously in the domain – resulting from the absence of a surfactant-dependence in the employed wetting energy – and the droplet will reach the equilibrium profile prescribed by Eqs. (4.16)-(4.18).

4.4.2. Fingering Instability

The presence of surfactant does not only influence the spreading speed of drops as discussed above, but can also affect their morphology. Marangoni fluxes have been shown to give rise to a fingering instability in the surfactant-assisted spreading of liquid drops [MC09]. This has first been observed experimentally in [ML81] and subsequently confirmed and studied in detail, e.g., in [TWS89, HK95, CCB$^+$99, ASLM03, ASLM04]. Transient growth analysis and numerical time simulations of hydrodynamic thin-film models have been employed to analyse this instability for films covered by insoluble surfactants [THS90, MT99] but have also been extended to soluble surfactants with sorption kinetics [WCM04b] and situations involving micelle formation [CM06]. Warner et al. [WCM02] showed that for the spreading of drops covered by insoluble surfactant, the thickness disparity between the spreading droplet and the underlying absorption layer is crucial for the observation of the fingering instability. Based on a transient stability analysis, the instability can be explained in terms of mobility gradients arising due to variations in the film thickness in the thinned region ahead of the drops which then leads to a faster spreading of thicker regions that subsequently elongate into fingers [WCM04a].

Figure 4.8 shows that also in the model given by Eqs. (4.53)-(4.54), we observe a transversal instability for surfactant-laden fronts spreading towards their equilibrium shape. The initial condition of the numerical time simulation is given by a (steep) planar front covered by surfactants with constant concentration $\Gamma = 0.5$ on an absorption layer with negligible

---

[10]A fit of the data for r_h in the initial interval $t \in [0, 2 \times 10^5]$ with the function $r_h = a\, t^b$ gives $a \approx 33.8$ and $b \approx 0.155$.
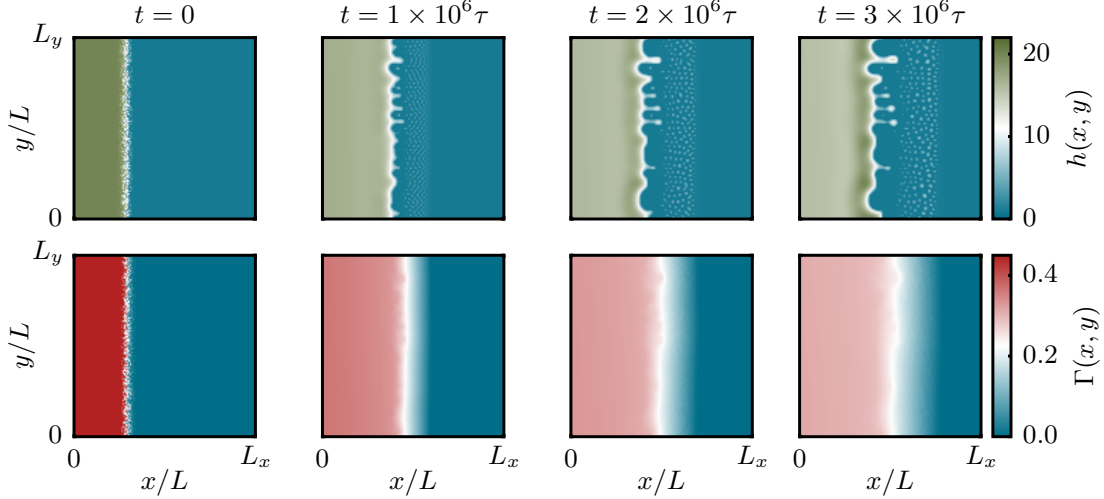
Figure 4.8.: Transversal instability observed for the spreading of a surfactant-laden planar front. The top and bottom row show the height and surfactant concentration distributions at equidistant points in time, respectively. Parameters: $W_s = 0.05$, $\tilde{D} = 0.01$. The domain of size $L_x = L_y = 5000$ is discretised on $N_x \times N_y = 256 \times 256$ grid points.

presence of surfactant[11]. The front in the height profile (top row) becomes transversally unstable and small protrusions grow in time, giving rise to thin, ramified fingers. The instability is less pronounced in the surfactant concentration profile, which shows a nearly linear decay ahead of the spreading front that is approximately constant in the y-direction. The formation of fingers can be suppressed by increasing the wettability parameter W_s, i.e. the contact angle, and thus favouring a straight contact line or by increasing the diffusivity $\tilde{D}$ of the surfactant, smoothing out the gradients in the surfactant concentration (data not shown).

In contrast to previous modelling approaches, we use a wetting energy that describes a partially wetting liquid. Therefore, the 'foot' in the height profile observed in the spreading of one-dimensional droplets in the previous section (see inset in Fig. 4.7 (a)) is transversally unstable. This leads to the formation of small droplets ahead of the spreading front. Furthermore, we do not observe a thinned region such that the reason for the transversal instability can in our model not be given by the mobility gradients associated with it.[12]

4.5. Delayed Coalescence of Surfactant-Laden Droplets

After illustrating the effect of surfactants on the spreading speed and morphology of droplets, we now briefly discuss how surfactants influence the coalescence of two droplets. We employ the model presented in Sec. 4.3 to study the delayed coalescence as, e.g., observed experimentally in [BCKS18]. As the fluids used in this experiment completely wet the substrate, the wetting contribution does not need to be accounted for, i.e., we use

---

[11]The initial condition is given by $h(t = 0) = 10 \left[1 - \tanh(0.01(x - \frac{L_x}{4} + \frac{L_x}{70}\text{rand}(Nx, Ny)))\right]$ and $\Gamma(t = 0) = 0.25 \left[1 - \tanh(0.01(x - \frac{L_x}{4} + \frac{L_x}{70}\text{rand}(Nx, Ny)))\right]$, where $\text{rand}(N_x, N_y)$ corresponds to a 2D array filled with random float numbers from the half-open interval $[0.0, 1.0)$.

[12]Note that, unfortunately, a transversal linear stability analysis similar to the one performed in Sec. 5.4.2 is not possible in this set-up, as the system does not exhibit stationary fronts due to the limited amount of liquid and surfactant. It is, however, possible for surfactant-covered films flowing down an inclined plate, where a similar analysis has been performed in [EMC05, GN15].

$f_w(h, \Gamma) = 0$. The surfactant is again assumed to be non-interacting and of low concentration and, as previously, we employ the energetic contribution

$$f_s(\Gamma) = \gamma^0 + \frac{kT}{a^2}\Gamma[\log(\Gamma) - 1] \tag{4.60}$$

where Γ again represents a dimensionless packing fraction of surfactant at the interface. In this case, the evolution equations (4.49)-(4.50) for the height profile h and the surfactant concentration Γ take the simple form

$$\partial_t h = \nabla \cdot \left[\frac{h^3}{3\eta}\nabla(-\gamma^0 \Delta h)\right] + \frac{kT}{a^2}\nabla \cdot \left[\frac{h^2}{2\eta}\nabla\Gamma\right] \tag{4.61}$$

$$\partial_t \Gamma = \nabla \cdot \left[\frac{h^2\Gamma}{3\eta}\nabla(-\gamma^0 \Delta h)\right] + \frac{kT}{a^2}\nabla \cdot \left[\frac{h\Gamma}{\eta}\nabla\Gamma\right] + \frac{kT}{a^2}D\Delta\Gamma. \tag{4.62}$$

For the analysis, it is expedient to rescale the model by introducing the length scale l for both, horizontal and vertical direction and the time scale $\tau = \eta l/\gamma^0$. By not implying different length scales in horizontal and vertical directions, the contact angle is not affected by the rescaling. The solutions are characterised by a dimensionless diffusivity $\tilde{D}$ and the model parameter

$$\epsilon_1 = \frac{k_B T}{a^2\gamma^0} \tag{4.63}$$

as already introduced in Eq. (4.36). This parameter represents the effective strength of the surfactant and defines the variation of the surface tension with the surfactant concentration.

Figure 4.9 shows one-dimensional time simulations performed with the finite element method outlined in Sec. A.1.1. Both simulations are initialised with two droplets of identical volume with a parabolic profile on an adsorption layer of height $h_a = 1$. The left droplet is initially covered by surfactant. Figure 4.9 (a) shows profiles for the film height h (top) and surfactant concentration Γ (bottom) taken at equidistant points in time for an initial condition consisting of droplets with initial height $h_{init}/l = 75$ corresponding to an initial contact angle $\theta_{init} \approx 0.29$. After contact, coalescence (C) of the droplets can be observed as they merge into one. The simulation presented in Fig. 4.9 (b) is initiated with two droplets of the same volume as in (a), but with a smaller initial height $h_{init}/l = 25$ corresponding to $\theta_{init} \approx 0.03$. The droplets thus meet at a smaller contact angle. In this case, the droplets do not merge and we observe a temporary state of non-coalescence (NC). This two qualitatively different scenarios can be characterised by tracking the position of the droplets, defined as the maxima of the height profile. These are shown in Fig. 4.9 (c) for coalescence (black lines) and temporary non-coalescence (blue lines). In the latter case, the droplet which is initially covered by surfactant (and thus has a lower surface tension) moves towards the droplet which is initially free of surfactant and 'chases' it over the substrate[13]. The two scenarios can also be distinguished by monitoring the height of the neck region between the droplets, which is presented in Fig. 4.9 (d). In the case of coalescence (black line), the height rapidly grows, whereas in the case of temporary non-coalescence (blue lines), the height stays roughly constant.

The mechanism behind the non-coalescence is illustrated in Fig. 4.10 (a) that shows a zoom of the neck region. The capillary pressure gives rise to a flow into the neck region that promotes the coalescence. In the state of temporary non-coalescence, this flow is

---

[13]The sharp bend in the time evolution of $x(h_{max})/l$ at $t/\tau \approx 1.1 \times 10^6$ for the case of non-coalescence (blue line in Fig. 4.9 (c)) results from a shape deformation of the right droplet leading to shift of the maximum.
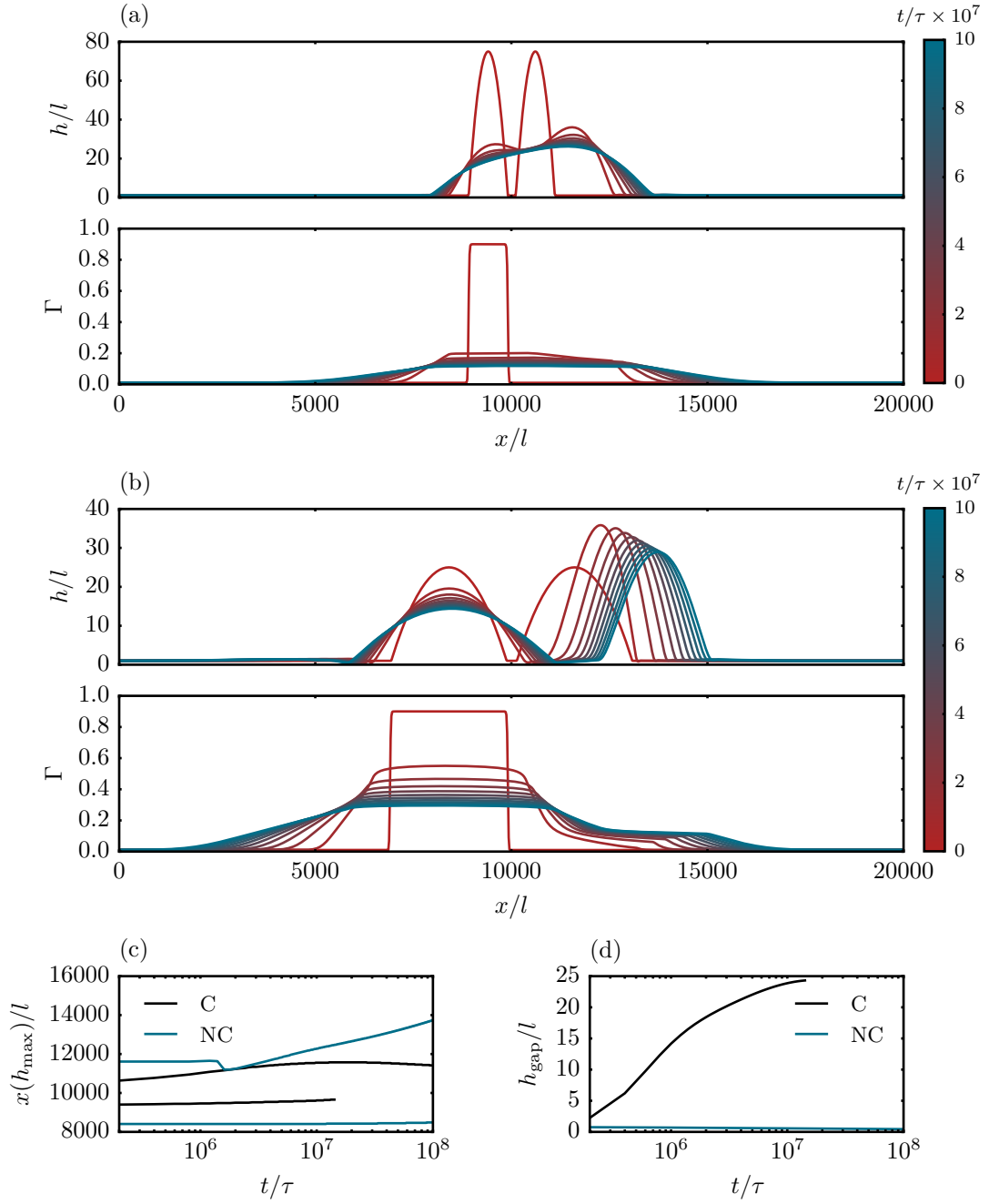
Figure 4.9.: (a) Height and surfactant concentration taken at equidistant points in time for two coalescing droplets with initial height $h_{init}/l = 75$ corresponding to $\theta_{init} \approx 0.29$. (b) The contact angle at which the droplets meet is lower for a simulation initialised with droplets of the same volume but initial height $h_{init}/l = 25$ (corresponding to $\theta_{init} \approx 0.03$). In this case, the coalescence of the droplets is significantly delayed. (c) Position of the maxima of the droplets for the scenario of coalescence and temporary non-coalescence. In the case of coalescence, the droplets merge at $t/\tau \approx 1.44 \times 10^7$ and afterwards, only one maximum of the height profile is detected. (d) Height of the neck region between the droplets defined as the minimum of the height profile between them. The remaining parameters are $\tilde{D} = 1$ and $\epsilon_1 = 0.1$. The domain is discretised on $N_x = 1024$ equidistant mesh points.

compensated by the Marangoni flow out of the connecting neck. The resulting velocity profile (black arrows) thus causes a motion of both droplets to the right and prevents immediate coalescence.

In experiments, the difference in surface tension and the contact angle at the moment of drop-drop contact have been identified as key parameters [BCKS18]. In our model, these quantities can be varied by choosing different values for the model parameter ϵ_1 and the initial contact angle θ_{init} of the droplets while keeping the volume of the droplets and the initial distance between their contact lines constant. Figure 4.10 (b) shows a parameter scan, identifying the conditions for temporary non-coalescence in the $(\epsilon_1 - \theta_{\text{init}})$ parameter space. In qualitative agreement with the experimental observation in [BCKS18], we find temporary non-coalescence for low contact angles (low θ_{init}) and a low difference in surface tension (low ϵ_1).

(a)

(b)
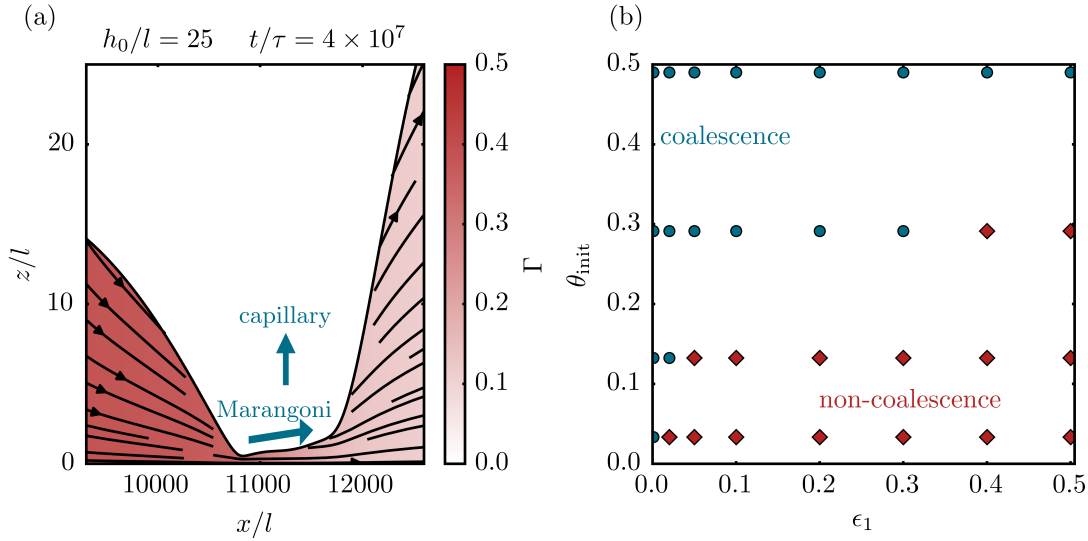
Figure 4.10.: (a) Illustration of the mechanism of temporary non-coalescence using a zoom in the neck-region of the time simulation for $h_{\text{init}}/l = 25$ and $\epsilon_1 = 0.1$ at $t/\tau = 4 \times 10^7$ shown in Fig. 4.9. The capillary pressure causes a flow of liquid into the neck region. This flow is, however, over-compensated by the Marangoni flow pointing from low surface tension (high surfactant concentration Γ) to high surface tension (low surfactant concentration Γ). The velocity profile (black arrows) indicates a flow of both droplets to the right, preventing immediate coalescence. (b) Parameter scan based on time simulations that identifies the region of coalescence (blue dots) and temporary non-coalescence (red diamonds) in the $(\epsilon_1 - \theta_{\text{init}})$ parameter space at fixed volume of the drops $V = 25000$. The initial distance of the drops is defined by the distance of the contact lines is $d_{\text{init}}/l = 200$. The surfactant diffusivity is set to $\tilde{D} = 0.1$. The domain of length $L_x = 20000$ is discretised on $N_x = 1024$ grid points and the state of coalescence is evaluated at $t/\tau = 10 \times 10^7$.

To summarise this chapter, we have discussed the modelling of passive droplets covered by insoluble surfactants. In addition to considerations for equilibrium situations, we have briefly and exemplarily studied some dynamical effects – namely the spreading of surfactant-laden droplets, the fingering instability and temporary non-coalescence of droplets – to illustrate how the presence of surfactants changes the spreading of passive droplets. After this excursus, we investigate in the following chapter how surfactants influence the expansion of bacterial colonies where such surface-active molecules are in many cases produced by the bacteria.

5. Surfactant-Driven Spreading of Bacterial Colonies

In chapter 3, we have studied the osmotic spreading of bacterial colonies over substrates. This mechanism for colony expansion is not driven by the active motion of individual bacteria, but by the physico-chemical properties of the involved interfaces. As discussed in Sec. 1.2, bacterial colonies can exhibit various modes of surface colonisation. Another expansion mechanism which relies on (passive) physical fluxes is the surfactant-driven spreading of bacterial colonies. In this chapter, we first briefly introduce this mechanism and discuss experimental observations. Then, we develop and analyse a mathematical model which is again based on a thin-film description. The model allows us to study the effect of wettability and Marangoni fluxes on the spreading velocity as well as on the arising morphology of the bacterial colony.

Note that the results presented in this chapter have in part been published[1] in

[TJT18]   Sarah Trinschek, Karin John and Uwe Thiele. *Modelling of surfactant-driven front instabilities in spreading bacterial colonies* Soft Matter 14.22, 4464-4476 (2018).

5.1. Mechanism and Experimental Findings

For many bacterial strains, the chemical signalling molecules involved in the quorum sensing mechanism have been found to play a double role. Besides allowing for a cell-cell communication, they act as bio-surfactants at physiologically relevant concentrations. In chapter 3, we have already discussed that such bio-surfactants can promote the spreading of bacterial colonies by improving the wettability. In addition, gradients in surfactant concentration at the edges of the colony induce Marangoni fluxes which further drive its expansion [FPB$^+$12, DDFMV15, YTST17, CSO05]. If the concentration of bio-surfactants is high at the centre of the colony (where bacteria produce these molecules) the surface tension is lowered in this region. This results in an outward-pointing flow along the surface tension gradient which promotes the spreading of the colony. Genetic and physico-chemical experiments [FPB$^+$12, YTST17, KSF03, ARK$^+$09, CSO05] show that in *Bacillus subtilis* and *Pseudomonas aeruginosa* colonies, this surface tension gradient – induced by the respective bio-surfactants *surfactin* and *rhamnolipids* – is an important driver of colony expansion. Besides enhancing the spreading speed, Marangoni fluxes may also be responsible for the striking finger-like colony patterns observed in experiments.

Figure 5.1 shows visible light images of an experiment performed by Fauvart et al., that demonstrates the effect of surfactant production in *P. aeruginosa* colonies [FPB$^+$12]. The wild-type strain which is shown in the left part of each image undergoes a rapid surface colonisation. The colony spreads outwards and forms pronounced fingers. The signal intensity plots in the lower row of Fig. 5.1 show the existence of a capillary rim at the

---

[1]Chapter 5 is based on and closely follows [TJT18]. It contains figures and text adapted from Trinschek et al. Soft Matter, 14.22, 4464-4476 (2018) © Royal Society of Chemistry (2018) particularly in Sec. 5.1 (p.65 l.18-33 and p.66 l.12-25), Sec. 5.2 (p.68 l.1 - p.70 l.20) and Sec. 5.3 - 5.5.

edge of the spreading colony. In contrast, a mutant strain deficient in surfactant production shown in the right part of each image is arrested in a small circular shape and is not able to spread over the substrate, in spite of all other conditions being equal.
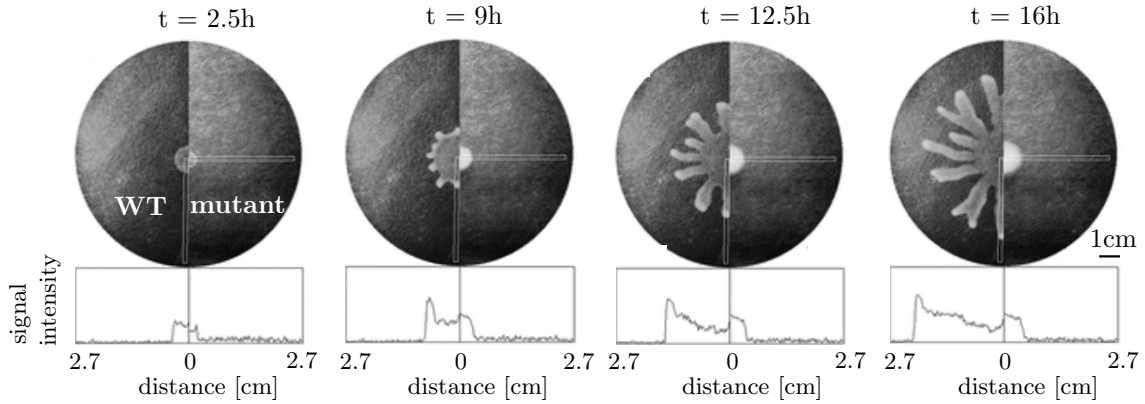
Figure 5.1.: Visible light images (top) of *P. aeruginosa* colonies at different points in time. The surfactant producing wild type (left side of the images, WT) spreads outwards and forms pronounced fingers whereas a mutant strain deficient in surfactant production (right side of the images, mutant) can not expand. Signal intensity plots (bottom) along the rectangular regions indicated in the visible light images show the presence of a pronounced rim for the wild-type colonies. Adapted with permission from [FPB+12] © Royal Society of Chemistry (2011).

The surfactant-driven spreading is also observed for other bacterial strains: Genetic knockout experiments [DRH+06] show that surface-active *AHL* (N-acyl-homoserine lactone) molecules are crucial for an efficient expansion of *Rhizobium etli* colonies. The experimentally observed colony shapes and spreading speeds of about 0.5μm/s agree with those estimated from a spreading driven by Marangoni forces. Growth measurements verify that for *Paenibacillus dendritiformis* colonies, the spreading velocity indeed depends on the surfactant concentration but not on the motility of the individual bacteria [BSZ+09]. Besides the surfactant-induced instability, also chemotactic effects and nutrient limitation are possible causes for the dendritic morphology of bacterial colonies (for a critical review, see [MHH+10]). However, the demonstration that the expansion can be prevented by counter-gradients of surfactant [FPB+12] strongly hints at the existence of a surfactant-driven expansion mechanism. The swarming of a colony can be inhibited by the addition of purified surfactant to the agar substrate as well as by the bio-surfactant production of nearby colonies [CSO05]. In both cases, the necessary gradients in surface tension are suppressed. Figure 5.2 shows the growth of *P. aeruginosa* colonies on an agar substrate, onto which a ring pattern was stamped using a sterile ring. When this ring is just wetted with water, the colony swarms over the imprint. When, in contrast, the ring is wetted with *rhamnolipids* in a concentration close to the *in vivo* one, the expansion of the colony is slowed down and eventually stops [FPB+12]. In this case, the gradients in surface tension due to the bio-surfactants produced by the bacteria are counterbalanced by the surfactant in the imprint and the driving Marangoni fluxes are suppressed.[1]

5.2. Mathematical Modelling

In this section, we introduce a model for the surfactant-driven spreading of bacterial colonies. The model focuses on the influence of Marangoni fluxes and wettability on the

Figure 5.2.: Inhibition of swarming in *P. aeruginosa* colonies. Bio-surfactant is added exogeneously in a ring pattern around the colony in increasing concentration c_{rel} relative to the *in vivo* concentration. At suffici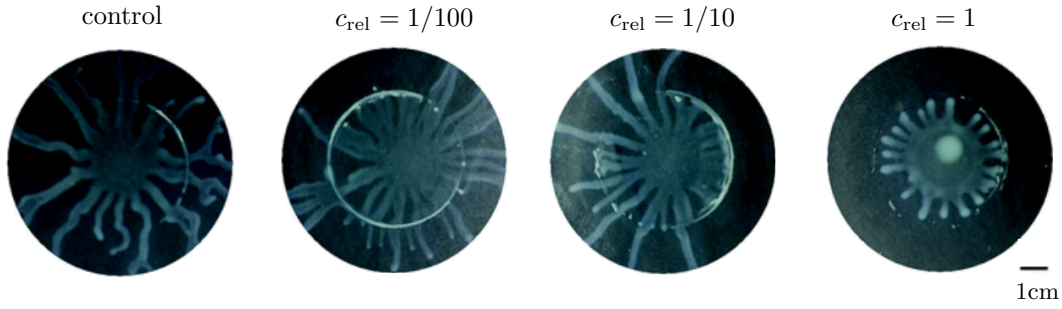ently high concentration, this results in a counter-gradient of surfactant that suppresses the outward-pointing Marangoni fluxes and the expansion of the colony slows down and eventually stops. Adapted with permission from [FPB$^+$12] © Royal Society of Chemistry (2011).

spreading dynamics and the morphology of the colony. As for the osmotic spreading mechanism in Sec. 3.2, the description is based on a thin-film model for the corresponding passive limiting case. Here, we treat the bacterial colony as a thin film of height $h(x, y, t)$ covered by insoluble surfactant molecules of concentration $\Gamma(x, y, t)$ and supplement the hydrodynamic equations with bioactive growth processes for the film height and surfactant concentration.

Similar thin-film models have successfully been applied in the context of surfactant-mediated spreading of bacterial colonies to study the movement of a *B. subtilis* biofilm up a wall on waves of surfactant [ARK$^+$09] or bacterial swarming in colonies of *P. aeruginosa* in a one-dimensional setting [FPB$^+$12]. However, the focus of these studies does not lie on the effect of Marangoni effects on the morphology of the colony and they do, in particular, not contain two-dimensional hydrodynamic simulations of the proposed models.

Passive Part of the Model

As mentioned above, the model for surfactant-driven spreading of bacterial colonies is based on the description of passive thin films covered by insoluble surfactant presented in Sec. 4.3. Here, the evolution equations (4.49)-(4.50) are supplemented with terms describing bioactive processes. The focus of the model lies on the study of the interplay between the bioactive growth and production processes and the passive surface and interface forces. Therefore, we choose relatively simple, well-studied forms for the energetic contributions that determine the passive part of the dynamics. We again use the wetting energy $f_{\mathrm{w}}(h)$ given by Eq. (2.14) and the interfacial energy $f_{\mathrm{s}}(\Gamma)$ given by Eq. (4.51) that have already been employed in Sec. 4.4 to study the spreading of passive droplets covered by insoluble surfactant. They describe situations with a relatively low surfactant density, for which the assumption of a linear equation of state is reasonable. The wetting energy is assumed to depend only on the film height, neglecting the influence of the surfactants on the equilibrium contact angle. This means that variations in the wettability on the one hand and gradients in the surface tension on the other hand – which can both be induced by the presence of bio-surfactants – are treated as two separate effects. The separation of this two physical parameters facilitates the disentanglement of their respective impact on the growth dynamics. However, care should be taken when comparing to experimental observations. There, the difference between a bacterial strain deficient in surfactant production and a surfactant producing strain implies that the latter likely experiences a higher surfactant concentration resulting in Marangoni fluxes *and* a higher wettability.

Bioactive Terms

To describe the surfactant-driven spreading of bacterial colonies, the hydrodynamic model for passive liquids is extended by biological growth and production processes. Over time, the bacteria in the colony grow and multiply by cell division and possibly produce polymeric substances and osmolytes. As discussed in chapter 3, this processes may give rise to a difference of the osmotic pressures in the film and in the underlying moist substrate which results in the influx of water into the colony [SAW$^+$12]. We assume that this influx is fast as compared to the growth processes. Then, the biomass production and osmotic influx can be written as one effective growth term $G(h)$ as discussed in Sec. 3.2.2. Recall that the resulting biomass growth term[2] is of the form

$$G(h) = gh \left(1 - \frac{h}{h^\star}\right) f_{\mathrm{mod}}(h)$$

$$\text{with} \quad f_{\mathrm{mod}}(h) = \left(1 - \frac{h_{\mathrm{u}}}{h}\right)\left(1 - \phi_{\mathrm{eq}}\right)\left[1 - \exp\left(\phi_{\mathrm{eq}}\frac{h_{\mathrm{a}} - h}{h_{\mathrm{a}}}\right)\right]$$

$$(5.1)$$

and the growth rate g.

The second bioactive process that needs to be included in the model is the production of surfactant molecules by the bacteria. As the produced surfactant quickly diffuses to the liquid-air interface due to the small height of the colony as compared to its lateral extension, we assume the production of surfactant $P(h, \Gamma)$ to be proportional to the biofilm height. In addition, we assume that the production decreases with increasing surfactant concentration and approaches zero when the local surfactant concentration reaches a limiting value Γ_{max}. This results in the production term

$$P(h, \Gamma) = ph \left(\Gamma_{\mathrm{max}} - \Gamma\right) \Theta(\Gamma_{\mathrm{max}} - \Gamma) \Theta(h - h_{\mathrm{u}}) \tag{5.2}$$

where the step-functions Θ are introduced to ensure that the production only takes place inside the colony (where the film height exceeds that value h_{u}) and not in the adsorption layer. In addition, they prevent a degradation of the surfactant if the concentration Γ_{max} is overcome [TJT18].[3]

We include biomass growth and surfactant production as additional non-conserved flux terms into the evolution equations (4.49)-(4.50) describing the passive system. Using the entropic energy of the surfactant given by Eq. (4.51) and the mobility matrix given in Eq. (4.46) results in the following model

$$\partial_t h = \nabla \cdot \left[\frac{h^3}{3\eta}\nabla(\partial_h f_{\mathrm{w}} - \gamma^0 \Delta h)\right] + \frac{kT}{a^2}\nabla \cdot \left[\frac{h^2}{2\eta}\nabla\Gamma\right] + G(h) \tag{5.3}$$

$$\partial_t \Gamma = \nabla \cdot \left[\frac{h^2 \Gamma}{3\eta}\nabla(\partial_h f_{\mathrm{w}} - \gamma^0 \Delta h)\right] + \frac{kT}{a^2}\nabla \cdot \left[\frac{h\Gamma}{\eta}\nabla\Gamma\right] + \frac{kT}{a^2}D\Delta\Gamma + P(h, \Gamma). \tag{5.4}$$

for the surfactant-driven spreading of bacterial colonies [TJT18].[1]

Non-Dimensional Form of the Equations

To obtain a dimensionless form of the model (5.3)-(5.4) and thereby facilitate the analysis, we employ the same scaling as for the passive surfactant model in Sec. 4.4, namely

$$t = \tau\tilde{t} \qquad x = L\tilde{x} \qquad y = L\tilde{y} \qquad h = l\tilde{h} \qquad f_{\mathrm{w,s}} = \kappa\tilde{f}_{\mathrm{w,s}} \tag{5.5}$$

---

[2]Recall that, as discussed in Sec. 3.2.2, this choice for $G(h)$ corresponds to a logistic growth term that accounts for the fact that the biomass production ceases if the biofilm becomes too thick and reaches the height $h^\star$. Furthermore, a small threshold value of biomass $\phi_{\mathrm{eq}}h_{\mathrm{u}}$ needs to be overcome to initiate growth.

[3]In the numerical calculations, they are approximated by $\Theta(x) \approx 0.5[1 + \tanh(100x)]$.

where a tilde indicates dimensionless quantities. Note that Γ describes the (dimensionless) packing fraction of surfactant at the interface. Employing the scaling

$$\tau = \frac{L^2\eta}{\kappa l} \qquad \kappa = \frac{kT}{a^2} \qquad l = h_a \qquad L = \sqrt{\frac{\gamma^0}{\kappa}}\, l\,, \tag{5.6}$$

for time, energy and vertical and horizontal lengths, respectively, results in the dimensionless biomass growth rate $\tilde{g} = \tau g$, the dimensionless surfactant production rate $\tilde{p} = \tau l p$, the dimensionless diffusivity $\tilde{D} = \frac{\eta}{l}D$ and the wettability parameter

$$W_s = \frac{Aa^2}{h_a^2 k_B T}\,, \tag{5.7}$$

as already given in Eq. (4.59). Recall that it is connected to the equilibrium contact angle θ_{eq} of passive stationary droplets (without bioactive terms) by $\theta_{eq} \propto \sqrt{W_s}$ so that larger values of W_s result in a less wettable substrate and larger contact angles. The evolution equations in the dimensionless form are given in appendix A.4.1. If not stated otherwise, we fix the parameters to $\tilde{g} = 10^{-5}$, $\tilde{p} = 10^{-6}$, $\tilde{h}^\star = 20$ and $\tilde{D} = 0.01$ throughout the analysis and focus on the effect of the wettability parameter W_s and the maximal surfactant concentration Γ_{max} on the growth of the colonies. These two parameters capture, e.g., the difference between a surfactant-producing bacterial strain and a mutant strain deficient in surfactant production.[1]

Experimental Calibration

Bacterial colonies are complex living systems which can in general only be expected to be described qualitatively by a simple model, not quantitatively. However, in the following we estimate the parameters and scales from an exemplary calibration to experiments on the spreading of *P. aeruginosa* or *B. subtilis* colonies as described, e.g., in Refs. [FPB$^+$12, ARK$^+$09]. Using the parameters summarised in Table 5.1 results in the scales

$$\tau \approx 0.03\text{s} \qquad l \approx 1\mu\text{m} \qquad L \approx 10\mu\text{m} \qquad \kappa \approx 4\cdot 10^{-4}\,\frac{\text{J}}{\text{m}^2}\,. \tag{5.8}$$

surface tension of water	$\gamma^0 \approx 70\text{mN/m}$
height of the wetting layer	$h_a \approx 1\mu\text{m}$
viscosity of the colony	$\eta \approx 0.1\text{Pas}$
typical surfactant length scale	$a \approx 3\text{nm}$
thermal energy at 25°	$k_B T \approx 4\cdot 10^{-21}\text{J}$

Table 5.1.: Parameters used to determine the time, length and energy scales in the model for surfactant-driven spreading of bacterial colonies. (cf. [TJT18])

Then, the dimensionless growth rate $\tilde{g} = 10^{-5}$ corresponds to a dimensional value of $g = \frac{\tilde{g}}{\tau} \approx 1.2\frac{1}{\text{h}}$ which fits well to the experimentally obtained doubling time that is – depending on the growth conditions – in the order of $30\text{min} - 1.5\text{h}$ [LW12]. A dimensionless limiting height $\tilde{h}^\star = 20$ corresponds to a dimensional value $h^\star = \tilde{h}^\star l \approx 20\mu\text{m}$ which is in accordance with the experimentally measured value of $15 - 20\,\mu\text{m}$ in Ref. [FPB$^+$12]. We use a dimensionless production rate $\tilde{p} = pl\tau = 10^{-6}$, which results in a maximal production rate[4] of $p\Gamma_{max} \approx 1\ldots 20\,\text{s}^{-1}\,\text{m}^{-1}$ using the scales for l and τ above and $\Gamma_{max} = 0.02\ldots 0.5$.

---

[4]Comparing with Ref. [ARK$^+$09], the surfactant production can be roughly estimated from the change of the surface tension over time $\frac{d\gamma}{dt} = 0.2\frac{\text{mN}}{\text{m}}\frac{1}{\text{h}} = \frac{k_B T}{a^2}\frac{d\Gamma}{dt} = \frac{k_B T}{a^2}p\Gamma_{max}h$. Using a film thickness of $h_{max} = 20\,\mu\text{m}$, we find a surfactant production rate constant $p\Gamma_{max} = 6\,\text{s}^{-1}\,\text{m}^{-1}$ for a *B. subtilis* colony, which fits well with our estimated $p\Gamma_{max}$.

	dimensionless value	corresponding dimensional value	literature value
growth rate	$\tilde{g} = l\tau p = 10^{-5}$	$g = 1.2\frac{1}{\text{h}}$	doubling time of *P. aeruginosa* [LW12]: 30min-1.5h
colony height	$\tilde{h} = \frac{h}{l} = 20$	$h = 20\mu\text{m}$	colony height of a *P. aeruginosa* colony [FPB$^+$12]: $15 - 20\,\mu\text{m}$
max. surfactant production rate	$\tilde{p}\Gamma_{\max} = 0.02...0.5 \times 10^{-6}$ for $\Gamma_{\max} = 0.02..0.5$	$p\Gamma_{\max} = 1...20\frac{1}{\text{sm}}$	surfactant production rate in a *B. subtilis* biofilm [ARK$^+$09], estimated from the drop in surface tension: $p\Gamma_{\max} = 6\,\text{s}^{-1}\,\text{m}^{-1}$
translational diffusion coefficient	$\tilde{D} = D_{\text{T}}\tau/L^2 = 0.01$ (diffusivity)	$D_{\text{T}} = 3 \times 10^{-11}\,\text{m}^2\,\text{s}^{-1}$ (diffusion coefficient)	diffusion coefficient calculated for surfactin on a water/hexane interface [Nic03]: $1.8\ldots6.7 \times 10^{-10}\,\text{m}^2\,\text{s}^{-1}$

Table 5.2.: Estimation of the parameters in the model for surfactant-driven spreading of bacterial colonies for the scaling given in Eq. (5.8) and comparison to values found in the literature. (cf. [TJT18])

The chosen dimensionless parameter $\tilde{D} = 0.01 = D_{\text{T}}\tau/L^2 = \kappa D\tau/L^2$ corresponds to a translational diffusion coefficient $D_{\text{T}} = 3 \times 10^{-11}\,\text{m}^2\,\text{s}^{-1}$. This is lower than the diffusion coefficient calculated for *surfactin* on a water/hexane interface ($1.8\ldots6.7 \times 10^{-10}\,\text{m}^2\,\text{s}^{-1}$ [Nic03]) but still in an acceptable range. The estimated parameters are summarised and compared to literature values in Table 5.2 [TJT18].

In the next sections, we analyse the presented model, focusing on the influence of Marangoni fluxes and wettability on spreading dynamics and morphology. First, we perform time simulations of initially circular colonies at different parameter values W_{s} and limiting surfactant concentrations $\Gamma_{\max}$. These serve as illustrative examples and can already be employed to gain a graphic representation and a qualitative understanding of the spreading behaviour. Next, the observed effects are studied for planar fronts by parameter continuation techniques [DO09]. This yields a more technical description that allows, e.g., for the analysis of the emerging front instability by a transversal linear stability analysis. In the last part of the section, counter-gradients of surfactant are exemplarily tested as a strategy to prevent the expansion of bacterial colonies, providing an illustrative application of the model.[1]

5.3. Four Types of Spreading for Colonies in Radial Geometry

In a first step, the dynamics of colony growth in the model is studied by performing two-dimensional numerical time simulations of Eq. (5.3)-(5.4) in the dimensionless form and in a circular geometry. These simulations reveal the influence of the wettability and Marangoni fluxes on the spreading speed and morphology of the emerging bacterial colonies. We employ a finite element scheme as outlined in appendix A.1.1 on a simulation

domain $\Omega = [-L_x, L_x] \times [-L_y, L_y]$ with $L_x = L_y = 5000$ discretised on a regular mesh using $N_x \times N_y = 512 \times 512$ grid points. On the boundaries, no-flux conditions are applied for the film height and the surfactant concentration. The initial condition is given by a small circular bacterial colony with surfactant concentration $\Gamma_{\max}$ on the colony and $0.05 \times \Gamma_{\max}$ on the surrounding substrate.

The time simulations of (5.3)-(5.4) show that – depending on the wettability and the strength of the Marangoni fluxes in the system – four qualitatively different types of spreading behaviour can be observed for colonies growing in a circular geometry [TJT18]. These are shown in Fig. 5.3 (a) to (d) for different choices of the parameters W_{s} and $\Gamma_{\max}$. The respective top left plots show the contour lines of the colony height (defined by $h(x, y) = 0.5 h^{\star}$) at equidistant points in time. The film height and surfactant distribution at the end of the simulation are shown in the respective top and bottom right plots. The respective bottom left plots in Fig. 5.3 give the time dependence of the mean values of the maximal and minimal radii of the colony to characterise its shape evolution.

We first discuss the spreading behaviour of the system for low surfactant concentrations (low $\Gamma_{\max}$). Consistent with the biofilm spreading model without surfactant presented in chapter 3, the system shows a transition between continuously expanding and arrested colonies depending on the wettability parameter W_{s}. For high wettability and thus small equilibrium contact angles (low W_{s}, Fig. 5.3 (c)), the bacterial colony first swells vertically and horizontally until it reaches the limiting film height $h^{\star}$. Subsequently, it expands horizontally over the substrate with a constant speed and a *circular* (type C) colony shape. In contrast, at low wettability and thus high contact angle (high W_{s}, Fig. 5.3 (d)), the height evolves towards a stationary profile of fixed extension and contact angle and the spreading of the bacterial colony is *arrested* (type A). This is consistent with the spreading dynamics observed in the biofilm model discussed in Sec. 3.3 and Sec. 3.4.

For both spreading modes, the production of a significant amount of surfactant (high $\Gamma_{\max}$) improves the ability of the bacterial colony to expand outwards over the substrate. It gives rise to a higher surfactant concentration $\Gamma(x, y)$ at the centre of the colony than on the surrounding substrate. The emerging surface tension gradients induce outward-pointing Marangoni flows that facilitate the expansion of the colony over the substrate [TJT18].

For a continuously spreading colony, these Marangoni flows increase the spreading speed and also induce *modulations* of the circular colony shape (low W_{s}, Fig. 5.3 (a)). However, eventually the growth of these undulations slows down. For large times, the tips and troughs of the front line translate with a similar velocity over the substrate, which can also be seen in the time evolution of the mean values of the maximal and minimal radii of the colony shape. With the scales presented above in Sec. 5.2, the numerically measured dimensionless expansion rate of roughly 5×10^{-4} corresponds to a speed of about $10 \mu m/min$, which compares well to the value of $5 - 40 \mu m/min$ found in experiments [FPB$^+$12].

For the initially arrested spreading at low wettability (high W_{s} in Fig. 5.3 (b)), the consequences of the surfactant production are even more drastic: It enables a horizontal expansion of the colony by the formation of pronounced *fingers* (type F). At large times, the tips of the fingers expand outwards with a constant velocity whereas the troughs of the front line stay behind at a fixed position.

A similar distinction of two types of front instabilities, for which the shape of the evolving front modulations becomes stationary (type M) or corresponds to continuously growing fingers (type F), has been made for advancing coating films driven by gravity or shear stress [ESR00].

The mechanism behind the formation of pronounced fingers in the colony shape becomes clear when studying the distribution of surfactant on the colony and the surrounding sub-
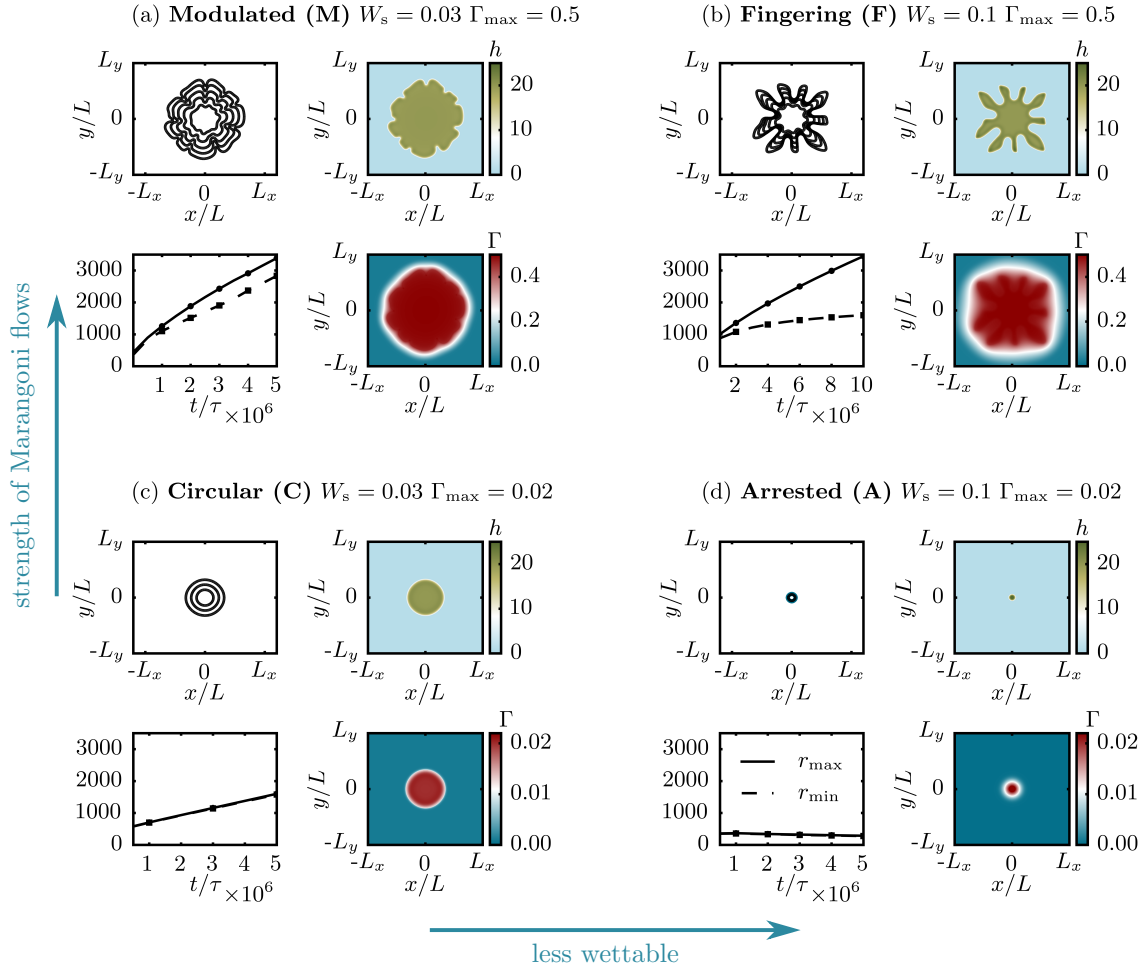
Figure 5.3.: Panels (a) to (d) show the four different types of spreading that may occur depending on the wettability parameter W_s and the maximal surfactant concentration Γ_{max}. The respective bottom left plots show the time dependence of the mean values of the maximal and minimal radii of the colony while the respective top left plots show snapshots of the $h(x,y) = 0.5\,h^\star$ contour line at points in times indicated by square symbols in the bottom left plots. The respective top and bottom right plots show the film height and surfactant distribution, respectively, at the end of the simulation on a domain with $L_x = L_y = 5000$. Without surfactant, the shape of the bacterial colony is circular. At high wettability (c), the colony expands over the substrate with a stable circular front. At low wettability (d), the spreading of the colony is arrested. If the colony produces a significant amount of surfactant Γ_{max}, spreading is promoted by Marangoni fluxes and the circular front becomes unstable. At high wettability (a), the front continuously advances but is modulated. At low wettability (b), the colony forms pronounced fingers which expand over the substrate while the troughs stay arrested. (cf. [TJT18])

strate in more detail. Figure 5.4 shows a 3D top-view of the height profile of a colony with pronounced fingers at $t = 10^7 \tau$ which is colour-coded with the respective surfactant concentration. Due to the limiting film height $\tilde{h}^\star$ in the biomass growth term, the centre of the colony is relatively flat. In agreement with the experimental observation [FPB+12], the height profile has a rim at the edges of the colony that is particularly pronounced at the tips of the fingers. The surfactant concentration allows us to understand the development of expanding fingers in the colony shape. In the troughs close to the centre of the colony, the surfactant concentration is overall high. In this region, the gradients in Γ are small, resulting in only small Marangoni fluxes that are not sufficient to overcome the arrested spreading behaviour. In contrast, at the tips of the fingers, gradients in Γ and thus Marangoni fluxes are strong and drive the tips further outwards. If the diffusion of the surfactant is not too strong, this gradient in surfactant concentration is maintained during the spreading and the fingers can continuously expand over the substrate [TJT18].

Note again that in experiments, the presence of surfactants is expected to give rise to Marangoni flows but also to increase wettability. Therefore, a real surfactant producing strain has a higher surfactant concentration Γ_{max} *and* a higher wettability W_{s} than a bacterial strain deficient in surfactant production.
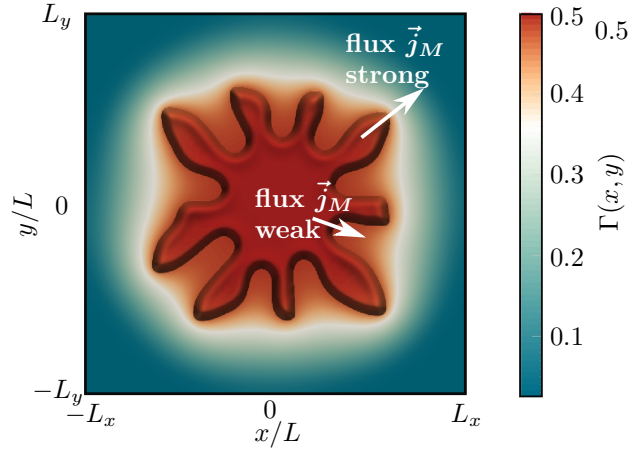
Figure 5.4.: Details of the colony spreading with pronounced fingers for $W_{\mathrm{s}} = 0.1$ and $\Gamma_{\mathrm{max}} = 0.5$. The height profile $h(x,y)$ at $t = 10^7 \tau$ is shown as a top-view on a domain with $L_x = L_y = 5000$ and colour-coded with the respective surfactant concentration $\Gamma(x,y)$. The gradient in surface tension and thus the Marangoni flux $\vec{j}_M$ is strong at the tips of the fingers, driving them further outwards. In the troughs, the surfactant concentration Γ is overall high which results in weak Marangoni fluxes that do not suffice to overcome the arrested spreading. (cf. [TJT18])

To obtain a more complete picture of the front instability, we briefly investigate the influence of the remaining dimensionless parameters and test the robustness of the observed phenomena. A simulation with parameters $W_{\mathrm{s}} = 0.05$, $\Gamma_{\mathrm{max}} = 0.5$, $\tilde{g} = 10^{-5}$, $\tilde{p} = 10^{-6}$, $\tilde{h}^\star = 20$ and $\tilde{D} = 0.01$ is used as a reference and each parameter is individually varied. Fig. 5.5 shows time simulations which are initiated with a quarter of a small bacterial colony with surfactant concentration Γ_{max} on a domain $\Omega = [0, 5000] \times [0, 5000]$ discretised on an equidistant mesh of $N_x \times N_y = 256 \times 256$ grid points.

A larger biomass production rate $\tilde{g}$ reduces the formation of fingers (see Fig. 5.5 (a)). This can be attributed to a decrease of the relative importance of Marangoni flows versus the tendency of the biomass to expand via growth, provided the wettability of the substrate is favourable for expansion. A similar type of argument holds when increasing the max-

(a) biomass production (b) colony height (c) diffusivity (d) surfactant production
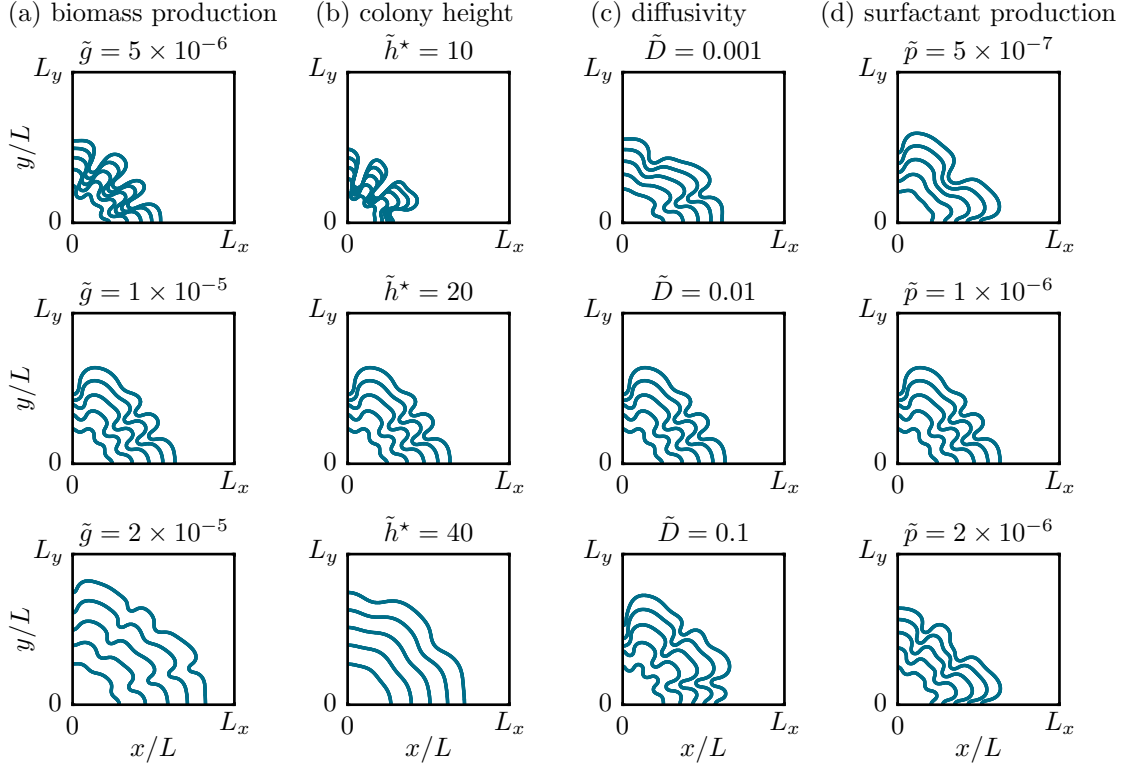
Figure 5.5.: Influence of the parameters $\tilde{g}$, $\tilde{h}^\star$, $\tilde{D}$ and $\tilde{p}$ on the morphology of bacterial colonies expanding via the surfactant-driven spreading mechanism. The contour line $h(x,y) = 0.5h^\star$ is shown at equidistant points in time with $\Delta t/\tau = 10^6$. In each run, one parameter is varied as compared to a reference parameter set (middle row) with $W_s = 0.05$, $\Gamma_{\max} = 0.5$, $\tilde{g} = 10^{-5}$, $\tilde{p} = 10^{-6}$, $\tilde{h}^\star = 20$ and $\tilde{D} = 0.01$ on a domain with $L_x = L_y = 5000$. (cf. [TJT18])

imal film height h^* which also weakens the instability (see Fig. 5.5 (b)). The flux that drives the colony spreading is composed of different contributions, which either favour a round colony expansion like the film flow and the biomass growth or trigger the instability, like the Marangoni flux. These flux contributions have a different, film height-dependent mobility such that a change in film height can affect the respective time scales and thus the trade-off between the different fluxes. A change of the surfactant diffusion $\tilde{D}$ or the production rate $\tilde{p}$ does not drastically change the morphology of the colonies (see Fig. 5.5 (b) and (c), respectively).[1]

5.4. Spreading of Planar Fronts

The time simulations for the growth of bacterial colonies in a circular geometry have identified the wettability parameter W_s and the amount of surfactant $\Gamma_{\max}$ as two key parameters which influence the spreading speed and morphology. To gain a deeper understanding of the system and the spreading dynamics , we next investigate planar fronts. In this geometry, a transformation into the co-moving frame that moves with the same velocity as the front is possible, which greatly facilitates the analysis.

5.4.1. Front Velocity and Shape

For planar fronts, it is possible to perform a more systematic analysis of the system employing parameter continuation. This technique allows for a direct observation of the

influence of W_s and Γ_max on the spreading of the colony. To that end, the evolution equations (5.3)-(5.4) are transformed into the co-moving coordinate system with a constant velocity v. This transformation yields

$$\partial_t h = \nabla \cdot [Q_{hh}\nabla[\partial_h f_\mathrm{w} - \gamma \Delta h] + Q_{h\Gamma}\nabla(\partial_\Gamma f_\mathrm{s})] + G(h) + v\partial_x h$$
$$= \mathscr{F}_1(\nabla, v)[h, \Gamma] \tag{5.9}$$

$$\partial_t \Gamma = \nabla \cdot [Q_{\Gamma h}\nabla[\partial_h f_\mathrm{w} - \gamma \Delta h] + Q_{\Gamma\Gamma}\nabla(\partial_\Gamma f_\mathrm{s})] + P(h, \Gamma) + v\partial_x \Gamma$$
$$= \mathscr{F}_2(\nabla, v)[h, \Gamma], \tag{5.10}$$

where we introduced $\mathscr{F}_{1,2}(\nabla, v)$ as a short hand notation for the nonlinear operators defined by the right-hand sides of the evolution equations (5.9)-(5.10). Planar fronts $(h_0(x), \Gamma_0(x))$ which only depend on one spatial coordinate x and move with a constant profile and velocity v in the resting coordinate frame now correspond to stationary solutions

$$\partial_t h_0(x) = \mathscr{F}_1(\nabla, v)[h_0(x), \Gamma_0(x)] = 0 \tag{5.11}$$
$$\partial_t \Gamma_0(x) = \mathscr{F}_2(\nabla, v)[h_0(x), \Gamma_0(x)] = 0. \tag{5.12}$$

in the co-moving frame. In the parameter continuation analysis, we fix the surfactant concentration far away from the colony to a small but finite value.
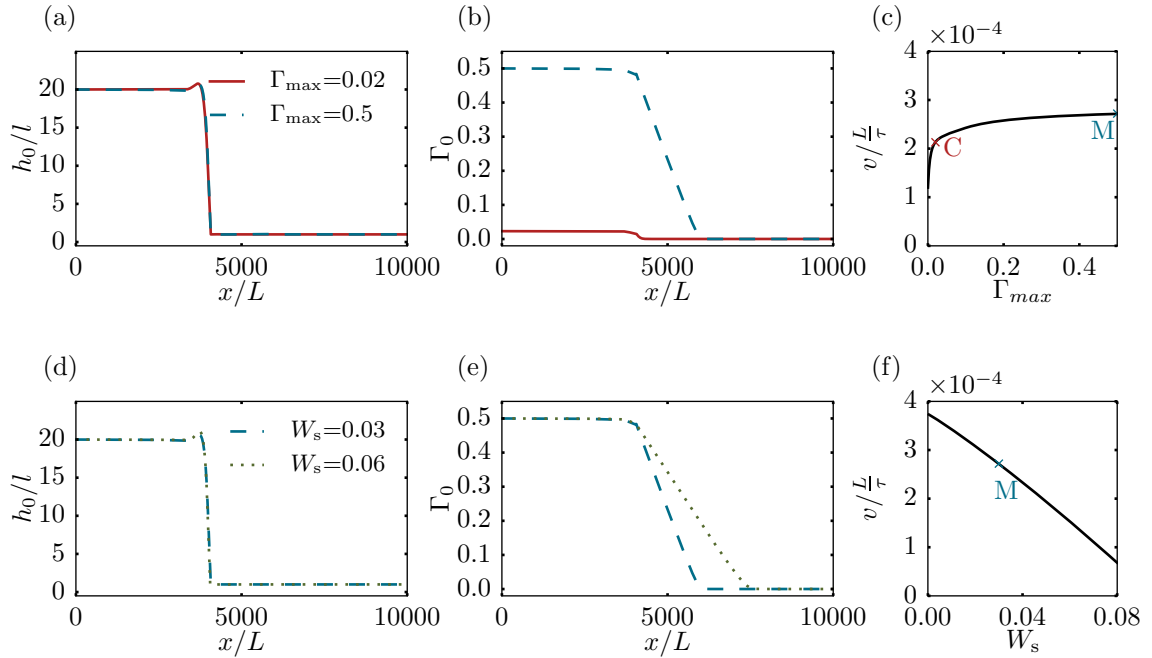
Figure 5.6.: Front profiles and velocity in the surfactant-driven spreading of planar bacterial colonies. (a) and (b) show the front profiles of film height h and surfactant concentration Γ for a parameter combination corresponding to the circular colony spreading at low surfactant concentration (type C for $W_\mathrm{s} = 0.03$, $\Gamma_\mathrm{max} = 0.02$) and spreading with a modulated morphology at higher surfactant concentration (type M for $W_\mathrm{s} = 0.03$, $\Gamma_\mathrm{max} = 0.5$). (d) and (e) show the influence of the wettability on the front profiles. The front velocity v strongly depends on the maximal surfactant amount Γ_max (c) as well as on the wettability parameter W_s (f). (cf. [TJT18])

Figure 5.6 shows the influence of the maximal surfactant concentration Γ_max (top row) and the wettability parameter W_s (bottom row) on the front profile and its velocity. For

the studied parameter combinations, the height profile of the front shows a typical capillary rim. Behind the spreading front, film height and surfactant concentration reach their respective saturation values $h^\star$ and $\Gamma_{\max}$. The surfactant diffuses in front of the moving colony, resulting in a linear decay. As discussed more generally in [WJ01], this is a typical profile for a moving source of surfactant.

Figures 5.6 (a) and (b) show the front profiles $(h_0(x), \Gamma_0(x))$ for the parameter combinations corresponding to modulated (M) and circular (C) spreading in the radial geometry (Fig 5.3) which differ in the parameter value of $\Gamma_{\max}$. Although the height profile h does not show strong differences, the velocity of the front (see Fig. 5.6 (c)) is strongly affected by the maximal surfactant concentration $\Gamma_{\max}$. For a bacterial colony with very small $\Gamma_{\max}$, corresponding e.g. to a mutant strain deficient in surfactant production, the front velocity is roughly a factor of two smaller than in a colony with $\Gamma_{\max} = 0.5$. This indicates that the Marangoni effect indeed strongly contributes to the outward flux driving the expansion of the colony. Figures 5.6 (d)-(f) show the influence of the wettability parameter W_{s} on the front profile and its velocity. In analogy to the transition from continuous to arrested spreading observed in biofilms without Marangoni flows discussed in Sec. 3.4, the colony expansion slows for low wettability (large W_{s}).

For completeness, we also briefly investigate the effect of the remaining parameters $\tilde{g}$, $\tilde{h}^\star$, $\tilde{D}$ and $\tilde{p}$ on the front profile and the spreading velocity. The analysis presented in Fig. 5.7 shows that the velocity is strongly influenced by the biomass production rate $\tilde{g}$ and the colony height $\tilde{h}^\star$. In contrast, a variation of the surfactant diffusivity $\tilde{D}$ and the production rate $\tilde{p}$ only have a small effect on the velocity.

The time simulations for radial geometry discussed in Sec. 5.3 demonstrate that the presence of surfactant not only affects the spreading velocity of the colonies, but also influences its morphology. We focus on this aspect in the next section.[1]

5.4.2. Transversal Linear Stability Analysis

Now, we study the influence of surfactant production on the morphology of bacterial colonies by performing a transversal linear stability analysis. We employ the ansatz

$$h(x, y, t) = h_0(x) + \epsilon h_1(x) \exp(ik_y y + \sigma t) \tag{5.13}$$
$$\Gamma(x, y, t) = \Gamma_0(x) + \epsilon \Gamma_1(x) \exp(ik_y y + \sigma t) \tag{5.14}$$

with $\epsilon \ll 1$ for film height and surfactant profile. This ansatz corresponds to fronts consisting of a y-invariant base state given by the stationary fronts $(h_0(x), \Gamma_0(x))$ plus a small perturbation with x-dependence $(h_1(x), \Gamma_1(x))$ which is modulated in the y-direction with a wavenumber k_y and grows or decays exponentially in time with the rate σ. Inserting this ansatz into the evolution equations (5.9)-(5.10) results to $O(\epsilon)$ in the linear problem

$$\sigma h_1(x) = \mathscr{F}'_{1h}|_{h_0(x),\Gamma_0(x)} h_1(x) + \mathscr{F}'_{1\Gamma}|_{h_0(x),\Gamma_0(x)} \Gamma_1(x) \tag{5.15}$$
$$\sigma \Gamma_1(x) = \mathscr{F}'_{2h}|_{h_0(x),\Gamma_0(x)} h_1(x) + \mathscr{F}'_{2\Gamma}|_{h_0(x),\Gamma_0(x)} \Gamma_1(x), \tag{5.16}$$

for the eigenvalues σ and the eigenfunctions $(h_1(x), \Gamma_1(x))$. $\mathscr{F}'_{i,h}$ and $\mathscr{F}'_{i,\Gamma}$ are operators denoting the Fréchet-derivatives of the non-linear operator $\mathscr{F}_i$ with respect to h and Γ, respectively. The linear stability of the front $(h_0(x), \Gamma_0(x))$ can now be determined from the largest eigenvalue σ. It indicates if the perturbation grows (for $\mathrm{Re}(\sigma) > 0$) or decays (for $\mathrm{Re}(\sigma) < 0$) in time. We again employ continuation techniques to solve the linear eigenvalue problem (5.15)-(5.16). To that end, the set of equations for the stationary front profiles $h_0(x)$ and $\Gamma_0(x)$ analysed in Sec. 5.4.1 is supplemented by a set of equations
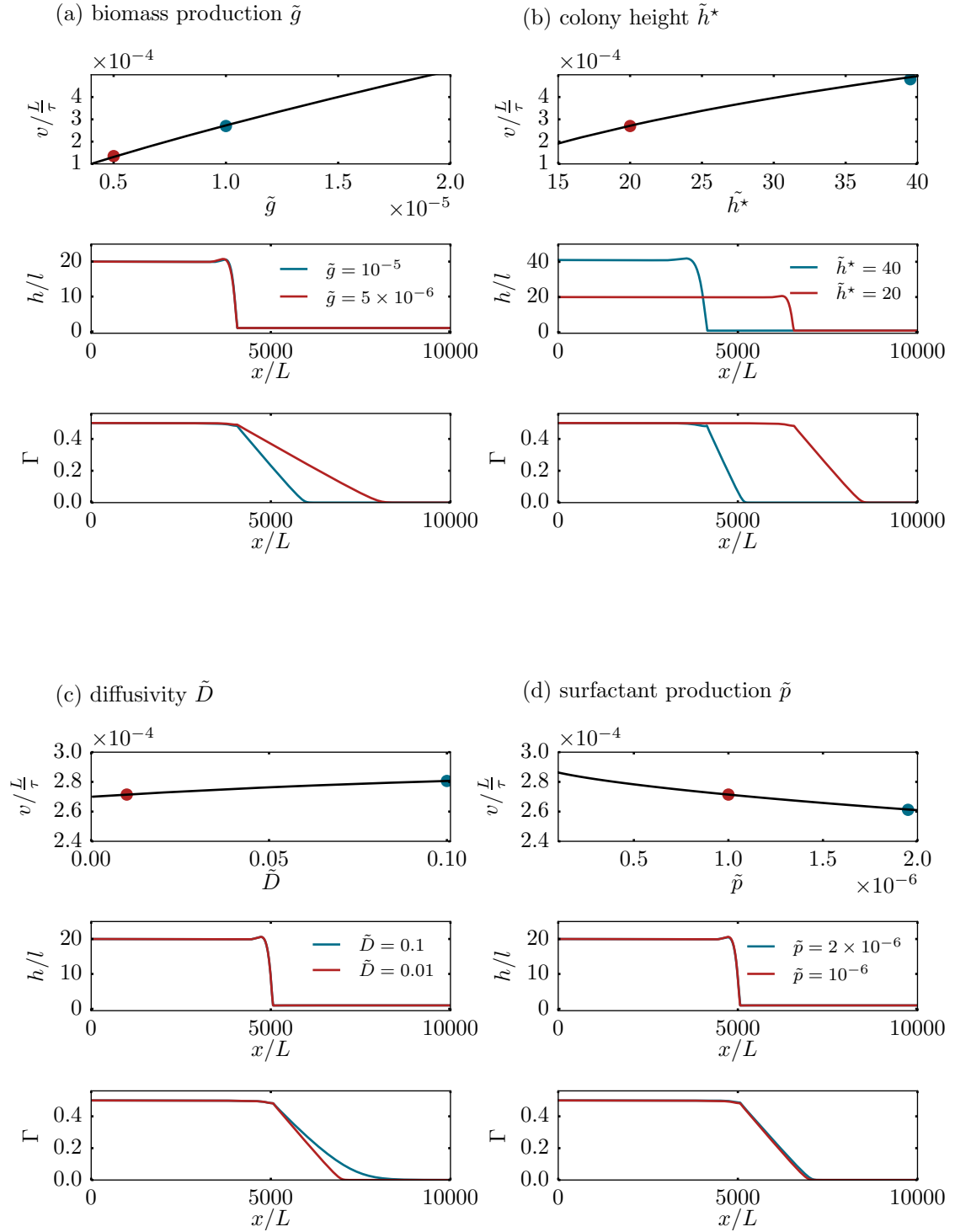
Figure 5.7.: Effect of the parameters $\tilde{g}$, $\tilde{h}^\star$, $\tilde{D}$ and $\tilde{p}$ on the profile and velocity of planar fronts. A simulation with the parameters $W_s = 0.03$, $\Gamma_{max} = 0.5$, $\tilde{g} = 10^{-5}$, $\tilde{p} = 10^{-6}$, $\tilde{h}^\star = 20$ and $\tilde{D} = 0.01$ is used as a reference and each parameter is varied individually. The front velocity is shown in the top row. For two parameter values marked by red and blue circles in the velocity plot, the corresponding height and surfactant profiles are shown in the middle and bottom row.
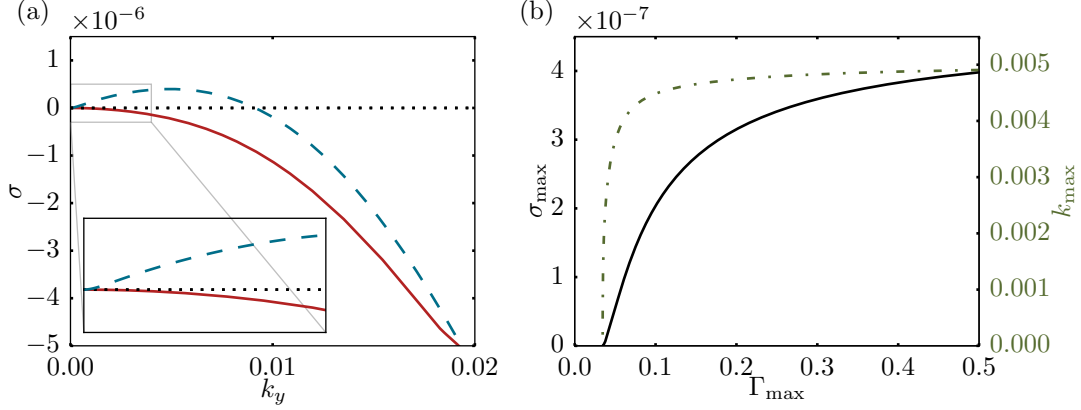
Figure 5.8.: Eigenvalues obtained by the transversal linear stability analysis for planar fronts with $W_s = 0.03$. The dispersion relation shown in (a) monotonically decreases for $\Gamma_{max} = 0.02$ (red) but has a maximum $\sigma_{max} > 0$ for $\Gamma_{max} = 0.5$ (blue) indicating a front that is unstable with respect to transversal perturbations. Following the maximum of the dispersion relation in dependence of Γ_{max} shown in (b) as black solid line reveals that for $W_s = 0.03$, the largest eigenvalues σ_{max} is positive for $\Gamma_{max} > 0.0268$ and the front profile is thus unstable in this parameter regime. The dot-dashed green line gives the wavenumber k_{max} corresponding to the maximum of the dispersion relation. (cf. [TJT18])

for the eigenfunctions. These are assumed to fulfill the same boundary conditions as the base state. The transversal wave number k_y and eigenvalue σ are treated as parameters in a pseudo-arclength continuation. This approach is presented in tutorial form in Ref. [Thi15b] and outlined for this particular model in appendix A.5.

We again analyse the front profiles for two parameter sets that differ in the maximum of the surfactant concentration Γ_{max} and correspond to the modulated (M) and circular (C) spreading mode in the radial geometry (Fig. 5.3). Recall that the respective base states $(h_0(x), \Gamma_0(x))$ are displayed in Fig. 5.6. To analyse the transversal stability of these fronts, we determine the corresponding dispersion relations $\sigma(k_y)$. For the parameter set (C) with a low surfactant concentration $\Gamma_{max} = 0.02$, the dispersion relation decays monotonically (red solid line in Fig. 5.8 (a)). The largest eigenvalue is $\sigma_{max} = 0$ at $k_y = 0$ and the front is thus transversally stable. The eigenfunction $(h_1(x), \Gamma_1(x))$ corresponding to the largest eigenvalue (red solid lines in Fig. 5.9) is the neutrally stable (Goldstone) mode representing the translational symmetry of the equations. As expected, it is identical to the spatial derivative of the front profiles (data not shown) [TJT18].

For the other parameter set (M) corresponding to the situation that a significant amount of surfactant $\Gamma_{max} = 0.5$ is produced by the bacteria, the dispersion relation is shown in Fig. 5.8 (a) with blue dashed lines. The largest eigenvalue is positive at a finite wavenumber ($\sigma_{max} = 3.98 \times 10^{-7}$ at $k_y = 4.89 \times 10^{-3}$) and the front is thus transversally unstable.[5] These values are consistent with linear results extracted from the fully nonlinear time simulation in a planar geometry (data not shown). The eigenfunctions corresponding to the largest eigenvalue (blue dashed lines in Fig. 5.9) are strongly localised in the front region. To determine at which surfactant concentration the transition from transversally stable to unstable fronts takes place, we follow the maximum of the dispersion relation

---

[5]For comparison, the value of the eigenvalue $\sigma(k_y = 0)$ at zero wavenumber ranges from $10^{-14}..10^{-12}$ in the continuation runs which can be used as an estimate for the error.

(a)

(b)
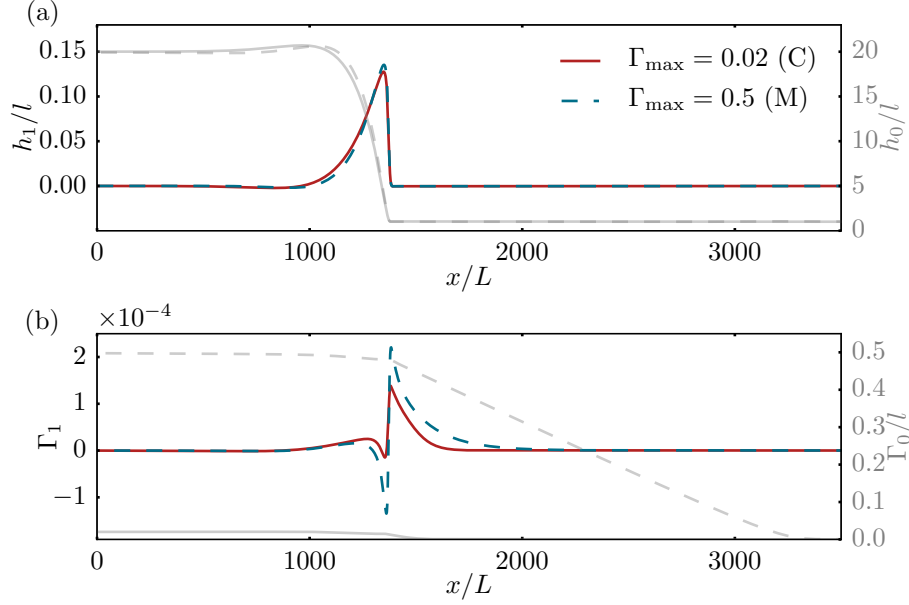
Figure 5.9.: Eigenfunctions obtained by the transversal linear stability analysis for planar two-dimensional fronts with $W_s = 0.03$. The eigenfunctions corresponding to the transversal wave number k_y with the largest eigenvalue $\sigma_{\max}$ are shown in (a) for the height profile and in (b) for the surfactant concentration with red solid lines for $\Gamma_{\max} = 0.02$ and blue dashed lines for $\Gamma_{\max} = 0.5$, respectively. The corresponding base states that have already been presented in Fig. 5.6 are given with grey lines for comparison. (cf. [TJT18])

$\sigma_{\max}$ while varying $\Gamma_{\max}$ (Fig. 5.8 (b)). We find that $\sigma_{\max}$ is positive and the front profile thus transversally unstable for $\Gamma_{\max} > 0.0268$ if the wettability parameter is $W_s = 0.03$. The transversal linear stability analysis thus confirms the observation made in the time simulations: If a significant amount of surfactant is being produced by the bacteria, the colony spreads with a transversally unstable front profile and modulations of the contact line occur which (at least initially) grow in time [TJT18].

The front profiles in our model for the spreading of bacterial colonies exhibit some of the main characteristics of fronts occurring in models for the surfactant-driven spreading of passive thin liquid films: For instance, we find a capillary rim near the edge of the front and a linear decay of the surfactant concentration in front of the drop. However, as already discussed in Sec. 4.4.2, we do not observe the typical thinned region in front of the advancing colony which is often assumed to be the cause for the front instability occurring in the surfactant-driven spreading of passive drops on horizontal substrates [MC09]. Instead, the analysis of our model for surfactant-driven colony spreading shows similarity to a surfactant-covered drop sliding down an inclined substrate [EMC04, EMC05, GN15]. In this set-up, the spreading of the drop is – in addition to the Marangoni fluxes – driven by gravity, that acts as a body force on the liquid. In our model, the driving is realised by the non-conserved production of biomass. The fingering instability and the eigenfunctions of the unstable mode observed in our model strongly resemble the transversal perturbations found for sliding drops in a constant-flux configuration in [EMC05] which are also located at the front edge rather than in the region ahead of it.[1]

5.4.3. Morphological Phase Diagram

The analysis of planar fronts is completed by a comparison of the results from the transversal linear stability analysis with time simulations for planar fronts. The simulations are performed on a domain $\Omega = [0, L_x] \times [0, L_y]$ with $L_x = 3000$ and $L_y = 6000$ discretised on an equidistant $N_x \times N_y = 256 \times 512$ mesh with the same integration method and boundary conditions as applied in Sec. 5.3. The initial condition consists of a planar front given by the corresponding stationary front profile $(h_0(x), \Gamma_0(x))$ plus small random noise for each parameter set. The end time of the simulation is $T_{\mathrm{end}} = 10^7 \tau$. For initially planar fronts, we find three different spreading regimes as shown in Fig. 5.10: Moving planar fronts (red triangles), moving modulated fronts (blue squares) for which the transversal perturbations grow in time and arrested planar fronts, which do not advance (grey dots) [TJT18]. A helpful measure to distinguish these spreading modes is the height profile integrated in the direction of front movement $I_y = \int \tilde{h}(\tilde{x}, \tilde{y}) \mathrm{d}\tilde{y}$ that is shown in Fig. 5.10 (d), (b) and (e) at equidistant points in time for the three types of spreading, respectively. Concerning the influence of wettability and surfactant production on the spreading of the colony, we obvserve the same tendencies as in the circular geometry studied in Sec. 5.3: At low surfactant concentrations, the front spreads with a circular colony shape for a small contact angle (low W_s) but its expansion is arrested for high wettability parameters W_s. An increased surfactant concentration leads to transversal instabilities resulting in a modulated front.

These findings are now compared to the predictions obtained from the transversal linear stability analysis. We identify the region in which the ansatz (5.13)-(5.14) of moving fronts (stationary h and Γ in the co-moving frame) is valid. The breakdown of the ansatz of stationary fronts manifests itself in a positive eigenvalue for $k_y = 0$, corresponding to an unstable profile. In the grey region to the right of the dashed line in Fig. 5.10, we do not expect stationary moving fronts. This is in accordance with the arrested spreading observed in time simulations for these parameter values. Note that in this situation, the height evolves towards a stationary profile but the produced surfactant still spreads outwards. The arrested growth mode does therefore not correspond to a stationary front with $v = 0$ for both fields h and Γ.

The strength of the transversal instability of the moving fronts is in the transversal linear stability analysis predicted by the magnitude of largest eigenvalue $\sigma_{\max}$. To the left of the dotted line in Fig. 5.10, the eigenvalue is larger than $\sigma_{\max} = 10^{-8}$ and the modulation of the front is expected to be observable within our simulation time $T_{\mathrm{end}}/\tau = 5 \cdot 10^6 .. 10^7$. This is in good agreement with the time simulations.

Interestingly, the formation of pronounced fingers cannot be observed for time simulations initiated with planar fronts that are only slightly perturbed. In general, the transversal instability appears to be much weaker than in the radial geometry. This observation can be explained by a dilution effect of the surfactant: In the radial geometry, the produced surfactant is diluted more strongly when it spreads outwards from the colony as compared to the planar front. In consequence, the surfactant profile decays faster with the distance to the front. This results in stronger gradients in surfactant concentration and larger Marangoni flows driving the transversal instability. To test if the fingering mode still exists in the planar geometry, we perform time simulations with an initial condition consisting of a planar front with a finite-size perturbation in the form of a small finger as shown in Fig. 5.10 (c). The time simulations demonstrate that, indeed, the arrested spreading mode can for this front shape be overcome for large surfactant concentrations (grey dots with yellow circles in Fig. 5.10): The initial finger continuously grows while the rest of the front stays behind. In conclusion, the instability and especially the formation of fingers are generically occurring in the planar and the radial geometry, however, the onset and strength critically
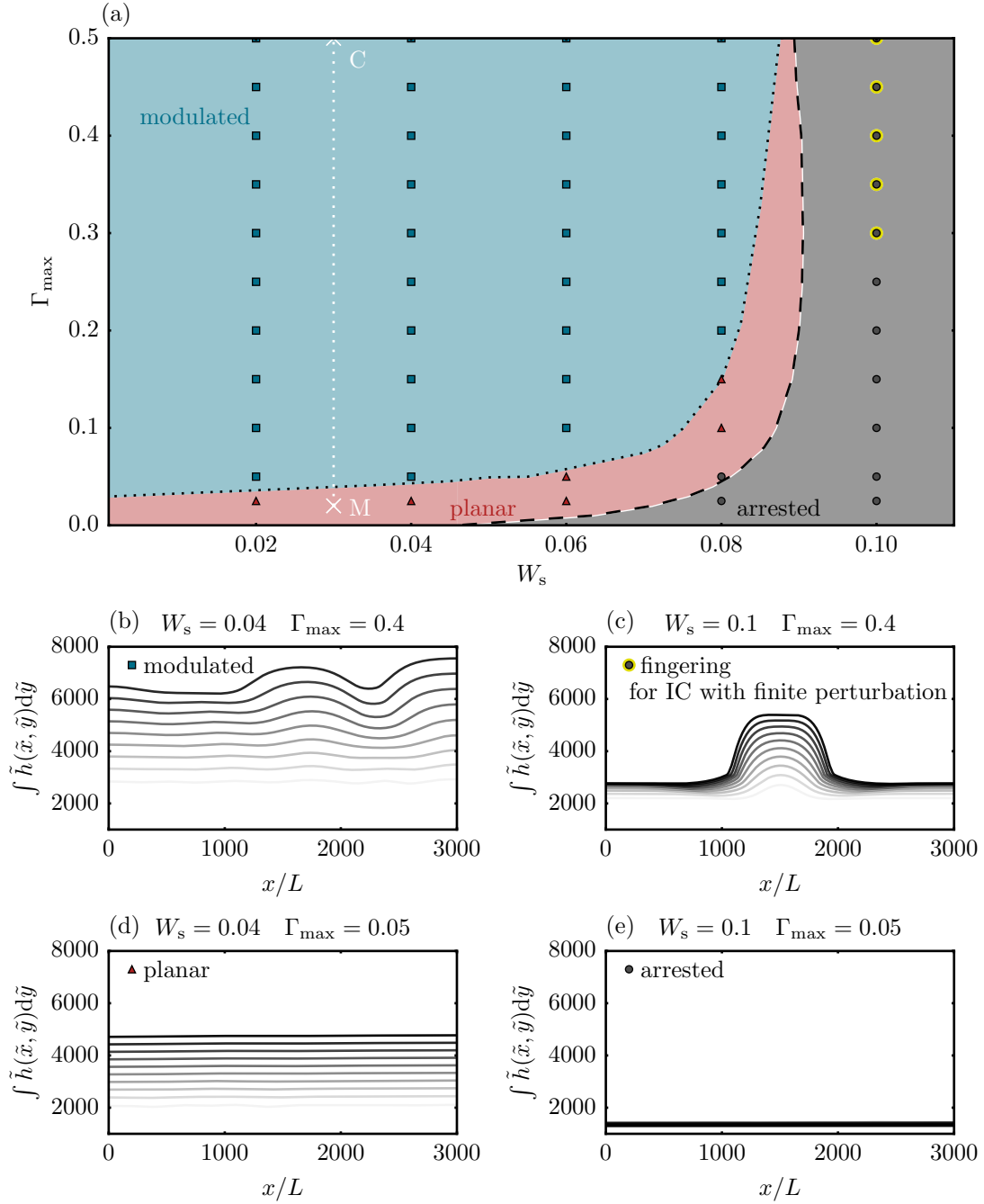
Figure 5.10.: (a) Morphological phase diagram for the spreading of two-dimensional planar fronts. To the left (right) of the black dashed line, the fronts of the height profile h are moving (not moving). The linear stability analysis predicts modulated moving fronts to the left of the black dotted line (the largest eigenvalue σ_{max} is $> 10^{-8}$). In numerical time simulations initiated with a noisy planar front, three types of spreading occur: transversally stable planar fronts (red triangles), modulated fronts (blue squares) and arrested fronts which can not expand over the substrate (grey dots). The grey dots with yellow circles mark parameter sets for which a finite perturbation in the initial condition leads to the growth of a pronounced finger. The white dotted line in (a) corresponds to the continuation run from parameter set (M) to parameter set (C) presented in Fig. 5.8 (b). (cf. [TJT18]) (b)-(e) Profiles of the respective integrated height profile I_y at equidistant times with $\Delta t/\tau = 5 \times 10^5$.

depend on the colony shape [TJT18]. When comparing the shape of the modulated planar fronts in the bioactive model (see Fig. 5.10 (b)) to the front instability observed in the passive system (see Fig. 4.8), one finds that the instability is much more ramified in the latter case. This can be explained by the expansion of the biomass via growth which broadens the structures and results in a colonisation of the substrate between existing protrusions, provided the wettability of the substrate is favourable for expansion.[1]

5.5. Preventing Growth by Counter-Gradients of Surfactant

After analysing the model mathematically in the previous sections, we now illustrate the consequences of the surfactant-driven spreading mechanism with an example. One strategy that has been proposed to prevent the spreading of bacterial colonies are counter-gradients of surfactants. As discussed in Sec. 5.1, experiments for *P. aeruginosa* [FPB+12] show that, indeed, the expansion of a colony can be arrested by exogeneously adding biosurfactant to the agar substrate in a circular pattern around the colony with a concentration comparable to the *in vivo* one. This effect can also occur when two surfactant-producing colonies approach each other [CSO05].
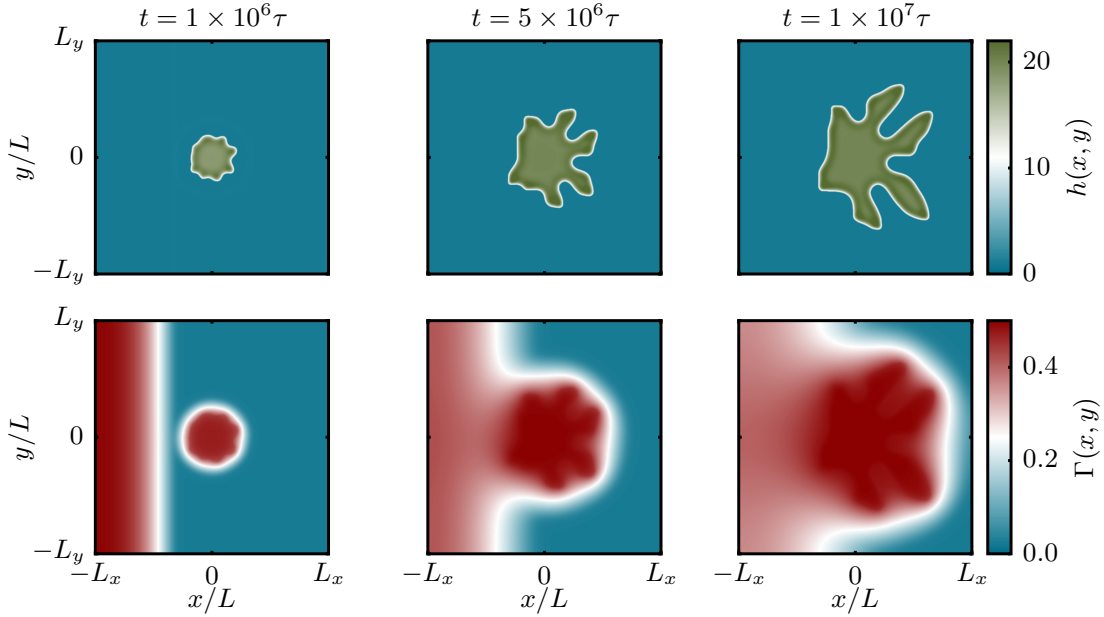
Figure 5.11.: Counter-gradients of surfactant represent a possible strategy to inhibit colony expansion. A small bacterial colony is initiated in the centre of the simulation domain (upper row). Initially, additional surfactant is deposited on the left border of the domain (lower row). The counter-gradient of external surfactant influences the spreading dynamics and prevents fingering towards the left side of the domain . The top row shows the colony height h at different points in time, the bottom row shows the respective surfactant concentration Γ. Parameters are $W_\mathrm{s} = 0.1$ and $\Gamma_\mathrm{max} = 0.5$. (cf. [TJT18])

To exemplarily test counter-gradients of surfactants as a strategy for the prevention of colony expansion in our model, we perform a time simulation with $W_\mathrm{s} = 0.1$ and $\Gamma_\mathrm{max} = 0.5$ that is shown in Fig. 5.11. The initial condition is given by a surfactant-laden colony at the centre of the simulation domain and additional surfactant to the left of the colony. We observe that the growth of the colony towards the left hand side slows down as soon as

the colony 'senses' the additional surfactant and eventually its growth is arrested. At the other side, the colony performs the finger-like growth expected in this parameter regime [TJT18].

In other experimental set-ups however, the growth prevention by counter-gradients of surfactants is counteracted by the favouring of wettability due to the presence of surfactants – an effect which is not directly included in our model. Indeed, experiments on *B. subtilis* [LMB$^+$06] show that the expansion of an only weakly surfactant producing 'target strain' can be promoted by the presence of a nearby surfactant-producing 'helper' colony that improves the wettability. Similar experiments for *P. aeruginosa* [DRvDX14] show that the spreading dynamics also depends on the initial distance between the two colonies. If the promoting effect of the increased wettability or the preventing effect due to a counter-gradient in surface tension dominates the spreading behaviour thus seems to depend on the experimental set-up and the bacterial strain.[1]

6. Towards a Model for Thin Liquid Films with Active Motion

The active motion of individual bacteria does not play a decisive role in colonies which expand via the discussed osmotically or surfactant-driven spreading mechanism. It is, however, important for other modes of colony growth such as collective swarming. In this chapter, we take a first step towards the incorporation of random individual and coherent collective bacterial motility into our thin-film description. The resulting model couples the dynamics of the film height profile with the dynamics of a height-averaged polarisation field. In the future, models of this type may provide an advance in the understanding of the interplay of biologically controlled physico-chemical processes (such as osmosis and Marangoni flows) and the active motion of bacteria. The developed model is of a generic nature and describes a droplet of active fluid or gel and could, e.g., also represent an actomyosin solution - a system often used as cytoskeleton model.

In the following, we first give an overview over related approaches existing in the literature on the modelling of active media before proposing our model. It is then briefly analysed for a one-dimensional geometry to get a first impression of the features of the model. The results presented in this chapter are, however, not meant to be a rigorous derivation or an exhaustive analysis. In contrast, they represent a phenomenologically derived suggestion for a class of simple models that could prove a useful starting point for future investigation and development.

6.1. Features and Continuum Description of Active Fluids

Active fluids are a class of soft materials that typically consist of or contain a large number of self-propelled active particles. Bacterial suspensions are one example for a living active fluid. The individual bacteria act as *self-driven particles* that swim in a direction determined by their driving engine, the cell geometry and possible external forces. Another example for a living active fluid is the cytoskeleton of cells [JR10, KJJ+05]. In this system, *active stresses* are induced into a network of actin filaments by motor molecules which align or slide filaments w.r.t. each other. There are also various examples of non-living active matter (for a review, see [MJR+13]), such as, e.g., so-called Janus particles – artifical microswimmers which have two different sides with different physical or chemical properties.

Often, active fluids consist of rod-shaped particles which at high densities show a tendency to orientational order. In many situations, such as in bacterial suspensions, the constituent particles of the active fluid possess a head-tail asymmetry. They can cooperatively order either in a polar phase (particles are on average aligned in the same direction and with the same sense of direction) or in a nematic phase (particles are on average oriented parallel but with random orientation or are head-tail symmetric). The polar order can be described by the *polarisation* – a vectorial order parameter that measures the locally averaged orientation of the particles.

Active fluids show an important conceptual difference from passive systems: Energy coming from the constituent particles is constantly dissipated into the surroundings. In bacterial suspensions for example, every bacterium consumes energy by nutrient uptake and

dissipates it through its self-propulsion. In consequence, active fluids are – in contrast to passive fluids – even in a stationary state typically far away from thermodynamic equilibrium. The energy input is local and occurs at the particle level rather than, e.g., at the system boundaries as in classical hydrodynamic systems. These properties of active matter clearly distinguish it from the passive case. In consequence, interesting novel effects may occur: Large-scale vortex structures [SWS⁺10, SNS⁺12], bacterial turbulence [DCC⁺04, WDH⁺12], dynamical clustering [PSJ⁺12, BBK⁺13, ZBFS10] and motility-induced phase separation [SLVC⁺12] are some examples of intriguing new phenomena observed in experiments.

In a coarse-grained approach, active particles in a fluid can be described by a small number of macroscopic fields, such as the particle density and a macroscopic polarisation $\mathbf{p}$ that is usually defined as the local average over the "microscopic polarisation" of the individual particles. The time evolution of these fields is then prescribed by a set of continuum equations. An important class of coarse grained models for active materials is based on liquid crystal hydrodynamics [Cha92, Pro95]. The passive theory is supplemented with a new feature that introduces activity into the models: The particles are endowed with self-generated *active stresses* that enter the hydrodynamic evolution equations. These stresses can be extensile or contractile and depend on the specific features and geometry of the particles. The respective equations can either be written phenomenologically based on symmetry arguments [HRRS04] or be derived from microscopic interactions [BM09, LM06]. In the context of the cytoskeleton of living cells, a description as a visco-elastic gel driven out of equilibrium [KJJ⁺05, JKPJ07, JP09, PJJ15] was developed and applied successfully to study, e.g, the presence of defect structures [KJJ⁺04], the transition to spontaneous flow [TCM11], concentration banding [GML08], multi-component [JJKP07] or compressible [VJP06] active polar films. Similar phase-field models have been employed to study the cytoskeleton on surfaces [ZSA12] and the collective motion of cells [LZA15]. A detailed review of the modelling of active media can, e.g., be found in [MJR⁺13, Men15, Ram10].

Often, active fluids are found in spatial confinement, such as suspensions of bacteria in porous media, or in an adaptive geometry, such as the cytoskeleton of cells enclosed by the cell membrane. Droplets of active liquid have a free surface. In this system, intriguing novel features such as spontaneous symmetry breaking [SK14], self-organisation of defect-structures [SNS⁺12], large-scale flows [WWD⁺13, PSD⁺12], or even self-sustained motility of active droplets [SCD⁺12] can be observed experimentally. Therefore, this geometry poses an interesting problem for mathematical modelling.

In previous theoretical studies of two- and three-dimensional active drops entirely immersed in a passive fluid, activity has been found to lead to spontaneous symmetry breaking, accompanied by deformation and self-propulsion of the droplets [TMC12, WMVH14, MWP15, WH16] similar to drops of simple liquid driven by chemical reactions [VRR96]. The problem of active drops on flat solid surfaces has only been scarcely addressed in the literature. In a recent numerical study of a drop of polar active liquid, motile steady states with biologically relevant shapes have been observed [TTMC15]. However, three-dimensional simulations of active droplets are computationally expensive. This problem can be circumvented by applying a thin-film approximation to reduce the dimensions of the model. For passive nematic systems, a thin-film description has been derived [BC01, LCA⁺13] and used to study droplet spreading [LKTC13]. A similar approach has been employed for active polar fluids to study free-surface films [SR09] and the effect of a highly symmetric polarisation field on spreading laws and stationary shapes of droplets [JR12]. The self-propulsion of active drops has been associated with topologi-
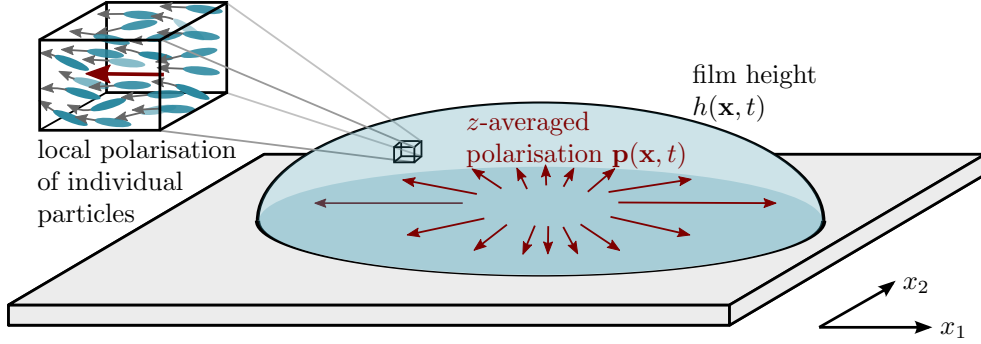
Figure 6.1.: Generic model for a droplet consisting of an active polar fluid. The polarisation field $\mathbf{p}(\mathbf{x}, t)$) (red arrows) represents the local height-averaged value of the polarisation of the individual particles (grey arrows in the inset). Its dynamics is coupled to the dynamics of the film height $h(\mathbf{x}, t)$. The total local polarisation is given by $\mathbf{P}(\mathbf{x}, t) = h(\mathbf{x}, t)\,\mathbf{p}(\mathbf{x}, t)$.

cal defects in the polarisation field [KA15]. However, often these models do not include a dynamical evolution equation for the polarisation but instead prescribe a polarisation pattern. Recently, a thin-film theory for an active liquid crystal has been derived based on the Beris-Edwards theory that uses a tensorial order parameter (instead of a polarisation field) [KMW17]. However, it does not result in a closed form of evolution equations.

Here, we follow a different approach and construct a phenomenological model for a self-propelled polar fluid. It is based on a gradient dynamics on the free energy functional valid for the passive system that is supplemented by active terms. Unlike previous modelling approaches, we explicitly account for wettability. This allows for a study of the interplay between passive effects like capillarity and surface tension and activity introduced by active stresses and self-propulsion.

6.2. Mathematical Modelling

In the following section, we propose a generic model which couples a polarisation field to an evolution equation for the height profile of the active droplet. The polarisation represents the locally averaged orientation of the constituent particles.

6.2.1. General Framework and Structure

We consider a film or droplet of height $h(x_1, x_2)$ consisting of an active polar fluid, e.g. motile bacteria, as sketched in Fig. 6.1. The polarisation vector $\mathbf{p}$ is introduced as the height-averaged value of the local microscopic z-dependent polarisation of the individual particles. By assuming ad hoc that the third component is small as compared to the other two, it can be written as

$$\mathbf{p} = \begin{pmatrix} p_1(x_1, x_2) \\ p_2(x_1, x_2) \end{pmatrix}. \tag{6.1}$$

As the polarisation reflects the orientational order of the microscopic particles, it may occur spontaneously and is also influenced by the surface profile. In contrast to the film thickness, the total polarisation is thus not a conserved quantity.

Although we study an *active* polar fluid, we again base our model on a free energy functional. This guarantees that in the absence of activity, the model describes a well-defined

equilibrium state. We introduce the free energy functional

$$\mathcal{F}_{\text{pld}}[h, \mathbf{p}] = \mathcal{F}_{\text{cap}} + \mathcal{F}_{\text{wet}} + \mathcal{F}_{\text{spo}} + \mathcal{F}_{\text{el}} + \mathcal{F}_{\text{coupl}} \tag{6.2}$$

for a drop of polar liquid. It accounts for various effects that possibly influence the dynamics, namely capillarity, wettability, spontaneous polarisation, an elastic energy of the polarisation and a coupling between the polarisation vector and the shape of the free surface of the drop. The specific choices of the energetic contributions are discussed below. To write evolution equations for the film height and the polarisation, one has to notice that – similar to the description of suspensions – the free energy functional needs to be expressed in variables that can be varied independently. Therefore, we introduce the local total amount of polarisation $\mathbf{P} = h\mathbf{p}$ and transform the free energy functional via

$$F_{\text{pld}}[h, \mathbf{P}] = \mathcal{F}_{\text{pld}}[h, \mathbf{p}(h, \mathbf{P})] \,. \tag{6.3}$$

By constructing a gradient dynamics based on this energy functional, we can describe the dynamics of a *passive* polar fluid close to but out of equilibrium.

Activity is introduced into the model by assuming that the polarisation causes an active stress in the drop. This stress can be described by the tensor $\underline{\boldsymbol{\sigma}}^{\text{a}}$ [Ram10] with the components

$$\sigma_{kj}^{\text{a}} = -c_{\text{a}} p_k p_j \,. \tag{6.4}$$

It forces the system out of equilibrium and can thus not be derived from the free energy functional. Instead, it is introduced into the evolution equations as a non-variational term. The active stress is extensile for $c_{\text{a}} > 0$ (describing, e.g., bacterial suspensions) and contractile for $c_{\text{a}} < 0$ (describing, e.g., actomyosin solutions).

As a second active contribution to our model, we assume that the self-propulsion of the particles in the direction of $\mathbf{p}$ causes an active flux of the form

$$\boldsymbol{\alpha} = 3\frac{\alpha_0 \eta}{h^2}\mathbf{p} = 3\frac{\alpha_0 \eta}{h^3}\mathbf{P} = \sum_k \alpha_k \mathbf{e}_k \tag{6.5}$$

where α_0 is a constant and η denotes the viscosity. This second active ingredient of the model breaks the $\mathbf{P} \to -\mathbf{P}$ symmetry for $\alpha_0 \neq 0$.

The general form of the evolution equations [1] for h and $\mathbf{P}$ is then given by

$$\partial_t h = \sum_k \partial_{x_k} \left\{ Q_{hh}\left[\partial_{x_k}\frac{\delta F_{\text{pld}}}{\delta h} - \alpha_k + \sum_j \partial_{x_j}\sigma_{kj}^{\text{a}}\right] + \sum_j Q_{hP_j}\partial_{x_k}\frac{\delta F_{\text{pld}}}{\delta P_j} \right\} \tag{6.6}$$

$$\partial_t P_i = \sum_k \partial_{x_k} \left\{ Q_{hP_i}\left[\partial_{x_k}\frac{\delta F_{\text{pld}}}{\delta h} - \alpha_k + \sum_j \partial_{x_j}\sigma_{kj}^{\text{a}}\right] + \sum_j Q_{P_iP_j}\partial_{x_k}\frac{\delta F_{\text{pld}}}{\delta P_j} \right\} - Q_{\text{NC}}\frac{\delta F_{\text{pld}}}{\delta P_i} \,. \tag{6.7}$$

The film-height equation is a conserved dynamics while the polarisation equation combines a conserved and a non-conserved dynamics. The former represents the transport of

---

[1] In this section, we use the following notations for the vector operations in cartesian coordinates (here given for a scalar h, a vector $\mathbf{a} = \sum_i a_i \mathbf{e}_i$ and a tensor $\underline{\mathbf{A}} = \sum_{ij} A_{ij}\mathbf{e}_i\mathbf{e}_j$ with the components A_{ij}):

scalar product between vectors: $\mathbf{a} \cdot \mathbf{b} = \sum_i a_i b_i$
product between tensor and vector: $\underline{\mathbf{A}} \cdot \mathbf{a} = \sum_{ij} A_{ij}a_j\mathbf{e}_i$
gradient of a scalar: $\nabla h = \sum_i \partial_{x_i}h\,\mathbf{e}_i$
gradient of a vector: $(\nabla \mathbf{a})_{ij} = \partial_{x_j}a_i$
derivative of a scalar w.r.t. a vector: $\frac{\partial g}{\partial \mathbf{a}} = \sum_i \frac{\partial g}{\partial a_i}\mathbf{e}_i$

Laplace operator: $\Delta h = \sum_i \partial_{x_i x_i}h$
divergence of a vector: $\nabla \cdot \mathbf{a} = \sum_i \partial_{x_i}a_i$
divergence of a tensor: $\nabla \cdot \underline{\mathbf{A}} = \sum_{ij} \partial_{x_j}A_{ij}\mathbf{e}_i$
double inner product: $\underline{\mathbf{A}} : \underline{\mathbf{B}} = \sum_{ij} A_{ij}B_{ij}$
outer product between vectors: $(\mathbf{ab})_{ij} = a_i b_j$

polarisation with the flow while the latter describes reorientation, e.g., due to spontaneous polarisation. Q_{NC} is the corresponding mobility. Activity is introduced by the active stress $\boldsymbol{\sigma}^{\mathrm{a}}$ and the self-propulsion $\boldsymbol{\alpha}$ both in the conserved part. The mobilities are given by

$$
\begin{aligned}
Q_{hh} &= \frac{h^3}{3\eta} \\
Q_{hP_i} &= \frac{h^2 P_i}{3\eta} = h^3 \frac{p_i}{3\eta} \\
Q_{P_i P_j} &= h\left(\frac{P_i P_j}{3\eta} + M\delta_{ij}\right) = \frac{h^3 p_i p_j}{3\eta} + hM\delta_{ij}
\end{aligned}
\tag{6.8}
$$

where δ_{ij} denotes the Kronecker symbol. They correspond to scalar, vector and tensor quantities, respectively, and can be understood in analogy to Ref. [XTQ15].
After introducing the convective flux $\mathbf{j}^{\mathrm{C}}$, the diffusive fluxes $\mathbf{j}^{DP_i}$ and the reactive flux $\mathbf{j}^{\mathrm{R}}$ as

$$
\begin{aligned}
\mathbf{j}^{\mathrm{C}} &= -\frac{h^3}{3\eta}\left[\nabla\frac{\delta F_{\mathrm{pld}}}{\delta h} + \sum_j p_j \nabla\frac{\delta F_{\mathrm{pld}}}{\delta P_j}\right] - \frac{h^3}{3\eta}\nabla\cdot\boldsymbol{\sigma}^{\mathrm{a}} + \alpha_0 \mathbf{P} \tag{6.9} \\
\mathbf{j}^{DP_i} &= -hM\nabla\frac{\delta F_{\mathrm{pld}}}{\delta P_i} \tag{6.10} \\
j_i^{\mathrm{R}} &= -Q_{\mathrm{NC}}\frac{\delta F_{\mathrm{pld}}}{\delta P_i}, \tag{6.11}
\end{aligned}
$$

respectively, the equations of motion can be expressed in the compact form

$$
\begin{aligned}
\partial_t h &= -\nabla\cdot\mathbf{j}^{\mathrm{C}} \tag{6.12} \\
\partial_t P_i = \partial_t(hp_i) &= -\nabla\cdot\left[p_i\mathbf{j}^{\mathrm{C}} + \mathbf{j}^{DP_i}\right] + j_i^{\mathrm{R}}. \tag{6.13}
\end{aligned}
$$

6.2.2. Specific Choices for the Energetic Contributions

Now, we specify the energetic contributions to the free energy functional (6.2) that determine the dynamics of the active droplet. We use

$$
\begin{aligned}
\mathcal{F}_{\mathrm{pld}}[h, \mathbf{p}] &= \mathcal{F}_{\mathrm{cap}} + \mathcal{F}_{\mathrm{wet}} + \mathcal{F}_{\mathrm{spo}} + \mathcal{F}_{\mathrm{el}} + \mathcal{F}_{\mathrm{coupl}} \tag{6.14} \\
&= \int\left[\gamma\left(1 + \tfrac{1}{2}(\nabla h)^2\right) + f_{\mathrm{w}}(h, \mathbf{p}^2) + hf_{\mathrm{spo}}\left(\mathbf{p}^2\right) + hf_{\mathrm{el}}(h, \mathbf{p}) + f_{\mathrm{coupl}}(h, \mathbf{p})\right]\mathrm{d}\mathbf{x} \tag{6.15}
\end{aligned}
$$

which includes the following effects:

- The first two terms also occur in the description of simple fluids in Sec. 2.1.3 and describe the energetic contributions of capillarity (in the limit of small interface slopes) and wettability, respectively. The interfacial tension is denoted by γ. Note that here, the wettability may also depend on the magnitude $\mathbf{p}^2$ of the local mean polarisation. We employ a wetting energy of the product form

$$
f_{\mathrm{w}}(h, \mathbf{p}^2) = \hat{f}_{\mathrm{w}}(h)(1 + \chi\mathbf{p}^2) = A\left(-\frac{1}{2h^2} + \frac{h_{\mathrm{a}}^3}{5h^5}\right)(1 + \chi\mathbf{p}^2) \tag{6.16}
$$

  with a constant χ that is motivated and specified below. $\hat{f}_{\mathrm{w}}(h)$ is the wetting energy for droplets of partially wetting simple liquids given by Eq. 2.14. Recall that A and h_{a} denote the Hamaker constant and the adsorption layer height, respectively.

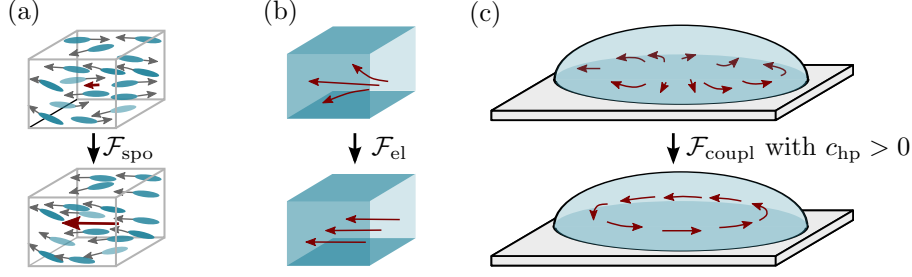## 6. Towards a Model for Thin Liquid Films with Active Motion

Figure 6.2.: Schematic illustration of the effect of the energetic contributions occurring in droplets consisting of polar particles. $\mathcal{F}_{\text{spo}}$ describes a transition between an isotropic, microscopically disordered state with $|\mathbf{p}| \approx 0$ to an ordered state with $|\mathbf{p}| \approx 1$. $\mathcal{F}_{\text{el}}$ is a liquid crystal elastic energy that represents the energetic cost of gradients in the polarisation. $\mathcal{F}_{\text{coupl}}$ couples the polarisation to the gradient of the free interface, so that it is energetically favoured if the polarisation is orthogonal to the interface gradient for $c_{\text{hp}} > 0$. Note again that we assume $\mathbf{p}$ to be always parallel to the substrate.

- The contribution $\mathcal{F}_{\text{spo}}$ accounts for the polarisation energy, describing a transition between an isotropic, microscopically disordered and a polarised state as illustrated in Fig. 6.2 (a). This can be described by the "Mexican hat" energy

$$f_{\text{spo}}(\mathbf{p}^2) = -\frac{c_{\text{sp}}}{2}\mathbf{p} \cdot \mathbf{p} + \frac{c_{\text{sp}}}{4}(\mathbf{p} \cdot \mathbf{p})^2 \tag{6.17}$$

that for $c_{\text{sp}} > 0$ allows for the existence of an unstable disordered ($|\mathbf{p}| = 0$) and an energetically favoured ordered state ($|\mathbf{p}| = 1$). For stability, the constant c_{sp} needs to be chosen positive.

We assume that in the droplet, the polarisation is normally $|\mathbf{p}| \approx 1$ whereas it vanishes in the adsorption layer, i.e., $|\mathbf{p}| \approx 0$. For the polarisation energy $f_{\text{spo}}(\mathbf{p}^2)$ given in Eq. (6.17), this can be achieved by employing a specific form of the wetting energy [2]

$$f_{\text{w}}(h, \mathbf{p}^2) = \hat{f}_{\text{w}}(h)\left(1 + \chi\mathbf{p}^2\right) \quad \text{with} \quad \chi = \frac{h_{\text{a}}}{\hat{f}_{\text{w}}(h_{\text{a}})}c_{\text{sp}}. \tag{6.20}$$

- The contribution $f_{\text{el}}(h, \mathbf{p}) = \frac{c_{\text{p}}}{2}\nabla\mathbf{p} : \nabla\mathbf{p}$ is a two-dimensional liquid crystal elastic energy that represents the energetic cost of gradients in the polarisation as illustrated in Fig. 6.2 (b). Note that for simplicity we assume the same value of stiffness associated with splay and bend deformations, i.e. we use the single elastic constant c_{p} [Pro95].

- The last term $f_{\text{coupl}}(h, \mathbf{p}) = \frac{c_{\text{hp}}}{2}(\mathbf{p} \cdot \nabla h)^2$ couples the polarisation and the gradient of the free surface. c_{hp} is a constant that can be chosen positive (for alignment of

---

[2] Then, the respective contributions in the free energy take the form

$$\mathcal{F}_{\text{pld}}^{\text{a}} = \int \left\{\hat{f}_{\text{w}}(h_{\text{a}}) + h_{\text{a}}\left(\frac{c_{\text{sp}}}{2}\mathbf{p}^2 + \frac{c_{\text{sp}}}{4}(\mathbf{p}^2)^2\right)\right\} d\mathbf{x} \tag{6.18}$$

in the adsorption layer of height $h = h_{\text{a}}$. The fluid does not polarise spontaneously in the adsorption layer, since the only admissible fixed point is $\mathbf{p} = \mathbf{0}$. Far away from the interface in the droplet with $h \gg h_{\text{a}}$ the wetting energy goes to zero, i.e., $f_{\text{w}}(h) \to 0$ and the free energy takes the form

$$\mathcal{F}_{\text{pld}}^{\text{droplet}} = \int \left\{h\left(-\frac{c_{\text{sp}}}{2}\mathbf{p}^2 + \frac{c_{\text{sp}}}{4}(\mathbf{p}^2)^2\right)\right\} d\mathbf{x} \tag{6.19}$$

which admits the additional fixed point $|\mathbf{p}| = 1$ corresponding to spontaneous polarisation.

the polarisation orthogonal to the interface slope ∇h) or negative (for a polarisation parallel to ∇h) as shown in Fig. 6.2 (c). Note that alternatively, coupling terms $\sim \mathbf{p} \cdot \nabla h$ may be applied to energetically favour an outward- or inward-pointing polarisation.

6.2.3. Reduction to a One-Dimensional Geometry

In a one-dimensional geometry under the assumption of vanishing gradients and polarisation in the x_2-direction, the polarisation and all mobilities become scalar quantities and the evolution equations drastically simplify. In the following, we use the notations $x = x_1$, $p = p_1$ and $P = hp_1$. The coupling between the polarisation and the interface slope does not contribute in a one-dimensional geometry (in which the polarisation can not minimise the interaction with the interface by rotating in the substrate plane) and is omitted in the following. The free energy functional F_{pld} given in Eq. (6.14) then reduces to

$$F_{\mathrm{pld}}[h, P] = \int \left[\gamma(1 + \tfrac{1}{2}(\partial_x h)^2) + f_{\mathrm{w}}\left(h, P^2\right) + c_{\mathrm{sp}} h \left[-\tfrac{1}{2}\left(\tfrac{P}{h}\right)^2 + \tfrac{1}{4}\left(\tfrac{P}{h}\right)^4 \right] + \tfrac{c_{\mathrm{p}}}{2} h \left(\partial_x \left(\tfrac{P}{h}\right) \right)^2 \right] \mathrm{d}x$$

after transforming to the total polarisation P. The variations with respect to film height and polarisation are given by

$$\frac{\delta F_{\mathrm{pld}}}{\delta h} = -\gamma \partial_{xx} h + \partial_h f_{\mathrm{w}} - \frac{p}{h} \partial_p f_{\mathrm{w}} + f_{\mathrm{spo}} - p \partial_p f_{\mathrm{spo}} + \frac{c_{\mathrm{p}}}{2}(\partial_x p)^2 + \frac{c_{\mathrm{p}} p}{h} \partial_x (h \partial_x p) \quad (6.21)$$

$$\frac{\delta F_{\mathrm{pld}}}{\delta P} = \frac{1}{h} \partial_p f_{\mathrm{w}} + \partial_p f_{\mathrm{spo}} - \frac{c_{\mathrm{p}}}{h} \partial_x (h \partial_x p) \ . \quad (6.22)$$

The equations of motions in the one-dimensional geometry read

$$\partial_t h = -\partial_x j^{\mathrm{C}} \quad (6.23)$$

$$\partial_t (hp) = -\partial_x \left(p j^{\mathrm{C}} + j^{\mathrm{D}} \right) + j^{\mathrm{R}} \quad (6.24)$$

with the fluxes

$$j^{\mathrm{C}} = -\frac{h^3}{3\eta} \left[\partial_x \frac{\delta F_{\mathrm{pld}}}{\delta h} + p \partial_x \frac{\delta F_{\mathrm{pld}}}{\delta P} \right] - \frac{h^3}{3\eta} c_{\mathrm{a}} \partial_x (p^2) + \alpha_0 hp \quad (6.25)$$

$$j^{\mathrm{D}} = -hM \partial_x \frac{\delta F_{\mathrm{pld}}}{\delta P} \quad (6.26)$$

$$j^{\mathrm{R}} = -Q_{\mathrm{NC}} \frac{\delta F_{\mathrm{pld}}}{\delta P} \ . \quad (6.27)$$

Note that there is no direct contribution of f_{spo} to the convective flux j^{C} as the respective terms cancel out (similar to the mixing energy f_{m} in Eq. (3.14) in the model for passive mixtures and suspensions discussed in Sec. 3.2.1).

6.2.4. Linear Stability Analysis of the Flat Film

Next, we analyse the linear stability of a flat homogeneous one-dimensional film. There are three stationary flat-film solutions of film height h_0 with a constant polarisation P_0. They can be determined from the condition of a vanishing non-conserved flux j^{R}, i.e., $\frac{\delta F_{\mathrm{pld}}}{\delta P} = 0$. The fixed points are shown in Fig. 6.3 (a) and correspond to non-polarised films $(h, P) = (h_0, 0)$ or polarised films

$$(h, P) = (h_0, P_0) = (h_0, \pm B h_0) \quad \text{with} \quad B = \sqrt{1 - \tfrac{10}{3}\left(\tfrac{h_{\mathrm{a}}}{h_0}\right)^3 + \tfrac{4}{3}\left(\tfrac{h_{\mathrm{a}}}{h_0}\right)^6} \ . \quad (6.28)$$
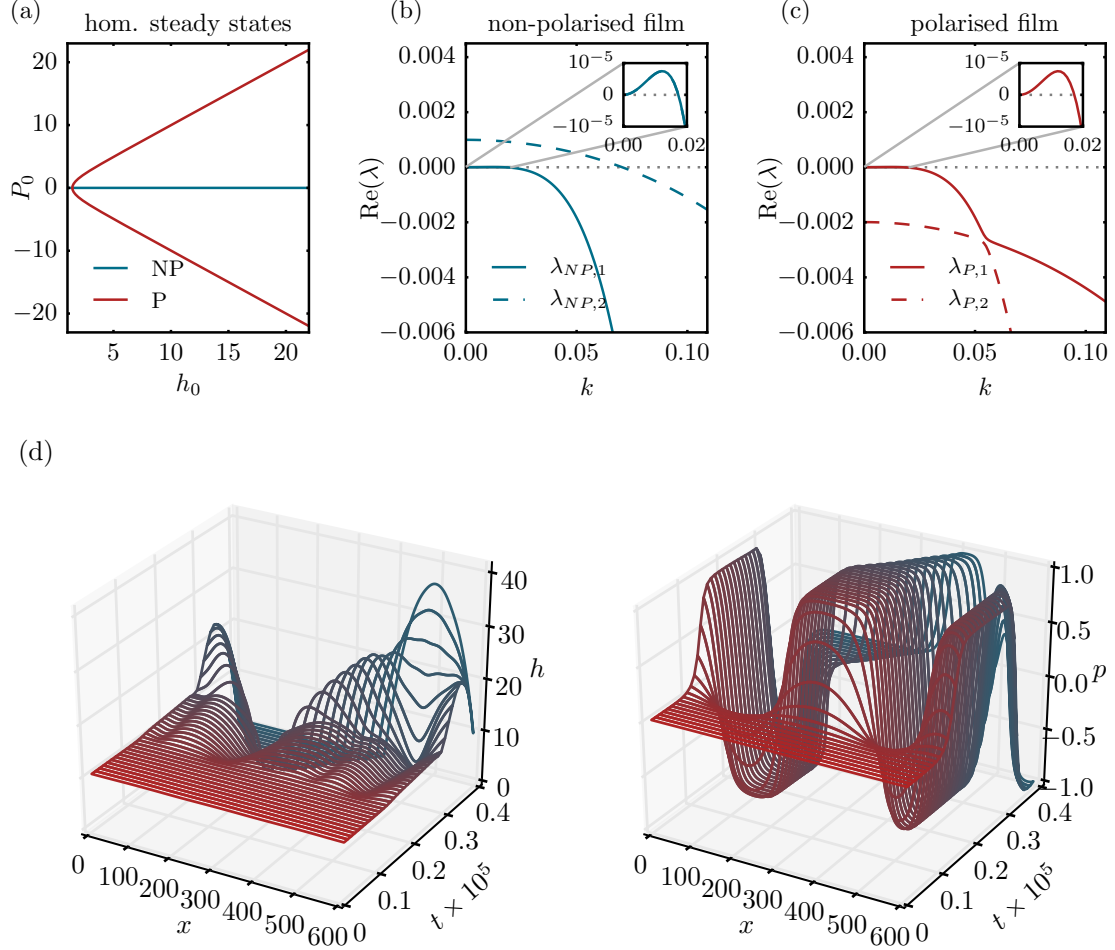
Figure 6.3.: (a) Possible stationary solutions (h_0, P_0) for homogeneous non-polarised ($P_0 = 0$, blue lines) and polarised ($P_0 = Bh_0$, red lines) flat films that can be determined from the condition of a vanishing non-conserved contribution, i.e. $\delta F_{\mathrm{pld}}/\delta P = 0$. (b) and (c) give corresponding dispersion relations for the non-polarised and polarised film of height $h_0 = 10$. Note that the eigenvalues $\lambda_{P,i}$ are complex for the polarised film. (d) Time simulation initialised with a non-polarised flat film plus small noise for periodic boundary conditions. The height profile h (left) and mean polarisation p (right) are shown at equidistant points in time. First, the flat film polarises and domains with positive and negative polarisation are created. Subsequently, the film dewets and droplets (with different orientation of the polarisation) form. These droplets undergo a complex dynamics and coalescence. The remaining parameters are $c_{\mathrm{a}} = 0.01$, $c_{\mathrm{sp}} = 0.01$, $A = 1$, $M = 1$, $h_{\mathrm{a}} = 1$, $\eta = 1$, $\gamma = 1$, $c_{\mathrm{p}} = 2$, $Q_{\mathrm{NC}} = 1$ and $\alpha_0 = 0.001$.

The latter exist for film heights $\frac{h_0}{h_a} > \left(\frac{4}{5-\sqrt{13}}\right)^{1/3} \approx 1.42$ and approach a mean polarisation of $P_0/h_0 \approx \pm 1$ for thick films with $h_0 \gg h_a$.

By inserting the ansatz

$$h(x) = h_0 + \epsilon h_1 e^{ikx+\lambda t} \tag{6.29}$$

$$P(x) = P_0 + \epsilon P_1 e^{ikx+\lambda t} \tag{6.30}$$

with $\epsilon \ll 1$ into the evolution equations (6.23)-(6.24) and solving the resulting eigenvalue problem, we determine the linear stability of the flat homogeneous film.

For the *non-polarised flat film* with $(h, P) = (h_0, 0)$, we find the eigenvalues

$$\lambda_{\text{NP},1} = -\frac{h_0^3 \gamma}{3\eta} k^4 + \left[1 - 2\left(\frac{h_a}{h_0}\right)^3\right] \frac{A}{\eta h_0} k^2$$

$$= -\frac{h_0^3 \gamma}{3\eta} k^2 [k^2 - k_c^2] \quad \text{with} \quad k_c^2 = \left[1 - 2\left(\frac{h_a}{h_0}\right)^3\right] \frac{3A}{h_0^3 \gamma}$$

$$\lambda_{\text{NP},2} = -M c_p k^4 - \frac{1}{h_0}\left[Q_{\text{NC}} c_p - M h_0 c_{\text{sp}} B^2\right] k^2 + Q_{\text{NC}} \frac{c_{\text{sp}}}{h_0} B^2 .$$

These are shown in Fig. 6.3 (b) and can easily be interpreted because the effects of film height and polarisation decouple: The eigenvalue $\lambda_{NP,1}$ represents the dispersion relation of a simple thin-film equation [Thi07]. It exhibits a long-wave instability (with onset at $k = 0$ and an unstable band of wavenumbers $0 \leq k \leq k_c$ with fastest growing mode at $k = k_c/\sqrt{2}$) and the film tends to dewet [Mit93]. The eigenvalue $\lambda_{NP,2}$ captures the influence of the polarisation. The spontaneous polarisation destabilises the non-polarised state of the film. Due to the elastic energetic cost of gradients in the polarisation, the instability has the largest growth rate at $k = 0$. For $c_p = 0$, the eigenvalue $\lambda_{NP,2}$ diverges for large wavenumbers k so that the elastic energy is a crucial ingredient to provide a cut-off of small scale instabilities and thus obtain stable solutions in the model.

The eigenvalues of the *polarised flat film* with $(h, P) = (h_0, Bh_0)$ shown in Fig. 6.3 (c) can also be obtained analytically, however, in the form of rather lengthy expressions (not shown). In the limit of thick films, i.e., $(h_a/h_0)^3 \ll 1$, they reduce to

$$\lambda_{P,1} = -\frac{\gamma h_0^3}{3\eta} k^4 + \frac{A}{\eta h_0} k^2 - i\alpha_0 k$$

$$\lambda_{P,2} = -c_p M k^4 - 2\left(M c_{\text{sp}} + \frac{Q_{\text{NC}}}{h_0} c_p\right) k^2 - i\alpha_0 k - \frac{Q_{\text{NC}}}{h_0} 2 c_{\text{sp}} .$$

Both eigenvalues are now complex for $\alpha_0 \neq 0$. The thin-film instability is still present in $\lambda_{P,1}$, but the polarisation has now a stabilising effect in $\lambda_{P,2}$.

Figure 6.3 (d) shows the time evolution of a non-polarised flat film. The simulation is performed employing the finite element scheme outlined in appendix Sec. A.1.1 with periodic boundary conditions for an initially constant film height $h = 10$ and vanishing polarisation $p = 0$ with additional small random noise. It illustrates the consequences of the two unstable eigenvalues $\lambda_{NP,1}$ and $\lambda_{NP,2}$: First, the flat film polarises and domains with positive and negative polarisation form. Subsequently, the film dewets, leading to the formation of droplets with different orientation of the polarisation. These droplets undergo a complex dynamics and coalescence until only one (large) droplets persists. In the following section, we turn our attention to such droplets and study the effect of activity on their shape and dynamics.

6.3. Resting and Moving Active Droplets

For droplets consisting of active polar particles, self-propulsion of the particles and active stresses modify the fluxes within the droplet as compared to droplets consisting of passive liquids. In consequence, the coupling between the film height profile and the polarisation field can be expected to give rise to a modified spreading dynamics and even droplets that actively self-propel over a substrate. To get a first impression of the solutions of the model introduced in the previous section, we perform numerical time simulations for drops on one-dimensional substrates. First, we focus on the case where the activity is solely induced by self-propulsion and no active stress is present, i.e. $c_\mathrm{a} = 0$. The simulations are initiated with a parabolic droplet (with a contact angle corresponding to the passive equilibrium value) and a small random polarisation within the droplet. [3] Interestingly, the model exhibits multistability and possesses solutions that correspond to resting and moving active droplets for the same parameter values.

Figure 6.4 shows three qualitatively different types of active droplets that occur in the model. The most intuitive case is presented in Fig. 6.4 (a). In an initial self-polarisation stage starting from the contact lines regions, the polarisation within the droplet increases. It reaches a rather uniform plateau with $p = 1$. In the contact line region, the polarisation decreases to $|p| \approx 0$ smoothed by the elastic energy $\mathcal{F}_\mathrm{el}$ that penalises strong gradients in p. Subsequently, the self-propulsion of the particles results in a movement of the droplet over the substrate. The shape of the droplet is nearly unchanged as compared to the passive droplet. Ultimately, the drop moves with constant shape and velocity.
If, however, the polarisation does not evolve towards a uniform value within the droplet during the initial self-polarisation stage, stationary active droplets may occur. Figure 6.4 (b) shows such an evolution where the developing polarisation is positive in the left, and negative in the right hand side of the droplet. In this case, the self-propulsion of the left and right half of the drop counteract each other by pointing inwards. The droplet is slightly contracted, resulting in a slightly steeper contact angle. The polarisation profile is anti-symmetric (and the integral $\int ph\,\mathrm{d}x$ vanishes) so that there is no 'net' total self-propulsion and the droplet remains stationary. Figure 6.4 (c) shows an analogue resting droplet with the difference that now, the polarisation and thus the self-propulsion points outwards, so that the contact angle of the droplet is slightly lowered. Note that the states in (b) and (c) are not related by symmetry.

As the moving droplet is propelled over the substrate with a constant shape and velocity, we can employ the method of parameter continuation to efficiently study the effect of parameter changes on this solution type. To that end, we transform the evolution equations (6.23)-(6.24) into the co-moving coordinate system with a constant velocity v.
The dependence of the droplet velocity and shape on various parameters of the model is presented in Fig. 6.5. The first row shows the influence of (a) the self-propulsion speed α_0, (b) the active stress c_a, (c) the wetting energy A and (d) the elastic polarisation energy

---

[3] The initial condition is given by

$$h(x) = \max\left(h_0 - a(x - \tfrac{L_x}{2})^2, 1\right) \quad \text{with} \quad h_0 = 50 \quad \text{and} \quad a = \tfrac{3}{20}\tfrac{A}{h_0 - 1.} \tag{6.31}$$

$$P(x) = 0.01\,\mathrm{rand}(N_x)\,\tfrac{h(x)-1}{h_0}\,\mathrm{Sym}(x) \tag{6.32}$$

where $\mathrm{rand}(N_x)$ corresponds to a 1D array filled with random float numbers from the half-open interval [0.0,1.0). The function $\mathrm{Sym}(x)$ introduces a slight asymmetry into the initial condition and is chosen as $\mathrm{Sym}(x) = 1$ for the simulation shown in Fig. 6.4 (a), as $\mathrm{Sym}(x) = \sin(2\pi\tfrac{x}{L_x})$ for the simulation shown in (b) and as $\mathrm{Sym}(x) = -\sin(2\pi\tfrac{x}{L_x})$ for the simulation shown in (c).
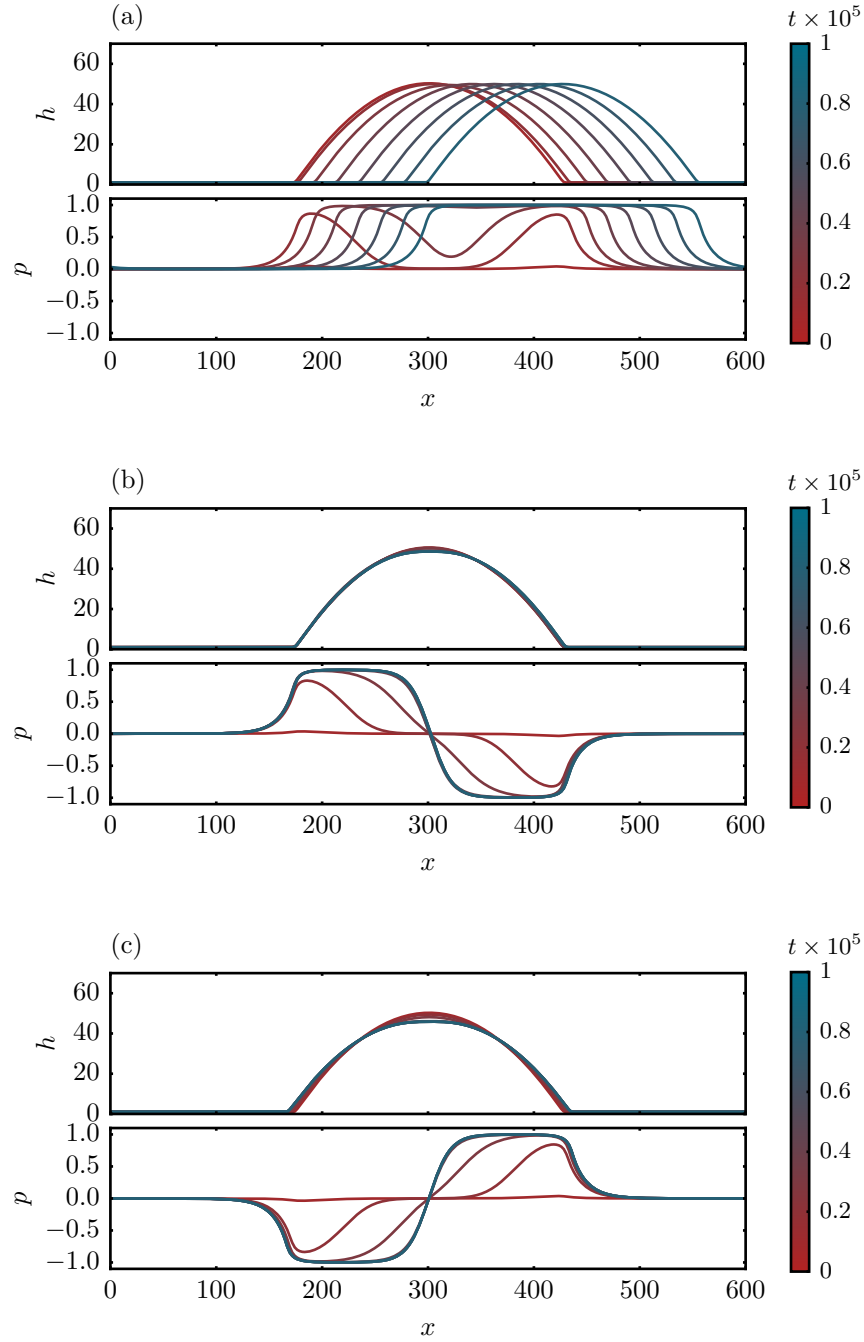
Figure 6.4.: Moving (a) and resting (b,c) active droplets occurring for the same set of parameters. The height profile h (top) and the mean polarisation p (bottom) are shown at equidistant points in time for three different simulations initiated with slightly different polarisation patterns within the droplet. If the polarisation profile is symmetric after a self-polarisation stage, the droplet moves over the substrate (a). If it is anti-symmetric and the integral over the polarisation thus vanishes, the droplets are resting (b-c). Parameters are: $c_{\mathrm{a}} = 0$, $c_{\mathrm{sp}} = 0.01$, $A = 1$, $M = 1$, $h_{\mathrm{a}} = 1$, $\eta = 1$, $\gamma = 1$, $c_{\mathrm{p}} = 2$, $Q_{\mathrm{NC}} = 1$ and $\alpha_0 = 0.002$

c_p on the velocity. The profiles of height h and polarisation p for two specific parameter combinations (given by red and blue dots) are presented in the second and third row.

The velocity of the drop is roughly proportional to the self-propulsion speed α_0 (see Fig. 6.5 (a)). Note that the height and polarisation profiles do not depend on this parameter and the droplets have a nearly parabolic shape even at high velocities.

The velocity is moderately influenced by the strength of the active stress $c_\mathrm{a} > 0$ (see Fig. 6.5 (b)). If the stress is contractile ($c_\mathrm{a} < 0$), the droplet is contracted, the contact angle is larger and the velocity decreases. For an extensile stress ($c_\mathrm{a} > 0$), the droplet widens and its velocity is enhanced.

Interestingly, the Hamaker constant A which is connected to the wettability, does nearly not influence the velocity (see Fig. 6.5 (c)). In particular, we do not observe a transition between resting and moving droplets when the wettability is modified as found in the models for osmotically or surfactant-driven spreading of bacterial colonies discussed in the previous sections. For a non-vanishing self-propulsion ($\alpha_0 \neq 0$), the droplets are always moving. A possible explanation for this is that – in contrast to the model for bacterial colonies – the motility of the drop is not accompanied by a shape deformation that might be energetically unfavourable in terms of capillarity and wetting. Instead, the motile active droplets maintain their parabolic shape.

The constant c_p that is connected to the elastic energy of gradients in the polarisation also only slightly affects the velocity of the droplet, but determines the width of the transition zone from $|p| \approx 0$ in the adsorption layer to $|p| \approx 1$ in the droplet (see Fig. 6.5 (d)).

The presented analysis can only give a glimpse onto the behaviour of the model and further development and investigation are necessary to evaluate its applicability. The exemplary numerical simulations have shown that it possesses moving and resting droplet solutions for the same set of parameters. These need to be further characterised and carefully compared to the equilibrium droplets of the passive system. It is to be expected that the resting solutions are unstable with respect to finite perturbations. It remains a subject of future research to determine the localisation and strength of the perturbation needed to trigger a propulsion of the droplet.

In addition, the dynamics of active fluids can be dramatically different when the polarisation field is fully two-dimensional or when it is allowed to move out of plane [TCM11]. Therefore, an analysis of the model in two dimensions should be performed. In this geometry, the existence of a splay-induced motility in the presence of active stress but without self-propulsion as observed in [TMC12, WMVH14, MWP15, WH16] could be tested. Another interesting question that could be addressed with this model is how the presence of a macroscopic polarisation affects the dewetting dynamics of thin films. In addition, the model is suitable to study activity-induced splitting of droplets on the one hand and coalescence of active droplets on the other hand.

To summarise, we have in this chapter presented a phenomenologically derived model for thin active polar films that explicitly includes wettability. Due to the reduced complexity in the thin-film description, it may serve as a computationally less expensive alternative to models applied in the literature for the study of active drops on substrates. For one spatial dimension, first numerical simulations have shown the occurrence of reasonable dynamical states. However, future investigation and an analysis in two dimensions are necessary to further characterise the model and its solutions. After further testing and validation, the suggested class of models could represent a useful alternative to existing models for active droplets on substrates and could for example also be coupled to the osmotically and surfactant-driven spreading mechanisms of bacterial colonies discussed in the previous chapters of this thesis.
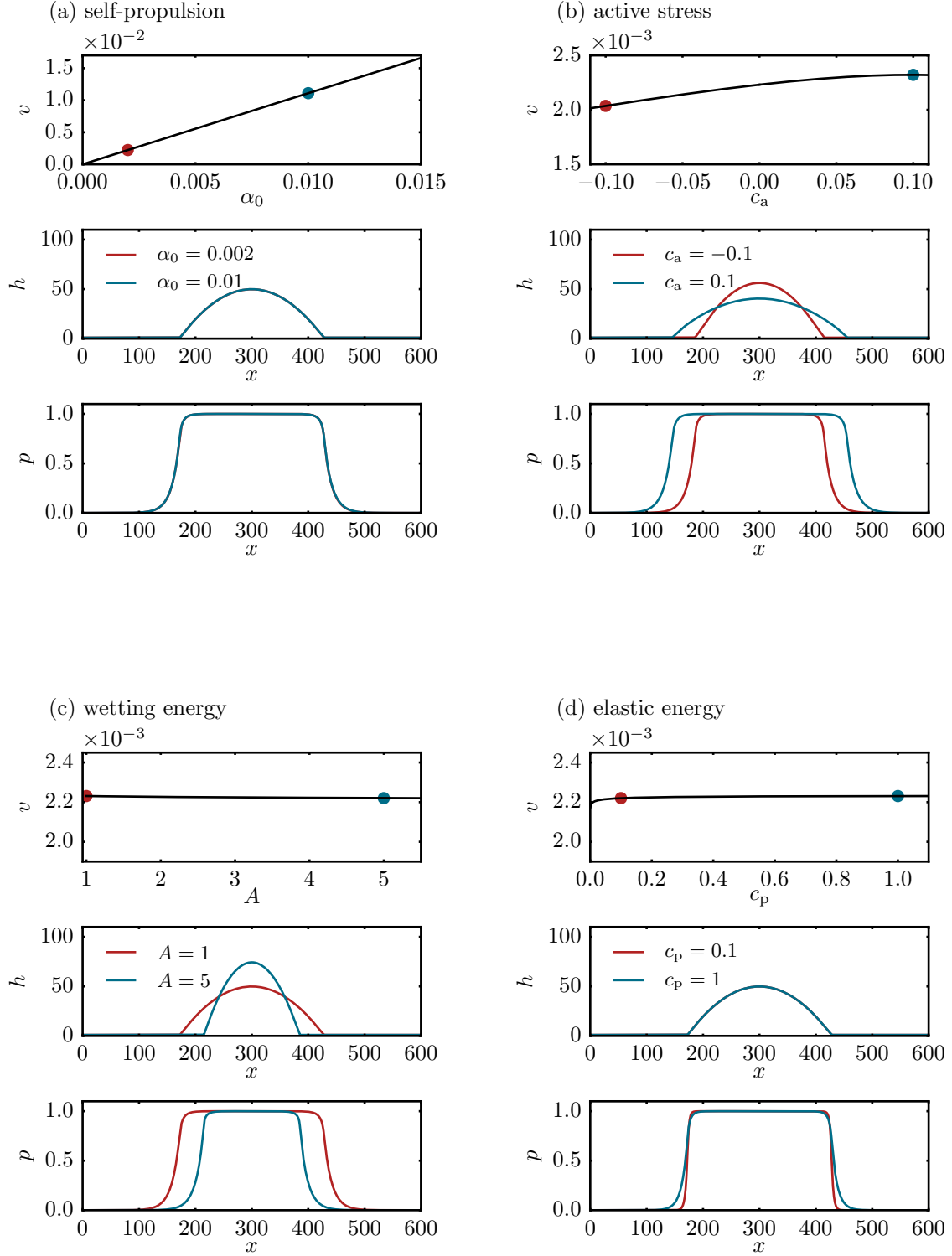
Figure 6.5.: Velocity of the active polar droplet (top row) depending on the self-propulsion speed (a), the strength of the active stress (b), the wetting energy (c) and the elastic energy (d). One parameter is varied in a parameter continuation, respectively, taking the solution for $c_a = 0$, $c_{sp} = 0.01$, $A = 1$, $M = 1$, $h_a = 1$, $\eta = 1$, $\gamma = 1$, $c_p = 2$, $Q_{NC} = 1$ and $\alpha_0 = 0.002$ in Fig. 6.4 (a) as a reference. The respective second (third) row shows height (polarisation) profiles for two specific parameter combinations as indicated by filled circles in the respective line colour in the velocity plots.

7. Summary and Outlook

In addition to the conclusions drawn within the individual chapters, we now summarise the whole thesis and present a brief outlook. The main objective of this thesis was to develop and analyse simple models to clarify the role of passive physico-chemical forces – such as osmosis, surface tension effects and wettability – on the spreading of bacterial colonies that grow at solid-air interfaces. The applied models add bioactive processes to a hydrodynamic approach within a thermodynamically consistent framework. We mainly focused on two spreading mechanisms that bacterial colonies employ at solid-air interfaces: The osmotic spreading of biofilms and the promotion of spreading by the presence of bio-surfactants. These mechanisms rely on the physico-chemical properties of the interfaces rather than on the active motion of individual bacteria.

The models employed in this thesis are based on a thin-film description of fluids. Thereby, the foundation for the model development was laid in Chapter 2 by discussing the properties of equilibrium droplets. Then, the thin-film equation for simple fluids was introduced as a mesoscopic modelling approach and related to the macroscopic description of droplets. In Chapter 3, we turned our attention towards the first biological example and developed a simple model for the *osmotic spreading of biofilms*. The analysis of our model by numerical time simulations showed that – in accordance with the experimental observation [SAW+12] – the colony first swells (mainly) vertically with increasing steepness of the colony height and subsequently expands laterally with a roughly constant contact angle. At large times, biomass growth, matrix production and osmotic influx are mainly located in a region close to the leading edge of the colony [TJT16]. The influence of the physical parameters of the model on the spreading speed and contact angle of the colony was studied by parameter continuation – a very efficient method for problems involving stationary (front) solutions.

Furthermore, our analysis confirmed that wetting crucially affects the spreading dynamics of biofilms. Indeed, surface forces determine whether a biofilm can expand over a substrate or not. We observed a transition between continuous and arrested spreading depending on the wettability. The lateral expansion of the biofilm is restricted in the case of arrested spreading, although the colony is biologically active. However, a small reduction in surface tension of the biofilm suffices to enable spreading [TJLT17]. This modulation of the surface tension can, e.g., be induced by the presence of bio-surfactants. A phase diagram was generated to identify the transition in the parameter space spanned by wettability and bacterial growth rate. In Fig. 3.13, this phase diagram is connected to experimental findings. The results obtained within our model provide a qualitative understanding of the experimentally observed transition between arrested and continuous spreading that occurs in a *B. subtilis* strain upon the improvement of wettability by the addition of external surfactants [TJLT17]. In addition to modifying the wettability, bio-surfactants in bacterial colonies also affect the spreading dynamics by the generation of Marangoni fluxes. These fluxes could not be described by the model presented in Chapter 3 because the approach does not capture non-uniform surfactant concentrations.

The next logical extension of the model was thus the incorporation of a spatially inhomogeneous surfactant concentration. To that end, it was first necessary to gain a deeper understanding of the *modelling of surfactant-covered thin films in the passive case*. In

Chapter 4, we employed equilibrium considerations to establish the link between mesoscopic and macroscopic descriptions of static surfactant-covered drops on solid substrates. The quantities occurring in the two approaches are related by the requirement of consistency of the mesoscopic and macroscopic description, implying that the dependencies of wetting and interface energies on the surfactant concentration may not be chosen independently. In particular, properties of the mesoscopic wetting energy are directly related to the solid-gas interfacial tension in the macroscopic description [TSTJ18]. By analysing static drops via energetic considerations, find that the structural form of Young's law remains unchanged in the presence of surfactants. However, the surfactant concentrations on the drop and on the surrounding adsorption layer and the resulting interfacial tensions adapt self-consistently. The addition of surfactant to the system may have a qualitatively different effect on the contact angle, depending on the relation between the free energies of the liquid-gas and the solid-gas interface [TSTJ18]. Even in the simple example with purely entropic free energies of the surfactant discussed in Sec. 4.2.3, the contact angle is either lowered with increasing amount of surfactant in the system or increased, corresponding to an autophobing effect [TSTJ19].

The ansatz of a factorised wetting energy $f_{\mathrm{w}}(h) = \hat{f}_{\mathrm{w}}(h)\chi(\Gamma)$ employed in Sec. 4.2.3 is only one possible choice and actually strongly restricts the physical phenomena that can be captured by the model. To describe, e.g., the behaviour close to a wetting transition, other assumptions regarding the form of the wetting energy are necessary [TSTJ18]. The main arguments and results presented in Chapter 4 are, however, independent of the specific form of the wetting energy and of general nature. They also apply to the theoretical description of dynamical phenomena through hydrodynamic modelling. Many effects associated with surfactants, e.g. autophobing and spreading, are typically studied in dynamic and out of equilibrium settings. However, the underlying mesoscopic theoretical model should for large times always result in the same equilibrium state as the corresponding macroscopic description. This is often not the case in the literature. In future work, the results presented in the first part of the chapter may be extended to a number of more complex situations involving, e.g., soluble surfactants and the formation of micelles [TSTJ18].

After these equilibrium considerations, we introduced a thin-film description for the dynamics of drops covered by insoluble surfactant in the second part of Chapter 4. By performing numerical time simulations, some dynamical effects such as the enhanced spreading rate of surfactant-covered droplets and the transversal instability of their contact line were demonstrated.

After this excursus on passive surfactant-laden droplets, we developed a model for the second spreading mechanism of bacterial colonies studied within this thesis, namely the *surfactant-driven spreading*. In Chapter 5, we studied a model which includes the production of bio-surfactant by the bacteria and which also accounts for fluxes arising due to a non-uniform distribution of surfactant. The analysis of this model demonstrated that wetting properties and Marangoni flows both strongly affect the expansion rate and morphology of bacterial colonies. Variations in the wettability and the surfactant production are sufficient to reproduce four different types of spreading, ranging from arrested spreading over circular spreading and modulated spreading fronts to the formation of pronounced fingers [TJT18]. We showed that the Marangoni flows can significantly contribute to the spreading. Therefore, the production of bio-surfactants can enable a bacterial colony to spread over the substrate under conditions which are otherwise unfavourable for expansion. Our results are in qualitative agreement with experimental findings [FPB+12] showing that surfactant-producing *Pseudomonas aeruginosa* wild-type colonies spread outwards

and form pronounced fingers whereas a mutant deficient in surfactant production is arrested in a small circular shape and cannot expand. This corresponds to the transition from the arrested spreading mode to the fingering mode that occurs upon the production of a significant amount of bio-surfactant for low wettability in our model [TJT18]. For planar fronts, parameter continuation techniques were employed to generate a phase diagram that distinguishes the different arising morphologies in the parameter space spanned by wettability and surfactant production. It was successfully compared to results obtained by time simulations.

An interesting possible future extension of the model would be the direct incorporation of the influence of the bio-surfactant on the wetting properties, e.g., by the introduction of a surfactant-dependent wetting energy as discussed in Chapter 4. This could allow one to disentangle the interplay of the different spreading processes and to obtain a consistent interpretation of a class of experiments whose interpretations at the moment seem to sometimes contradict each other (as, e.g., discussed in Sec. 5.5 for experiments on the prevention of growth by counter-gradients of surfactant). In particular, the double or even triple role played by the bio-surfactants (changing interface energies, driving Marangoni flows and also acting as osmolytes) could be clarified. To resolve this issue, further experiments are also required. They should focus on the physico-chemical aspects of spreading, i.e. the dynamics of the surfactant and the influence of wettability, e.g., by using agar substrates with different wetting properties.

In this thesis, we employed simple two-field approaches: In Chapter 3, when dealing with the osmotic spreading mechanism, the colony was described as a mixture of biomass and water. In Chapter 5 on surfactant-driven spreading, the bacterial colony was treated as a complex fluid covered by surfactants. To describe situations involving both a non-homogeneous distribution of bio-surfactants and non-negligible variations of the colony composition (e.g., because of similar time scales for biomass growth and osmotic processes), the model can be extended to a three-field model. Furthermore, the model can be extended to soluble surfactants with a bulk concentration by adapting the approach for passive fluids presented in [TAP16].

In the modelling approach presented in this thesis, complex features such as cell differentiation and vertical gradients are neglected. It has been shown experimentally by highlighting surfactant production by autofluorescence [FPB+12], that there are only small spatio-temporal variations in the *rhamnolipid* production in *P. aeruginosa* colonies. However, cell differentiation is in general an important effect in bacterial colonies and biofilms. In addition, one may also incorporate the quorum sensing role of the bio-surfactants which allows for a basic form of communication between individual cells in future extensions of the model [TJT18].

The modelling framework presented in this thesis may furthermore easily be extended to other experimental set-ups. In many practical applications, biofilms form at liquid-solid interfaces under confinement. A channel geometry as shown in Fig. 7.1 could be employed to incorporate an ambient aqueous medium that may either be quiescent or flowing, thereby shearing the spreading bacterial colony. As the lower substrate is now a solid, osmotic fluxes connect the biofilm and the ambient medium. Also Marangoni stresses will act differently as they drive flows in the biofilm and in the ambient medium that itself becomes an important sink for the bio-surfactant. A model of this type could, e.g., be employed to study the coupling between flows in the external medium and the spreading process which is, e.g. relevant in the context of pipe blockage by biofilms.

In its last part, this thesis took a first step towards the incorporation of active collective
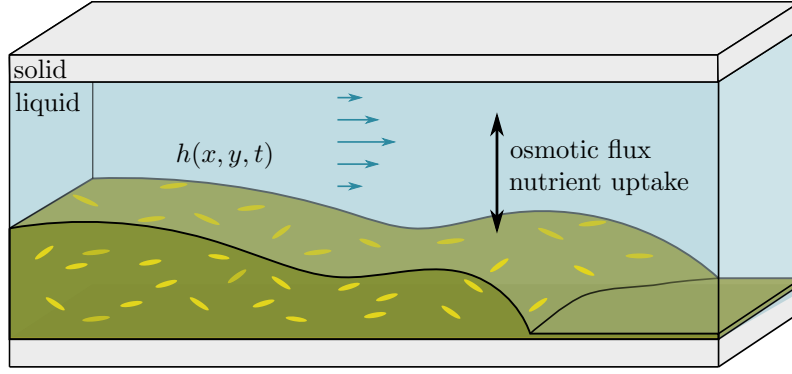
Figure 7.1.: Bacterial colony with a free interface profile $h(x, y, t)$ growing in contact with a nutrient-rich liquid in a confined channel geometry. Exchange processes – such as osmotic fluxes and the uptake of nutrients – take place via the free interface.

bacterial motion into thin-film models. In Chapter 6, a phenomenologically derived model for thin active polar films was proposed. The approach couples a thin-film equation for the film height to the dynamics of a polarisation field connected to self-propulsion and active stresses. Numerical simulations in one dimension showed reasonable dynamical behaviour and the model can describe moving and resting drops of active liquids. Due to the reduced complexity in the thin-film description, the model thus represents a candidate for a computationally less expensive alternative to models applied in the literature for the study of active drops on substrates. However, future testing and validation as well as an analysis for two-dimensional substrates are necessary to further characterise the model and its solutions. In a two-dimensional geometry, one could expect the existence of a splay-induced motility in the presence of active stress (but without self-propulsion) in the model as observed in [TMC12, WMVH14, MWP15, WH16]. Furthermore, the model could be employed to investigate how the presence of a macroscopic polarisation affects the dewetting dynamics of thin films and the coalescence of active droplets. In the future, the model could be coupled to the osmotically and surfactant-driven spreading mechanism of bacterial colonies.

To summarise, this thesis presented a framework for the modelling of spreading bacterial colonies. It focuses on the description of the influence of surface tension and wetting properties which are particularly important in the osmotically and surfactant-driven colony expansion. Although the developed model class neglects many processes that become important in mature bacterial colonies, it is, however, well-suited to describe the dynamics of the edge of spreading colonies. The spreading dynamics and the resulting colony shapes are in qualitative agreement with the experiments. It could thus be shown that in certain situations, physical effects suffice to explain important features of the spreading dynamics, such as the formation of pronounced fingers driven by bio-surfactants.

A. Appendix

A.1. Numerical Methods

For many geometries and problems, information about the solutions of nonlinear partial differential equations – such as the thin-film models discussed in this thesis – cannot be obtained by analytical methods. Instead, approximations and numerical methods need to be applied. Typically, the *dynamical* behaviour of a system is analysed by performing *time simulations* starting from a given initial state. Time simulations are a useful tool to observe time-dependent solutions or transient behaviour for a given initial condition and control parameter set, such as the transition from swelling to subsequent horizontal expansion of osmotically spreading biofilms studied in Sec. 3.3.1. In many cases, however, the system evolves towards a stationary solution, such as the fronts[1] emerging in the long-time limit of spreading biofilms as discussed in Sec. 3.3.2. If one is interested in the effect of a parameter on these stationary solutions – for example the influence of the wettability on the front velocity – it is inefficient to perform separate time simulations at each parameter value. In addition, time-stepping methods are unable to determine unstable solutions and can therefore only give an incomplete picture of the solution structure of the system and its change with parameters. These problems can be circumvented by applying *continuation methods* [DKK91, Kuz13, DWC$^+$14, KOB07] which directly follow *stationary solutions* in parameter space.

In this chapter we briefly introduce the employed methods for time simulations and parameter continuation, largely following the description in [Wil16]. We provide a demonstrative sketch of the methods rather than a mathematically precise description.

A.1.1. Numerical Time Simulations

The studied models describe the time evolution of spatially extended fields – such as the film height or surfactant concentration – in terms of nonlinear partial differential equations that also depend on the spatial derivatives of the fields. After introducing a spatial discretisation of the problem on a mesh, it is thus necessary to evaluate these spatial derivatives. In addition, a time-stepping method is necessary to determine the temporal evolution of the solution. Various different approaches exist for these two main ingredients of the numerical procedure. In this thesis, we employ a finite element method coupled to an implicit Runge-Kutta scheme as briefly outlined in the following.

Spatial Discretisation and Finite Element Method

The finite element method is based on the idea to subdivide the domain into small subdomains of simple shape, the so-called elements. Therefore, it is often applied when dealing with highly irregular geometries as occurring for example in solid mechanics and structural engineering. Here, we sketch the main ideas of the approach, following [Wil16] and [HH17]. A detailed description of the method can be found in standard textbooks (e.g.

---

[1] Front solutions which move with a constant velocity and shape correspond to stationary solutions after transforming the system into the co-moving coordinate frame.

A. Appendix

[BCO81, PS05, EG13]).

Before applying the finite element method, the problem is written in the so-called 'weak formulation'. In general, a second-order scalar partial differential equation for a field $u(x, y)$ on a two-dimensional domain Ω can be expressed in the residual form

$$\mathcal{R}\left(x, y, u(x, y)\right) = 0 \quad \text{in} \quad \Omega \tag{A.1}$$

accompanied by appropriate boundary conditions. To keep the notation compact, we suppress the explicit dependence of $\mathcal{R}$ on the derivatives of u. A classical (or strong) solution of the problem is any function $u(x, y)$ that satisfies the partial differential equation and the boundary condition at every point in the domain Ω. The concept of a *weak* solution $u_\mathrm{w}(x, y)$ of the problem is based on a slight relaxation of this criterion. A weak solution is a function that satisfies the boundary condition and for which the weighted residual

$$r = \int_\Omega \mathcal{R}\left(x, y, u_\mathrm{w}(x, y)\right) \phi^{test}(x, y)\mathrm{d}\mathbf{x} \tag{A.2}$$

vanishes for an arbitrary 'test function' $\phi^{test}(x, y)$ [HH17]. The advantage of writing the problem in the weak formulation is that it weakens the requirements of the differentiability of the solution. For the simple thin-film equation

$$\partial_t h = -\nabla \cdot \left[\frac{h^3}{3\eta}\nabla(\Delta h + \Pi(h)) \right] \tag{A.3}$$

introduced in Eq. (2.52), one can write a weak formulation that is of second order in space by introducing the variable $w = \Delta h + \Pi(h)$. It is given by

$$0 = \int_\Omega \left[(\partial_t h) + \nabla \cdot \left(\frac{h^3}{3\eta}\nabla w \right) \right] \phi_1^{test}\mathrm{d}\mathbf{x} \tag{A.4}$$

$$0 = \int_\Omega \left[\Delta h + \Pi(h) - w \right] \phi_2^{test}\mathrm{d}\mathbf{x} \tag{A.5}$$

for test functions ϕ_1^{test} and ϕ_2^{test}. By applying integration by parts to all terms which contain second order spatial derivatives of the fields, one obtains

$$0 = \int_\Omega (\partial_t h)\phi_1^{test}\mathrm{d}\mathbf{x} - \int_\Omega \left(\frac{h^3}{3\eta}\nabla w \right) \cdot \nabla\phi_1^{test}\mathrm{d}\mathbf{x} + \int_{\partial\Omega} \frac{h^3}{3\eta}\phi_1^{test}\nabla w \cdot \mathrm{d}\mathbf{s} \tag{A.6}$$

$$0 = \int_\Omega \left[\Pi(h) - w \right] \phi_2^{test}\mathrm{d}\mathbf{x} - \int_\Omega \nabla h \cdot \nabla\phi_2^{test}\mathrm{d}\mathbf{x} + \int_{\partial\Omega} \phi_2^{test}\nabla h \cdot \mathrm{d}\mathbf{s} \tag{A.7}$$

where $\mathrm{d}\mathbf{s}$ denotes the line element of the boundary $\partial\Omega$ pointing in the direction of the outside normal. The boundary conditions of the problem can be implemented through the boundary integrals. In this thesis, we use Neumann boundary conditions (if not stated otherwise) that lead to vanishing boundary integrals as $\nabla h = 0$ and $\nabla w = 0$ (equivalent to $\nabla h = \Delta \nabla h = 0$).
The corresponding weak formulations for the more complex models studied in this thesis (e.g. mixtures or surfactant-covered films) are given in Sec. A.2.3 and Sec. A.4.3.

In this thesis, we consider liquid films and droplets on flat solid substrates and analyse the systems on a two dimensional rectangular domain

$$\Omega = [0, L_x] \times [0, L_y] \tag{A.8}$$
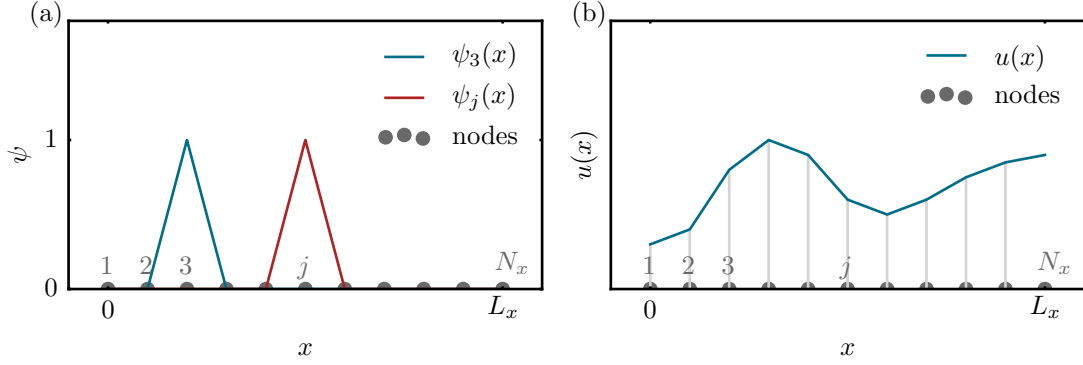
Figure A.1.: (a) Linear finite element ansatz function in one dimension which has the values at the nodes as degrees of freedom. (b) The superposition of the ansatz functions provides a piecewise linear interpolation.

with the spatial domain sizes L_x and L_y in the x- and y-direction, respectively. This simple geometry facilitates the *spatial discretisation*. For rectangular elements with the constant size $\Delta x \times \Delta y$, the decomposition of the domain is given by

$$\Omega = \bigcup_{i,j} \Omega_{i,j} \quad \text{with} \quad \Omega_{i,j} = [i\Delta x, (i+1)\Delta x] \times [j\Delta y, (j+1)\Delta y] \tag{A.9}$$

$$\text{for} \quad i = 0, \dots, \tfrac{L_x}{\Delta x} \quad \text{and} \quad j = 0, \dots, \tfrac{L_y}{\Delta y}. \tag{A.10}$$

The key feature of the finite element method is to expand the field $u(x, y)$ and – following the classical Galerkin method [EG13] also the test functions – in basis functions $\psi_i(x, y)$ which only have compact support, i.e., differ from zero only in a few cells. In practice, the expansion is truncated after a finite number of terms and we obtain the approximations

$$u_{\mathrm{w}}(x, y) \approx \sum_k U_k \psi_k(x, y) \qquad \phi^{test}(x, y) \approx \sum_j \Phi_j \psi_j(x, y). \tag{A.11}$$

In the performed numerical simulations, we use simple ansatz functions $\psi_i(x, y)$ which are linear in x- and y-direction. They have a finite value at the corners of the elements, the so-called *nodes*, as sketched in Fig. A.1 (a) for a one-dimensional system. Inserting the approximation (A.11) of the field and the test-functions into the weak formulation of the problem and replacing the integrals by appropriate weighted sums yields a set of equations for the yet unknown coefficients U_k [HH17]. Let us for the moment assume that we have already appropriately treated the time-derivatives which occur in the weak formulation of the problem. Then, the resulting nonlinear algebraic equations are solved for the unknown coefficients using, e.g., Newton's method [Deu04]. For the employed linear ansatz functions, the obtained approximation for the field $u_{\mathrm{w}}(x, y)$ is a piecewise linear interpolation between the values at the nodes as sketched in Fig. A.1 (b). The quality of the solution could, e.g., be improved by using non-uniformly spaced nodes or higher-order ansatz functions [HH17].

A. Appendix

Time Stepping Method

In this section, we briefly discuss the treatment of the temporal derivatives occurring in the coupled ordinary equations that result from the weak formulation of the problem by discretising space and applying the finite element method, again following [Wil16].
Let us consider a general system of first order ordinary differential equations

$$\frac{\mathrm{d}}{\mathrm{d}t}\mathbf{u}(t) = \mathbf{f}(\mathbf{u}(t), t) \tag{A.12}$$

for a time-dependent vector $\mathbf{u}(t)$. In the context of treating the time derivatives in a finite element scheme for partial differential equations, $\mathbf{u}(t)$ is an array consisting of the values of the field at the nodes. The function $\mathbf{f}(\mathbf{u}(t), t)$ contains the expressions obtained by applying the finite element method.
A good overview of numerical methods for ordinary differential equations can, e.g., be found in [But16]. The simplest time-stepping method which illustrates the main idea behind many time stepping methods is the *explicit Euler scheme*. This algorithm is based on the forward difference approximation of the temporal derivative and makes the prediction

$$\mathbf{u}(t + \Delta t) = \mathbf{u}(t) + \Delta t \mathbf{f}(\mathbf{u}(t), t) \tag{A.13}$$

for $\mathbf{u}$ at the next time step. The accuracy of the method depends on the size of the time step Δt and it can be shown that the truncation error is proportional to the step size. One way to improve the accuracy of the method is to approximate $\mathbf{f}$ with intermediate values at several stages within the time interval $[t, t+\Delta t]$ instead of assuming a constant value for the whole time interval. This is done in the *explicit Runge-Kutte schemes* [But16] which can be formulated as

$$\mathbf{u}(t + \Delta t) = \mathbf{u}(t) + \Delta t \sum_{i=1}^{s} b_i \mathbf{k}_i \tag{A.14}$$

where the $\mathbf{k}_i$ represent the approximation for $\mathbf{f}(\mathbf{u}(t), t)$ at the intermediate stages and are given by

$$\mathbf{k}_i = \mathbf{f}\left(\mathbf{u}(t) + \Delta t \sum_{j=1}^{i-1} a_{ij} \mathbf{k}_j, \ t + c_i \Delta t\right). \tag{A.15}$$

The coefficients a_{ij}, c_i and b_i for a specific Runge-Kutta scheme are often displayed in a compact form in a Butcher tableau as shown in Table A.1 (a) for a method of s stages.

(a)	0					(b)	c_1	a_{11}	a_{12}	$\cdots$	a_{1s}
	c_2	a_{21}					c_2	a_{21}	a_{22}	$\cdots$	a_{2s}
	c_3	a_{31}	a_{32}				c_3	a_{31}	a_{32}	$\cdots$	a_{3s}
	$\vdots$	$\vdots$	$\vdots$	$\ddots$			$\vdots$	$\vdots$	$\vdots$	$\ddots$	$\vdots$
	c_s	a_{s1}	a_{s2}	$\cdots$	a_{ss}		c_s	a_{s1}	a_{s2}	$\cdots$	a_{ss}
		b_1	b_2	$\cdots$	b_s			b_1	b_2	$\cdots$	b_s

Table A.1.: General form of the Butcher tableau for an explicit (a) and an implicit (b) Runge-Kutta method of s stages.

Explicit Runge-Kutta time-stepping methods have the advantage that the new step can be easily calculated from the information available at time t. However, they are usually not suitable for the solution of stiff equations containing higher order derivatives, such as the thin-film equation. The reason is that their region of numerical stability is small which

results in strict constraints for the possible time step Δt. This can be circumvented by applying *implicit Runge-Kutte schemes*, which can be written in the form

$$\mathbf{u}(t + \Delta t) = \mathbf{u}(t) + \Delta t \sum_{i=1}^{s} b_i \mathbf{k}_i \tag{A.16}$$

with

$$\mathbf{k}_i = \mathbf{f}\left(\mathbf{u}(t) + \Delta t \sum_{j=1}^{s} a_{ij} \mathbf{k}_j \, , \, t + c_i \Delta t\right) \, . \tag{A.17}$$

The difference as compared to an explicit time stepping method is the time at which $\mathbf{f}(\mathbf{u}(t)\,,\,t)$, which enters into the coefficients $\mathbf{k}_i$, is evaluated. This can also be seen in the Butcher tableau which has the form depicted in Table A.1 (b) and is no longer given by a lower triangle as for explicit time-stepping methods. In consequence, a system of algebraic equations has to be solved at every time step which increases the computational cost considerably. Nevertheless, this increased effort is – especially for stiff equations – often out-weighted by the possible larger step Δt [But16].

A special class of such methods are the diagonally implicit Runge-Kutta (DIRK) schemes [Ale77] for which every stage is implicit, i.e., all diagonal coefficients a_{ii} are non-zero. Throughout this thesis, we employ a scheme as given in the Butcher tableau in Table A.2.

$$
\begin{array}{c|cc}
\alpha & \alpha & 0 \\
1 & 1 - \alpha & \alpha \\
\hline
 & 1 - \alpha & \alpha
\end{array}
$$

Table A.2.: Butcher tableau for the employed second-order DIRK method, where $\alpha = 1 + \frac{1}{2}\sqrt{2}$.

A further improvement of the time-stepping method can be achieved by using an *adaptive time step* which is not of constant size but instead controlled by the local truncation error of a single Runge-Kutta step. This can be done by comparing two methods which are of different order of accuracy and adapting the time step in such a way that it stays within a given bound. [But16]

Practical Implementation Using DUNE-PDElab

The numerical time simulations are implemented using the open source framework *DUNE* (Distributed and Unified Numerics Environment) [BBD+08a, BBD+08b, BHM10]. This C++ based toolbox is designed to solve partial differential equations using grid-based methods such as finite differences, finite volume or finite element approaches. *DUNE* provides several modules that target the specific tasks, such as *DUNE-pdelab* for the discretisation using for example finite elements, *DUNE-grid* for grid managing and *DUNE-istl* for the implementation of iterative solvers. The template-based toolbox serves as an interface between these modules and allows for high-performance computing. Most of the simulations presented in this thesis were performed parallelized on the computer grid *PALMA* of the University of Münster.

The specific implementation used in this thesis extends a code for the simple thin-film equation written by Markus Wilczek [Wil16] and Walter Tewes [Tew18]. An implicit second order Runge-Kutta scheme with adaptive time step is used for the time-integration. The resulting linear problem is solved with a biconjugate gradient stabilised method (BiCGStab) and a symmetric successive overrelaxation (SSOR) as preconditioner.

A. Appendix

A.1.2. Parameter Continuation

In this section, we briefly introduce continuation methods by sketching the procedure of a *natural parameter continuation*, largely following the lecture notes by Thiele [Thi15c] and the descriptions in [Wil16] and [Eng17]. For stationary states, the studied model systems can – after spatial discretisation of the fields and their derivatives – be written as a set of nonlinear equations

$$\frac{d\mathbf{u}}{dt} = 0 = \mathbf{G}(\mathbf{u}, \lambda) \tag{A.18}$$

where $\mathbf{u}$ represents the solution array containing, e.g., the profile of the film height on the grid points, and λ represents a control parameter. Continuation methods now rely on the fact that any regular solution $(\mathbf{u}^0, \lambda^0)$ is part of a unique continuum of solutions, called a solution branch. A slight change in the control parameter thus only results in a small change of the solution [Thi15c]. This assumption is based on the *Implicit Function Theorem* which states that if the Jacobian matrix is non-singular and $\mathbf{G}(\mathbf{u}, \lambda)$ and the Jacobian are smooth near $(\mathbf{u}^0, \lambda^0)$, then there exists a whole family $\mathbf{u}(\lambda)$ close to $\mathbf{u}^0(\lambda^0)$. A mathematically precise formulation, proof and further applications of this theorem can be found in [KP12]. The strategy of continuation methods is now to start from a given solution $(\mathbf{u}^0, \lambda^0)$ and successively follow the solution branch by slightly varying the parameter λ and adapting the solution [Wil16].

The first step in a continuation procedure is to obtain the solution $(\mathbf{u}^0, \lambda^0)$ which serves as a starting point. For many cases, including most systems discussed here, an analytical solution of the problem is not available. One possibility is to start from a numerical solution that a time-stepping procedure converged to at large times. However, this relies on the availability of an adequate implementation and a sufficient convergence of the numerical solution. Another strategy, which is pursued in most cases in this thesis, is a homotopy method. In this approach, the system is written in a form that consists of a model of reduced complexity (for which an analytical solution is known) and the remaining terms multiplied by an artificial parameter, for example μ. The continuation procedure is initiated from the analytical solution at $\mu = 0$ which is subsequently continued to the full model of interest by successively varying the artificial parameter to $\mu = 1$ [Wil16]. Following this approach, most continuation runs in this thesis are initiated by the flat film solution of a simple thin-film equation.

The continuation procedure itself, which is applied to follow the solution $(\mathbf{u}^i, \lambda^i)$ along a solution branch by varying the control parameter to $\lambda^{i+1} = \lambda^i + \Delta\lambda$, consists of two steps as depicted in Fig. A.2: First, in a prediction step, the known solution branch is linearly extrapolated using the tangent vector $\boldsymbol{\nu} = \frac{\partial \mathbf{u}}{\partial \lambda}$ of the curve $\mathbf{u}(\lambda)$ to obtain an initial guess for the solution $\hat{\mathbf{u}}^{i+1}$ at λ^{i+1}. Next, this test solution is developed into a "true" solution (to arbitrary exactness) of Eq. (A.18) by applying a Newton iteration procedure [Deu04] at fixed control parameter λ^{i+1}. These steps are repeatedly performed to continue along a solution branch. The tangential vector $\boldsymbol{\nu}(\mathbf{u}^i)$ which is used in the prediction step to generate the test solution

$$\hat{\mathbf{u}}^{i+1} = \mathbf{u}^i + \Delta\lambda\,\boldsymbol{\nu}(\mathbf{u}^i) \tag{A.19}$$

can be obtained from a differentiation of Eq. (A.18) as

$$\boldsymbol{\nu} = -\underline{\mathbf{J}}^{-1}\frac{\partial G}{\partial \lambda} \tag{A.20}$$

where $\underline{\mathbf{J}}$ is the Jacobian [Eng17]. The subsequent correction of the test solution by Newton's method corresponds to a vertical step in the $(\mathbf{u}, \lambda)$ space. The step size $\Delta\lambda$ used in the prediction step can be adapted dynamically during the continuation along the branch
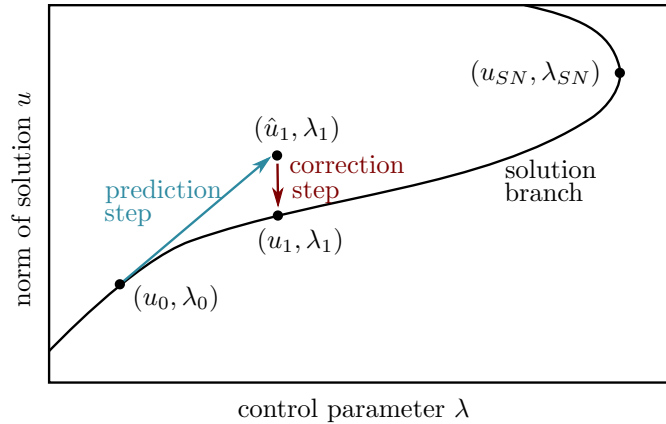
Figure A.2.: Sketch of a natural parameter continuation procedure. In a prediction step, a test solution is generated by extrapolating the known solution branch. Subsequently, this solution is corrected using an iterative Newton method. This simple procedure is, however, not suitable to follow solution branches around saddle-node bifurcations.

to ensure fast convergence of the Newton method.

One drawback of the natural parameter continuation procedure sketched above is that is relies on a one-to-one correspondence of solutions $\mathbf{u}$ and parameter λ and it can therefore not follow solution branches around saddle-node bifurcations such as the fold point (u_{SN}, λ_{SN}) depicted in Fig. A.2. This can be fixed by employing the *pseudo-arclength continuation* or *Keller method* [Kel79] which introduces an additional parameter s representing the approximate arclength along the solution branch $\mathbf{u}(\lambda)$ and writes both $\mathbf{u}(\lambda(s))$ and $\lambda(s)$ as functions of the new control parameter s. Then, the Newton correction steps are performed at fixed s. In consequence, this method allows for changes in the direction of the parameter λ and thus the continuation around fold points [Thi15c].

If the system under study fulfils certain symmetries, such as translational symmetry or invariance w.r.t. a change in volume as is, e.g., the case for the simple thin-film equation, the continuation of a solution along a branch is no longer possible as solutions are not unique anymore. Instead, a continuous spectrum of solutions exists at each λ which all have the same morphology but, in our example possess different volumes or are shifted along the x-axis. To guarantee the existence of a unique solution which can be followed, the 'neutrally stable' eigenmodes of the system need to be suppressed in the continuation procedure by the introduction of additional conditions [Eng17]. For volume conservation in the thin-film equation, where the solution $\mathbf{u}$ represents the height profile h, the respective condition is the integral condition

$$0 = \int_{\Omega} h \, dx - V_0 \,. \tag{A.21}$$

The translation symmetry can be broken by introducing the integral condition

$$0 = \int_{\Omega} \frac{\partial h^{i-1}}{\partial x} (h^i - h^{i-1}) \, dx \tag{A.22}$$

which requests that the projection of the solution in the i-th iteration step onto the translation mode of the $(i-1)$-th solution is zero [Eng17].

One possible implementation of the above described continuation method, which is applied here, is provided by the software package *Auto07p* [DO09]. Many tutorials on the

application of *Auto07p* to different types of systems and problems can be found in the *Münsteranian Torturials On Continuation* [Thi15a]. Note that – in contrast to other software packages such as *pde2path* [UWR14] or *oomph-lib* [HH06] – *Auto07p* is limited to one-dimensional geometries. In Sec. A.5 the implementation of a parameter continuation using *Auto07p* is discussed in more detail. There, it is also shown how the procedure can be extended to study the (transversal) stability of fronts.

A.2. Details of the Thin-Film Model for Osmotic Biofilm Spreading

A.2.1. Non-dimensional Form of the Model

The model

$$\partial_t h = \nabla \cdot \left[Q_{hh} \nabla \frac{\delta F_{\mathrm{mix}}}{\delta h} + Q_{h\psi} \nabla \frac{\delta F_{\mathrm{mix}}}{\delta \psi} \right] + \zeta(h, \psi) \tag{A.23}$$

$$\partial_t \psi = \nabla \cdot \left[Q_{\psi h} \nabla \frac{\delta F_{\mathrm{mix}}}{\delta h} + Q_{\psi\psi} \nabla \frac{\delta F_{\mathrm{mix}}}{\delta \psi} \right] + G(h, \psi) \tag{A.24}$$

as introduced in Eqs. (3.22)-(3.23) in a hydrodynamic formulation with the energetic contributions, mobilities and bioactive terms as defined in Eqs. (3.1)-(3.4), (3.8)-(3.9) and (3.16)-(3.21) describes the osmotically driven spreading of biofilms. It is brought into a non-dimensional form by introducing the scaling

$$t = \tau \tilde{t} \qquad x = L\tilde{x} \qquad y = L\tilde{y} \qquad h = l\tilde{h} \qquad \psi = l\tilde{\psi} \qquad f_{\mathrm{w,m}} = \kappa \tilde{f}_{\mathrm{w,m}} \tag{A.25}$$

for time, space and energy, assuming that in a thin-film geometry, the horizontal x- and y-direction scale differently than the vertical z-direction. Dimensionless quantities are indicated by tildes. The scales are chosen as

$$\tau = \frac{L^2 \eta_0}{\kappa l} \qquad l = h_{\mathrm{a}} \qquad L = \sqrt{\frac{\gamma}{\kappa}} l \qquad \kappa = \frac{k_B T}{a^3} l \,. \tag{A.26}$$

The non-dimensional form of the evolution equations then reads

$$\partial_{\tilde{t}} \tilde{h} = \tilde{\nabla} \cdot \left[\tilde{Q}_{hh} \tilde{\nabla} \frac{\delta \tilde{F}_{\mathrm{mix}}}{\delta \tilde{h}} + \tilde{Q}_{h\psi} \tilde{\nabla} \frac{\delta \tilde{F}_{\mathrm{mix}}}{\delta \tilde{\psi}} \right] + \tilde{\zeta}(\tilde{h}, \tilde{\psi}) \tag{A.27}$$

$$\partial_{\tilde{t}} \tilde{\psi} = \tilde{\nabla} \cdot \left[\tilde{Q}_{\psi h} \tilde{\nabla} \frac{\delta \tilde{F}_{\mathrm{mix}}}{\delta \tilde{h}} + \tilde{Q}_{\psi\psi} \tilde{\nabla} \frac{\delta \tilde{F}_{\mathrm{mix}}}{\delta \tilde{\psi}} \right] + \tilde{G}(\tilde{h}, \tilde{\psi}) \,. \tag{A.28}$$

Note that the nondimensional variations are given by

$$\frac{\delta \tilde{F}_{\mathrm{mix}}}{\delta \tilde{h}} = \frac{lL^2}{\kappa L^2} \frac{\delta F_{\mathrm{mix}}}{\delta h} = \frac{l}{\kappa} \frac{\delta F_{\mathrm{mix}}}{\delta h} \qquad\qquad \frac{\delta \tilde{F}_{\mathrm{mix}}}{\delta \tilde{\psi}} = \frac{l}{\kappa} \frac{\delta F_{\mathrm{mix}}}{\delta \psi} \tag{A.29}$$

since the functional derivatives scale as

$$\frac{\delta}{\delta h(x)} = \frac{1}{L^2 l} \frac{\delta}{\delta \tilde{h}(\tilde{x})} \qquad\qquad \frac{\delta}{\delta \psi(x)} = \frac{1}{L^2 l} \frac{\delta}{\delta \tilde{\psi}(\tilde{x})} \,. \tag{A.30}$$

This gives

$$\frac{\delta \tilde{F}_{\mathrm{mix}}}{\delta \tilde{h}} = W_{\mathrm{m}} \left(\frac{1}{\tilde{h}^3} - \frac{1}{\tilde{h}^6} \right) - \tilde{\Delta} \tilde{h} \tag{A.31}$$

$$\frac{\delta \tilde{F}_{\mathrm{mix}}}{\delta \tilde{\psi}} = \ln\left(\frac{\tilde{\psi}}{\tilde{h}} \right) - \ln\left(1 - \frac{\tilde{\psi}}{\tilde{h}} \right) \tag{A.32}$$

with a dimensionless parameter

$$W_{\mathrm{m}} = \frac{A}{l^3} \frac{a^3}{k_B T} \tag{A.33}$$

representing the ratio between the wetting and the entropic bulk contributions to the free energy. It is therefore called wettability parameter.

The mobility matrix is given by

$$\tilde{\mathbf{Q}} = \frac{\eta_0}{l^3}\mathbf{Q} = \frac{1}{3\hat{\eta}}\begin{pmatrix} \tilde{h}^3 & \tilde{h}^2\tilde{\psi} \\ \tilde{h}^2\tilde{\psi} & \tilde{h}\tilde{\psi}^2 \end{pmatrix} + \begin{pmatrix} 0 & 0 \\ 0 & \tilde{D}\tilde{\psi} \end{pmatrix} \tag{A.34}$$

with the dimensionless diffusivity

$$\tilde{D} = \frac{\delta^2}{6\pi\hat{\eta}} \quad \text{with} \quad \delta = \frac{a}{h_{\mathrm{a}}}. \tag{A.35}$$

The biomass production term reads

$$\tilde{G}(\tilde{h}, \tilde{\psi}) = \tilde{g}\tilde{h}\frac{\tilde{\psi}}{\tilde{h}}\left(1 - \frac{\tilde{\psi}}{\tilde{h}}\right)\left(1 - \frac{\tilde{\psi}}{\phi_{\mathrm{eq}}\tilde{h}^\star}\right)f_{\mathrm{mod}}(\tilde{h}, \tilde{\psi}) \tag{A.36}$$

with the dimensionless growth rate $\tilde{g} = g\tau$ and the dimensionless limiting height $\tilde{h}^\star = \frac{h^\star}{l}$. The local modification of the growth term for small amounts of biomass is given by

$$f_{\mathrm{mod}}\left(\tilde{h}, \tilde{\psi}\right) = (1 - \frac{\phi_{\mathrm{eq}}\tilde{h}_u}{\tilde{\psi}})\left(1 - \exp(\phi_{\mathrm{eq}} - \tilde{\psi})\right) \tag{A.37}$$

with $\tilde{h}_u = \frac{h_u}{l}$. The osmotic influx term reads

$$\tilde{\zeta}(\tilde{h}, \tilde{\psi}) = \tilde{Q}_{\mathrm{osm}}\left(-\frac{\delta\tilde{F}_{\mathrm{mix}}[\tilde{h}, \tilde{\psi}]}{\delta\tilde{h}} - \tilde{\Pi}_{\mathrm{agar}}\right) \tag{A.38}$$

with the dimensionless osmotic mobility constant $\tilde{Q}_{\mathrm{osm}} = \frac{\tau\kappa}{l^2}Q_{\mathrm{osm}}$ and $\tilde{\Pi}_{\mathrm{agar}} = \frac{l}{\kappa}\Pi_{\mathrm{agar}}$.

A.2.2. Formulation for Parameter Continuation

To analyse the model for osmotic biofilm spreading with parameter continuation, we transform the evolution equations (A.27)-(A.28) into the co-moving coordinate system moving with a constant velocity v via the coordinate transformation $x \to x + vt$. The equations contain derivatives of the film height h up to fourth order and derivatives of the biomass height ψ up to second order. For the parameter continuation using *AUTO07p*, the system needs to be written as a system of first order differential equations. We omit the tildes that indicate dimensionless quantities and choose the variables

$$u_1 = \psi \qquad u_2 = h \qquad u_3 = \psi_x \qquad u_4 = h_x \qquad u_5 = h_{xx} \qquad u_6 = h_{xxx} \tag{A.39}$$

where subscipt x stand for spatial derivatives. Then, we define the ODE system with $N_{\mathrm{DIM}} = 6$ as

$$\begin{aligned} \partial_x u_1 &= u_3 & \partial_x u_4 &= u_5 \\ \partial_x u_2 &= u_4 & \partial_x u_5 &= u_6 \\ \partial_x u_3 &= \psi_{xx} & \partial_x u_6 &= h_{xxxx}. \end{aligned} \tag{A.40}$$

The steady versions of Eqs. (A.27)-(A.28) in the co-moving frame with velocity v are solved for the yet unknown expressions for ψ_{xx} and h_{xxxx}. This yields

$$\begin{aligned} \psi_{xx} =& \frac{1}{\hat{\eta}h^6}(2\hat{\eta}h^8\psi_x h_{xxx}\pi - 2\hat{\eta}h_x\psi h_{xxx}\pi h^7 - 6G(\psi,h)\hat{\eta}^2 h^6\pi \\ &+ 6\zeta(\psi,h)h^5\pi\hat{\eta}^2\psi + 6\hat{\eta}h^4 h_x\psi_x W_{\mathrm{m}}\pi - 6\hat{\eta}h_x^2\psi W_{\mathrm{m}}\pi h^3 \\ &+ \hat{\eta}h_{xx}h^5\psi + \hat{\eta}h^5 h_x\psi_x - \hat{\eta}h^4 h_x^2\psi \\ &+ \hat{\eta}_x h^6\psi_x - \hat{\eta}_x h^5 h_x\psi - 12\hat{\eta}hh_x\psi_x W_{\mathrm{m}}\pi + 12\hat{\eta}h_x^2\psi W_{\mathrm{m}}\pi \\ &- 6h^6\psi_x\hat{\eta}^2\pi v + 6h^5 h_x\psi\hat{\eta}^2\pi v) \end{aligned} \tag{A.41}$$

and

$$
\begin{aligned}
h_{xxxx} ={} & \frac{1}{\hat{\eta}h^8\psi\pi}(-\hat{\eta}h^8\psi_x h_{xxx}\pi - 2\hat{\eta}h_x\psi h_{xxx}\pi h^7 \\
& + \hat{\eta}_x h^8\psi h_{xxx}\pi + 3G(\psi,h)\hat{\eta}^2 h^6\pi - 3\hat{\eta}h_{xx}h^4\psi W_\mathrm{m}\pi \\
& - 3\hat{\eta}h^4 h_x\psi_x W_\mathrm{m}\pi + 6\hat{\eta}h_x^2\psi W_\mathrm{m}\pi h^3 + 3\hat{\eta}_x h^4 h_x\psi W_\mathrm{m}\pi \\
& - \tfrac{1}{2}\hat{\eta}h_{xx}h^5\psi + \tfrac{1}{2}\hat{\eta}\psi_{xx}h^6 - \tfrac{1}{2}\hat{\eta}h^5 h_x\psi_x \\
& + \tfrac{1}{2}\hat{\eta}h^4 h_x^2\psi - \tfrac{1}{2}\hat{\eta}_x h^6\psi_x + \tfrac{1}{2}\hat{\eta}_x h^5 h_x\psi \\
& + 6\hat{\eta}h_{xx}h\psi W_\mathrm{m}\pi + 6\hat{\eta}h h_x\psi_x W_\mathrm{m}\pi - 30\hat{\eta}h_x^2\psi W_\mathrm{m}\pi - 6\hat{\eta}_x h h_x\psi W_\mathrm{m}\pi \\
& + 3h^6\psi_x\hat{\eta}^2\pi v)
\end{aligned}
\tag{A.42}
$$

with

$$
\hat{\eta} = \frac{\frac{\eta_b}{\eta_0}\psi + h - \psi}{h} \qquad \hat{\eta}_x = \frac{\frac{\eta_b}{\eta_0}\psi_x + h_x - \psi_x}{h} - \frac{(\frac{\eta_b}{\eta_0}\psi + h - \psi)h_x}{h^2} \,.
\tag{A.43}
$$

As boundary conditions, we apply $h_x = \psi_x = h_{xxx} = 0$ at both boundaries, yielding $N_\mathrm{BC} = 6$ equations and at the same time breaking the translation symmetry. One integral condition is used to measure the drop volume ($N_\mathrm{INT} = 1$). Thus, the problem has ($N_\mathrm{BC} + N_\mathrm{INT} - N_\mathrm{DIM} + 1$) = 2 free parameters. The continuation run is initiated from a numerical solution obtained by a finite element method using *DUNE* for a stationary (relatively flat) biofilm droplet. In the runs for stationary (arrested) profiles, the velocity v is fixed to zero and the drop volume is used as an adapting (pseudo-)free parameter when studying the influence of other control parameters (for example the biomass growth rate g). For the analysis of the front profiles, the drop volume is fixed (i.e. the integral condition becomes a 'true' condition and not just a measure) and the velocity is adapted.

A.2.3. Weak Formulation Used in Time Simulations

For the time simulations, the osmotic biofilm model is written in a symmetric formulation presented by Xu et al. in [XTQ15], i.e.

$$
\partial_t\psi = \nabla \cdot \left[Q_{\psi_\mathrm{w}}\nabla\frac{\delta F_\mathrm{mix}[\psi,\psi_\mathrm{w}]}{\delta\psi} + Q_{\psi\psi_\mathrm{w}}\nabla\frac{\delta F_\mathrm{mix}[\psi,\psi\psi_\mathrm{w}]}{\delta\psi_\mathrm{w}} \right] + G(\psi,\psi_\mathrm{w})
\tag{A.44}
$$

$$
\partial_t\psi_\mathrm{w} = \nabla \cdot \left[Q_{\psi_\mathrm{w}\psi}\nabla\frac{\delta F_\mathrm{mix}[\psi,\psi_\mathrm{w}]}{\delta\psi} + Q_{\psi_\mathrm{w}\psi_\mathrm{w}}\nabla\frac{\delta F_\mathrm{mix}[\psi,\psi_\mathrm{w}]}{\delta\psi_\mathrm{w}} \right] - G(\psi,\psi_\mathrm{w}) + \zeta(\psi,\psi_\mathrm{w})
\tag{A.45}
$$

where we again omit the tildes identifying dimensionless quantities. The energy functional F_mix and the bioactive terms are expressed through the effective thickness of biomass ψ and water ψ_w and the mobility matrix is defined as

$$
\begin{pmatrix} Q_{\psi\psi} & Q_{\psi\psi_\mathrm{w}} \\ Q_{\psi_\mathrm{w}\psi} & Q_{\psi_\mathrm{w}\psi_\mathrm{w}} \end{pmatrix} = \frac{\psi + \psi_\mathrm{w}}{3\hat{\eta}}\begin{pmatrix} \psi^2 + M & \psi\psi_\mathrm{w} - M \\ \psi\psi_\mathrm{w} - M & \psi_\mathrm{w}\psi_\mathrm{w} + M \end{pmatrix}
\tag{A.46}
$$

with

$$
M = \frac{\psi\psi_\mathrm{w}\delta^2}{2\pi(\psi + \psi_\mathrm{w})^2} \,.
\tag{A.47}
$$

We formulate the system in terms of four variables

$$
u_0 = \psi \qquad u_1 = \frac{\delta F_\mathrm{mix}}{\delta\psi} \qquad w_0 = \psi_\mathrm{w} \qquad w_1 = \frac{\delta F_\mathrm{mix}}{\delta\psi_\mathrm{w}}
\tag{A.48}
$$

A. Appendix

to reduce the order of the differential equations by two derivatives. The evolution equations are then given by

$$\partial_t u_0 = \nabla \cdot [Q_{\psi\psi} \nabla u_1 + Q_{\psi\psi_{\mathrm{w}}} \nabla w_1] + G \tag{A.49}$$

$$u_1 = \frac{\delta F_{\mathrm{mix}}}{\partial u_0} = W_{\mathrm{m}} \left(\frac{1}{(u_0+w_0)^3} - \frac{1}{(u_0+w_0)^6} \right) + \ln \left(\frac{u_0}{u_0+w_0} \right) - \Delta(u_0 + w_0) \tag{A.50}$$

$$\partial_t w_0 = \nabla \cdot [Q_{\psi_{\mathrm{w}}\psi} \nabla u_1 + Q_{\psi_{\mathrm{w}}\psi_{\mathrm{w}}} \nabla w_1] - G + \zeta \tag{A.51}$$

$$w_1 = \frac{\delta F_{\mathrm{mix}}}{\partial w_0} = W_{\mathrm{m}} \left(\frac{1}{(u_0+w_0)^3} - \frac{1}{(u_0+w_0)^6} \right) + \ln \left(\frac{w_0}{u_0+w_0} \right) - \Delta(u_0 + w_0) \tag{A.52}$$

We choose linear test- and ansatz-functions $\phi_0, ..., \phi_3$, multiply Eqs. (A.49)-(A.52) with these functions and integrate over the whole domain. After partial integration and applying Neumann boundary conditions (resulting in vanishing boundary integrals), the weak formulation of the problem used for the implementation in *DUNE* is given by

$$0 = \int_\Omega \mathrm{d}\mathbf{x} \; [\partial_t u_0 \phi_0 + [Q_{\psi\psi} \nabla u_1 + Q_{\psi\psi_{\mathrm{w}}} \nabla w_1] \cdot \nabla \phi_0 - G \phi_0]$$

$$0 = \int_\Omega \mathrm{d}\mathbf{x} \; \left[\left[-u_1 + W_{\mathrm{m}} \left(\frac{1}{(u_0+w_0)^3} - \frac{1}{(u_0+w_0)^6} \right) + \ln \left(\frac{u_0}{u_0+w_0} \right) \right] \phi_1 + (\nabla u_0 + \nabla w_0) \cdot \nabla \phi_1 \right]$$

$$0 = \int_\Omega \mathrm{d}\mathbf{x} \; [\partial_t w_0 \phi_2 + [Q_{\psi_{\mathrm{w}}\psi} \nabla u_1 + Q_{\psi_{\mathrm{w}}\psi_{\mathrm{w}}} \nabla w_1] \cdot \nabla \phi_2 + (G - \zeta) \phi_2]$$

$$0 = \int_\Omega \mathrm{d}\mathbf{x} \; \left[\left[-w_1 + W_{\mathrm{m}} \left(\frac{1}{(u_0+w_0)^3} - \frac{1}{(w_0+w_0)^6} \right) + \ln \left(\frac{w_0}{u_0+w_0} \right) \right] \phi_3 + (\nabla u_0 + \nabla w_0) \cdot \nabla \phi_3 \right] .$$

A.3. Details of the Model for Drops Covered by Insoluble Surfactant

A.3.1. Non-dimensional Form of the Model

To write a non-dimensional version of the model for surfactant-covered drops with surfactant-dependent wettability introduced in Eqs. (4.49)-(4.50) in Sec. 4.3, the energy is rescaled by the interfacial tension without surfactant γ_0 and the length scales in vertical and horizontal direction are rescaled by the adsorption layer height. Note that in this model, Γ represents a surface number density (with dimension $1/m^2$). The rescaling of the equations results in

$$x = l\tilde{x} \qquad h = l\tilde{h} \qquad \Gamma_{\mathrm{p}} = l^2 \tilde{\Gamma}_{\mathrm{p}} \qquad t = \tau\tilde{t} \qquad F = \kappa l^2 \tilde{F} \tag{A.53}$$

with the scales

$$l = h_{\mathrm{a}} \qquad \tau = \frac{\eta l}{\kappa} \qquad \kappa = \gamma^0 \,. \tag{A.54}$$

Note that here, the vertical and horizontal length scales are rescaled in the same way. The non-dimensional form of the evolution equations is then given by

$$\partial_{\tilde{t}}\tilde{h} = \tilde{\nabla} \cdot \left[\tilde{Q}_{11} \tilde{\nabla} \frac{\delta\tilde{F}_{\mathrm{surf}}}{\delta\tilde{h}} + \tilde{Q}_{12} \tilde{\nabla} \frac{\delta\tilde{F}_{\mathrm{surf}}}{\delta\tilde{\Gamma}_{\mathrm{p}}} \right] \tag{A.55}$$

$$\partial_{\tilde{t}}\tilde{\Gamma}_{\mathrm{p}} = \tilde{\nabla} \cdot \left[\tilde{Q}_{21} \tilde{\nabla} \frac{\delta\tilde{F}_{\mathrm{surf}}}{\delta\tilde{h}} + \tilde{Q}_{22} \tilde{\nabla} \frac{\delta\tilde{F}_{\mathrm{surf}}}{\delta\tilde{\Gamma}_{\mathrm{p}}} \right] \,. \tag{A.56}$$

The variations scale as

$$\frac{\delta\tilde{F}_{\mathrm{surf}}}{\delta\tilde{h}} = \frac{ll^2}{\kappa l^2} \frac{\delta F_{\mathrm{surf}}}{\delta h} = \frac{l}{\kappa} \frac{\delta F_{\mathrm{surf}}}{\delta h} \qquad \frac{\delta\tilde{F}_{\mathrm{surf}}}{\delta\tilde{\Gamma}_{\mathrm{p}}} = \frac{1}{\kappa} \frac{\delta F_{\mathrm{surf}}}{\delta\Gamma_{\mathrm{p}}} \tag{A.57}$$

since the functional derivatives are given by

$$\frac{\delta}{\delta h} = \frac{1}{l^2 l} \frac{\delta}{\delta\tilde{h}(\tilde{x})} \qquad \frac{\delta}{\delta\Gamma_{\mathrm{p}}} = \frac{1}{l^2} \frac{\delta}{\delta\tilde{\Gamma}_{\mathrm{p}}(\tilde{x})} \,. \tag{A.58}$$

The free energy functional $\tilde{F}_{\mathrm{surf}}$ (written as a function of $\tilde{\Gamma}$) reads

$$\tilde{F}_{\mathrm{surf}} = \int \underbrace{\left[1 + \epsilon_1 \tilde{\Gamma}(\ln\tilde{\Gamma} - 1) \right]}_{\tilde{g}(\tilde{\Gamma})} \zeta + \underbrace{\epsilon_2 \left(-\frac{1}{2\tilde{h}^2} + \frac{1}{5\tilde{h}^5} \right) \left[1 + \frac{10}{3} \frac{\epsilon_1}{\epsilon_2} \ln\delta\tilde{\Gamma} \right]}_{\tilde{f}_{\mathrm{w}}(\tilde{h},\tilde{\Gamma})} \mathrm{d}\tilde{\mathbf{x}} \tag{A.59}$$

with the dimensionless parameters

$$\delta = \frac{a^2}{a_{\mathrm{sg}}^2} \qquad \epsilon_1 = \frac{k_B T}{a^2 \gamma^0} \qquad \epsilon_2 = \frac{A}{h_{\mathrm{a}}^2 \gamma^0} \tag{A.60}$$

representing the ratio of the effective molecular length scales of the surfactant on the liquid-gas and solid-gas interface, the ratio of the entropic energetic contribution of the surfactant as compared to the surface tension without surfactant and the ratio of the wetting energy as compared to the surface tension, respectively. The dimensionless diffusivity is given by $\tilde{D} = D\eta a^2/h_{\mathrm{a}}$. Note that for performing the variations, the surfactant concentration in $\tilde{F}_{\mathrm{surf}}$ has to be expressed in terms of its projection onto the flat substrate $\tilde{\Gamma}_{\mathrm{p}}$ by using $\tilde{\Gamma} = \frac{\tilde{\Gamma}_{\mathrm{p}}}{\xi}$.

In the following, we omit the tildes that indicate dimensionless quantities.

A.3.2. Formulation for Parameter Continuation

To study the steady state solutions of the evolution equations (A.55)-(A.56) with the free energy functional given in Eq. (A.59), we formulate the problem as a set of ordinary differential equations suitable for parameter continuation. In thermodynamic equilibrium, the fluxes stemming from $\nabla \frac{\delta F_{\text{surf}}}{\delta h}$ and $\nabla \frac{\delta F_{\text{surf}}}{\delta \Gamma_{\text{p}}}$ vanish separately. The variations thus become constant across the system

$$(I) \quad \frac{\delta F_{\text{surf}}}{\delta h} = \partial_h f_{\text{w}} - \partial_x [(g - \lambda_\Gamma \Gamma) \frac{\partial_x h}{\xi}] = p \qquad (A.61)$$

$$(II) \quad \frac{\delta F_{\text{surf}}}{\delta \Gamma_p} = \frac{1}{\xi} \partial_\Gamma f_{\text{w}} + \partial_\Gamma g = \lambda_\Gamma \qquad (A.62)$$

where p denotes the pressure and λ_Γ denotes the chemical potential as given in Eqs. (4.13) and (4.14). For the entropic energy and the product ansatz used in Sec. 4.2.3, one can derive an expression for the surfactant coverage $\Gamma(\lambda, h)$ from Eq. (A.62). One finds a second order ordinary differential equation for $h(x)$ by inserting this expression into Eq. (A.61) . By introducing the variables

$$u_1 = h \qquad u_2 = h_x , \qquad (A.63)$$

the problem can be reformulated as a set of two first order differential equation given by

$$\frac{\mathrm{d}}{\mathrm{d}x} u_1 = h_x = u_2 \qquad (A.64)$$

$$\frac{\mathrm{d}}{\mathrm{d}x} u_2 = h_{xx} = \frac{\xi^3}{C} \left(\chi \partial_h \hat{f}_{\text{w}} - p - \frac{h_x^2}{\xi^2} (\partial_\Gamma g - \lambda_\Gamma) \frac{M}{\epsilon_1} \Gamma \partial_h \hat{f}_{\text{w}} \right) \qquad (A.65)$$

with

$$M = \frac{10}{3} \frac{\epsilon_1}{\epsilon_2} \ln \delta \quad \text{and} \quad C = g - \lambda \Gamma - (\partial_\Gamma g - \lambda) \Gamma \frac{M}{\epsilon_1} \lambda \hat{f}_{\text{w}} \frac{h_x^2}{\xi} .$$

A.4. Details of the Thin-Film Model for Surfactant-Driven Spreading of Bacterial Colonies

A.4.1. Non-dimensional Form of the Model

The model

$$\partial_t h = \nabla \cdot \left[\frac{h^3}{3\eta} \nabla(\partial_h f_\text{w} - \gamma^0 \Delta h) \right] + \frac{kT}{a^2} \nabla \cdot \left[\frac{h^2}{2\eta} \nabla \Gamma \right] + G(h) \tag{A.66}$$

$$\partial_t \Gamma = \nabla \cdot \left[\frac{h^2 \Gamma}{3\eta} \nabla(\partial_h f_\text{w} - \gamma^0 \Delta h) \right] + \frac{kT}{a^2} \nabla \cdot \left[\frac{h\Gamma}{\eta} \nabla \Gamma \right] + \frac{kT}{a^2} D \Delta \Gamma + P(h, \Gamma) \,. \tag{A.67}$$

presented in Sec. 5.2 with $f_\text{w}(h)$, $G(h)$ and $P(h, \Gamma)$ as defined in Eqs. (4.52), (5.1) and (5.2) is brought into a non-dimensional form by introducing the scaling

$$t = \tau \tilde{t} \qquad x = L\tilde{x} \qquad y = L\tilde{y} \qquad h = l\tilde{h} \qquad \Gamma = \tilde{\Gamma} \qquad f_{\text{w,s}} = \kappa \tilde{f}_{\text{w,s}} \,. \tag{A.68}$$

for time, space, concentration and energy. Note that in this model, Γ represents the (dimensionless) packing fraction of surfactant at the interface. The scales are chosen as

$$l = h_\text{a} \qquad \kappa = \frac{kT}{a^2} \qquad L = \sqrt{\frac{\gamma^0}{\kappa}} l \qquad \tau = \frac{L^2 \eta}{\kappa l} \,. \tag{A.69}$$

The non-dimensional form of the evolution equations can then be written as

$$\partial_{\tilde{t}} \tilde{h} = \tilde{\nabla} \cdot \left[\tilde{Q}_{hh} \tilde{\nabla}[W_\text{s}(\tfrac{1}{\tilde{h}^3} - \tfrac{1}{\tilde{h}^6}) - \tilde{\Delta} h] + \tilde{Q}_{h\Gamma} \tilde{\nabla} \ln(\tilde{\Gamma}) \right] + \tilde{G}(\tilde{h}) \tag{A.70}$$

$$\partial_{\tilde{t}} \tilde{\Gamma} = \tilde{\nabla} \cdot \left[\tilde{Q}_{\Gamma h} \tilde{\nabla}[W_\text{s}(\tfrac{1}{\tilde{h}^3} - \tfrac{1}{\tilde{h}^6}) - \tilde{\Delta} h] + \tilde{Q}_{\Gamma\Gamma} \tilde{\nabla} \ln(\tilde{\Gamma}) \right] + \tilde{P}(\tilde{h}, \tilde{\Gamma}) \tag{A.71}$$

with the dimensionless parameter

$$W_\text{s} = \frac{Aa^2}{h_\text{a}^2 k_B T} \tag{A.72}$$

defining the relative strength of wetting as compared to the energetic influence of the surfactant. The mobilities are given by

$$\tilde{Q}_{hh} = \frac{\tilde{h}^3}{3} \qquad \tilde{Q}_{\Gamma h} = \tilde{Q}_{h\Gamma} = \frac{\tilde{h}^2 \tilde{\Gamma}}{2} \qquad Q_{\tilde{\Gamma}\tilde{\Gamma}} = \tilde{h}\tilde{\Gamma}^2 + \tilde{D}\tilde{\Gamma} \tag{A.73}$$

with a dimensionless diffusivity $\tilde{D} = \frac{\eta}{l} D$. The growth rate and production term in the dimensionless model read

$$\tilde{G}(\tilde{h}) = \tilde{g}(\tilde{h} - \tilde{h}_\text{u})\left(1 - \frac{\tilde{h}}{\tilde{h}^\star}\right)(1 - \exp(\tilde{h}_\text{s} - \tilde{h})) \tag{A.74}$$

$$\tilde{P}(\tilde{h}, \tilde{\Gamma}) = \tilde{p}\tilde{h}(\tilde{\Gamma}_\text{max} - \tilde{\Gamma})\Theta(\tilde{\Gamma}_\text{max} - \tilde{\Gamma})\Theta(\tilde{h} - h_\text{u}) \tag{A.75}$$

with the dimensionless biomass growth rate $\tilde{g} = \tau g$, the dimensionless surfactant production rate $\tilde{p} = \tau p l$ and the dimensionless film heights $\tilde{h}^\star = \frac{h^\star}{l}$ and $\tilde{h}_\text{s} = \frac{h_\text{s}}{l}$.
In the following, we omit the tildes that indicate dimensionless quantities.

A. Appendix

A.4.2. Formulation for Parameter Continuation

To analyse the model for surfactant-driven spreading of bacterial colonies with parameter continuation, we transform the evolution equations (A.70)-(A.70) into the co-moving coordinate system moving with a constant velocity v via the coordinate transformation $x \to x + vt$. The resulting equations contain derivatives of the film height h up to fourth order and derivatives of the surfactant concentration Γ up to second order. For the parameter continuation using *AUTO07p*, the system needs to be transformed into a system of first order differential equations. We choose the variables

$$u_1 = h \qquad u_2 = \Gamma \qquad u_3 = h_x \qquad u_4 = \Gamma_x \qquad u_5 = h_{xx} \qquad u_6 = h_{xxx} \tag{A.76}$$

where subscipt x stands for a spatial derivative and define the system of ordinary differential equations with $N_{\mathrm{DIM}} = 6$ as

$$\begin{aligned} \partial_x u_1 &= u_3 & \partial_x u_4 &= \Gamma_{xx} \\ \partial_x u_2 &= u_4 & \partial_x u_5 &= u_6 \\ \partial_x u_3 &= u_5 & \partial_x u_6 &= h_{xxxx}\,. \end{aligned} \tag{A.77}$$

The stationary version of Eqs. (A.70)-(A.71) thus need to be solved for the yet unknown expressions for Γ_{xx} and h_{xxxx}. After introducing the abbreviations

$$f_1 = W_{\mathrm{s}}(\tfrac{1}{h^3} - \tfrac{1}{h^6}) \tag{A.78}$$

$$f_3 = \ln(\Gamma)\,, \tag{A.79}$$

solving (A.70)-(A.71) for h_{xxxx} yields

$$h_{xxxx} = \tfrac{1}{Q_{hh}}[Q_{hh,x}(f_{1,x} - h_{xxx}) + Q_{hh}f_{1,xx} + Q_{h\Gamma,x}f_{3,x} + Q_{h\Gamma}f_{3,xx} + G + vh_x] \tag{A.80}$$

$$h_{xxxx} = \tfrac{1}{Q_{\Gamma h}}[Q_{\Gamma h,x}(f_{1,x} - h_{xxx}) + Q_{\Gamma h}f_{1,xx} + Q_{\Gamma\Gamma,x}f_{3,x} + Q_{\Gamma\Gamma}f_{3,xx} + P + v\Gamma_x]\,. \tag{A.81}$$

These two expressions for h_{xxxx} can be combined to obtain

$$\begin{aligned} f_{3,xx} = \frac{1}{\frac{Q_{\Gamma\Gamma}}{Q_{\Gamma h}} - \frac{Q_{h\Gamma}}{Q_{hh}}} &\left[\left(\frac{Q_{hh,x}}{Q_{hh}} - \frac{Q_{\Gamma h,x}}{Q_{h\Gamma}}\right)(f_{1,x} - h_{xxx}) + \left(\frac{Q_{h\Gamma,x}}{Q_{hh}} - \frac{Q_{\Gamma\Gamma,x}}{Q_{\Gamma h}}\right)f_{3,x} \right. \\ &\left. + \frac{vh_x + G}{Q_{hh}} - \frac{v\Gamma_x + P}{Q_{h\Gamma}} \right] - f_{2,xx}\,. \end{aligned} \tag{A.82}$$

The term $f_{3,xx}$ can also be expressed via the derivation of Eq. (A.79) w.r.t x. By combining the expressions, we find

$$\Gamma_{xx} = \Gamma\left(f_{3,xx} + \frac{\Gamma_x^2}{\Gamma^2}\right) \tag{A.83}$$

which can be used in Eqs. (A.80) to obtain h_{xxxx}.

As boundary conditions, we apply $h_x = \Gamma_x = h_{xxx} = 0$ on the left boundary and $h_x = \Gamma_x = 0$ and $\Gamma = \Gamma_0$ on the right boundary ($N_{\mathrm{BC}} = 6$), thereby fixing the surfactant concentration on the adsorption layer to a constant value. One integral condition is used to measure the drop volume ($N_{\mathrm{INT}} = 1$). This yields ($N_{\mathrm{BC}} + N_{\mathrm{INT}} - N_{\mathrm{DIM}} + 1) = 2$ free parameters.
The continuation run is initiated by a homotopy method, starting from a flat thin film without surfactant production with a small perturbation of critical wavelength as described in the tutorial [Thi15b].

A.4.3. Weak Formulation Used in Time Simulations

For the time simulations of the dimensionless evolution equations

$$\partial_t h = \nabla \cdot \left[Q_{hh} \nabla [W_{\mathrm{s}}(\tfrac{1}{h^3} - \tfrac{1}{h^6}) - \Delta h] + Q_{h\Gamma} \nabla \ln(\Gamma) \right] + G(h) \tag{A.84}$$

$$\partial_t \Gamma = \nabla \cdot \left[Q_{\Gamma h} \nabla [W_{\mathrm{s}}(\tfrac{1}{h^3} - \tfrac{1}{h^6}) - \Delta h] + Q_{\Gamma\Gamma} \nabla \ln(\Gamma) \right] + P(h, \Gamma) \,, \tag{A.85}$$

we formulate the system in terms of four variables

$$u_0 = h \qquad u_1 = W_{\mathrm{s}}(\tfrac{1}{h^3} - \tfrac{1}{h^6}) - \Delta h \qquad w_0 = \Gamma \qquad w_1 = \ln(\Gamma) \tag{A.86}$$

to reduce the order of the differential equations. The evolution equations are then given by

$$\partial_t u_0 = \nabla \cdot [Q_{hh} \nabla u_1 + Q_{h\Gamma} \nabla w_1] + G \tag{A.87}$$

$$u_1 = W_{\mathrm{s}}(\tfrac{1}{u_0^3} - \tfrac{1}{u_0^6}) - \Delta u_0 \tag{A.88}$$

$$\partial_t w_0 = \nabla \cdot [Q_{\Gamma h} \nabla u_1 + Q_{\Gamma\Gamma} \nabla w_1] + P \tag{A.89}$$

$$w_1 = \ln(w_0) \,. \tag{A.90}$$

We choose linear test- and ansatz-functions $\phi_0, ..., \phi_3$, multiply Eqs. (A.87)-(A.90) with these functions and integrate over the whole domain. After partial integration and applying Neumann boundary conditions (resulting in vanishing boundary integrals), the weak formulation of the problem used for the implementation in *DUNE* is given by

$$0 = \int_\Omega \mathrm{d}\mathbf{x} \left[\partial_t u_0 \phi_0 + [Q_{hh} \nabla u_1 + Q_{h\Gamma} \nabla w_1] \cdot \nabla \phi_0 - G \phi_0 \right] \tag{A.91}$$

$$0 = \int_\Omega \mathrm{d}\mathbf{x} \left[\left[-u_1 + W_{\mathrm{s}}(\tfrac{1}{u_0^3} - \tfrac{1}{u_0^6}) \right] \phi_1 + \nabla u_0 \cdot \nabla \phi_1 \right] \tag{A.92}$$

$$0 = \int_\Omega \mathrm{d}\mathbf{x} \left[\partial_t w_0 \phi_2 + [Q_{\Gamma h} \nabla u_1 + Q_{\Gamma\Gamma} \nabla w_1] \cdot \nabla \phi_2 - P \phi_2 \right] \tag{A.93}$$

$$0 = \int_\Omega \mathrm{d}\mathbf{x} \left[[-w_1 + \ln(w_0)] \phi_3 \right] \,. \tag{A.94}$$

A.5. Tutorial on the Implementation of a Transversal Linear Stability Analysis

The following section presents a tutorial on the implementation of a transversal linear stability analysis in *AUTO07p*. We focus on involved evolution equations which require the use of a symbolic computing environment to obtain an adequate formulation of the problem. We first briefly review the mathematical concept of a transversal stability analysis before presenting the method using the equations for surfactant-driven spreading of bacterial colonies as an example.

A.5.1. Concept of the Transversal Linear Stability Analysis

In general, linear stability analysis is a standard method to determine the stability of solutions with respect to small perturbations. Here, we are interested in the front solutions of the model for surfactant-driven spreading of bacterial colonies and therefore transform the evolution equations (A.84)-(A.85) into the co-moving frame in which front solutions correspond to stationary profiles. This yields

$$
\begin{aligned}
\partial_t h &= \nabla \cdot \left[Q_{hh} \nabla [W_{\mathrm{s}}(\tfrac{1}{h^3} - \tfrac{1}{h^6}) - \Delta h] + Q_{h\Gamma} \nabla \ln(\Gamma) \right] + G(h) - v\partial_x h \\
&= \mathscr{F}_1(\nabla, x, v)[h, \Gamma]
\end{aligned} \tag{A.95}
$$

$$
\begin{aligned}
\partial_t \Gamma &= \nabla \cdot \left[Q_{\Gamma h} \nabla [W_{\mathrm{s}}(\tfrac{1}{h^3} - \tfrac{1}{h^6}) - \Delta h] + Q_{\Gamma\Gamma} \nabla \ln(\Gamma) \right] + P(h, \Gamma) - v\partial_x \Gamma \\
&= \mathscr{F}_2(\nabla, x, v)[h, \Gamma]
\end{aligned} \tag{A.96}
$$

where we introduced $\mathscr{F}_{1,2}(\nabla, x, v)$ as a short hand notation for the nonlinear operators defined by the right-hand sides of the evolution equations. We assume the existence of a stationary front solution $(h_0(x), \Gamma_0(x))$ that fulfills

$$
0 = \nabla \cdot \left[Q_{hh} \nabla [W_{\mathrm{s}}(\tfrac{1}{h^3} - \tfrac{1}{h^6}) - \Delta h] + Q_{h\Gamma} \nabla \ln(\Gamma) \right] + G(h) - v\partial_x h \tag{A.97}
$$

$$
0 = \nabla \cdot \left[Q_{\Gamma h} \nabla [W_{\mathrm{s}}(\tfrac{1}{h^3} - \tfrac{1}{h^6}) - \Delta h] + Q_{\Gamma\Gamma} \nabla \ln(\Gamma) \right] + P(h, \Gamma) - v\partial_x \Gamma \tag{A.98}
$$

and study the temporal evolution of this solution under the influence of a small perturbation $(\delta_h(x, y, t), \delta_\Gamma(x, y, t))$. Inserting the ansatz

$$
h(x, y) = h_0(x) + \delta_h(x, y, t) \tag{A.99}
$$

$$
\Gamma(x, y) = \Gamma_0(x) + \delta_\Gamma(x, y, t) \tag{A.100}
$$

into Eqs. (A.95)-(A.96) and expanding $\mathscr{F}_{1,2}$ about the front solution $(h_0(x), \Gamma_0(x))$ gives

$$
\begin{aligned}
\tfrac{\partial}{\partial t} h_0(x) + \tfrac{\partial}{\partial t} \delta_h(x, y, t) &= \mathscr{F}_1[h_0(x) + \delta_h(x, t), \Gamma_0(x) + \delta_\Gamma(x, y, t)] \\
&= \mathscr{F}_1[h_0(x), \Gamma_0(x)] + \mathscr{F}'_{1h}|_{h_0(x), \Gamma_0(x)} \delta_h(x, y, t) + \mathscr{F}'_{1\Gamma}|_{h_0(x), \Gamma_0(x)} \delta_\Gamma(x, y, t) + O(\delta_h^2, \delta_\Gamma^2)
\end{aligned} \tag{A.101}
$$

$$
\begin{aligned}
\tfrac{\partial}{\partial t} \Gamma_0(x) + \tfrac{\partial}{\partial t} \delta_\Gamma(x, y, t) &= \mathscr{F}_2[h_0(x) + \delta_h(x, y, t), \Gamma_0(x) + \delta_\Gamma(x, y, t)] \\
&= \mathscr{F}_2[h_0(x), \Gamma_0(x)] + \mathscr{F}'_{2h}|_{h_0(x), \Gamma_0(x)} \delta_h(x, y, t) + \mathscr{F}'_{2\Gamma}|_{h_0(x), \Gamma_0(x)} \delta_\Gamma(x, y, t) + O(\delta_h^2, \delta_\Gamma^2).
\end{aligned} \tag{A.102}
$$

Here, $\mathscr{F}'_{h,\Gamma}$ are linear operators denoting the Fréchet-derivatives of the nonlinear operators $\mathscr{F}$ with respect to h and Γ. The terms in order zero vanish because $(h_0(x), \Gamma_0(x))$ is a stationary front solution. The first order in δ gives two coupled linear evolution equations for the perturbation

$$
\tfrac{\partial}{\partial t} \delta_h(x, y, t) = \mathscr{F}'_{1h}|_{h_0(x), \Gamma_0(x)} \delta_h(x, y, t) + \mathscr{F}'_{1\Gamma}|_{h_0(x), \Gamma_0(x)} \delta_\Gamma(x, y, t) \tag{A.103}
$$

$$
\tfrac{\partial}{\partial t} \delta_\Gamma(x, y, t) = \mathscr{F}'_{2h}|_{h_0(x), \Gamma_0(x)} \delta_h(x, y, t) + \mathscr{F}'_{2\Gamma}|_{h_0(x), \Gamma_0(x)} \delta_\Gamma(x, y, t). \tag{A.104}
$$

To analyse the transversal stability of the front solutions in the co-moving frame, we employ the ansatz

$$h = h_0(x) + \sum_j h_{1,j}(x) \exp(ik_y y + \sigma_j t) \tag{A.105}$$

$$\Gamma = \Gamma_0(x) + \sum_j \Gamma_{1,j}(x) \exp(ik_y y + \sigma_j t) \tag{A.106}$$

which corresponds to a plane-wave ansatz for the perturbation in y-direction with an exponential time dependence. Inserting it into Eqs. (A.103)-(A.104) results in the equations

$$\sigma_j h_{1,j}(x) = \mathscr{F}'_{1h}|_{h_0(x),\Gamma_0(x)} h_{1,j}(x) + \mathscr{F}'_{1\Gamma}|_{h_0(x),\Gamma_0(x)} \Gamma_{1,j}(x) \tag{A.107}$$

$$\sigma_j \Gamma_{1,j}(x) = \mathscr{F}'_{2h}|_{h_0(x),\Gamma_0(x)} h_{1,j}(x) + \mathscr{F}'_{2\Gamma}|_{h_0(x),\Gamma_0(x)} \Gamma_{1,j}(x) \tag{A.108}$$

for the j-th eigenmode. Statements about the linear stability of the front $(h_0(x), \Gamma_0(x))$ can now be made by determining the largest eigenvalue $\sigma_j(k_y)$ which tells if the perturbation grows (for $\sigma_j > 0$) or decays (for $\sigma_j < 0$) in time (here assuming σ_j is real).

A.5.2. Implementation in AUTO07p

The linear eigenvalue problem (A.107)-(A.108) is solved by parameter continuation employing the software package *AUTO07p*. To that end, the set of equations for the stationary front profiles $h_0(x)$ and $\Gamma_0(x)$ are supplemented by a set of equations for the eigenfunctions $h_1(x)$ and $\Gamma_1(x)$. This approach, in which transversal wave number and eigenvalue are treated as parameters in a pseudo-arclength continuation is presented in tutorial form in [Thi15b]. For the implementation in *AUTO07p*, the system is formulated as a system of first order differential equations by introducing the variables

$$\begin{aligned} u_1 &= h_0 \quad u_2 = \Gamma_0 \quad u_3 = h_{0,x} \quad u_4 = \Gamma_{0,x} \quad u_5 = h_{0,xx} \quad u_6 = h_{0,xxx} \\ u_7 &= h_1 \quad u_8 = \Gamma_1 \quad u_9 = h_{1,x} \quad u_{10} = \Gamma_{1,x} \quad u_{11} = h_{1,xx} \quad u_{12} = h_{1,xxx} \end{aligned} \tag{A.109}$$

where subscipt x stands for a spatial derivative. The system of ordinary differential equations with $N_{\mathrm{DIM}} = 12$ is then defined as

$$\begin{aligned} \partial_x u_1 &= u_3 & \partial_x u_4 &= \Gamma_{0,xx} & \partial_x u_7 &= u_9 & \partial_x u_{10} &= \Gamma_{1,xx} \\ \partial_x u_2 &= u_4 & \partial_x u_5 &= u_6 & \partial_x u_8 &= u_{10} & \partial_x u_{11} &= u_{12} \\ \partial_x u_3 &= u_5 & \partial_x u_6 &= h_{0,xxxx} & \partial_x u_9 &= u_{11} & \partial_x u_{12} &= h_{1,xxxx} \, . \end{aligned} \tag{A.110}$$

In a first step, Eqs. (A.97)-(A.98) and Eqs. (A.107)-(A.108) for (h_1, Γ_1) thus need to be solved for the yet unknown expressions for $\Gamma_{0,xx}$, $h_{0,xxxx}$, $\Gamma_{1,xx}$ and $h_{1,xxxx}$. This is done by implementing the problem in the software package *maple* as presented below in Sec. A.5.3.

We apply $N_{\mathrm{BC}} = 12$ boundary conditions

$$\begin{aligned} h_{0,x} = \Gamma_{0,x} = h_{0,xxx} = h_{1,x} = \Gamma_{1,x} = h_{1,xxx} = 0 \quad &\text{on the left boundary} \\ h_{0,x} = h_{0,xxx} = h_{1,x} = \Gamma_{1,x} = h_{1,xxx} = 0 \quad \Gamma_0 = \Gamma_{\mathrm{a}} \quad &\text{on the right boundary} \,, \end{aligned} \tag{A.111}$$

thereby fixing the surfactant concentration on the adsorption layer to a constant value Γ_{a}. One integral condition is applied to measure the drop volume $V_{h0} = \frac{1}{L} \int h_0(x) \mathrm{d}x$, another one is applied to measure the volume of the eigenfunction $V_{h1} = \frac{1}{L} \int h_1(x) \mathrm{d}x$, so that $N_{\mathrm{INT}} = 2$. This results in $(N_{\mathrm{BC}} + N_{\mathrm{INT}} - N_{\mathrm{DIM}} + 1) = 3$ free parameters.

A.5.3. Formulation in Maple

The objective of the implementation of the transversal linear stability analysis in *maple* is to obtain expressions for $\Gamma_{0,xx}$, $h_{0,xxxx}$, $\Gamma_{1,xx}$ and $h_{1,xxxx}$ needed for the formulation of the problem in *AUTO07p*. To that end, we use the same procedure as outlined in Sec. A.4.2. However, now the evolution equations need to be considered in a two-dimensional geometry.

The equivalent of Eq. (A.80) is given by

$$
\Delta^2 h = \frac{1}{Q_{hh}} \Big[\underbrace{\nabla Q_{hh} \cdot \nabla f_1}_{=:T_1} + \underbrace{Q_{hh} \Delta f_1}_{=:T_2} + \underbrace{\nabla Q_{h\Gamma} \cdot \nabla f_3}_{=:T_3} + \underbrace{Q_{h\Gamma} \Delta f_3}_{=:T_4}
$$
$$
\underbrace{- \nabla Q_{hh} \cdot \nabla \Delta h}_{=:T_5} + \underbrace{G + v h_x - \partial_t h}_{=:T_6} \Big] .
$$

(A.112)

The zeroth order in δ is used obtain an expression for $h_{0,xxxx}$, the first order in δ is employed to find an expression for $h_{1,xxxx}$. The term $\Delta^2 h$ can also be written as

$$
\Delta^2 h = h_{0,xxxx} + \Big(h_{1,xxxx} - 2 k_y^2 h_{1,xx} + k_y^4 h_1 \Big) e^{i k_y y + \sigma t} .
$$

(A.113)

The equivalent of Eq. (A.82) in two dimensions is

$$
\Delta f_3 = \frac{1}{\frac{Q_{\Gamma\Gamma}}{Q_{\Gamma h}} - \frac{Q_{h\Gamma}}{Q_{hh}}} \Big[\underbrace{\frac{1}{Q_{hh}} \nabla Q_{hh} \cdot \nabla (f_1 - \Delta h)}_{=:T_7} - \underbrace{\frac{1}{Q_{\Gamma h}} \nabla Q_{\Gamma h} \cdot \nabla (f_1 - \Delta h)}_{=:T_8} + \underbrace{\frac{1}{Q_{h\Gamma}} \nabla Q_{h\Gamma} \cdot \nabla f_3}_{=:T_{10}}
$$
$$
\underbrace{- \frac{1}{Q_{h\Gamma}} \nabla Q_{\Gamma\Gamma} \cdot \nabla f_3}_{=:T_{11}} + \underbrace{\frac{G}{Q_{hh}} - \frac{P}{Q_{h\Gamma}} + v \frac{h_x}{Q_{hh}} - v \frac{\Gamma_x}{Q_{h\Gamma}} - \frac{1}{Q_{hh}} \partial_t h + \frac{1}{Q_{h\Gamma}} \partial_t \Gamma}_{=:T_{12}} \Big] .
$$

(A.114)

The term Δf_3 can also be expressed via the spatial derivation of Eq. (A.79) and we find

$$
\Gamma_{xx} = \Gamma \Delta f_3 + \frac{\Gamma_x^2}{\Gamma} - \Gamma_{yy} + \frac{\Gamma_{yy}}{\Gamma} .
$$

(A.115)

Listing A.1 below shows a code excerpt of the file 'LTSABioSurfactantModel.mw' which contains the implementation in *maple*. After loading necessary packages (l. 1-4), the energetic contributions, mobilities and non-conserved terms are defined in terms of functions $h(x, y, t)$ and $\Gamma(x, y, t)$ (l. 6-20). Next, the ansatz for the transversal linear stability analysis consisting of planar fronts with harmonic perturbations in y-direction as given in Eqs. (A.105)-(A.106) is specified (l. 17-19).

The expressions for $\Gamma_{0,xx}$ and $\Gamma_{1,xx}$ are derived first. To that end, the terms contributing to Eq. (A.114) are defined (l. 24-30) and summed (l. 33-37). Note that the surfactant production P containing tanh-terms is treated separately (l. 42-45), as it causes problems with the *maple* routine for simplifying expressions. The expression obtained for Γ_{xx} is expanded in a series in ϵ, a parameter employed to introduce the smallness of the eigenfunctions (l. 39-40). The zeroth and first order are used to obtain expressions for $\Gamma_{0,xx}$ and $\Gamma_{1,xx}$, respectively (l. 47-51). These can then be transformed to Fortran code (l. 53-68) to facilitate the implementation in *AUTO07p*.

The same procedure is performed to obtain expressions for $h0, xxxx$ and $h_{1,xxxx}$ from Eqs. (A.112) and (A.113).

```
 1  # Load necessary packages
 2  > restart:
 3  > with(LinearAlgebra):
 4  > with(codegen):

 6  # Define the energies, mobility matrix and non-conserved terms:
 7  > f1 := W*(1/h(x,y,t)^3-1/h(x, y, t)^6):
 8  > f3 := log(G(x,y,t)):
 9  > Qhh := (1/3)*h(x,y,t)^3:
10  > QGh := (1/2)*h(x,y,t)^2*G(x,y,t):
11  > QhG := (1/2)*h(x,y,t)^2*G(x,y,t):
12  > QGG := h(x,y,t)*G(x,y,t)^2+Diff*G(x,y,t):
13  > Production := (.5*pr*(Gmax-G(x,y,t))*(tanh(c1*(Gmax-G(x,y,t)))+1.)*.5)
14              *(tanh(c2*(h(x,y,t)-hu))+1.)*h(x,y,t):
15  > Growth := gr*(h(x,y,t)-hu)*(1.-h(x,y,t)/hstar)*(1.-exp(hp-h(x,y,t))):

17  # Ansatz for h and Gamma:
18  > h := h0(x)+eps*h1(x)*exp(I*k*y+sigma*t):
19  > G := G0(x)+eps*G1(x)*exp(I*k*y+sigma*t):
20  > Lh := diff(h(x,y,t),x,x)+diff(h(x,y,t),y,y):

22  # Obatin the expression for Gamma_{xx}

24  # Implementation of the terms contributing to Laplace(f3)
25  > T7 := ((diff(Qhh,x))*(diff(f1-Lh,x))+(diff(Qhh,y))*(diff(f1-Lh,y)))/Qhh:
26  > T8 := -((diff(QGh,x))*(diff(f1-Lh,x))+(diff(QGh,y))*(diff(f1-Lh,y)))/QGh:
27  > T10 := ((diff(QGh,x))*(diff(f3,x))+(diff(QGh,y))*(diff(f3,y)))/Qhh:
28  > T11 := -((diff(QGG,x))*(diff(f3,x))+(diff(QGG,y))*(diff(f3,y)))/QGh:
29  > T12 := Growth/Qhh+vel*(diff(h(x,y,t),x))/Qhh-vel*(diff(G(x,y,t),x))/QGh
30          -(diff(h(x,y,t),t))/Qhh+(diff(G(x,y,t),t))/QGh:

32  # expression for Laplace(f3)(without the terms containing tanh)
33  > equation126 := -(T7+T8+T10+T11+T12)/(QGh/Qhh-QGG/QGh):

35  # expression for Gamma_{xx} (without the terms containing tanh)
36  > equation127 := G(x,y,t)*equation126+(diff(G(x,y,t),x))^2/G(x,y,t)
37                  +(diff(G(x,y,t),y))^2/G(x,y,t)-(diff(G(x,y,t),y,y)):

39  # Expand expression for Gamma_{xx} in a series in eps:
40  > equation127 := simplify(series(equation127, eps, 2)):

42  # treat the terms with tanh separately, as maple has problems with
43  # simplifying the terms otherwise.
44  > PTerm := G(x,y,t)*Production/((QGh/Qhh-QGG/QGh)*QGh):
45  > PTerm := series(PTerm, eps, 2);

47  # Terms of zeroth order in eps:
48  > equation1270 := simplify(op(1,equation127)) + simplify(op(1,PTerm)):
49  # Terms of first order in eps:
50  > equation1271 := simplify(op(3, equation127)*exp(-I*k*y-sigma*t))
51                  + simplify(op(3, PTerm)*exp(-I*k*y-sigma*t)) ;

53  # No more derivatives need to be performed, introduce symbolic expressions
54  > equation1270subs:=subs({G0(x)=G, G1(x)=G1, diff(G0(x),x)=Gx,
55          diff(h0(x),x)=hx, diff(h1(x),x)=h1x, diff(G0(x),x,x)=Gxx,
56          diff(G1(x),x,x)=G1xx, diff(h0(x),x,x)=hxx, diff(h1(x),x,x)=h1xx,
57          diff(h0(x),x,x,x)=hxxx, diff(h1(x),x,x,x)=h1xxx, diff(G1(x),x)=G1x,
58          h0(x)=h, h1(x)=h1}, equation1270 + PTerm0)
59  > equation1271subs:=subs({G0(x)=G, G1(x)=G1, diff(G0(x),x)=Gx,
60          diff(h0(x),x)=hx, diff(h1(x),x)=h1x, diff(G0(x),x,x)=Gxx,
61          diff(G1(x),x,x)=G1xx, diff(h0(x),x,x)=hxx, diff(h1(x),x,x)=h1xx,
62          diff(h0(x),x,x,x)=hxxx, diff(h1(x),x,x,x)=h1xxx, diff(G1(x),x)=G1x,
```

```
63                  h0(x)=h, h1(x)=h1}, equation1271 + PTerm1)

65  # Transform the expressions to Fortran Code:
66  > fortran(equation1270subs);
67  > fortran(equation1271subs);

69  # Obatin the expression for h_{xxxx}

71  # Implementation of the terms contributing to Laplace(h)

73  > T1 := (diff(Qhh, x))*(diff(f1, x))+(diff(Qhh, y))*(diff(f1,y));
74  > T2 := Qhh*(diff(f1,x,x)+diff(f1,y,y));
75  > T3 := (diff(QGh,x))*(diff(f3,x))+(diff(QGh, y))*(diff(f3,y));
76  > T4 := QhG*(diff(f3,x,x)+diff(f3+f3,y,y));
77  > T5 := -(diff(Qhh,x))*(diff(Lh,x))-(diff(Qhh,y))*(diff(Lh,y));
78  > T6 := Growth+vel*(diff(h(x,y,t),x))-(diff(h(x,y,t),t));

80  # Series expansion of expression for Laplace(h)
81  > equation124 := simplify(series((T1+T2+T3+T4+T5+T6)/Qhh, eps, 2));

83  # Terms of zeroth order in eps:
84  > equation1240 := simplify(op(1, equation124));
85  # Terms of first order in eps:
86  >  equation1241 := simplify(op(3, equation124)*exp(-I*k*y-sigma*t));

88  # No more derivatives need to be performed, introduce symbolic expressions
89  > equation1240subs:=subs({G0(x)=G, G1(x)=G1, diff(G0(x),x)=Gx,
90              diff(h0(x),x)=hx, diff(h1(x),x)=h1x, diff(G0(x),x,x)=Gxx,
91              diff(G1(x),x,x)=G1xx, diff(h0(x),x,x)=hxx, diff(h1(x),x,x)=h1xx,
92              diff(h0(x),x,x,x)=hxxx, diff(h1(x),x,x,x)=h1xxx, diff(G1(x),x)=G1x,
93              h0(x)=h, h1(x)=h1}, equation1240)
94  > equation1241subs:=subs({G0(x)=G, G1(x)=G1, diff(G0(x),x)=Gx,
95              diff(h0(x),x)=hx, diff(h1(x),x)=h1x, diff(G0(x),x,x)=Gxx,
96              diff(G1(x),x,x)=G1xx, diff(h0(x),x,x)=hxx, diff(h1(x),x,x)=h1xx,
97              diff(h0(x),x,x,x)=hxxx, diff(h1(x),x,x,x)=h1xxx, diff(G1(x),x)=G1x,
98              h0(x)=h, h1(x)=h1}, equation1241)
99  > equation1241 = simplify(equation1241subs)

101 # Take care of y- derivatives in Laplace^2(h), need expr. for h_{1,xxxx}
102 > equation1241subs := -h1*k^4+2*h1xx*k^2+equation1241subs;

104 # Transform the expression to Fortran Code:
105 > fortran(equation1240subs);
106 > fortran(equation1241subs);
```

Listing A.1: Excerpt from the file 'LTSABioSurfactantModel.mw' containing the implementation of the transversal linear stability analysis in *maple*.

A.5.4. Performing the Parameter Continuation in AUTO07p

All necessary files for the linear stability analysis are compressed in the folder 'LTSA.zip'. The continuation is coordinated by the python script 'bioskript.auto' which loads the correct equation and parameter file for each run. It can be executed with the command

```
auto bioskript.auto
```

in the unix shell. Listing A.2 exemplarily shows how a run named 'prep2run1' is executed starting from the point 'UZ1' of the previous run 'prep1run1' using the equation file 'BiofilmFluxTSA' and the constants file 'c.prep2run1' and how it is subsequently saved and plotted.

```
32   prep2run1=run('prep1run1',e='BiofilmFluxTSA',c='prep2run1',IRS='UZ1')
33   save(prep2run1,'prep2run1')
34   plot prep2run1
35   wait()
```

Listing A.2: Excerpt from the file 'bioskript.auto' showing how a run can be started, saved and plotted using python commands.

The parameter continuation consists of two main stages which are outlined in the following.

Preparation Stage: Start the Parameter Continuation and Go to Moving Fronts

The continuation run is initiated starting from a flat thin film without surfactant production as described in the tutorial [Thi15b]. As starting solution for (h_0, Γ_0), we use a film of height $h_0 = 2$ with a small amplitude modulation of wavelength $L = 2\pi/k_c$ and constant surfactant concentration $\Gamma_0 = 0.0001$. Here,

$$k_c = \sqrt{-\frac{\partial^2 f_{\mathrm{w}}}{\partial h^2}\bigg|_{h=h_0}} = \sqrt{-W_{\mathrm{m}}\left(-\frac{3}{h_0^4} + \frac{6}{h_0^7}\right)} \tag{A.116}$$

is the critical wavenumber for the linear instability of a flat film of thickness h_0. The starting solution for the eigenfunctions is the trivial eigenfunction $h_1 = \Gamma_1 = 0$.

In the first two runs, we study steady profiles without bioactivity and go from a flat film towards droplet solutions. In the runs 'prep2run2' to 'prep2run4', the biomass growth rate g and the surfactant production rate p are increased. Note that at this stage, the correct tanh-terms for the approximation of the Θ-functions in the production term have not been activated yet. In the third part of the preparation stage, we study moving fronts, vary the model parameters to the parameter regime for which the transversal instability is expected and introduce the correct tanh-terms.

The runs performed in the preparation stage for transversal linear stability analysis are summarised in Table A.3.

run	continuation parameters	description
prep1run1	L, g, p	Go from a flat film solution to a droplet, starting at the critical L with one period of a small-amplitude sinusoidal solution
prep2run1	V_{h0}, g, p	Increase the volume of the droplet
prep2run2 - prep2run3	g, V_{h0}, V_{h1}	Increase the biomass production from 0 to 10^{-3} and let drop volume adapt, considering arrested profiles
prep2run4	p, v, V_{h1}	Increase the surfactant production from 0 to 10^{-6} and let v adapt, now considering moving fronts.
prep3run1 -prep3run8	X, v, V_{h1}	Go to the parameter regime in which the LTSA shall be performed, modify one parameter X in each run. An exception is prep3run6, in which the tanh-terms are switched on.

Table A.3.: Summary of the runs executed in the preparation stage for the transversal linear stability analysis with *AUTO07p*.

LTSA Stage: Introduce the Eigenfunctions and Calculate the Dispersion Relation

This stage contains the runs connected to the transversal linear stability analysis. First, we introduce the eigenfunctions. To that end, the eigenvalue σ is varied in run 'LTSA1run1'. This is possible because the eigenfunctions still correspond the trivial solution. 'True' eigenvalues are detected as branching points if we set the parameter ISP=3. These detected branching points can then be used as a starting point for the run 'LTSA1run2' in which the branch is switched by setting ISW=-1 and the volume of the eigenfunction is increased. The dispersion relation can be calculated by varying the wave number k_y.

The code excerpt from 'bioskript.auto' in Listing A.3 shows how running *AUTO07p* with python commands can be used to perform sequences of commands automatically. In the run 'LTSA2run1', stops are created at two different parameter values of $\Gamma_{\max}$, for which the dispersion relation shall be calculated. Then, a loop construction can be used to perform the respective runs in k_y (l. 139-143), save (l. 147-149) and plot (l. 153-158) the dispersion relations. In addition, we save the solutions for (h_0, Γ_0) and (h_1, Γ_1) at the maximum of the dispersion relation (l. 160-172).

To find the onset of the transversal instability, the maximum of the dispersion relation can be followed by employing a fold continuation. This is done in the third part of the LTSA stage for a variation of the parameter $\Gamma_{\max}$. The fold point is detected in run 'LTSA2run1' and subsequently followed in runs 'LTSA2run2'-'LTSA2run3'.

All runs performed in the transversal linear stability analysis are summarised in Table A.4.

```
127   LTSA2run1=run('LTSA1run2',e='BiofilmFluxTSA',c='LTSA2run1',IRS='EP1',
128          UZR = {7:[0.5,0.02]},UZSTOP = {7:0.019})
129   save(LTSA2run1,'LTSA2run1')
130   plot LTSA2run1
131   wait()

133   for Start in ['UZ1','UZ2']:
134     if Start=='UZ1': Gmax = 0.5
135     if Start=='UZ2': Gmax = 0.02

137     # calculate the dispersion relation for Gmax = 0.5 and Gmax = 0.02

139     LTSA2run2 = run('LTSA2run1', e='BiofilmFluxTSA', c='LTSA2run2', IRS = Start,
140        UZR= {44:[1e-10, 4.85e-03 ]}, UZSTOP = {44:   0.02})
141     save(LTSA2run2,'LTSA2run2')
142     plot LTSA2run2
143     wait()

145     # save the dispersion relation

147     k     =  np.array(LTSA2run2['PAR(44)'])
148     sigma =  np.array(LTSA2run2['PAR(43)'])
149     np.savetxt('Disp_Gmax='+str(Gmax)+'.dat', np.transpose([k, sigma]))

151     # plot the dispersion relation

153     plt.figure()
154     plt.xlabel('$k_y$')
155     plt.ylabel('$sigma$')
156     plt.plot(k, sigma)
157     plt.tight_layout()
158     plt.savefig('Disp_Gmax='+str(Gmax)+'.png')

160     # save the solutions at the maximum of the disp. relation
161     if Gmax == 0.5:
162       stopper='UZ2'  # corresp. to max. of the disp. relation at ky = 4.85e-03
163       x  = LTSA2run2(stopper)['t']*LTSA2run2(stopper)['per']
164       h,G  = LTSA2run2(stopper)['h'],LTSA2run2(stopper)['G']
165       h1,G1= LTSA2run2(stopper)['h1'],LTSA2run2(stopper)['G1']
166       np.savetxt('Solution_Gmax=0.5_k=kmax', np.transpose([x,h,G,h1,G1]))
167     if Gmax == 0.02:
168       stopper='UZ1'# corresp. to max. fo the disp. relation at ky = 0
169       x  = LTSA2run2(stopper)['t']*LTSA2run2(stopper)['per']
170       h,G  = LTSA2run2(stopper)['h'],LTSA2run2(stopper)['G']
171       h1,G1= LTSA2run2(stopper)['h1'],LTSA2run2(stopper)['G1']
172       np.savetxt('Solution_Gmax=0.02_k=0', np.transpose([x,h,G,h1,G1]))
```

Listing A.3: Excerpt from the file 'bioskript.auto' showing how running *AUTO07p* with python commands can be used to perform sequences of commands automatically. A loop construction is employed to perform (l. 139-143), save (l. 147-149) and plot (l. 153-158) runs in k_y to obtain the dispersion relations for different values of Γ_{max}.

run	continuation parameters	ISP	ISW	description
LTSA1run1	σ, v, V_{h1}	ISP= 3	ISW= 1	Change the eigenvalue σ from zero for the trivial eigenfunction $h_1 = \Gamma_1 = 0$. 'True' eigenvalues are detected as branching points.
LTSA1run2	σ, v, V_{h1}	ISP= 1	ISW= -1	Restarting at a branching point, we switch branch. This 'blows up' the corresponding eigenfunction (h_1, Γ_1) from zero. Its norm is measured by the second integral condition.
LTSA2run1	$\Gamma_{\max}$, v, σ	ISP= 1	ISW= 1	Generate a run in $\Gamma_{\max}$ with two stops at $\Gamma_{\max} = 0.5$ and $\Gamma_{\max} = 0.02$ which serve as starting points to obtain the respective dispersion relation
LTSA2run2	k_y, v, σ	ISP= 1	ISW= 1	Calculate the dispersion relation by starting at the respective point on run LTSA2run1 and varying the wave number k_y.
LTSA3run1	σ, k_y, $\Gamma_{\max}$	ISP= 1	ISW= 1	Find the maximum of the dispersion relation as a fold point.
LTSA3run2 LTSA3run3	σ, k_y, $\Gamma_{\max}$	ISP= 1	ISW= 2	Restart at the fold point and perform a fold continuation varying $\Gamma_{\max}$ and tracking the maximum of the dispersion relation as a fold.

Table A.4.: Summary of the runs executed in the LTSA stage of the transversal linear stability analysis with *AUTO07p*.

List of Recurrent Symbols and Abbreviations

$h(\mathbf{x}, t)$: film height

$\mathcal{F}$: free energy functional

γ : liquid-gas interfacial tension

γ_{sl} : solid-liquid interfacial tension

γ_{sg} : solid-gas interfacial tension

κ : curvature of the free surface

p : pressure

f_{w} : wetting energy

A : Hamaker constant

h_{a} : adsorption layer thickness

$\Pi(h)$: disjoining pressure

θ_{eq} : equilibrium contact angle

Q : mobility

$\mathbf{u}^{(3)}$: three-dimensional velocity field within the film

$\mathbf{u}$: components of the three-dimensional velocity parallel to the substrate

η : (kinematic) viscosity

$\underline{\tau}$: stress tensor

f_{m} : free energy density of mixing

W_{m} : wettability parameter in the model for thin films of mixtures

G : biomass growth term

ζ : osmotic influx into the biofilm

$\phi_{1/2}(\mathbf{x}, t)$: local concentration of solvent/solute in the model for films of mixtures

$\psi_{1/2}(\mathbf{x}, t)$: effective layer thickness of solvent/solute in the model for films of mixtures

ϕ_{eq} : equilibrium biomass concentration in the biofilm representing osmotic equilibrium

Q_{osm} : mobility of the osmotic influx

Π_{s} : osmotic pressure in the biofilm

Π_{agar} : osmotic pressure in the agar substrate

A. Appendix

$\eta_{b/0}$: viscosity of solute / solvent

$\hat{\eta}$: dimensionless function to model the concentration-dependent viscosity

v : velocity of fronts or moving active droplets

$g(\Gamma)$: free energy of the surfactant-covered liquid-gas interface

$g_{sg}(\Gamma)$: free energy of the surfactant-covered solid-gas interface

ξ : metric factor describing the curved free surface

Γ : surfactant concentration on the surface

$\Gamma_{a/d/w}$: surfactant concentration on the adsorption layer / drop / wedge

$\epsilon_{1/2}$: dim.less parameters in the model for passive drops covered by insoluble surfactant

Γ_p : surfactant concentration projected onto the solid substrate

W_s : wettability parameter in the model for thin films covered by insoluble surfactant

$\mathbf{p}(\mathbf{x}, t)$: height-averaged mean polarisation vector

$\mathbf{P}(\mathbf{x}, t)$: height-averaged total polarisation vector

$\boldsymbol{\sigma}^a$: active stress tensor

$\boldsymbol{\alpha}$: active flux due to self-propulsion

M : diffusion constant of the polarisation

c_p : constant defining the strength of the liquid crystal elastic energy

c_{sp} : constant defining the strength of the spontaneous polarisation

c_{hp} : constant defining the strength of the coupling of polarisation and interface

c_a : constant defining the strength of the active stress

α_0 : strength of self-propulsion

List of Publications

The following articles were produced during the course of this thesis and contain pre-publications of results:

- S. Trinschek, K. John and U. Thiele. *From a thin film model for passive suspensions towards the description of osmotic biofilm spreading* AIMS Materials Science, 3, 1138-1159 (2016)
  Original research article introducing and analysing the model for osmotic biofilm spreading. The model was developed and the results interpreted by ST, KJ and UT. Text, numerical simulation data and figures were produced by ST, with critical review of KJ and UT.

- S. Trinschek, K. John, S. Lecuyer and U. Thiele. *Continuous versus arrested spreading of biofilms at solid-gas interfaces: The role of surface forces.* Physical Review Letters, 119, 078003 (2016)
  Original research article analysing the non-equilibrium transition between arrested and continuously spreading biofilms. Text, numerical simulation data and figures were produced by ST, with critical review of KJ and UT. The experimental data and description of the experiment were provided by SL.

- U. Thiele, J. Snoeijer, S. Trinschek, K. John. *Equilibrium contact angle and adsorption layer properties with surfactants* Langmuir 34, 7210–7221 (2017)
  Original research article discussing the relation between a macroscopic and mesoscopic description of surfactant-covered drops. The calculations were performed by KJ, UT, JS and ST following an idea of JS and UT. The text was mainly written by ST and KJ with contributions of UT and critical review of JS. The numerical simulation data and figures were produced by ST.

- U. Thiele, J. Snoeijer, S. Trinschek, K. John. *Correction to 'Equilibrium contact angle and adsorption layer properties with surfactants'* Langmuir 35, 4788-4789 (2019)
  Correction to the aforementioned article in response to constructive criticism of Mathis Plapp. The calculations were performed by KJ, UT, JS and ST. The text was written by ST and KJ with critical review of UT and JS. The numerical simulation data and figures were produced by ST.

- S. Trinschek, K. John, and U. Thiele. *Modelling of surfactant-driven front instabilities in spreading bacterial colonies* Soft Matter, 14, 4464-4476 (2018)
  Original research article introducing and analysing the model for the surfactant-driven spreading of bacterial colonies. The model was developed and the results interpreted by ST, KJ and UT. Text, numerical simulation data and figures were produced by ST, with critical review of KJ and UT

The following article resulted from a collaboration with the group 'AG Betz: Mechanics of Cellular Systems' and is not discussed in this thesis:

- B. Wallmeyer, S. Trinschek, S. Yigit, U. Thiele, T. Betz. *Collective Cell Migration in Embryogenesis Follows the Laws of Wetting* Biophysical journal 114.1, 213-222

A. Appendix

(2018)

Original research article studying the influence of wetting on the embryogenesis of zebrafish. BW, SY, and TB designed the experimental research. BW performed and analyzed the experiments. BW, ST, UT, and TB developed the presented model. ST performed the simulations. BW and TB wrote the manuscript. All authors together developed the interpretation and progression of experiments and modelling.

Bibliography

[AK07] E. Alpkvist and I. Klapper. A multidimensional multispecies continuum model for heterogeneous biofilm development. *Bull. Math. Biol.*, 69(2):765–789, 2007.

[AKR$^+$12] M. Asally, M. Kittisopikul, P. Rué, Y. Du, Z. Hu, T. Çağatay, A. B. Robinson, H. Lu, J. Garcia-Ojalvo, and G. M. Süel. Localized cell death focuses mechanical forces during 3d patterning in a biofilm. *Proc. Natl. Acad. Sci. U. S. A.*, 109(5):18891–6, 2012.

[Ale77] R. Alexander. Diagonally implicit Runge–Kutta methods for stiff ODEs. *SIAM Journal on Numerical Analysis*, 14(6):1006–1021, 1977.

[ALG$^+$05] D. G. Aarts, H. N. Lekkerkerker, H. Guo, G. H. Wegdam, and D. Bonn. Hydrodynamics of droplet coalescence. *Phys. Rev. Lett.*, 95(16):164503, 2005.

[ARK$^+$09] T. Angelini, M. Roper, R. Kolter, D. A. Weitz, and M. P. Brenner. Bacillus subtilis spreads by surfing on waves of surfactant. *Proc. Natl. Acad. Sci. USA*, 106(43):18109–18113, 2009.

[ASLM03] A. B. Afsar-Siddiqui, P. F. Luckham, and O. K. Matar. Unstable spreading of aqueous anionic surfactant solutions on liquid films. Part 1. Sparingly soluble surfactant. *Langmuir*, 19(3):696–702, 2003.

[ASLM04] A. Afsar-Siddiqui, P. Luckham, and O. Matar. Dewetting behavior of aqueous cationic surfactant solutions on liquid films. *Langmuir*, 20(18):7575–7582, 2004.

[BBD$^+$08a] P. Bastian, M. Blatt, A. Dedner, C. Engwer, R. Klöfkorn, R. Kornhuber, M. Ohlberger, and O. Sander. A generic grid interface for parallel and adaptive scientific computing. Part I: Abstract framework. *Computing*, 82(2-3):103–119, 2008.

[BBD$^+$08b] P. Bastian, M. Blatt, A. Dedner, C. Engwer, R. Klöfkorn, R. Kornhuber, M. Ohlberger, and O. Sander. A generic grid interface for parallel and adaptive scientific computing. Part II: Implementation and tests in DUNE. *Computing*, 82(2-3):121–138, 2008.

[BBK$^+$13] I. Buttinoni, J. Bialké, F. Kümmel, H. Löwen, C. Bechinger, and T. Speck. Dynamical clustering and phase separation in suspensions of self-propelled colloidal particles. *Phys. Rev. Lett.*, 110(23):238301, 2013.

[BC00] N. Balmforth and R. Craster. Dynamics of cooling domes of viscoplastic fluid. *J. Fluid Mech.*, 422:225–248, 2000.

[BC01] M. Ben Amar and L. J. Cummings. Fingering instabilities in driven thin nematic films. *Phys. Fluids*, 13(5):1160–1166, 2001.

BIBLIOGRAPHY

[BCKS18]   M. A. Bruning, M. Costalonga, S. Karpitschka, and J. H. Snoeijer. Delayed coalescence of surfactant containing sessile droplets. *Phys. Rev. Fluids*, 3:073605, 2018.

[BCO81]   E. Becker, G. Carey, and J. Oden. *Finite Elements: An Introduction*. Texas finite element series. Prentice-Hall, 1981.

[BDS⁺16]   B. Bera, M. Duits, M. Stuart, D. van den Ende, and F. Mugele. Surfactant induced autophobing. *Soft Matter*, 12:4562–4571, 2016.

[BEI⁺09]   D. Bonn, J. Eggers, J. Indekeu, J. Meunier, and E. Rolley. Wetting and spreading. *Rev. Mod. Phys.*, 81:739–805, May 2009.

[BHM10]   P. Bastian, F. Heimann, and S. Marnach. Generic implementation of finite element methods in the distributed and unified numerics environment (DUNE). *Kybernetika*, 46(2):294–315, 2010.

[BJST⁺94]   E. Ben-Jacob, O. Schochet, A. Tenenbaum, I. Cohen, A. Czirok, and T. Vicsek. Generic modelling of cooperative growth patterns in bacterial colonies. *Nature*, 368(6466):46, 1994.

[BK07]   J. Burke and E. Knobloch. Homoclinic snaking: structure and stability. *Chaos*, 17(3):037102, 2007.

[BKW86]   I. Burdett, T. Kirkwood, and J. Whalley. Growth kinetics of individual Bacillus subtilis cells and correlation with nucleoid extension. *J. Bacteriol.*, 167(1):219–230, 1986.

[BM09]   A. Baskaran and M. C. Marchetti. Statistical mechanics and hydrodynamics of bacterial suspensions. *Proc. Natl. Acad. Sci. U.S.A*, 106(37):15567–15572, 2009.

[BSZ⁺09]   A. Be'er, R. S. Smith, H. Zhang, E.-L. Florin, S. M. Payne, and H. L. Swinney. Paenibacillus dendritiformis bacterial colony growth depends on surfactant but not on bacterial motion. *J. Bacteriol.*, 191(18):5758–5764, 2009.

[But16]   J. C. Butcher. *Numerical methods for ordinary differential equations*. John Wiley & Sons, 2016.

[BVFK05]   S. S. Branda, A. Vik, L. Friedman, and R. Kolter. Biofilms: the matrix revisited. *Trends Microbiol.*, 13(1):20–26, 2005.

[BWDMQDG91]   F. Brochard-Wyart, J. M. Di Meglio, D. Quére, and P. G. De Gennes. Spreading of nonvolatile liquids in a continuum picture. *Langmuir*, 7(2):335–338, 1991.

[Cah65]   J. W. Cahn. Phase separation by spinodal decomposition in isotropic systems. *J. Chem. Phys*, 42(1):93–99, 1965.

[CC99]   M. Cachile and A. Cazabat. Spontaneous spreading of surfactant solutions on hydrophilic surfaces: C_nE_m in ethylene and diethylene glycol. *Langmuir*, 15(4):1515–1521, 1999.

[CCB⁺99]   M. Cachile, A. Cazabat, S. Bardon, M. Valignat, and F. Vandenbrouck. Spontaneous spreading of surfactant solutions on hydrophilic surfaces. *Colloids Surf. A*, 159(1):47–56, 1999.

[Cha92]   S. Chandrasekhar. *Liquid Crystals*. Cambridge University Press, 2 edition, 1992.

[CK04]   N. G. Cogan and J. P. Keener. The role of the biofilm matrix in structural development. *Math. Med. Biol.*, 21(2), 2004.

[CM06]   R. Craster and O. Matar. Numerical simulations of fingering instabilities in surfactant-driven thin films. *Phys. Fluids*, 18(3):032103, 2006.

[CM07]   R. Craster and O. Matar. On autophobing in surfactant-driven thin films. *Langmuir*, 23:2588–2601, 2007.

[CM09]   R. V. Craster and O. K. Matar. Dynamics and stability of thin liquid films. *Rev. Mod. Phys.*, 81:1131–1198, 2009.

[CS86]   A. Cazabat and M. C. Stuart. Dynamics of wetting: effects of surface roughness. *J. Phys. Chem.*, 90(22):5845–5849, 1986.

[CSO05]   N. C. Caiazza, R. M. Shanks, and G. O'Toole. Rhamnolipids modulate swarming motility patterns of Pseudomonas aeruginosa. *J. Bacteriol.*, 187(21):7351–7361, 2005.

[CW89]   J.-D. Chen and N. Wada. Wetting dynamics of the edge of a spreading drop. *Phys. Rev. Lett.*, 62(26):3050, 1989.

[DCC$^+$04]   C. Dombrowski, L. Cisneros, S. Chatkaew, R. E. Goldstein, and J. O. Kessler. Self-concentration and large-scale coherence in bacterial dynamics. *Phys. Rev. Lett.*, 93(9):098103, 2004.

[DD69]   A. Dupré and P. Dupré. *Théorie mécanique de la chaleur*. Gauthier-Villars, 1869.

[DDFMV15]   R. De Dier, M. Fauvart, J. Michiels, and J. Vermant. The role of biosurfactants in bacterial systems. In *The Physical Basis of Bacterial Quorum Communication*, pages 189–204. Springer, 2015.

[Der87]   B. V. Derjaguin. Some results from 50 years' research on surface forces. In *Surface Forces and Surfactant Systems*, pages 17–30. Springer, 1987.

[Deu04]   P. Deuflhard. *Newton methods for nonlinear problems: affine invariance and adaptive algorithms*. Springer Series in Computational Mathematics. Springer, Berlin Heidelberg, 2004.

[DFFGI96]   R. Dillon, L. Fauci, A. Fogelson, and D. Gaver III. Modeling biofilm processes using the immersed boundary method. *J. Comput. Phys.*, 129(1):57–73, 1996.

[dG85]   P.-G. de Gennes. Wetting: Statics and dynamics. *Rev. Mod. Phys.*, 57:827–863, 1985.

[dGBWQ04]   P.-G. de Gennes, F. Brochard-Wyart, and D. Quéré. *Capillarity and wetting phenomena: Drops, bubbles, pearls, waves*. Springer, New York, 2004.

[DGN$^+$11]   S. Douezan, K. Guevorkian, R. Naouar, S. Dufour, D. Cuvelier, and F. Brochard-Wyart. Spreading dynamics and wetting transition of cellular aggregates. *Proc. Natl. Acad. Sci. U.S.A*, 108(18):7315–7320, 2011.

BIBLIOGRAPHY

[Die88]   S. Dietrich. Wetting phenomena. In C. Domb and J. L. Lebowitz, editors, *Phase Transitions and Critical Phenomena*. Academic Press, London, 1988.

[DKK91]   E. J. Doedel, H. B. Keller, and J. P. Kernevez. Numerical analysis and control of bifurcation problems (i): bifurcation in finite dimensions. *Int. J. Bifurcation Chaos*, 1(03):493–520, 1991.

[DO09]   E. J. Doedel and B. E. Oldeman. *AUTO07p: Continuation and Bifurcation Software for Ordinary Differential Equations*. Concordia University, Montreal, 2009.

[Doi13]   M. Doi. *Soft matter physics*. Oxford University Press, 2013.

[Don02]   R. M. Donlan. Biofilms: Microbial life on surfaces. *Emerg. Infect. Dis.*, 8(9):881–890, 2002.

[DRH+06]   R. Daniels, S. Reynaert, H. Hoekstra, C. Verreth, J. Janssens, K. Braeken, M. Fauvart, S. Beullens, C. Heusdens, I. Lambrichts, et al. Quorum signal molecules as biosurfactants affecting swarming in Rhizobium etli. *Proc. Natl. Acad. Sci. U.S.A*, 103(40):14965–14970, 2006.

[DRvDX14]   P. Deng, L. Roditi, D. van Ditmarsch, and J. Xavier. The ecological basis of morphogenesis: branching patterns in swarming colonies of bacteria. *New J. Phys.*, 16:015006, 2014.

[DTH14]   G. E. Dilanji, M. Teplitski, and S. J. Hagen. Entropy-driven motility of Sinorhizobium meliloti on a semi-solid surface. *Proc. R. Soc. B*, 281(1784), 2014.

[DVM04]   R. Daniels, J. Vanderleyden, and J. Michiels. Quorum sensing and swarming migration in bacteria. *FEMS Microbiol. Rev.*, 28(3):261–289, 2004.

[DWC+14]   H. A. Dijkstra, F. W. Wubs, A. K. Cliffe, E. Doedel, I. F. Dragomirescu, B. Eckhardt, A. Y. Gelfgat, A. Hazel, V. Lucarini, A. G. Salinger, E. T. Phipps, J. Sanchez-Umbria, H. Schuttelaars, L. S. Tuckerman, and U. Thiele. Numerical bifurcation methods and their application to fluid dynamics: Analysis beyond simulation. *Commun. Comput. Phys.*, 15:1–45, 2014.

[EDKNB11]   H. J. Ensikat, P. Ditsche-Kuru, C. Neinhuis, and W. Barthlott. Superhydrophobicity in perfection: the outstanding properties of the lotus leaf. *Beilstein journal of nanotechnology*, 2:152, 2011.

[EG13]   A. Ern and J.-L. Guermond. *Theory and practice of finite elements*, volume 159. Springer Science & Business Media, 2013.

[EMC04]   B. Edmonstone, O. Matar, and R. Craster. Flow of surfactant-laden thin films down an inclined plane. *J. Eng. Math.*, 50(2):141–156, 2004.

[EMC05]   B. Edmonstone, O. Matar, and R. Craster. Surfactant-induced fingering phenomena in thin film flow down an inclined plane. *Physica D*, 209(1):62–79, 2005.

[Eng17]   S. Engelnkemper. *Nonlinear Analysis of Physicochemically Driven Dewetting – Statics and Dynamics –*. PhD thesis, Institute of Theoretical Physics, Westfälische Wilhelms-Universität Münster, 2017.

[EPVL01]   H. J. Eberl, D. F. Parker, and M. Van Loosdrecht. A new deterministic spatio-temporal continuum model for biofilm development. *Comput. Math. Methods Med.*, 3(3):161–175, 2001.

[ESR00]   M. H. Eres, L. W. Schwartz, and R. V. Roy. Fingering phenomena for driven coating films. *Phys. Fluids*, 12:1278–1295, 2000.

[EWS13]   A. Eddi, K. Winkels, and J. H. Snoeijer. Influence of droplet geometry on the coalescence of low viscosity drops. *Phys. Rev. Lett.*, 111(14):144502, 2013.

[FPB$^+$12]   M. Fauvart, P. Phillips, D. Bachaspatimayum, N. Verstraeten, J. Fransaer, J. Michiels, and J. Vermant. Surface tension gradient control of bacterial swarming in colonies of Pseudomonas aeruginosa. *Soft Matter*, 8(1):70–76, 2012.

[FW10]   H. Flemming and J. Wingender. The biofilm matrix. *Nat. Rev. Microbiol.*, 8:623–633, 2010.

[GKCBJ98]   I. Golding, Y. Kozlovsky, I. Cohen, and E. Ben-Jacob. Studies of bacterial branching growth using reaction-diffusion models for colonial development. *Physica A*, 260:510–554, 1998.

[GML08]   L. Giomi, M. C. Marchetti, and T. B. Liverpool. Complex spontaneous flows and concentration banding in active polar films. *Phys. Rev. Lett.*, 101(19):198101, 2008.

[GN15]   J. V. Goddard and S. Naire. The spreading and stability of a surfactant -laden drop on an inclined prewetted substrate. *J. Fluid Mech.*, 772:535–568, 2015.

[GSC$^+$12]   E. Ghelardi, S. Salvetti, M. Ceragioli, S. A. Gueye, F. Celandroni, and S. Senesi. Contribution of surfactin and SwrA to flagellin expression, swimming, and surface motility in Bacillus subtilis. *Appl. Environ. Microbiol.*, 78(18):6540–6544, 2012.

[HCB03]   D. L. Hu, B. Chan, and J. W. Bush. The hydrodynamics of water strider locomotion. *Nature*, 424(6949):663, 2003.

[HCPC04]   A. Hamraoui, M. Cachile, C. Poulard, and A. Cazabat. Fingering phenomena during spreading of surfactant solutions. *Colloids Surf. A*, 250(1-3):215–221, 2004.

[Her01]   S. W. Hermanowicz. A simple 2d biofilm model yields a variety of morphological features. *Math. Biosci.*, 169(1):1–14, 2001.

[HH06]   M. Heil and A. L. Hazel. oomph-lib – an object-oriented multiphysics finite-element library. In *Fluid-structure interaction*, pages 19–49. Springer, 2006.

[HH17]   M. Heil and A. Hazel. The finite element method. In *Documentation on oompoh-lib*. University of Manchester, 2017. available at http://oomph-lib.maths.man.ac.uk/doc/intro.

[Hil98]   R. Hill. Superspreading. *Curr. Opin. Colloid Interface Sci*, 3(3):247–254, 1998.

[HK95]   S. He and J. Ketterson. Surfactant-driven spreading of a liquid on a vertical surface. *Phys. Fluids*, 7:2640–2647, 1995.

[HL14]   H. Horn and S. Lackner. Modeling of biofilm systems: A review. In K. Muffler and R. Ulber, editors, *Productive Biofilms*, volume 146, pages 53–76. Springer International Publishing, 2014.

[HRRS04]   Y. Hatwalne, S. Ramaswamy, M. Rao, and R. A. Simha. Rheology of active-particle suspensions. *Phys. Rev. Lett.*, 92(11):118101, 2004.

[HSLES12]   J. Hernández-Sánchez, L. Lubbers, A. Eddi, and J. H. Snoeijer. Symmetric and asymmetric coalescence of drops on a substrate. *Phys. Rev. Lett.*, 109(18):184502, 2012.

[HTA17]   A. P. Hughes, U. Thiele, and A. J. Archer. Influence of the fluid structure on the binding potential: Comparing liquid drop profiles from density functional theory with results from mesoscopic theory. *J. Chem. Phys.*, 146:064705, 2017.

[Isr85]   J. N. Israelachvili. *Intermolecular and Surface Forces (With Applications to Colloidal and Biological Systems)*. Academic Press, 1985.

[JJKP07]   J.-F. Joanny, F. Jülicher, K. Kruse, and J. Prost. Hydrodynamic theory for multi-component active polar gels. *New J. Phys.*, 9(11):422, 2007.

[JKPJ07]   F. Jülicher, K. Kruse, J. Prost, and J.-F. Joanny. Active behavior of the cytoskeleton. *Phys. Rep*, 449(1-3):3–28, 2007.

[JOHS05]   D. Julkowska, M. Obuchowski, I. B. Holland, and S. J. Séror. Comparative analysis of the development of swarming communities of Bacillus subtilis 168 and a natural wild type: critical effects of surfactin and the composition of the medium. *J. Bacteriol.*, 187(1):65–76, 2005.

[JP09]   J.-F. Joanny and J. Prost. Active gels as a description of the actin-myosin cytoskeleton. *HFSP journal*, 3(2):94–104, 2009.

[JR10]   J.-F. Joanny and S. Ramaswamy. Biological physics: Filaments band together. *Nature*, 467(7311):33, 2010.

[JR12]   J.-F. Joanny and S. Ramaswamy. A drop of active matter. *J. Fluid Mech.*, 705:46–57, 2012.

[KA15]   D. Khoromskaia and G. P. Alexander. Motility of active fluid drops on surfaces. *Phys. Rev. E*, 92:062311, 2015.

[KBB08]   K. Koch, B. Bhushan, and W. Barthlott. Diversity of structure, morphology and wetting of plant surfaces. *Soft Matter*, 4(10):1943–1963, 2008.

[KBK+95]   C. B. Kimmel, W. W. Ballard, S. R. Kimmel, B. Ullmann, and T. F. Schilling. Stages of embryonic development of the zebrafish. *Dev. Dyn.*, 203(3):253–310, 1995.

[KD02]   I. Klapper and J. Dockery. Finger formation in biofilm layers. *SIAM J Appl Math*, 62(3):853–869, 2002.

[KD10]   I. Klapper and J. Dockery. Mathematical description of microbial biofilms. *SIAM Rev.*, 52(2):221–265, 2010.

[Kea10]   D. B. Kearns. A field guide to bacterial swarming motility. *Nat. Rev. Microbiol.*, 8(9):634, 2010.

[Kel79]   H. B. Keller. Constructive methods for bifurcation and nonlinear eigenvalue problems. In *Computing Methods in Applied Sciences and Engineering, 1977, I*, pages 241–251. Springer, 1979.

[KHC+15]   W.-J. Ke, Y.-H. Hsueh, Y.-C. Cheng, C.-C. Wu, and S.-T. Liu. Water surface tension modulates the swarming mechanics of Bacillus subtilis. *Front Microbiol*, 6:1017, 2015.

[KHFR14]   S. Karpitschka, C. Hanske, A. Fery, and H. Riegler. Coalescence and noncoalescence of sessile drops: impact of surface forces. *Langmuir*, 30(23):6826–6830, 2014.

[KJJ+04]   K. Kruse, J.-F. Joanny, F. Jülicher, J. Prost, and K. Sekimoto. Asters, vortices, and rotating spirals in active gels of polar filaments. *Phys. Rev. Lett.*, 92(7):078101, 2004.

[KJJ+05]   K. Kruse, J.-F. Joanny, F. Jülicher, J. Prost, and K. Sekimoto. Generic theory of active polar gels: a paradigm for cytoskeletal dynamics. *Eur. Phys. J. E*, 16(1):5–16, 2005.

[KMM+97]   K. Kawasaki, A. Mochizuki, M. Matsushita, T. Umeda, and N. Shigesada. Modeling spatio-temporal patterns generated by Bacillus subtilis. *J. Theor. Biol.*, 188(2):177–185, 1997.

[KMW17]   G. Kitavtsev, A. Münch, and B. Wagner. Thin film models for active gels. *arXiv preprint arXiv:1710.00309*, 2017.

[KOB07]   J. Krauskopf, H. Osinga, and G.-V. B, editors. *Numerical continuation methods for dynamical systems - Path following and boundary value problems.* Springer, 2007.

[KP12]   S. G. Krantz and H. R. Parks. *The implicit function theorem: history, theory, and applications.* Springer Science & Business Media, 2012.

[KPWvL01]   J.-U. Kreft, C. Picioreanu, J. W. Wimpenny, and M. C. van Loosrecht. Individual-based modelling of biofilms. *Microbiology*, 147(11):2897–2912, 2001.

[KR12]   S. Karpitschka and H. Riegler. Noncoalescence of sessile drops from different but miscible liquids: hydrodynamic analysis of the twin drop contour as a self-stabilizing traveling wave. *Phys. Rev. Lett.*, 109(6):066103, 2012.

BIBLIOGRAPHY

[KR14]   S. Karpitschka and H. Riegler. Sharp transition between coalescence and non-coalescence of sessile drops. *J. Fluid Mech.*, 743, 2014.

[KSF03]   R. F. Kinsinger, M. C. Shirk, and R. Fall. Rapid surface motility in Bacillus subtilis is dependent on extracellular surfactin and potassium ion. *J. Bacteriol.*, 185(18):5627–5631, 2003.

[Kuz13]   Y. A. Kuznetsov. *Elements of applied bifurcation theory*, volume 112. Springer Science & Business Media, 2013.

[LCA+13]   T.-S. Lin, L. J. Cummings, A. J. Archer, L. Kondic, and U. Thiele. Note on the hydrodynamic description of thin nematic films: strong anchoring model. *Phys. Fluids*, 25(8):082102, 2013.

[LKLY16]   M.-H. Lin, W.-J. Ke, C.-C. Liu, and M.-W. Yang. Modulation of staphylococcus aureus spreading by water. *Sci. Rep*, 6:25233, 2016.

[LKTC13]   T.-S. Lin, L. Kondic, U. Thiele, and L. J. Cummings. Modelling spreading dynamics of nematic liquid crystals in three spatial dimensions. *J. Fluid Mech.*, 729:214–230, 2013.

[LKYY12]   M. W. Lee, D. K. Kang, S. S. Yoon, and A. L. Yarin. Coalescence of two drops on partially wettable substrates. *Langmuir*, 28(8):3791–3798, 2012.

[LM06]   T. B. Liverpool and M. C. Marchetti. Rheology of active filament solutions. *Phys. Rev. Lett.*, 97(26):268101, 2006.

[LMB+06]   V. Leclère, R. Marti, M. Bóchet, P. Fickers, and P. Jacques. The lipopeptides mycosubtilin and surfactin enhance spreading of Bacillus subtilis strains by their surface-active properties. *Arch. Microbiol.*, 186(6):475–483, 2006.

[LW12]   A. E. LaBauve and M. J. Wargo. Growth and laboratory maintenance of Pseudomonas aeruginosa. *Curr Protoc Microbiol*, pages 6E–1, 2012.

[LZA15]   J. Löber, F. Ziebert, and I. S. Aranson. Collisions of deformable cells lead to collective migration. *Sci. Rep*, 5:9172, 2015.

[MC09]   O. K. Matar and R. V. Craster. Dynamics of surfactant-assisted spreading. *Soft Matter*, 5:3801–3809, 2009.

[Men15]   A. M. Menzel. Tuned, driven, and active soft matter. *Phys. Rep*, 554:1 – 45, 2015.

[MF90]   M. Matsushita and H. Fujikawa. Diffusion-limited growth in bacterial colony formation. *Physica A: Statistical Mechanics and its Applications*, 168(1):498 – 506, 1990.

[MGB+17]   H. Morita, S. Grigolon, M. Bock, S. G. Krens, G. Salbreux, and C.-P. Heisenberg. The physical basis of coordinated tissue spreading in zebrafish gastrulation. *Dev. Cell*, 40(4):354–366, 2017.

[MHH+10]   A. Marrocco, H. Henry, I. Holland, M. Plapp, S. Séror, and B. Perthame. Models of self-organizing bacterial communities and comparisons with experimental observations. *Math Model Nat Phenom*, 5(1):148–162, 2010.

[Mit93]   V. S. Mitlin. Dewetting of solid surface: Analogy with spinodal decomposition. *J. Colloid Interface Sci.*, 156(2):491–497, 1993.

[MJR$^+$13]   M. C. Marchetti, J. F. Joanny, S. Ramaswamy, T. B. Liverpool, J. Prost, M. Rao, and R. A. Simha. Hydrodynamics of soft active matter. *Rev. Mod. Phys.*, 85:1143–1189, Jul 2013.

[ML81]   A. Marmur and M. D. Lelah. The spreading of aqueous surfactant solutions on glass. *Chem. Eng. Commun.*, 13(1-3):133–143, 1981.

[MN96a]   T. Matsuyama and Y. Nakagawa. Bacterial wetting agents working in colonization of bacteria on surface environments. *Colloids Surf B Biointerfaces*, 7(5):207 – 214, 1996.

[MN96b]   T. Matsuyama and Y. Nakagawa. Surface-active exolipids: analysis of absolute chemical structures and biological functions. *J. Microbiol. Methods*, 25(2):165 – 175, 1996.

[MSM00]   M. Mimura, H. Sakaguchi, and M. Matsushita. Reaction–diffusion modelling of bacterial colony patterns. *Physica A*, 282(1-2):283–303, 2000.

[MT99]   O. K. Matar and S. M. Troian. The development of transient fingering patterns during the spreading of surfactant coated films. *Phys. of Fluids*, 11(11):3232–3246, 1999.

[Mur02]   J. Murray. *Mathematical Biology.* Springer New York, 2002.

[MWP15]   S. Marth, V. Wieland, and A. Praetorius. A mechanism for cell motility by active polar gels. *J. Royal Soc. Interface*, 12(107):20150161, 2015.

[Nic03]   J. Nicolas. Molecular dynamics simulation of surfactin molecules at the water-hexane interface. *Biophys. J.*, 85(3):1377–1391, 2003.

[NT10]   L. Ó. Náraigh and J. L. Thiffeault. Nonlinear dynamics of phase separation in thin films. *Nonlinearity*, 23:1559–1583, 2010.

[ODB97]   A. Oron, S. Davis, and S. Bankoff. Long-scale evolution of thin liquid films. *Rev. Mod. Phys.*, 69:931–980, 1997.

[Ons31]   L. Onsager. Reciprocal relations in irreversible processes. I. *Phys. Rev.*, 37(4):405, 1931.

[OSDMM14]   A. Oslizlo, P. Stefanic, I. Dogsa, and I. Mandic-Mulec. Private link between signal and response in Bacillus subtilis quorum sensing. *Proc. Natl. Acad. Sci. U.S.A*, 111(4):1586–1591, 2014.

[PJJ15]   J. Prost, F. Jülicher, and J. Joanny. Active gel physics. *Nat. Phys*, 11(2):111–117, 2015.

[PKvL04]   C. Picioreanu, J.-U. Kreft, and M. C. van Loosdrecht. Particle-based multidimensional multispecies biofilm model. *Appl. Environ. Microbiol.*, 70(5):3024–3040, 2004.

[Pro95]   J. Prost. *The physics of liquid crystals*, volume 83. Oxford university press, 1995.

[PS05]   J. Peiró and S. Sherwin. *Handbook of Materials Modeling*, chapter Finite Difference, Finite Element and Finite Volume Methods for Partial Differential Equations, pages 2415 – 2446. Springer, Dordrecht, 2005.

[PSD+12]   M. Pinot, V. Steiner, B. Dehapiot, B.-K. Yoo, F. Chesnel, L. Blanchoin, C. Kervrann, and Z. Gueroui. Confinement induces actin flow in a meiotic cytoplasm. *Proc. Natl. Acad. Sci. U. S. A*, 109(29):11705–11710, 2012.

[PSJ+12]   F. Peruani, J. Starruß, V. Jakovljevic, L. Søgaard-Andersen, A. Deutsch, and M. Bär. Collective motion and nonequilibrium cluster formation in colonies of gliding bacteria. *Phys. Rev. Lett.*, 108(9):098102, 2012.

[PVL03]   C. Picioreanu and M. Van Loosdrecht. *Biofilms in Medicine, Industry and Environmental Biotechnology - Characteritics, Analysis and Control*, chapter Use of mathematical modelling to study biofilm development and morphology. IWA Publishing, 2003.

[PVLH+98]   C. Picioreanu, M. C. Van Loosdrecht, J. J. Heijnen, et al. Mathematical modeling of biofilm structure with a hybrid differential-discrete cellular automaton approach. *Biotechnol. Bioeng.*, 58(1):101–116, 1998.

[PVLH00]   C. Picioreanu, M. C. M. Van Loosdrecht, and J. J. Heijnen. Effect of diffusive and convective substrate transport on biofilm structure formation: A two-dimensional modeling study. *Biotechnol. Bioeng.*, 69(5):504–515, 2000.

[PWH+14]   L. Ping, Y. Wu, B. G. Hosu, J. X. Tang, and H. C. Berg. Osmotic pressure in a bacterial swarm. *Biophys. J.*, 107(4):871–878, 2014.

[Ram10]   S. Ramaswamy. The mechanics and statistics of active matter. *Annu. Rev. Condens. Matter Phys*, 1(1):323–345, 2010.

[RDBNO10]   J. M. Raaijmakers, I. De Bruijn, O. Nybroe, and M. Ongena. Natural functions of lipopeptides from Bacillus and Pseudomonas: more than surfactants and antibiotics. *FEMS Microbiol. Rev.*, 34(6):1037–1062, 2010.

[RK12]   M. J. Rosen and J. T. Kunjappu. *Surfactants and interfacial phenomena*. John Wiley & Sons, 2012.

[RM12]   B. E. Rittmann and P. L. McCarty. *Environmental biotechnology: principles and applications*. Tata McGraw-Hill Education, 2012.

[RMRS06]   W. Ristenpart, P. McCalla, R. Roy, and H. Stone. Coalescence of spreading droplets on a wettable substrate. *Phys. Rev. Lett.*, 97(6):064501, 2006.

[RR01]   E. Z. Ron and E. Rosenberg. Natural roles of biosurfactants. *Environ. Microbiol.*, 3(4):229–236, 2001.

[RSB+02]   S. Rafaï, D. Sarker, V. Bergeron, J. Meunier, and D. Bonn. Superspreading: aqueous surfactant drops spreading on hydrophobic surfaces. *Langmuir*, 18(26):10486–10488, 2002.

[SA13]   J. H. Snoeijer and B. Andreotti. Moving contact lines: scales, regimes, and dynamical transitions. *Annu. Rev. Fluid Mech.*, 45:269–292, 2013.

[SAW+12]   A. Seminara, T. Angelini, J. Wilking, H. Vlamakis, S. Ebrahim, R. Kolter, D. Weitz, and M. Brenner. Osmotic spreading of Bacillus subtilis biofilms driven by an extracellular matrix. *Proc. Natl. Acad. Sci. U. S. A*, 109:1116–1121, 2012.

[SCD+12]   T. Sanchez, D. T. Chen, S. J. DeCamp, M. Heymann, and Z. Dogic. Spontaneous motion in hierarchically assembled active matter. *Nature*, 491(7424):431, 2012.

[Sch90]   M. Schick. *Liquids at Interfaces*, chapter Introduction to wetting phenomena. 1990.

[Sha93]   A. Sharma. Equilibrium contact angles and film thicknesses in the apolar and polar systems: Role of intermolecular interactions in coexistence of drops with thin films. *Langmuir*, 9(12):3580–3586, 1993.

[SK14]   E. A. Shah and K. Keren. Symmetry breaking in reconstituted actin cortices. *Elife*, 3:e01433, 2014.

[SLVC+12]   J. Schwarz-Linek, C. Valeriani, A. Cacciuto, M. E. Cates, D. Marenduzzo, A. N. Morozov, and W. C. K. Poon. Phase separation and rotor self-assembly in active particle suspensions. *Proc. Natl. Acad. Sci. U. S. A*, 2012.

[SNS+12]   Y. Sumino, K. H. Nagai, Y. Shitaka, D. Tanaka, K. Yoshikawa, H. Chaté, and K. Oiwa. Large-scale vortex lattice emerging from collectively moving microtubules. *Nature*, 483(7390):448, 2012.

[SR85]   A. Sharma and E. Ruckenstein. Mechanism of tear film rupture and its implications for contact lens tolerance. *Am. J. Optom. Physiol. Opt.*, 62(4):246–253, 1985.

[SR09]   S. Sankararaman and S. Ramaswamy. Instabilities and waves in thin films of living fluids. *Phys. Rev. Lett.*, 102:118107, 2009.

[SSDC02]   P. Stoodley, K. Sauer, D. G. Davies, and J. W. Costerton. Biofilms as complex differentiated communities. *Annu. Rev. Microbiol.*, 56:187–209, 2002.

[SVK+18]   S. Srinivasan, I. D. Vladescu, S. A. Koehler, X. Wang, M. Mani, and S. M. Rubinstein. Matrix production and sporulation in Bacillus subtilis biofilms localize to propagating wave fronts. *Biophys. J*, 114(6):1490–1498, 2018.

[SWS+10]   V. Schaller, C. Weber, C. Semmrich, E. Frey, and A. R. Bausch. Polar patterns of driven filaments. *Nature*, 467(7311):73, 2010.

[Tan79]   L. Tanner. The spreading of silicone oil drops on horizontal surfaces. *J. Phys. D: Appl. Phys.*, 12(9):1473, 1979.

[TAP12]   U. Thiele, A. J. Archer, and M. Plapp. Thermodynamically consistent description of the hydrodynamics of free surfaces covered by insoluble surfactants of high concentration. *Phys. Fluids*, 24:102107, 2012.

[TAP16]   U. Thiele, A. Archer, and L. Pismen. Gradient dynamics models for liquid films with soluble surfactant. *Phys. Rev. Fluids*, 1:083903, 2016.

[TCM11]   E. Tjhung, M. E. Cates, and D. Marenduzzo. Nonequilibrium steady states in polar active fluids. *Soft Matter*, 7(16):7453–7464, 2011.

[Tew18]   W. Tewes. *Capillarity- and Wettability-Dominated Instabilities of Liquids on Solid Substrates*. PhD thesis, Institute of Theoretical Physics, Westfälische Wilhelms-Universität Münster, 2018.

[Thi07]   U. Thiele. Structure formation in thin liquid films. In S. Kalliadasis and U. Thiele, editors, *Thin Films of Soft Matter*, pages 25–93, Wien, 2007. Springer.

[Thi10]   U. Thiele. Thin film evolution equations from (evaporating) dewetting liquid layers to epitaxial growth. *J. Phys.: Condens. Matter*, 22:084019, 2010.

[Thi11]   U. Thiele. Note on thin film equations for solutions and suspensions. *Europ. Phys. J. - Special Topics*, 197(1):213–220, 2011.

[Thi15a]   U. Thiele. Münsteranian Torturials: CCH - Travelling drops and waves in the convective Cahn-Hilliard equation. In U. Thiele, O. Kamps, and S. V. Gurevich, editors, *Münsteranian Torturials on Nonlinear Science: Continuation*. CeNoS, Münster, 1 edition, 2015. available at https://www.uni-muenster.de/CeNoS/Lehre/Tutorials/.

[Thi15b]   U. Thiele. Münsteranian Torturials: LINDROP - Linear stability of steady solutions of a thin film equation for a horizontal homogeneous substrate. In U. Thiele, O. Kamps, and S. V. Gurevich, editors, *Münsteranian Torturials on Nonlinear Science: Continuation*. CeNoS, Münster, 1 edition, 2015. available at https://www.uni-muenster.de/CeNoS/Lehre/Tutorials/.

[Thi15c]   U. Thiele. Prelude to the Münsteranian Torturials: Numerical continuation - a step by step introduction. In U. Thiele, O. Kamps, and S. V. Gurevich, editors, *Münsteranian Torturials on Nonlinear Science: Continuation*. CeNoS, Münster, 2015. available at https://www.uni-muenster.de/CeNoS/Lehre/Tutorials/.

[THS90]   S. M. Troian, E. Herbolzheimer, and S. A. Safran. Model for the fingering instability of spreading surfactant drops. *Phys. Rev. Lett.*, 65:333–336, 1990.

[TJLT17]   S. Trinschek, K. John, S. Lecuyer, and U. Thiele. Continuous versus arrested spreading of biofilms at solid-gas interfaces: The role of surface forces. *Phys. Rev. Lett.*, 119(7):078003, 2017.

[TJT16]   S. Trinschek, K. John, and U. Thiele. From a thin film model for passive suspensions towards the description of osmotic biofilm spreading. *AIMS Materials Science*, 3:1138–1159, 2016.

[TJT18]   S. Trinschek, K. John, and U. Thiele. Modelling of surfactant-driven front instabilities in spreading bacterial colonies. *Soft Matter*, 14(22):4464–4476, 2018.

[TMC12]   E. Tjhung, D. Marenduzzo, and M. E. Cates. Spontaneous symmetry breaking in active droplets provides a generic route to motility. *Proc. Natl. Acad. Sci. U. S. A*, 109(31):12381–12386, 2012.

[TMTT13]   N. Tretyakov, M. Müller, D. Todorova, and U. Thiele. Parameter passing between molecular dynamics and continuum models for droplets on solid substrates: The static case. *J. Chem. Phys.*, 138:064905, 2013.

[TRLD07]   J. Tremblay, A.-P. Richardson, F. Lépine, and E. Déziel. Self-produced extracellular stimuli modulate the Pseudomonas aeruginosa swarming motility behaviour. *Environ. Microbiol.*, 9(10):2622–2630, 2007.

[TSTJ18]   U. Thiele, J. H. Snoeijer, S. Trinschek, and K. John. Equilibrium contact angle and adsorption layer properties with surfactants. *Langmuir*, 2018.

[TSTJ19]   U. Thiele, J. H. Snoeijer, S. Trinschek, and K. John. Correction to 'Equilibrium contact angle and adsorption layer properties with surfactants'. *Langmuir*, 35(13):4788–4789, 2019.

[TTL13]   U. Thiele, D. V. Todorova, and H. Lopez. Gradient dynamics description for films of mixtures and suspensions: Dewetting triggered by coupled film height and concentration fluctuations. *Phys. Rev. Lett.*, 111:117801, 2013.

[TTMC15]   E. Tjhung, A. Tiribocchi, D. Marenduzzo, and M. Cates. A minimal physical model captures the shapes of crawling cells. *Nat. Commun*, 6:5420, 2015.

[TVN$^+$01]   U. Thiele, M. G. Velarde, K. Neuffer, M. Bestehorn, and Y. Pomeau. Sliding drops in the diffuse interface model coupled to hydrodynamics. *Physical Review E*, 64(6):061601, 2001.

[TWS89]   S. M. Troian, X. L. Wu, and S. A. Safran. Fingering instability in thin wetting films. *Phys. Rev. Lett.*, 62:1496—1499, 1989.

[UWR14]   H. Uecker, D. Wetzel, and J. D. Rademacher. pde2path - A matlab package for continuation and bifurcation in 2d elliptic systems. *Numerical Mathematics: Theory, Methods and Applications*, 7(1):58–106, 2014.

[VALK08]   H. Vlamakis, C. Aguilar, R. Losick, and R. Kolter. Control of cell fate by the formation of an architecturally complex bacterial community. *Genes Dev.*, 22(7):945–953, 2008.

[VBD$^+$08]   N. Verstraeten, K. Braeken, B. Debkumari, M. Fauvart, J. Fransaer, J. Vermant, and J. Michiels. Living on a surface: swarming and biofilm formation. *Trends Microbiol.*, 16(10):496–506, 2008.

[VCB$^+$13]   H. Vlamakis, Y. Chai, P. Beauregard, R. Losick, and R. Kolter. Sticking together: building a biofilm the Bacillus subtilis way. *Nat. Rev. Microbiol.*, 11(3):157–168, 2013.

[vGVK15]   J. van Gestel, H. Vlamakis, and R. Kolter. From cell differentiation to cell collectives: Bacillus subtilis uses division of labor to migrate. *PLoS Biol.*, 13(4):e1002141, 2015.

[VJP06]   R. Voituriez, J. Joanny, and J. Prost. Generic phase diagram of active polar films. *Phys. Rev. Lett.*, 96(2):028102, 2006.

[VRR96]   M. G. Velarde, A. Y. Rednikov, and Y. S. Ryazantsev. Drop motions and interfacial instability. *J. Phys.: Condens. Matter*, 8:9233–9247, 1996.

[WAS$^+$11] J. N. Wilking, T. E. Angelini, A. Seminara, M. P. Brenner, and D. A. Weitz. Biofilms as complex fluids. *MRS Bulletin*, 36:385–391, 5 2011.

[WC97]   J. W. Wimpenny and R. Colasanti. A unifying hypothesis for the structure of microbial biofilms based on cellular automaton models. *FEMS Microbiol. Ecol.*, 22(1):1–16, 1997.

[WCM02]   M. Warner, R. Craster, and O. Matar. Dewetting of ultrathin surfactant-covered films. *Phys. Fluids*, 14(11):4040–4054, 2002.

[WCM04a]   M. Warner, R. Craster, and O. Matar. Fingering phenomena associated with insoluble surfactant spreading on thin liquid films. *J. Fluid Mech.*, 510:169–200, 2004.

[WCM04b]   M. Warner, R. Craster, and O. Matar. Fingering phenomena created by a soluble surfactant deposition on a thin liquid film. *Phys. Fluids*, 16(8):2933–2951, 2004.

[WDH$^+$12] H. Wensink, J. Dunkel, S. Heidenreich, K. Drescher, R. Goldstein, H. Lowen, and J. Yeomans. Meso-scale turbulence in living fluids. *Proc. Natl. Acad. Sci. U. S. A.*, 109:14308–14313, 2012.

[WG86]   O. Wanner and W. Gujer. A multispecies biofilm model. *Biotechnol. Bioeng.*, 28(3):314–328, 1986.

[WH16]   C. A. Whitfield and R. J. Hawkins. Instabilities, motion and deformation of active fluid droplets. *New J. Phys.*, 18(12):123016, 2016.

[Wil16]   M. Wilczek. *Pattern Formation in Driven Thin Layers of Simple and Complex Liquids*. PhD thesis, Institute of Theoretical Physics, Westfälische Wilhelms-Universität Münster, 2016.

[WJ01]   H. Williams and O. Jensen. Two-dimensional nonlinear advection-diffusion in a model of surfactant spreading on a thin liquid film. *IMA J. Appl. Math.*, 66:55–82, 2001.

[WK12]   J. Ward and J. King. Thin-film modelling of biofilm growth and quorum sensing. *J. Eng. Math.*, 73:71–92, 2012.

[WKK$^+$01] J. Ward, J. King, A. Koerber, P. Williams, J. Croft, and R. Sockett. Mathematical modelling of quorum sensing in bacteria. *IMA J. Math. Appl. Med. Biol.*, 18:263–292, 2001.

[WKW$^+$16] X. Wang, S. A. Koehler, J. N. Wilking, N. N. Sinha, M. T. Cabeen, S. Srinivasan, A. Seminara, S. Rubinstein, Q. Sun, M. P. Brenner, et al. Probing phenotypic growth in expanding Bacillus subtilis biofilms. *Appl. Microbiol. Biotechnol.*, 100(10):4607–4615, 2016.

[WMVH14]   C. A. Whitfield, D. Marenduzzo, R. Voituriez, and R. J. Hawkins. Active polar fluid flow in finite droplets. *Eur. Phys. J. E*, 37(2):8, 2014.

[WTG⁺15]   M. Wilczek, W. B. H. Tewes, S. V. Gurevich, M. H. Köpf, L. Chi, and U. Thiele. Modelling pattern formation in dip-coating experiments. *Math. Model. Nat. Phenom.*, 10:44–60, 2015.

[WTY⁺18]   B. Wallmeyer, S. Trinschek, S. Yigit, U. Thiele, and T. Betz. Collective cell migration in embryogenesis follows the laws of wetting. *Biophys. J.*, 114(1):213–222, 2018.

[WWD⁺13]   H. Wioland, F. G. Woodhouse, J. Dunkel, J. O. Kessler, and R. E. Goldstein. Confinement stabilizes a bacterial suspension into a spiral vortex. *Phys. Rev. Lett.*, 110(26):268102, 2013.

[WZ10]   Q. Wang and T. Zhang. Review of mathematical models for biofilms. *Solid State Comm.*, 150(21 - 22):1009 – 1022, 2010.

[WZDV⁺13]   J. N. Wilking, V. Zaburdaev, M. De Volder, R. Losick, M. P. Brenner, and D. A. Weitz. Liquid transport facilitated by channels in Bacillus subtilis biofilms. *Proc. Natl. Acad. Sci. U. S. A.*, 110:848–852, 2013.

[XTQ15]   X. Xu, U. Thiele, and T. Qian. A variational approach to thin film hydrodynamics of binary mixtures. *J. Phys.: Condens. Matter*, 27(8):085005, 2015.

[YNS⁺17]   J. Yan, C. D. Nadell, H. A. Stone, N. S. Wingreen, and B. L. Bassler. Extracellular-matrix-mediated osmotic pressure drives Vibrio cholerae biofilm expansion and cheater exclusion. *Nat. Commun*, 8(1):327, 2017.

[You05]   T. Young. Iii. an essay on the cohesion of fluids. *Philos. Trans. Roy. Soc. London*, 95:65–87, 1805.

[YTST17]   A. Yang, W. S. Tang, T. Si, and J. X. Tang. Influence of physical effects on the swarming motility of Pseudomonas aeruginosa. *Biophys. J.*, 112(7):1462–1471, 2017.

[ZBFS10]   H.-P. Zhang, A. Be'er, E.-L. Florin, and H. L. Swinney. Collective motion and density fluctuations in bacterial colonies. *Proc. Natl. Acad. Sci. U. S. A*, 107(31):13626–13630, 2010.

[ZCW08a]   T. Zhang, N. Cogan, and Q. Wang. Phase field models for biofilms. I. theory and one-dimensional simulations. *SIAM Journal on Applied Mathematics*, 69(3):641–669, 2008.

[ZCW08b]   T. Zhang, N. Cogan, and Q. Wang. Phase field models for biofilms. II. 2-d numerical simulations of biofilm-flow interaction. *Commun. Comput. Phys*, 4(1):72–101, 2008.

[ZSA12]   F. Ziebert, S. Swaminathan, and I. S. Aranson. Model for self-polarization and motility of keratocyte fragments. *J. Royal Soc. Interface*, 9(70):1084–1092, 2012.

[ZSS⁺14]   W. Zhang, A. Seminara, M. Suaris, M. P. Brenner, D. A. Weitz, and T. E. Angelini. Nutrient depletion in Bacillus subtilis biofilms triggers matrix production. *New J. of Phys.*, 16(1):015028, 2014.

Danksagung

An dieser Stelle möchte ich mich bei all denjenigen bedanken, die mich während des Promotionsprojekts unterstützt haben:

... bei Prof. Dr. Uwe Thiele und Dr. Karin John für ihre sehr engagierte und unkomplizierte Betreuung meiner Promotion, die wertvolle Hilfe in vielen Fragen und die bereitwillige Inkaufnahme des organisatorischen Mehraufwandes, den ein binationales Promotionsprojekt mit sich bringt.

... bei der Studienstiftung des deutschen Volkes für die langjährige finanzielle und ideelle Förderung.

... bei Bernhard Wallmeyer, Sargon Yigit und Prof. Dr. Timo Betz für eine angenehme und erfolgreiche Kooperation, in der ich einiges über Zebrafische gelernt habe.

... bei Prof. Dr. Jacco Snoeijer für eine spannende Zusammenarbeit und aufschlussreiche Diskussionen.

... bei den derzeitigen und ehemaligen Mitgliedern der Arbeitsgruppe Thiele für zahlreiche nette Kaffeepausen und schöne Wanderungen im Kleinwalsertal sowie bei den Doktoranden des LiPhy für ihre Offenheit, Gastfreundschaft und das ein oder andere Bergabenteuer.

... bei meinen Korrekturlesern Lukas Ophaus, Walter Tewes, Fenna Stegemerten, Tobias Frohoff-Hülsmann, Tobias Schemmelmann und Florian Kirschke für die konstruktive Kritik und vielen Verbesserungen an dieser Arbeit.

... bei Markus Wilczek und Walter Tewes für ihr stets offenes Ohr, interessante Diskussionen, ihre große Hilfsbereitschaft bei vielen Fragen und die Starthilfe zum Thema DUNE.

... bei meinen Büro- und Nachbarbüro-Kollegen Lukas Ophaus, Felix Tabbert und Max Holl für die angenehme Arbeitsatmosphäre und Motivation, Ablenkung oder Aufmunterung zur rechten Zeit.

... bei meinen Eltern, Geschwistern und Florian für die bedingungslose Unterstützung in allen Lebenslagen und den Rückhalt, auf den ich immer zählen kann.

Lebenslauf

Name:	Sarah Christine Trinschek
Geburtsdatum:	23. August 1990
Geburtsort:	Hamm
Staatsangehörigkeit:	deutsch
Familienstand:	ledig

Schulbildung

1997 – 2001	Geistschule Hamm
2001 – 2009	Märkisches Gynmasium Hamm
06/2009	Allgemeine Hochschulreife (Note 1,0)

Studium

2009 – 2012	Bachelorstudium im Fach Physik an der Westfälischen Wilhelms-Universität Münster
09/2012	**Abschluss Bachelor of Science** (Note 1,1) Titel der Bachelorarbeit: Theoretische Untersuchungen der Spin-Bahn-Kopplung bei adsorbatbedeckten Halbleiteroberflächen
2012 – 2015	Masterstudium im Fach Physik an der Westfälischen Wilhelms-Universität Münster
09/2013 – 01/2014	Auslandsaufenthalt an der University of York, GB
03/2015	**Abschluss Master of Science** (Note 1,0) Titel der Masterarbeit: Dynamik attraktiv und repulsiv verkoppelter elementarer chaotischer Systeme

Promotionsstudium

06/2015 – 03/2019	**Binationale Promotion** am Institut für Theoretische Physik der Westfälischen Wilhelms-Universität Münster sowie am Laboratoire Inderdisciplinaire de Physique der Université Grenoble-Alpes, Frankreich unter der Betreuung von Prof. Dr. Uwe Thiele, Prof. Dr. Chaouqi Misbah und Dr. Karin John

Stipendien

11/2010 – 04/2015	Stipendium der Studienstiftung des deutschen Volkes
seit 09/2016	Promotionsstipendum der Studienstiftung des deutschen Volkes

Berufstätigkeit

10/2010 – 03/2012	Studentische Hilfskraft an der Westfälischen Wilhelms-Universität Münster
10/2012 – 09/2013	Studentische Hilfskraft an der Westfälischen Wilhelms-Universität Münster
05/2015 – 03/2016	Wissenschaftliche Hilfskraft am Institut für Theoretische Physik der Westfälischen Wilhelms-Universität Münster
04/2016 – 08/2016	Wissenschaftliche Mitarbeiterin am Institut für Theoretische Physik der Westfälischen Wilhelms-Universität Münster
seit 09/2016	Wissenschaftliche Hilfskraft am Institut für Theoretische Physik der Westfälischen Wilhelms-Universität Münster